ISSN 2186-7968

ELPH ANNUAL REPORT

2018

TOHOKU UNIVERSITY

Editor

MURAMATSU, Norihito
KIKUNAGA, Hidetoshi
ITOH, Takehiko
MUTO, Toshiya
TOKIYASU, Atsushi

Research Center for Electron Photon Science
Tohoku University
1-2-1 Mikamine, Taihaku, Sendai 982-0826
Japan

Phone: +81, 22-743-3400
Fax: +81, 22-743-3402
Web site: http://www.lns.tohoku.ac.jp/

982-0826　仙台市太白区三神峯1-2-1
東北大学電子光理学研究センター
電話　022-743-3400
Fax　022-743-3402

Preface

We are pleased to issue the “ELPH Annual Report 2018” that covers scientific and technical activities carried out at Research Center for Electron Photon Science (ELPH), Tohoku University in FY2018 (April, 2018 to March, 2019).

The ELPH has been in a second organization term of Joint Usage / Research Centers. The Joint Usage / Research Centers (JURC) system was engaged in FY2010 by the Ministry of Education, Culture, Sports, Science and Technology (MEXT) to encourage and promote collaborative research passing through the border of respective universities. In FY2018, an interim evaluation for the first half term was performed. The opinion insisting that the evaluation results should be reflected for budget distribution has been so intense that they employed a relative evaluation for JURC. The MEXT declared that 30 % of JURC would have budget reduction. This is not fully acceptable for the most of JURC members. I do not want to criticize the system here, fortunately ELPH succeeded to get some increased amount relying on strong supports from users and communities.

However, we have still suffered shortage of budget, particularly the cost of electricity for the accelerator operation is crucial. In FY2018, we, nevertheless, got loaned expense for replacing the RF power amp in the synchrotron for solid state one that is reducing electricity power.

“The ELPH Symposium”, which is to explore the interest of basic science and post the amount of scientific information for mutual collaboration between different scientific fields, has been annually held since FY2017. In March 2019, the 2nd ELPH symposium was carried out. This time we invited Prof. Tomoko Nakanishi of University of Tokyo, now the president of Hoshi University. She gave us a wonderful talk regarding radioisotope (RI) application for botanical science. Since RI production and its application is one of the major sciences in ELPH activity, we hope further collaboration is being spread and developed.

We sincerely ask facility users and related scientific field communities for continuous supports and cooperation.

November, 2019
Director
Hiroyuki Hama

ELPH Annual Report 2018

Contents

I. Topics

II. Papers

III. Status Report

I. Topics

A report on outreach activities at the Research Center for Electron Photon Science (ELPH)

Hiroaki Ohnishi*

§1. Introduction

The introduction of our scientific research projects and educational activities for science to the public is one of the important responsibilities imposed on the Joint Usage/Research center, such as the research center of ELectron Photon Science (ELPH). For that purpose, we have conducted an open campus event every other year to invite people including elementary, junior high school and high school students living near our facility. Moreover, we are constantly inviting high school students to try to get an understanding of the science that is being explored at ELPH using accelerators.

In this report, a digest of the open campus in 2018, and a summary of the facility tour event of students from Miyagi first senior High School will be introduced.

§2. Open Campus 2018

On April 14th, the ELPH Open Campus was held at the Mikamine campus of Tohoku University, where ELPH is located. Open Campus consisted of (1) ELPH facility tour, (2) experience conner and (3) General lecture by Prof. T. Suda entitled "Story on Elements - From the Lightest Hydrogen to the Super Heavy Element, i.e., Nihonium" In total, about two hundred people were coming to the events. We explained science projects we are conducting at the ELPH facility in front of the accelerator and experimental apparatus. Moreover, many participants, especially children, enjoyed the experience conner such as demonstration of a cloud chamber, production of hand made a simple light spectrometer, play with a magnet and gyroscope. Snapshot of the facility tour and experience conner was shown in Fig. 1

Research Center for Electron Photon Science, Tohoku University

東北大学電子光理学研究センター

一般公開 2018

お子様から大人まで楽しめる企画盛りだくさん！

特別講演　会場：三神峯ホール　13：00−13：50

東北大学電子光理学研究センター　教授　須田利美

元素についての話

〜最も軽い水素から超重元素ニホニウムまで〜

2018 年 4 月 14 日 10:00〜16:00 土

§3. Facility tour of Miyagi First Senior High school students

On October 17th in 2019, about eighty students visited ELPH as part of their science education. Prof. H. Ohnishi made a general lecture for an overview of the nuclear hadron physics and Associate Prof. H. Kikunaga did a lecture about introduction to radiochemistry. After the lecture, students visited the accelerator facility and experimental areas. Due to the passionate explanations by staff members and active discussions with students, the facility tour has ended well exceeded the allocated time slot.

---

[*] Present address: Research Center for Electron Photon Science, Tohoku University, Sendai, 982-0826

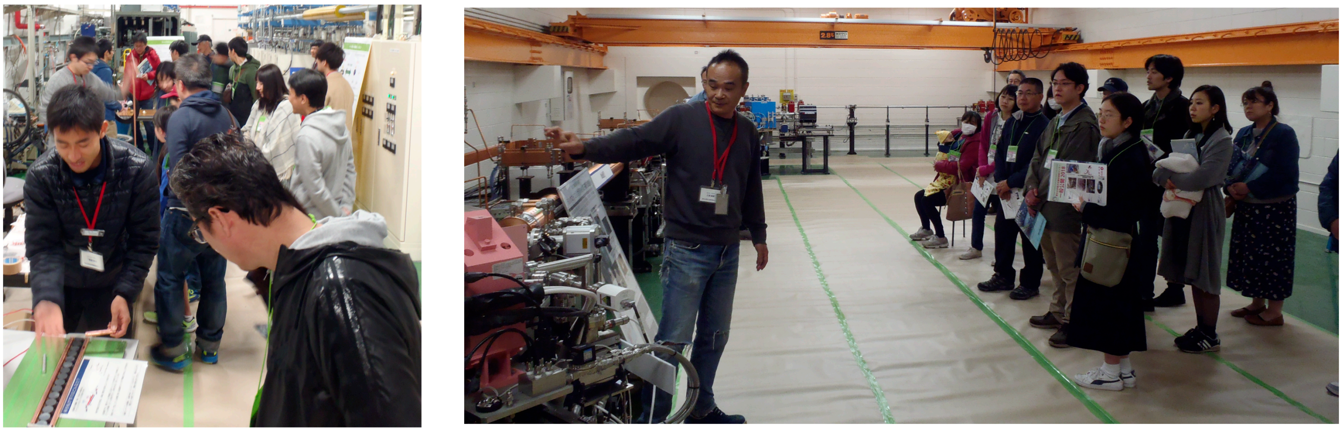

Fig.1. Snap shot of the facility tour and experience conner

Fig.2. Snap shot of the lecture and facility tour.

§4. Future prospectives

The next open campus is now planning in the spring of 2020. To invite more people, we need to explore efficient ways of advisement for the event. In addition, it may also be important to make a closed connection between the public relations section on the Faculty of Science at Tohoku University and ELPH. Moreover, we also need to find a way how can we reach the local community more closely. it will be excellent if we succeed to make a joint project with the local community as an outreach project for ELPH. The door on the ELPH is always open for the public, we need to continue to take actions to outside to enlighten science. It is one of the missions for us, ELPH.

Overview of Condensed Matter Nuclear Reaction Division

Yasuhiro Iwamura
Research Center for Electron Photon Science, Tohoku University, Sendai, 982-0826

Global warming has become an undisputed fact and an energy source that does not produce greenhouse gases such as carbon dioxide is more and more strongly demanded. Because of this, renewable energy use has increased worldwide, but the renewable energy has low energy density and the output energy fluctuates depending on weather conditions. On the other hand, nuclear energy has high energy density but has serious problems such as radioactive waste and the Fukushima disaster. It is expected that nuclear energy will not increase, because society opposes it.

The anomalous heat generation phenomenon, which cannot be explained by any known chemical process, has been reported in experimental systems that consist of nano-sized metal composite and hydrogen gas [1-5]. This phenomenon is recognized as one in a category of Condensed Matter Nuclear Reaction (CMNR). Strong and hazardous gamma-rays or neutrons, which effect the human body, have not been observed during the generation of anomalous heat. This phenomenon has potential for realization of a new safe and compact energy source that would provide us enough energy to meet all our needs without carbon dioxide emissions.

The Condensed Matter Nuclear Reaction Division of Research Center for Electron Photon Science at Tohoku University has started since April. 2015. It is the first official research division created for condensed matter nuclear reaction (CMNR) and its application in Japan. The organization of the division is illustrated in Fig.1. Y. Iwamura and T. Itoh were investigating nuclear transmutation reactions observed in the nano-sized Pd complexes induced by D2 gas permeation [6-8] and left Mitsubishi Heavy Industries, ltd. to join the division. Y. Iwamura is a research professor of Tohoku University and T. Itoh is a visiting associate professor. Itoh is also a director of Clean Planet Inc. J. Kasagi is a professor emeritus and has been investigating the electronic and ionic screening effects on low-energy nuclear reactions in condensed matter as described in the former section. H. Kikunaga is an associate professor and has been engaged in the field of radiochemistry. H. Yoshino is a visiting researcher in this division and a CEO of Clean Planet Inc.

Collaborative research with Clean Planet Inc. has been mainly performed and NEDO project research with Technova Inc., Nissan Motor Co. Ltd., Kobe Univ., Kyushu Univ. and Nagoya Univ. was done from 2015 to 2017 in addition to collaborative research with MHI on permeation-induced transmutation.

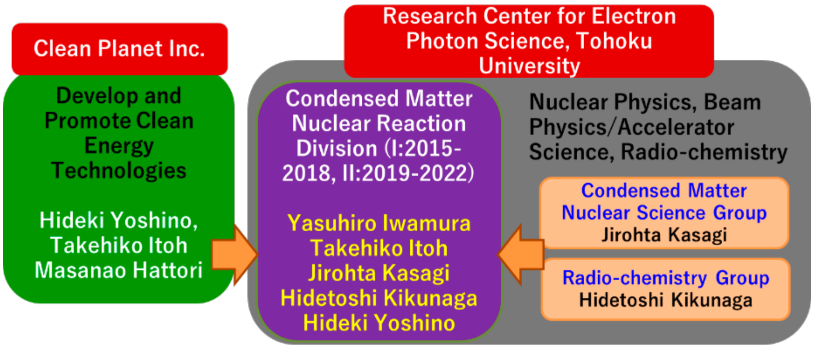

Fig.1 Organization of Condensed Matter Nuclear Reaction Division

Figure 2 shows the summary of experimental results on generated energy per fuel (hydrogen or deuterium) in our division from 2015 to 2018. Several experimental methods were tried, however, the combination of Ni based multilayer thin films and hydrogen gas demonstrated the best results. Anomalous heat generation was supposed to be induced during hydrogen diffusion process by heating up the metal multilayer thin film that absorbed hydrogen gas before heating. Generated excess energy ranged from 1 MJ/g to 1 GJ/g as shown in Fig.2. The 1 GJ/g corresponded to about 10 keV/H, which is too much to be explained by any known chemical process.

We will continue to investigate what is happening in the nano-sized multilayer metal composite and would like to obtain experimental key factors to control Condensed Matter Nuclear Reactions.

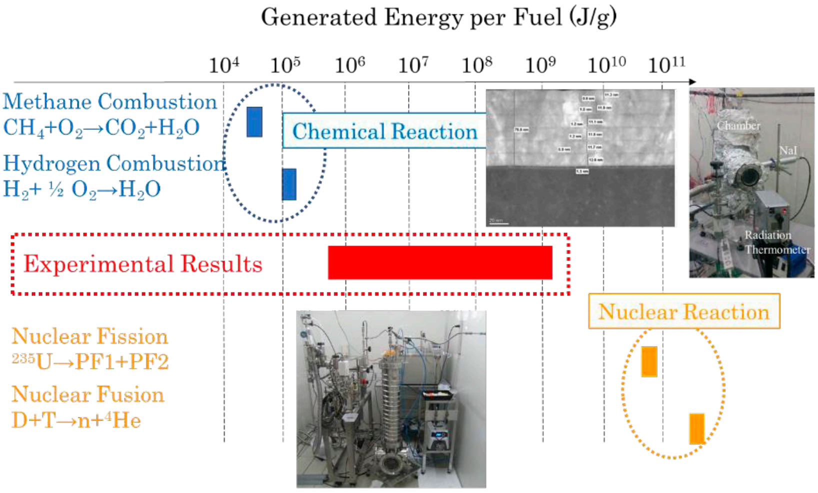

Fig.2 Obtained Anomalous Energy Generation per Fuel from 2015-2018.

Acknowledgment

The author deeply thanks Mr. T. Itoh (Tohoku U. and CLEAN PLANET Inc.), Mr. S. Murakami and Dr. M. Saito (CLEAN PLANET Inc.) for their considerable contribution for this work. The author also express appreciation to Prof. J. Kasagi (Tohoku U.) and Prof. H. Kikunaga (Tohoku U.) for valuable discussions. We also acknowledge Mr. H. Yoshino, Mr. S. Hirano, Mr. M. Ise and Mr. M. Hattori, who are the members of CLEAN PLANET Inc., for their significant assistance. This work is supported by CLEAN PLANET Inc., Thermal & Electric Energy Technology Foundation (TEET), Tanaka Kikinzoku Memorial Foundation and Research Center for Electron Photon Scieсe of Tohoku University.

References

[1] A. Kitamura *et al.*: International Journal of Hydrogen Energy **43** (2018) 16187.
[2] T. Itoh *et al.*: J. Condensed Matter Nucl. Sci. **24** (2017) 179.
[3] Y. Iwamura *et al.*: J. Condensed Matter Nucl. Sci. **29** (2019) 119.
[4] Y. Iwamura *et al.*: J. Condensed Matter Nucl. Sci. **24** (2017) 191.
[5] Y. Iwamura *et al.*: Cold Fusion; Advances in Condensed Matter Nuclear Science, ed. by J. Biberian, Elsevier, Amsterdam, to be published on Jan.01, 2020.
[6] Y. Iwamura, M. Sakano and T. Itoh, Jpn. J. Appl. Phys. 41 (2002) 4642-4648.
[7] Y. Iwamura, T. Itoh and S. Tsuruga, Current Science, Vol.108, No.4, (2015) 628-632.
[8] Y. Iwamura, T. Itoh, et.al, Fusion Technology, 33 (1998) 476-492.

II. Papers

(ELPH Experiment : #2623, #2640, #2655, #2694, #2710)

ωN Scattering Length from ω Photoproduction on the Proton near the Threshold

T. Ishikawa[1], H. Fujimura[1*], H. Fukasawa[1], R. Hashimoto[1†], Q. He[1‡],
Y. Honda[1], A. Hosaka[2,3], T. Iwata[4], S. Kaida[1], J. Kasagi[1], A. Kawano[6],
S. Kuwasaki[1], K. Maeda[5], S. Masumoto[7], M. Miyabe[1], F. Miyahara[1§],
K. Mochizuki[1], N. Muramatsu[1], A. Nakamura[1], S.X. Nakamura[8], K. Nawa[1],
S. Ogushi[1], Y. Okada[1], K. Okamura[1], Y. Onodera[1], K. Ozawa[9], Y. Sakamoto[6],
M. Sato[1], T. Sato[2], H. Shimizu[1], H. Sugai[1¶], K. Suzuki[1‖], Y. Tajima[4],
S. Takahashi[1], Y. Taniguchi[1], Y. Tsuchikawa[1**], H. Yamazaki[1††],
R. Yamazaki[1], and H.Y. Yoshida[4]

[1]*Research Center for Electron Photon Science (ELPH), Tohoku University, Sendai 982-0826, Japan*
[2] *Research Center for Nuclear Physics, Osaka University, Ibaraki 567-0047, Japan.*
[3] *Advanced Science Research Center, Japan Atomic Energy Agency (JAEA), Tokai 319-1195, Japan*
[4]*Department of Physics, Yamagata University, Yamagata 990-8560, Japan*
[5]*Department of Physics, Tohoku University, Sendai 980-8578, Japan*
[6]*Department of Information Science, Tohoku Gakuin University, Sendai 981-3193, Japan*
[7]*Department of Physics, University of Tokyo, Tokyo 113-0033, Japan*
[8]*University of Science and Technology of China, Hefei 230026, China*
[9]*Institute of Particle and Nuclear Studies, High Energy Accelerator Research Organization (KEK), Tsukuba 305-0801, Japan*

We have measured the total cross section as a function of the incident energy ranging from 1.08 to 1.15 GeV. The 1/2 and 3/2 spin-averaged scattering length $a_{\omega N}$ and effective range $r_{\omega N}$ between

---

[*] Present address: Department of Physics, Wakayama Medical University, Wakayama 641-8509, Japan

[†] Present address: Institute of Materials Structure Science (IMSS), High Energy Accelerator Research Organization (KEK), Tsukuba 305-0801, Japan

[‡] Present address: Department of Nuclear Science and Engineering, Nanjing University of Aeronautics and Astronautics (NUAA), Nanjing 210016, China

[§] Present address: Accelerator Laboratory, High Energy Accelerator Research Organization (KEK), Tsukuba 305-0801, Japan

[¶] Present address: Gunma University Initiative for Advanced Research (GIAR), Maebashi 371-8511, Japan

[‖] Present address: The Wakasa Wan Energy Research Center, Tsuruga 914-0192, Japan

[**] Present address: aterials and Life Science Division, J-PARC Center, Japan Atomic Energy Agency (JAEA), Tokai 319-1195, Japan

[††] Present address: Radiation Science Center, High Energy Accelerator Research Organization (KEK), Tokai 319-1195, Japan

the ω meson and nucleon are extracted from the excitation function of the total cross section using a model with the final-state ωN interaction based on the Lippmann-Schwinger scattering equation. The obtained values are $a_{\omega p} = \left(-0.97^{+0.16}_{-0.16}\right) + i\left(0.07^{+0.15}_{-0.14}\right)$ fm and $r_{\omega p} = \left(+2.78^{+0.68}_{-0.54}\right) + i\left(-0.01^{+0.46}_{-0.50}\right)$ fm, suggesting a strong repulsive force. The details are described in a preprint [T. Ishikawa *et al.*, arXiv: 1904.02797 (2019)].

§1. Introduction

The structure of hadrons and dynamical hadron-mass generation are the most important subjects to be studied in the non-perturbative domain of quantum chromodynamics (QCD). Investigation of the properties of hadrons will provide a clear picture for unraveling the dynamics of their internal structure. The ω meson (ω) is one of the best established hadrons, and it is considered to give a short-ranged repulsive central force and a strong spin-orbit force between two nucleons (Ns) [1]. Nevertheless, the fundamental properties of ω such as the interaction with N is not known yet due to the difficulties in realizing scattering experiments because of the neutral and unstable nature of ω. Detailed information on ωN scattering would not only reveal highly excited nucleon resonances (N^*) but also have a strong relevance to the equation of state describing the interior of neutron stars [2].

The low-energy ωN scattering is characterized by the scattering length $a_{\omega N}$ and effective range $r_{\omega N}$. These parameters are obtained from an effective-range expansion of the S-wave phase shift $\delta(p)$ with the ω momentum p in the ωN center-of-mass (CM) frame as defined in the following equation:

$$p\cot\delta(p) = \frac{1}{a_{\omega N}} + \frac{1}{2}\, r_{\omega N}\, p^2 + \ldots. \tag{1}$$

A positive (negative) Re $a_{\omega N}$ gives attraction (repulsion) in this definition. Recently, the A2 collaboration at the Mainz MAMI facility has reported $|a_{\omega N}| = 0.82 \pm 0.03$ fm, which is extracted from ω photoproduction on the proton ($\gamma p \to \omega p$) near the threshold assuming a vector meson dominance (VMD) model [3]. The unknown sign of $a_{\omega N}$ leaves a naive question of whether low-energy ωN scattering is repulsive or attractive.

To determine the low-energy ωN scattering parameters $a_{\omega N}$ and $r_{\omega N}$, we measured the total cross sections for the $\gamma p \to \omega p$ reaction very close to the reaction threshold where the S-wave ωN contribution is dominant. We have determined the $a_{\omega N}$ and $r_{\omega N}$ values from the shape of the total cross section as a function of the incident energy (excitation function) through ωN rescattering in the final-state interaction.

§2. Total Cross section

We have measured the total cross section for the $\gamma p \to \omega p$ reaction at $E_\gamma < 1.15$ GeV [6] using the FOREST detector [5]. The ω mesons are identified in the $\omega \to \pi^0\gamma$ decay mode. All the data for incident energies above 1.08 GeV are divided into ten bins so that every bin includes four photon-tagging channels. The data are also divided into ten bins for the $\pi^0\gamma$ emission angle $\cos\theta$ in the γp-CM frame. Each $\pi^0\gamma$ invariant-mass ($M_{\pi\gamma}$) distribution shows a prominent peak with a centroid of ~ 0.78 GeV, and has a broad background contribution in the lower side. This background contribution is well reproduced by a Monte-Carlo (MC) simulation based on Geant4 [8] for the $\gamma p \to \pi^0\pi^0 p \to \gamma\gamma\gamma\gamma p$ reaction [9], where one γ out of four is not detected with FOREST. The number of the ω produced events is estimated after subtracting the background $\gamma p \to \pi^0\pi^0 p$ contribution for each bin, and the angular differential cross section is obtained. Fig. 2 in Ref. [10] shows the typical angular differential cross section. The total cross section σ is obtained by integrating $d\sigma/d\Omega$s all over the ten emission-angle bins. Fig. 3 in Ref. [10] shows σ as a function the incident photon energy E_γ.

§3. Scattering parameters

We determine $a_{\omega p}$ and $r_{\omega p}$ from the shape of the excitation function. We evaluate the excitation function for the $\gamma p \to \omega p$ reaction using a model with final-state ωp interaction (FSI) based on the Lippmann-Schwinger equation. We assume that the S-wave contribution is dominant at $E_\gamma = 1.08$–1.15 GeV. The total cross section for a fixed ω mass M and γp-CM energy W can be calculated using a transition amplitude $T_{\gamma p\to\omega p}(W, M)$:

$$\sigma_0(W, M) = \frac{1}{16\pi W^2}\frac{p(W, M)}{k}\left|T_{\gamma p\to\omega p}(W, M)\right|^2, \tag{2}$$

where k and p denote the momenta of an initial- and a final-state particles, respectively, in the γp-CM frame. The total cross section σ as a function of E_γ is obtained by averaging $\sigma_0(W(E_\gamma), M)$ over available ω masses:

$$\sigma(E_\gamma) = \int_{m_{\pi^0}}^{W(E_\gamma)-m_p} \sigma_0(W(E_\gamma), M) L_\omega(M) dM, \tag{3}$$

where the probability $L_\omega(M)$ stands for a Breit-Wigner function with a centroid of $M_\omega = 782.65$ MeV and a width of $\Gamma_\omega = 8.49$ MeV [4]. The $T_{\gamma p\to\omega p}$ is expressed by

$$T_{\gamma p\to\omega p} = V_{\gamma p\to\omega p} + T_{\omega p\to\omega p} G_{\omega p\to\omega p} V_{\gamma p\to\omega p}, \tag{4}$$

where $T_{\omega p\to\omega p}$ stands for the ωp scattering amplitude, $G_{\omega p\to\omega p}$ denotes the ωp propagator, and $V_{\gamma p\to\omega p}$ is the production amplitude without FSI. We evaluate the matrix element for $T_{\gamma p\to\omega p}$ with on-shell approximations for $T_{\omega p\to\omega p}$ and $V_{\gamma p\to\omega p}$, and introduce a Gaussian form factor in the integration of $G_{\omega p\to\omega p}$. The equation for the matrix element of $T_{\gamma p\to\omega p}$ is given in Ref. [10].

The excitation function with $a_{\omega p} = 0$ fm and $r_{\omega p} = 0$ fm corresponding to non FSI condition, which does not reproduce the experimental data. FSI is necessary and the optimal set of $a_{\omega p}$ and $r_{\omega p}$ are determined to reproduce the experimentally-obtained cross-section data. The deduced parameters are $a_{\omega p} = \left(-0.97^{+0.16}_{-0.16}\right) + i\left(0.07^{+0.15}_{-0.14}\right)$ fm and $r_{\omega p} = \left(+2.78^{+0.68}_{-0.54}\right) + i\left(-0.01^{+0.46}_{-0.50}\right)$ fm. The detailed discussion to deduce the scattering parameters are described in Ref. [10] including uncertainties from the Gaussian form factor in the ωp propagator, the P-wave contribution, the energy dependence of $V_{\gamma p\to\omega p}$, and mis-calibration of incident energies.

The obtained $a_{\omega p}$ is consistent with $|a_{\omega p}| = 0.82 \pm 0.03$ fm given by the A2 collaboration [3]. A positive $\mathrm{Re}\, a_{\omega p}$ value giving, an attraction, is rejected at a confidence level higher than 99.9%. No bound or virtual state is expected in the ωNchannel from the strong repulsion results. Slightly attractive ω-nucleus (ωA) interactions are reported with potential depths at normal nuclear density of $-42 \pm 17 \pm 20$

MeV [11] and $-15 \pm 35 \pm 20$ MeV [12] from ω photoproduction from nuclei. The measurement of ω line shape shows a decrease of ω mass by $9.2\% \pm 0.2\%$ (corresponding to ωA attraction) without any in-medium broadening [13, 14]. The relation between strong ωN repulsion and ωA attraction would be a subject of future discussions taking into consideration spin-dependent terms, higher partial waves, and partial restoration of chiral symmetry.

§4. Summary

The total cross sections have been measured for the $\gamma p \to \omega p$ reaction near the threshold. The ω is identified through the $\omega \to \pi^0\gamma$ decay. The spin-averaged scattering length $a_{\omega p}$ and effective range $r_{\omega p}$ between the ω and proton are estimated from the excitation function at incident photon energies ranging from 1.08 to 1.15 GeV: $a_{\omega p} = \left(-0.97^{+0.16}_{-0.16}\right) + i\left(0.07^{+0.15}_{-0.14}\right)$ fm and $r_{\omega p} = \left(+2.78^{+0.68}_{-0.54}\right) + i\left(-0.01^{+0.46}_{-0.50}\right)$ fm. The real and imaginary parts for $a_{\omega p}$ and $r_{\omega p}$ are determined separately for the first time. A small P-wave contribution does not affect the obtained values. The positive $\mathrm{Re}\, a_{\omega p}$ value indicates repulsion. The detailed discussions including comparison between previous experiments, and estimation of the systematic uncertainties are described in a preprint [T. Ishikawa *et al.*, arXiv: 1904.02797 (2019)].

Acknowledgments

The authors express their gratitude to the ELPH accelerator staff for stable operation of the accelerators in the FOREST experiments. They also acknowledge Mr. K. Matsuda, Mr. K. Nanbu, and Mr. I. Nagasawa for their technical support. This work was supported in part by the Ministry of Education, Culture, Sports, Science and Technology, Japan (MEXT) and Japan Society for the Promotion of Science (JSPS) through Grants-in-Aid for Specially Promoted Research No. 19002003, for Scientific Research (A) Nos. 24244022 and 16H02188, for Scientific Research (B) Nos. 17340063 and 19H01902, for Scientific Research (C) No. 26400287, and for Scientific Research on Innovative Areas Nos. 18H05407 and 19H05141.

References

[1] R. Machleidt: Adv. Nucl. Phys. **19**, 189 (1989).
[2] H. Shen, H. Toki, K. Oyamatsu, K. Sumiyoshi: Nucl. Phys. A **637**, 435 (1998).
[3] I.I. Strakovsky *et al.* (A2 collaboration at MAMI): Phys. Rev. C **91**, 045207 (2015).
[4] M. Tanabashi *et al.* (Particle Data Group): Phys. Rev. D **98**, 030001 (2018).
[5] T. Ishikawa *et al.*: Nucl. Instrum. Meth. A **832**, 108 (2016).
[6] T. Ishikawa *et al.*: Nucl. Instrum. Meth. A **622**, 1 (2010);
T. Ishikawa *et al.*: Nucl. Instrum. Meth. A **811**, 124 (2016);
Y. Matsumura *et al.*: Nucl. Instrum. Meth. A **902**, 103 (2018);
Y. Obara *et al.*: Nucl. Instrum. Meth. A **922**, 108 (2019).
[7] T. Ishikawa *et al.*: Phys. Lett. B **772**, 398 (2017); Phys. Lett. B **789**, 413 (2019).

[8] S. Agostinelli *et al.*: Nucl. Instrum. Meth. A **506**, 250 (2003);
J. Allison *et al.*: IEEE Trans. Nucl. Sci. **53**, 270 (2006);
see `http://geant4.cern.ch/`.

[9] A. Fix, H. Arenhövel: Euro. Phys. J. A **25**, 115 (2005);
The 2-PION-MAID calculations are available at `http://maid.kph.uni-mainz.de/twopion/`.

[10] T. Ishikawa *et al.*: arXiv: 1904.02797 (2019).

[11] V. Metag *et al.*: Prog. Part. Nucl. Phys. **67**, 530 (2012); Hyperfine Interact. bf 234, 25 (2015).

[12] S. Friedrich *et al.* (CBELSA/TAPS collaboration): Phys. Lett. B **736**, 26 (2014).

[13] K. Ozawa *et al.*: Phys. Rev. Lett. **86**, 5019 (2001).

[14] M. Naruki *et al.*: Phys. Rev. Lett. **96**, 092301 (2006).

(ELPH Experiment : #2623, #2640, #2655, #2694, #2710)

Study of dibaryons via $\gamma d \to \pi^0\pi^0 d$ at $E_\gamma = 0.75$–1.15 GeV (II)

T. Ishikawa[1], H. Fujimura[1*], H. Fukasawa[1], R. Hashimoto[1†], Q. He[1‡],
Y. Honda[1], T. Iwata[2], S. Kaida[1], H. Kanda[3§], J. Kasagi[1], A. Kawano[4],
S. Kuwasaki[1], K. Maeda[3], S. Masumoto[5], M. Miyabe[1], F. Miyahara[1¶],
K. Mochizuki[1], N. Muramatsu[1], A. Nakamura[1], K. Nawa[1], S. Ogushi[1],
Y. Okada[1], K. Okamura[1], Y. Onodera[1], K. Ozawa[6], Y. Sakamoto[4], M. Sato[1],
H. Shimizu[1], H. Sugai[1‖], K. Suzuki[1**], Y. Tajima[2], S. Takahashi[1],
Y. Taniguchi[1], Y. Tsuchikawa[1††], H. Yamazaki[1‡‡], R. Yamazaki[1],
and H.Y. Yoshida[2]

[1]*Research Center for Electron Photon Science (ELPH), Tohoku University, Sendai 982-0826, Japan*
[2]*Department of Physics, Yamagata University, Yamagata 990-8560, Japan*
[3]*Department of Physics, Tohoku University, Sendai 980-8578, Japan*
[4]*Department of Information Science, Tohoku Gakuin University, Sendai 981-3193, Japan*
[5]*Department of Physics, University of Tokyo, Tokyo 113-0033, Japan*
[6]*Institute of Particle and Nuclear Studies, High Energy Accelerator Research Organization (KEK), Tsukuba 305-0801, Japan*

The total and differential cross sections were measured for the $\gamma d \to \pi^0\pi^0 d$ reaction at incident energies ranging from 0.75 to 1.15 GeV by using the FOREST detector at ELPH: the excitation function of the total cross section, angular distributions of d and π^0s, invariant-mass distributions for $\pi^0 d$ and $\pi^0\pi^0$. The present work suggests a sequential process $\gamma d \to R_{\mathrm{IS}} \to \pi^0 R_{\mathrm{IV}} \to \pi^0\pi^0 d$ is dominant with

---

[*] Present address: Department of Physics, Wakayama Medical University, Wakayama 641-8509, Japan

[†] Present address: Institute of Materials Structure Science (IMSS), High Energy Accelerator Research Organization (KEK), Tsukuba 305-0801, Japan

[‡] Present address: Department of Nuclear Science and Engineering, Nanjing University of Aeronautics and Astronautics (NUAA), Nanjing 210016, China

[§] Research Center for Nuclear Physics (RCNP), Osaka University, Ibaraki 567-0047, Japan

[¶] Present address: Accelerator Laboratory, High Energy Accelerator Research Organization (KEK), Tsukuba 305-0801, Japan

[‖] Present address: Gunma University Initiative for Advanced Research (GIAR), Maebashi 371-8511, Japan

[**] Present address: The Wakasa Wan Energy Research Center, Tsuruga 914-0192, Japan

[††] Present address: aterials and Life Science Division, J-PARC Center, Japan Atomic Energy Agency (JAEA), Tokai 319-1195, Japan

[‡‡] Present address: Radiation Science Center, High Energy Accelerator Research Organization (KEK), Tokai 319-1195, Japan

two 2.47- and 2.63-GeV isoscalar dibaryons ($R_{\rm IS}$) and a 2.14-GeV isovector dibaryon ($R_{\rm IV}$). This issue has been already reported in the previous annual report. We discuss a modification in determining the mass and width of $R_{\rm IV}$ in the $\pi^0 d$ invariant-mass distributions. The details are described in a published paper [Phys. Lett. B 789, 413 (2019)].

§1. Mass and width of $R_{\rm IV}$

The mass and width are determined by fitting a function, expressed as a sum of a Breit-Wigner (BW) peak, its reflection, and phase-space contributions, to the $\pi^0 d$ invariant-mass ($M_{\pi d}$) data. In the previous report, a BW peak and its reflection were summed up at a cross-section level. The function was given by convolution of a Gaussian with an experimental mass resolution of $\sigma_M = 0.011$ GeV, and

$$N(m_1) = \int_{m_2} \left\{\alpha\left(L_{M,\Gamma}(m_1) + L_{M,\Gamma}(m_2)\right) + C\right\} V_{\rm PS}(m_1, m_2)\, dm_2, \qquad (1)$$

where $L_{M,\Gamma}(m)$ represents the BW function with M and Γ, and $V_{\rm PS}(m_1, m_2)$ expresses the phase-space contribution. The acceptance was taken into account depending on $M_{\pi\pi}$, $M_{\pi d}$, and $\cos\theta_d$ to estimate $V_{\rm PS}(m_1, m_2)$. The parameters obtained were $M = 2.15\pm0.01$ GeV and $\Gamma=0.11\pm0.01$ GeV. The mass is slightly lower than the sum of the N and Δ masses ($\sim$2.170 GeV), and the width is narrower than that of Δ ($\sim$0.117 GeV) [1].

Since the produced two π^0s are identical, we have changed a way to sum up BW-peaks at an amplitude level. The function is given by convolution of a Gaussian with an experimental mass resolution of $\sigma_M = 0.011$ GeV, and

$$N(m_1) = \int_{m_2} \left(\alpha\left|A^L_{M,\Gamma}(m_1) + A^L_{M,\Gamma}(m_2)\right|^2 + C\right) V_{\rm PS}(m_1, m_2)\, dm_2, \qquad (2)$$

where $A^L_{M,\Gamma}(m) = \left(m^2 - M^2 + iM\Gamma\right)^{-1}$ represents the BW amplitude with M and Γ. The parameters obtained are $M = 2.14\pm0.01$ GeV and $\Gamma=0.09\pm0.01$ GeV. The mass becomes slightly lower, and the width becomes narrower.

§2. Summary

The total and differential cross sections have been measured for the $\gamma d\to\pi^0\pi^0 d$ reaction at incident energies from 0.75 to 1.15 GeV. A sequential process $\gamma d \to R_{\rm IS} \to \pi^0 R_{\rm IV} \to \pi^0\pi^0 d$ is found to be dominant with 2.47- and 2.63-GeV $R_{\rm IS}$ and 2.14-GeV $R_{\rm IV}$. The way has been modified to determine the mass and width of $R_{\rm IV}$ in the $\pi^0 d$ invariant-mass distributions. The mass becomes slightly lower, and the width becomes narrower. The details including figures can be found in a published paper [Phys. Lett. B 789, 413 (2019)].

Acknowledgments

The authors express their gratitude to the ELPH accelerator staff for stable operation of the accelerators in the FOREST experiments. They also acknowledge Mr. K. Matsuda, Mr. K. Nanbu, and Mr. I. Nagasawa for their technical support. This work was supported in part by the Ministry of Education, Culture, Sports, Science and Technology, Japan through Grants-in-Aid for Scientific Research (B)

No. 17340063, for Specially Promoted Research No. 19002003, for Scientific Research (A) No. 24244022, for Scientific Research (C) No. 26400287, and for Scientific Research (A) No. 16H02188.

References

[1] C. Patrignani *et al.* (Particle Data Group): Chin. Phys. C **40**, 100001 (2016).

(ELPH Experiment : #2803, #2844, #2882, #2894)

Current status of the FOREST/BLC experiments at ELPH

T. Ishikawa[1], K. Aoki[2], H. Fujioka[3], Y. Honda[1], T. Hotta[4], Y. Inoue[1],
K. Itahashi[5], H. Kanda[4], H. Kawai[6], K. Maeda[7], Y. Matsumura[1], M. Miyabe[1],
S. Miyata[8], N. Muramatsu[1], T. Nishi[5], H. Ohnishi[1], K. Ozawa[2], H. Shimizu[1],
R. Shirai[1], M. Tabata[6], A.O. Tokiyasu[1], Y. Tsuchikawa[9], H. Yamazaki[1],
and C. Yoshida[1]

[1]*Research Center for Electron Photon Science (ELPH), Tohoku University, Sendai 982-0826, Japan*
[2]*Institute of Particle and Nuclear Studies, High Energy Accelerator Research Organization (KEK), Tsukuba 305-0801, Japan*
[3]*Department of Physics, Tokyo Institute of Technology, Tokyo 152-8551, Japan*
[4]*Research Center for Nuclear Physics (RCNP), Osaka University, Ibaraki 567-0047, Japan*
[5]*Nishina Center for Accelerator-Based Science, RIKEN, Wako 351-0198, Japan*
[6]*Department of Physics, Chiba University, Chiba 263-8522, Japan*
[7]*Department of Physics, Tohoku University, Sendai 980-8578, Japan*
[8]*Department of Physics, University of Tokyo, Tokyo 113-0033, Japan*
[9]*Department of Physics, Nagoya University, Nagoya 464-8602, Japan*

The FOREST/BLC experiments are conducted primarily aiming to determine low-energy S-wave ηn scattering parameters using the $\gamma d \to p\eta n$ reaction with a special kinematics. The photon beam with energies around 940 MeV can give the recoilless condition of produced η mesons by detecting the protons at 0°. The effects of the final-state ηn interaction must be enhanced due to the small relative momentum between the η meson and the residual neutron in this kinematics. In this year, the physics data were collected from June 6 to June 25 and October 12 to November 4 in 2018. In this report, a brief summary of the current status of the FOREST/BLC experiments and collected data are described.

§1. Introduction

The nucleon resonance $N(1535)S_{11}$ (N^*) is an interesting object, which can be an S-wave ηN molecule-like state and/or the chiral partner of the nucleon N. Whether N^* is composite or elementary can be given by the scattering length $a_{\eta N}$ and effective range $r_{\eta N}$ in an effective-range expansion of the S-wave phase shift:

$$k \cot \delta(k) = \frac{1}{a_{\eta N}} + \frac{1}{2} r_{\eta N} k^2 + O(k^4) \tag{1}$$

through the pole position of N^* [1]. The $a_{\eta N}$ values have been extracted by many theoretical analyses from the differential and total cross sections for the $\pi N \to \pi N$, $\pi N \to \eta N$, $\gamma N \to \pi N$, and $\gamma N \to \eta N$ reactions. Although the imaginary part of $a_{\eta N}$ (Im$[a_{\eta N}]$) concentrates $\sim$ 0.26 fm for different analyses, its real part (Re$[a_{\eta N}]$) scatters in a wide range from 0.2 to 1.1 fm [2]. This uncertainty comes from the fact that the existing experimental data do not include the ηN-scattering amplitude directly. We propose the $\gamma d \to \eta pn$ reaction to determine $a_{\eta N}$ at a certain kinematics, which enhances the ηN scattering effect.

The incident photon bombards the quasi-free proton in the deuteron and produces a virtual η meson with a very low momentum. Events are selected in which the incident energy is approximately 0.94 GeV and the proton is detected at 0°. The kinematics for these events satisfies the recoilless condition of the produced η mesons. Thus, low-energy ηn scattering is expected to take place in this condition, where the pn and ηp rescattering effects are suppressed owing to their large relative momenta ($\sim$ 0.94 GeV). The sensitivity to the Re[$a_{\eta n}$] and Re[$r_{\eta n}$] values are investigated and summarized in Ref. [3] by using a model based on a dynamical coupled-channel meson-baryon scattering analysis [4, 5].

§2. Experimental setup

The $\gamma d \to p\eta n$ reaction is measured at ELPH with the FOREST electromagnetic calorimeter system [6] together with an additional forward charged-particle spectrometer called BLC [7]. The incident photon energy ranges from 0.82 to 1.26 GeV [9] for the circulating energy of 1.32 GeV in the electron synchrotron called the booster storage (BST) ring [10]. The details of the FOREST detector including the liquid deuterium target are described elsewhere [8]. The forward scattered proton is momentum-analyzed with the BLC spectrometer behind FOREST. The trajectory of a charged particle is measured with 2 planar drift chambers (DCs), and the time of flight is measured with 14 plastic scintillator (PS) hodoscopes (PSH+). An additional e/π separation is made using 10 SF5 lead-glass Cherenkov counters (LGCs). The experimental setup has been fixed since November in 2017. In this year, the physics data were collected in the two periods: June 6 to June 25 (2018A) and October 12 to November 4 (2018B) in 2018.

The BLC magnet was excited every time at normal operation in this fiscal year with a coil current of 1400 A. The magnetic flux B_y at the center was monitored with a nuclear magnetic resonance (NMR) probe during the experiments, and $B_y = 716.0$ mT was adjusted by changing the coil current. Fig. 1 shows the magnetic flux B_y at the center for the 2018A and 2018B periods.

§3. Collected data

The physics data with the deuterium and hydrogen targets were collected both in the 2018A and 2018B periods. The BST ring was operated with a circulating energy of 1.32 GeV, a current of approximately 20 mA, and an RF frequency of 500.14 MHz. It should be noted that the frequency was 500.18 MHz before the 2011 earthquake. The data collections were basically stable both in the periods. A sudden huge earthquake at 3:36am on October 26 in 2018, however, made the pedestal width broader in the `Be203` channel. This problem was fixed 11:40pm on October 29 in 2018. Table 1 summarizes the number of spills and events of the collected data in this fiscal year (2018). The statistics for the hydrogen data is similar to that for the 2009D period, and that for the deuterium data is 1.5 times higher. The data analysis is on-going to perform the precise energy and timing calibrations of the STB-Tagger II, FOREST,

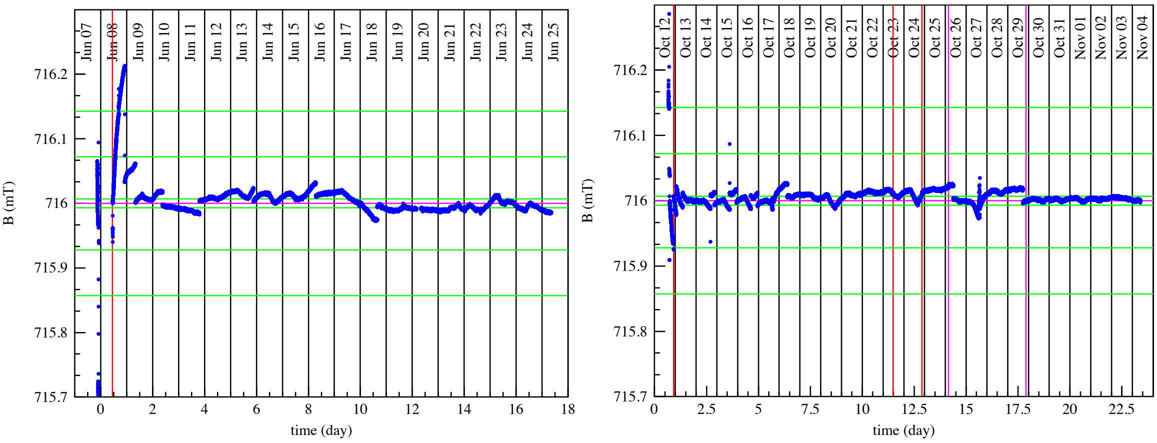

Fig.1. Magnetic flux B_y at the center for the 2018A (left) and 2018B (right) periods measured with an NMR probe. The horizontal solid lines correspond to the magnetic flux values increased by $\pm0.001\%$, $\pm0.01\%$, $\pm0.02\%$ from the central value 716.00 mT. The red vertical line in 2018A corresponds to the starting time to excite the magnet at normal operation. The red vertical lines in 2018B correspond to the starting times to collect the hydrogen, empty, and deuterium targets, and the magenta lines express a huge earthquake, and fixing the `Be203` pedestal trouble from the earthquake.

and BLC detectors. Additionally, the physics analysis has just started using the acquired data as shown in section 4.

Table 1. Numbers of spills and events collected in this fiscal year (2018). The circulating electron energy of the BST ring was 1.32 GeV. The targets used were liquid hydrogen, deuterium, and empty.

period	hydrogen		deuterium		empty	
	#spills	#events	#spills	#events	#spills	#events
2018A	36.39 k	467.60 M	36.64 k	492.38 M	9.63 k	86.90 M
2018B	49.48 k	747.72 M	47.34 k	878.91 M	6.27 k	68.36 M

§4. Preliminary results

In Ref. [3], it is confirmed that the ηn scattering effect is dominant at the low ηn invariant mass $M_{\eta n}$ (corresponding to the small ηn relative momentum), and that the $\pi n \to \eta n$ transition and pn rescattering effects are small. The differential cross section $d\sigma/dM_{\eta n}/d\Omega_p$ of 5% error per MeV bin in the low $M_{\eta n}$ region can determine Re[$a_{\eta N}$] at the precision of 0.1 fm. Currently, the determination of $d^3\sigma/dM_{\eta n}/d\Omega_p$s are in progress, and just the $M_{\eta n}$ distribution has been obtained. The incident photon energy ranges from 0.82 to 1.26 GeV using the circulating electron energy of 1.32 GeV in the electron synchrotron [10]. Fig. 2 shows the preliminary $M_{\eta n}$ distribution for the $\gamma d \to \eta pn$ reaction. The $M_{\eta n}$ value is calculated as a $d(\gamma, p)$ missing mass after the $\gamma d \to \eta pn$ reaction is identified. Although acceptance correction is not yet applied, a clear peak is observed at 0 MeV corresponding to quasi-free η production from the proton. The momentum calibration of the BLC spectrometer is not completed at this moment. Currently, the analysis efficiency is lower than expected, and we try to find the reason. In addition, the current data statistics is too poor to determine Re[$a_{\eta N}$], and we should continue the measurement to increase the statistics.

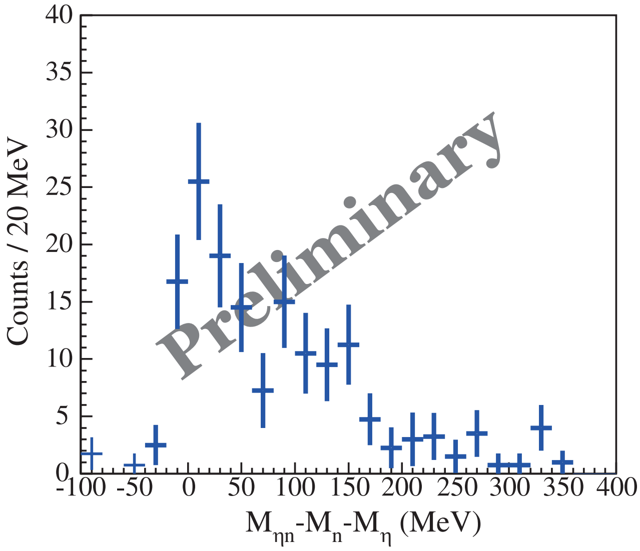

Fig.2. Preliminary $M_{\eta n}$ distribution for the $\gamma d \to \eta pn$ reaction. The $M_{\eta n}$ value is calculated as a $d(\gamma, p)$ missing mass after the $\gamma d \to \eta pn$ reaction is identified.

§5. Silica aerogel counter

The FOREST/BLC experiments also investigate the Λn interaction. This interaction is important to understand the baryon-baryon interaction in a comprehensive way. Charge symmetry breaking (CSB) in the $A = 4$ hypernuclei is one of the hot topics in hadron physics [13]. The energy difference between the 1^+ excited state and ground states are quite different for the mirror $A = 4$ hypernuclei (^{4}H and ^{4}He), and this value cannot reproduced by the theoretical calculations without a large CSB effect. The Λn interaction is expected to play a crucial role for understanding this difference and CSB in hypernuclei.

In the FOREST/BLC experiment, we investigate the Λn interaction through the Λn invariant mass $M_{\Lambda n}$ distribution in the $\gamma d \to K^+ \Lambda n$ reaction with K^+ detection at 0° similarly to the ηn interaction study. The differential cross section $d^3\sigma/dM_{\Lambda n}/d\Omega_K$ provide the strength of the Λn interaction independently of the Λp. We are now preparing the silica aerogel Cherenkov (AC) counters just in front of PSH+ to identify K^+ mesons effectively. The details of the AC counter, and its performance test will be reported in the next annual report.

§6. Summary

The first-stage FOREST/BLC experiment, aiming at the determination of the low-energy ηN scattering parameters Re[$a_{\eta N}$] and Re[$r_{\eta N}$], started from October 30 in 2017. The number of collected events for the deuterium target has been 1.6 G up to the end of this fiscal year. The energy and timing calibrations have been completed for STB-Tagger II, Backward Gamma, and PSH+ detectors, We are still working on those for the other detectors, and have just started the physics analysis. We should continue to collect data as soon as possible to determine Re[$a_{\eta N}$] with an accuracy of 0.1 fm.

Acknowledgments

The authors give thanks to the ELPH accelerator staff for their great efforts in the stable operation of the electron synchrotron. They deeply acknowledge S.X. Nakamura and H. Kamano for giving us the predictions for the ηn rescattering effect in the proposed $\gamma d \to p\eta n$ experiment. This work was supported in part by JSPS KAKENHI Grants Nos. 17340063, 19002003, 24244022, 26400287, 16H02188, 19H01902, and 19H05141.

References

[1] S. Weinberg: Phys. Rev. **137**, B672 (1965);
T. Hyodo: Phys. Rev. Lett. **111**, 132002 (2013).

[2] Q. Haider and L.C. Liu: Int. J. Mod. Phys. E **24**, 1530009 (2015);
and references therein.

[3] S.X. Nakamura, H. Kamano, and T. Ishikawa: Phys. Rev. C **96**, 042201 (R) (2017).

[4] A. Matsuyama, T. Sato, T.-S.H. Lee: Phys. Rep. **439**, 193 (2007).

[5] H. Kamano *et al.*: Phys. Rev. C **88**, 035209 (2013).

[6] T. Ishikawa *et al.*: Phys. Lett. B **772**, 398 (2017);
T. Ishikawa *et al.*: Phys. Lett. B **789**, 413 (2019);
T. Ishikawa *et al.*: PoS (Hadron2013) 095;
Y. Tsuchikawa *et al.*: JPS Conf. Proc. **17**, 062007 (2017);
T. Ishikawa *et al.*: PoS (INPC2016) 267.

[7] T. Ishikawa *et al.*: Acta. Phys. Polon. B **48**, 1801 (2017);
T. Ishikawa *et al.*: JPS Conf. Proc. **10**, 031001 (2016);
T. Ishikawa *et al.*: JPS Conf. Proc. **13**, 020031 (2017);

[8] T. Ishikawa *et al.*: Nucl. Instrum. and Meth. A **832**, 108 (2016).

[9] T. Ishikawa *et al.*: Nucl. Instrum. and Meth. A **622**, 1 (2010);
T. Ishikawa *et al.*: Nucl. Instrum. and Meth. A **811**, 124 (2016);
Y. Matsumura *et al.*: Nucl. Instrum. and Meth. A **902**, 103 (2018);
Y. Obara *et al.*: Nucl. Instrum. and Meth. A **932**, 108 (2019).

[10] F. Hinode *et al.*: J. Phys. Conf. Ser. **425**, 072011 (2013).

[11] T. Ishikawa *et al.*: ELPH annual report **2016**, 11 (2017).

[12] H. Yamazaki *et al.*: Nucl. Instrum. Meth. A **536**, 70 (2005).

[13] P. Achenbach (A1 collaboration): EPJ Web Conf. **130**, 07001 (2016).

(ELPH Experiment : #2815)

Profile measurement of circulating electrons in a synchrotron using an internal radiator

Y. Obara[1], T. Ishikawa[2], H. Hama[2], F. Hinode[2], H. Kanda[3]*, S. Kashiwagi[2],
M. Miyabe[2], T. Muto[2], K. Ozawa[4], H. Shimizu[2], and A.O. Tokiyasu[2]

[1]*Department of Physics, University of Tokyo, Tokyo 113-0033, Japan*
[2]*Research Center for Electron Photon Science (ELPH), Tohoku University, Sendai 982-0826, Japan*
[3]*Department of Physics, Tohoku University, Sendai 980-8578, Japan*
[4]*Institute of Particle and Nuclear Studies, High Energy Accelerator Research Organization (KEK), Tsukuba 305-0801, Japan*

An internal radiator made of a 11-μm-diameter carbon wire is employed to produce bremsstrahlung-photon beams from circulating electrons in a synchrotron at the Research Center for Electron Photon Science, Tohoku University. The horizontal electron-beam size at the radiator location is determined from the decay rate of the resultant photon intensity as a function of the distance between the fixed radiator position and the centroid of the electron beam. The horizontal beam size at the radiator location is found to be 0.74 mm with a statical error less than 0.01 mm for 1.3-GeV circulating electrons. The horizontal correlation between the position and momentum direction of the electron beam is also measured. The horizontal size and correlation are well-reproduced by the design values of the parameters of the synchrotron. The details are described in a published paper [Y. Obara *et al.*, Nucl. Instrum. Meth. A **922**, 108 (2019)].

§1. Introduction

The FOREST experiments are conducted at the Research Center for Electron Photon Science (ELPH), Tohoku University, to investigate the structure of hadrons through meson photoproduction [1, 2] with the FOREST electromagnetic calorimeter [3]. The experiments use a GeV bremsstrahlung-photon beam, which is produced from circulating electrons in a synchrotron called Booster STorage (BST) ring [5] by using an internal radiator made of a carbon wire with a diameter of 11 μm [4]. Currently ELPH is the only facility having an internal radiator system for producing a bremsstrahlung-photon beam.

§2. Horizontal beam size

The horizontal beam size σ_x is expressed as

$$\sigma_x = \sqrt{\beta_x \epsilon_x + \left(\eta_x \frac{\Delta p}{p}\right)^2}, \tag{1}$$

---

[*] Present address: Research Center for Nuclear Physics (RCNP), Osaka University, Ibaraki 567-0047, Japan

where $(\alpha_x, \beta_x, \gamma_x)$ and ϵ_x denote the Twiss parameters and emittance in the horizontal plane, respectively. The σ_x is affected by the momentum spread $\Delta p/p$ of the beam and by the dispersion η_x. The design values of the horizontal parameters at normal operation at the radiator location for the 1.3-GeV circulating electrons are

$$\begin{pmatrix} \alpha_x \\ \beta_x \\ \gamma_x \\ \epsilon_x \\ \eta_x \end{pmatrix} = \begin{pmatrix} 1.60 \pm 0.09 \\ 3.70 \pm 0.15\ \mathrm{m} \\ 0.96 \pm 0.06\ \mathrm{m}^{-1} \\ (1.375 \pm 0.009) \times 10^{-7} \\ 0.45 \pm 0.02\ \mathrm{m} \end{pmatrix}. \tag{2}$$

The momentum spread is estimated to be $\Delta p/p = (6.3 \pm 0.0) \times 10^{-4}$. A horizontal beam size of $\sigma_x = 0.77 \pm 0.01$ mm is expected.

We have measured σ_x with the radiator placed close to the centroid of the circulating electrons. The production rate of the bremsstrahlung photons is proportional to the number of electrons that hit the radiator. The photon intensity as a function of the time is given by

$$I(t) = I_0 \exp\left\{-\Gamma\, t\right\}. \tag{3}$$

Because the decay rate Γ is proportional to the fraction of electrons at the x position of the radiator. The $\Gamma(x)$ as a function of x gives the horizontal intensity distribution and σ_x. The $\Gamma(x)$ was determined by counting the number of signals for 16 photon-tagging channels out of 116 for every 0.1 s for a total time interval of 120 s. A method to determine σ_x and development of a special 16-channel 1200-depth 24-bit scaler were described in the previous annual report [7]. The measured σ_x of 0.74 mm is consistent with the expected σ_x of 0.77 ± 0.01 mm.

§3. Horizontal correlation between the position and momentum direction

Because bremsstrahlung photons are emitted along the momentum direction of the initial circulating electrons, the momentum direction $x' = dp_x/dp_z$ can be obtained from the centroid of the intensity map of the photon beam at downstream. For each fixed x position of the radiator, we measured the intensity map of the photon beam $(x^{\mathrm{BPM}}, y^{\mathrm{BPM}})$ with a developed photon-beam profile monitor (BPM) [6] located 20.8-m downstream from the radiator. To prevent the vignetting, the lead aperture located on the photon beamline in the GeV-γ experimental hall [4] was removed in this measurement, and the opening of the lead aperture was enlarged (20 mm in diameter) in the second experimental hall.

The centroid μ_x^{BPM} (μ_y^{BPM}) is determined by fitting a Gaussian function to the x_{BPM} (y_{BPM}) distribution of the photon beam. The x_{BPM} and x are shifted by adjusting these values to make $x = 0$ at the centroid of the electron beam, and $\mu_x^{\mathrm{BPM}} = 0$ at $x = -3$ mm. Fig. 1 shows μ_x^{BPM} as a function of x. The μ_x^{BPM} decreases with an increase of x. While the expected correlation between μ_x^{BPM} and x is expressed as

$$\mu_x^{\mathrm{BPM}} = x + \left(-\frac{\alpha_x}{\beta_x} x\right) z_{\mathrm{BPM}} = \left(1 - \frac{\alpha_x}{\beta_x} z_{\mathrm{BPM}}\right) x \tag{4}$$

with the horizontal Twiss parameters. The corresponding line is also plotted in Fig. 1. Although the acquired $\mu_x^{\rm BPM}$ as a function of x is almost reproduced in Eq. (4), the slope is steeper in the measurement. The μ_y decreases gradually with an increase of x, suggesting that the plane containing the closed orbit is tilted from the horizontal plane.

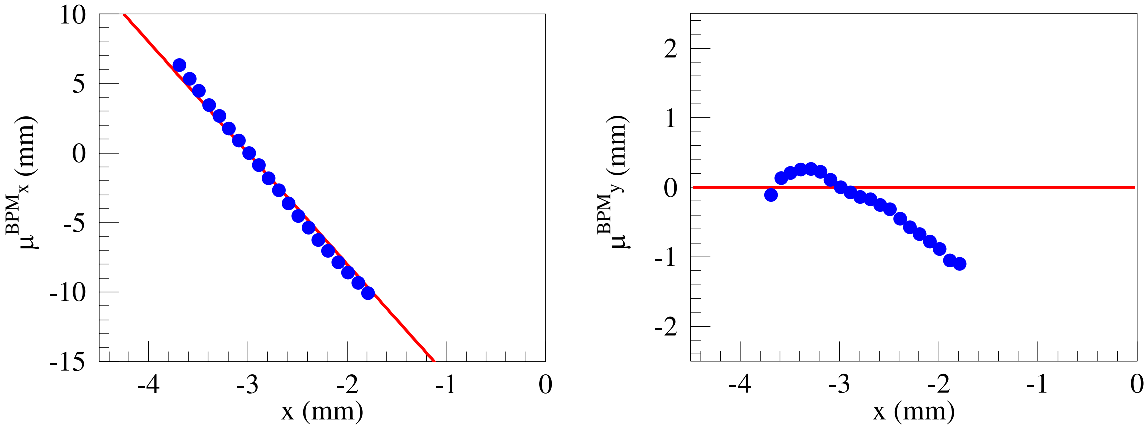

Fig.1. Horizontal centroid $\mu_x^{\rm BPM}$ and vertical centroid $\mu_y^{\rm BPM}$ of the photon beam as a function of the radiator position x. The solid line in the correlation between $\mu_x^{\rm BPM}$ and x is obtained by shifting the correlation Eq. (4) to make $\mu_x^{\rm BPM} = 0$ at $x = -3$ mm.

§4. Summary

The horizontal beam size of circulating electrons at the radiator location is estimated from the decay rate of the resulting photon intensity as a function of the distance between the fixed radiator position and the centroid of the electron beam. The horizontal beam size is determined to be 0.74 mm with a statical error of less than 0.01 mm for 1.3-GeV circulating electrons. The size is well-reproduced by the design values of the Twiss and the emittance parameters of the BST ring. The horizontal correlation of the electron beam between the position and momentum direction is also investigated from the intensity map of the bremsstrahlung photon beam measured 20.8-m downstream from the radiator location. The correlation is also well-reproduced by the design values of the BST-ring parameters. The details are described in a published paper [Y. Obara *et al.*, Nucl. Instrum. Meth. A **922**, 108 (2019)].

Acknowledgments

The authors express many thanks to the ELPH staff. This work was supported in part by Grants-in-Aid for Scientific Research (A) No. 24244022, for Scientific Research (C) No. 26400287, and for Scientific Research (A) No. 16H02188.

References

[1] T. Ishikawa *et al.*: Phys. Lett. B **772**, 398 (2017);
T. Ishikawa *et al.*: Phys. Lett. B **789**, 413 (2019).

[2] S.X. Nakamura, H. Kamano, T. Ishikawa: Phys. Rev. C **96**, 042201 (R) (2017);
T. Ishikawa, et al., Acta Phys. Polon. B **48**, 1801 (2017).

[3] T. Ishikawa *et al.*: Nucl. Instrum. Meth. A **832**, 108 (2016).

[4] T. Ishikawa *et al.*: Nucl. Instrum. Meth. A **622**, 1 (2010).

[5] F. Hinode *et al.*: Proceedings of 11th International Conference on Synchrotron Radiation Instrumentation (SRI2012), Journal of Physics: Conference Series **425** (2013) 072011;
F. Hinode *et al.*: Proceedings of the 7th International Particle Accelerator Conference (IPAC2016), p. 701.

[6] T. Ishikawa *et al.*: Nucl. Instrum. Meth. A 811 (2016) 124;
Y. Matsumura *et al.*: Nucl. Instrum. Meth. A 902 (2018) 103.

[7] Y. Obara *et al.*: ELPH Annual Report 2015, Tohoku University, p. 52 (2016).

The performance study of an electromagnetic calorimeter Foward Gamma

M. Miyabe[1], K. Kanomata[1], and GeV-γ group[1]

[1]*Research Center for Electron Photon Science, Tohoku University, Sendai, 982-0826, Japan*

The nuclear physics research department of Research Center for Electron PHoton Science (ELPH), Tohoku University conducts search experiments of nucleon resonance states and mesic nuclei using an electromagnetic calorimeter. In recent years, experiments are conducted at SPring-8/LEPS2 using the large solid angle electromagnetic calorimeter BGOegg. Subsequently, in our group, the forward gamma ray detector (FG) consisting of 252 PWO crystals is used to compensate for the forward angle, which is currently insensitive. The positron beam line in ELPH was used for performance tests, and an energy resolution of 2.7 % was obtained for 1 GeV positrons. In addition, the angular dependence of incident gamma could be obtained for the first time.

§1. Introduction

Hadron photo-production experiment was carried out at SPring-8/LEPS2 from 2014 to 2016 using a large solid angle electromagnetic calorimeter BGOegg constructed at ELPH. The current BGOegg is composed of 1320 BGO crystals, covering a polar angle of 24 to 144 degrees. In this configuration, BGOegg is insensitive to the region below 24 degrees at forward angle, therefore, by placing the drift chamber and the Resistive Plate Chamber on the downstream of BGOegg, charged particles are detected and the solid angle is compensated. In this setup, the η' mesic nuclei search experiment is conducted by measuring the momentum of the charged particle in the extremely forward angle, but when the decay gammas from the meson is captured only by BGOegg, the forward region is insensitive. In the region of $E_\gamma = 2$ GeV or more high energy where the multi meson production channel becomes dominant, it is difficult to evaluate the total cross section of the production. In addition, when investigating the resonance state that generates multiple π^0 and η, such as $\gamma p \to \eta' \to \pi^0\pi^0\eta p$ reaction, acceptance of the electromagnetic calorimeter becomes more important. In the future, we plan to cover the front area with the same shape of BGO crystal. However, our group has produced an another forward gamma detector (Foward Gamma, FG). Our group already developed FG in past and the solid angle of BGOegg can be compensated by adopting this detector. FG is consist of 252 PWO crystals of 22x22x180 mm^3, the width and height of the sensitive region are 418mm square. If FG is installed at 700mm downstream from the target, it will cover 3-16 degrees at forward angle. The remaining 16-24 degrees can cover by adding about two layers of BGO crystals (in future plan). FG was developed for SPring-8/LEPS experiments with Backward Gamma detectors [1] from October to November 2003. Evaluated performance of FG at this time is about 4.8 % at π^0 invariant mass resolution corresponding to $\sigma_{m_{\pi^0}} = 6.7$ MeV. Since these results are more than 10 years ago, the ELPH positron beamline was used for evaluation of the performance in this time. In particular, evaluation of angular dependence of incident particles and position resolution of FG depend on simulations, so we need to measure these performance using the positron beam to determine the actual energy and position resolution.

§2. Experimental setup and results

The experiment was conducted in June 2017 at the positron beam line in the GeV-γ irradiation room of ELPH. FG detector was installed in the positron beam line, and eBPM was installed upstream of the FG as a positron incident position detector. The experimental setup is shown in Fig. 1. As shown in Fig. 2, 252 PWO crystals are arranged in the front of FG detector. In this experiment, only 25 of these (the shaded area in the figure) were used. The incident position detector eBPM consists of 16 fibers per layer and two layers, it detects the x and y position of positrons. While changing the positron energy from 50-MeV to 800-MeV, the output light quantity of each 25 crystals around 170th crystal was measured. The gain of the crystal was adjusted by injecting the beam into the center of each crystal while changing the energy of the positron beam. After the gain adjustment for all 25 channels was completed, the energy resolution was evaluated by injecting the positron beam at the center crystal again while changing the energy.

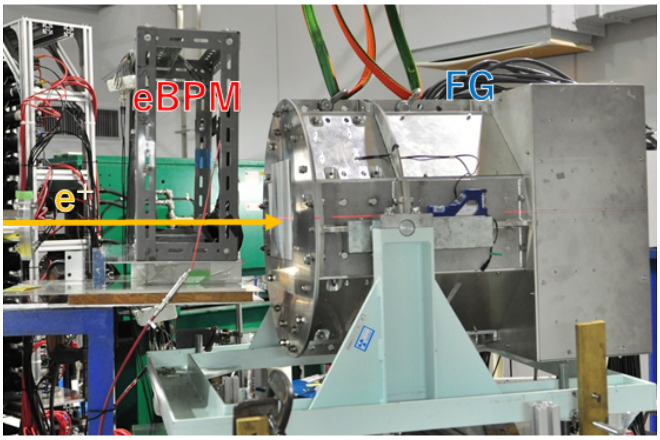

Fig.1. Experimental setup.

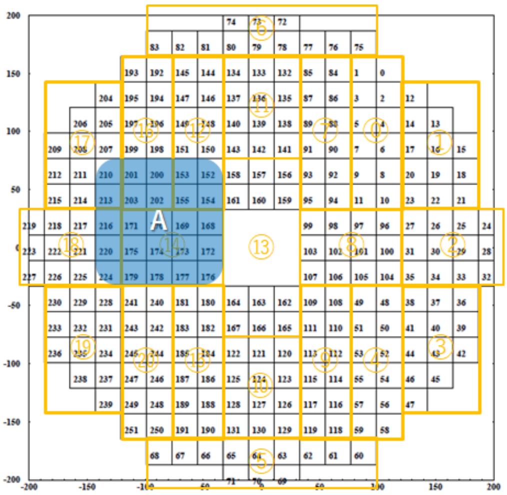

Fig.2. The crystal arrangement seen from the front of the FG, the shaded part is the channel used this experiment.

An energy resolution of 2.67% for 1 GeV positrons is obtained in Figure 3. This value is comparable to the results of previous experiments [2]. Next, an energy resolution was measured by shifting the beam incident position by 12 mm from the crystal center which corresponding to the edge region of PWO crystal. The energy resolution at this incident position was 2.71%. Finally, the energy resolution was evaluated by changing the angle of FG from 0° to 16° with the incident position centered on the crystal.

The result is shown in Figure 4.

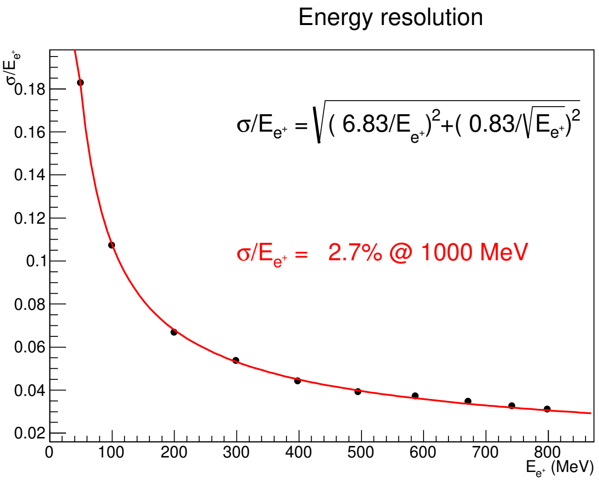

Fig.3. Energy resolution obtained when a positron is incident on the crystal center

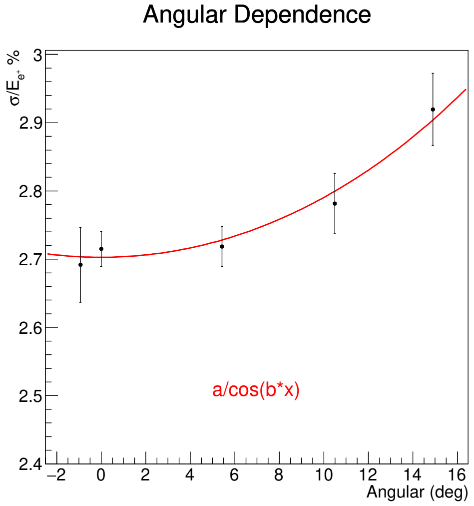

Fig.4. Energy resolution as a function of the incident angle of the positron beam

§3. Summary

We evaluated the performance of the FG detector at the positron beamline in Research Center for Electron PHoton Science, Tohoku University. As a result of the experiment, the FG detector achieved the expected energy resolution and obtained the new angular dependence data. The simulation parameters are determined from the obtained data and these results will be used for the analysis of experimental data using the BGOegg and FG detectors planned in the future. The FG detector that completed the performance evaluation experiment was transported from ELPH to the SPring-8/LEPS2 experimental building in February 2018 after replacement of several damaged PMTs, and is currently preparing for future experiment.

References

[1] T. Ishikawa, ”The FOREST detector for meson photoproduction experiments at ELPH”, Nucl. Instrum. and Meth. A 832, 108 (2016).

[2] H. Shimizu, ”Performance of a $PbWO_4$ crystal calorimeter for 0.2-1.0 GeV electrons” Nuclear Instruments and Methods in Physics Research A 447 (2000) 467-475

(ELPH Experiment : #2848)

Photo-production of a Neutral Kaon and/or a Lambda Hyperon on a deuteron near the threshold

Masashi Kaneta[1] for the NKS2 collaboration

[1]*Department of Physics, Graduate School of Science, Tohoku University, Sendai, 980-8578*

The NKS2 spectrometer and photon tagging system had been damaged due to the 2011 off the Pacific coast of Tohoku Earthquake. The experiment was conducted to show that the detector performance was sufficient after the recovery.

§1. Introduction

We had been studying the strangeness photo-production near the threshold using NKS2 spectrometer in the 2nd experimental hall at ELPH. The reaction we focus is $\gamma + d \rightarrow K^0 + \Lambda + (p)$. The photon beam was generated by the bremsstrahlung using a carbon wire in the BST ring, and tagged by the photon tagging system (tagger). The original tagger was damaged by the aftermath of the 2011 off the Pacific coast of Tohoku Earthquake. We developed and constructed new tagger using SiPM (MPPC by HAMAMATSU photonics) and plastic scintillator. The proposed experiment was the performance test of NKS2 spectrometer and tagger system. We will report that the while system is ready to the measurement using Λ measurement. This report is based on master's thesis of Ms. Ninomiya [1]

§2. Result of Λ analysis

The data was taken in Jun, 2016. We did not cover while energy coverage of tagger due to limited number of circuit module at that moment. we concentrated in high energy region (up to E_γ = 1.264 GeV in design value) to record the data, because the new tagger covered higher energy region than previous tagger (up to E_γ = 1.1 GeV). We set two-particle trigger for the data taking.

The particle identification was done by using Time-Of-Flight (TOF) and momenta. The TOF was computed hit timing information from Inner Hodoscope (IH) and Outer Hodoscope (OH). The momentum and flight path were reconstructed drift time information of Cylindrical Drift Chamber (CDC) and Vertex Drift Chamber (VDC). The detail information of the NKS2 spectrometer and tagger can be found in elsewhere. [2, 3]

After selecting proton and negative pion candidate, we adopted three type of cuts to reduce the background. We named those cuts as opening angle cut, decay volume cut, missing mass cut, and invariant mass cut.

The opening-angle (θ) cut was applied to reject electron-positron pair event. We selected event which had the π^- p candidate and opening angle between the two particles in $-0.9 < \cos\theta < 0.9$.

We reconstructed the decay position as midpoint on the distance-closed-approach of p and π^- trajectories. Part of the Λ decayed in outer region of the target cell because of weak decay. We requested that the decay point was out of the target cell to reduce accidental background.

The missing mass of the reaction $\gamma + n \to p + \pi^- + X$ is shown in Fig. 1. We assumed the rest of neutron in this calculation. Because of Fermi motion of the neutron in the deuteron, we saw the wider distribution than expected Kaon mass distribution.

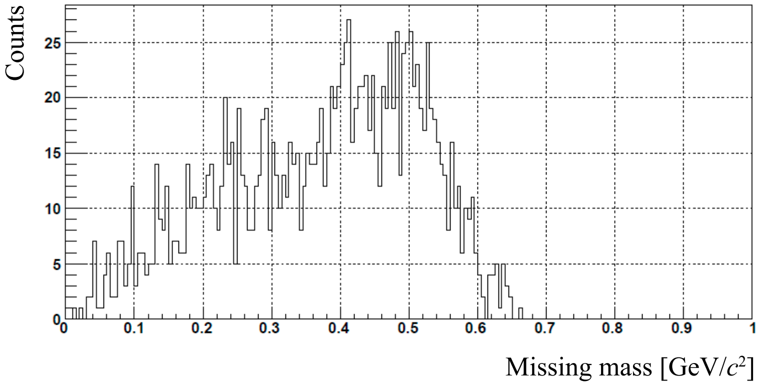

Fig.1. Missing mass distribution of X in $\gamma + n \to p + \pi^- + X$ reaction

The final cut to select Λ is the invariant mass selection. To increase the accuracy of particle identification, we checked correlations of the missing mass and invariant mass. Figure 2 shows the correlations.

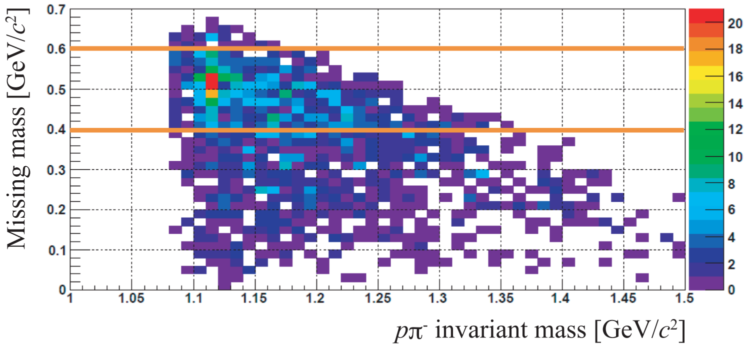

Fig.2. Correlation of the missing mass (M_X) in $\gamma + n \to p + \pi^- + X$ reaction and the invariant mass of $p\pi^-$. The lines indicate the region selected as Kaon candidates ($0.4 \leq M_X \leq 0.6$ GeV/c^2).

We chose the missing mass region in 0.4 - 0.6 GeV/c^2 as Kaon candidates. After selecting the region, we obtained the invariant mass distribution shown in Fig. 3. We saw the peak around 1116 MeV/c^2 in the figure. We obtained that the peak position is 1113.6 $\pm$ 0.6 MeV/c^2 and σ is 4.8$\pm$0.6 0.6 MeV/c^2. The number of Λ is 138$\pm$15 with selecting $\pm 3\sigma$ region.

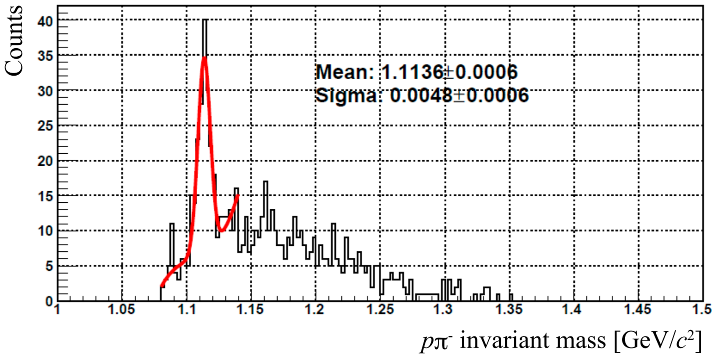

Fig.3. The invariant mass distribution of $p\pi^-$ after the missing mass cut. The curve is a fit result of Gaussian + 3rd order of polynomial.

§3. Summary

The orbit electron energy became 1.3 GeV from 1.2 GeV with update of the electron synchrotron. We developed and installed new tagger system along with the update. Current maximum energy of tagged photon is 1.264 GeV.

We carried out the experiment of strangeness photo-production using liquid deuterium target with 1.3 GeV electron energy. The data was analyzed and we obtained the identified Λ. The peak position of invariant mass of Λ was close to PDG value. On continuing the analysis, we will obtain the cross-section of Λ in photon beam energy region that NKS2 have not.

Acknowledgment

We would like to express our gratitude for the maintaining the accelerator operation of the accelerator group. We appreciate the engineering/technical staff, Mr. Umetsu for his support in the developing and construction of new tagger. This work is partly supported by JSPS Grant-in-Aid for Creative Research Program (16GS0201), JSPS Core-to-Core program (21002), JSPS Grant-in-Aid for Scientific Research (C) (23540334), and JSPS Grant-in-Aid for Scientific Research (A) (17H01121).

References

[1] 二宮亜紀 2017 修士論文「η 中間子および Λ 粒子光生成反応を用いた新光標識化装置の性能評価」.

[2] H. Yamazaki *et al.*: Nucl. Instrum. Meth. **A536** (2005) 70-68.

[3] M. Kaneta *et al.*: Nucl. Instrum. Meth. **A886** (2018) 88-103.

(ELPH Experiment : #2880)

The performance test for the time resolution of Multi-gap Resistive Plate Chamber (one of the experimental courses in Graduate Program on Physics for the Universe curriculum in Tohoku University)

Masashi Kaneta[1], Toshiyuki Gogami[1,*], and Satoshi N. Nakamura[1]

[1]*Department of Physics, Graduate School of Science, Tohoku University, Sendai, 980-8578*

This text experiment was carried out as one of the experimental courses in Graduate Program on Physics for the Universe (GP-PU) curriculum in Tohoku University. In this course, we requested to master analysis method of the intrinsic timing resolution from three combinations of Time-Of-Flight from three different counters.

§1. The GP-PU program and the experimental course

The GP-PU program is a part of the international joint graduate school programs. The Head of the division for the programs addresses the programs as the following. “The International Joint Graduate School Programs have been / will be established under the Division for International Joint Graduate Degree Programs, through strong collaboration with influential universities overseas in order to spread Tohoku University’s expertise beyond the bounds of existing educational systems. Based on an analysis of Tohoku University’s potential and strengths, the programs’ fields will tackle issues and global problems confronting humanity, promise future development, and lead the global community, exhibiting the capabilities of Tohoku University.” [1]

The GP-PU students need to take additional classes: the GP-PU seminar, the GP-PU experiment, and the GP-PU school. The GP-PU experiments cover the field of elemental particle physics, nuclear physics, and cosmology. “A role of the program is to make students learn a comprehensive view, which can be utilized to be a leader for either academic or other jobs after graduation, through classes in which cutting-edge experimental apparatuses and techniques are introduced and used. ” [2]

This test experiment is one of the GP-PU experiments and the GP-PU students had the following experience. (1) Construction of a test bench for detector test using cosmic-ray. (2) Assembling of Multi-gap Resistive Plate Chamber (MRPC) (3) Performance study by cosmic-ray and electron/positron beam.

§2. Multi-gap Resistive Plate Chamber

Figure 1 shows the structure of MRPC. It was consisted from two stack of five-gap spacing.

---

[*] Present address: Department of Physics, Graduate School of Science, Kyoto University, Kyoto, 606-8502

Table 1. Size of materials for MRPC

Parts	Material	size
Resistive plate	Soda-lime glass	$100^{W} \times 480^{H} \times 0.4^{T}$ [mm^3]
Insulator	Glass-epoxy	$120^{W} \times 500^{H} \times 0.6^{T}$ [mm^3]
Read-out pad	Gold plating copper	$40^{W} \times 460^{H} \times 0.018^{T}$ [mm^3] (rectangle region)
Spacer	Fishing wire	No.2, ∅ 0.235 mm
Electrode	Adhesive carbon tape	$100^{W} \times 480^{H} \times 0.09^{T}$ [mm^3]

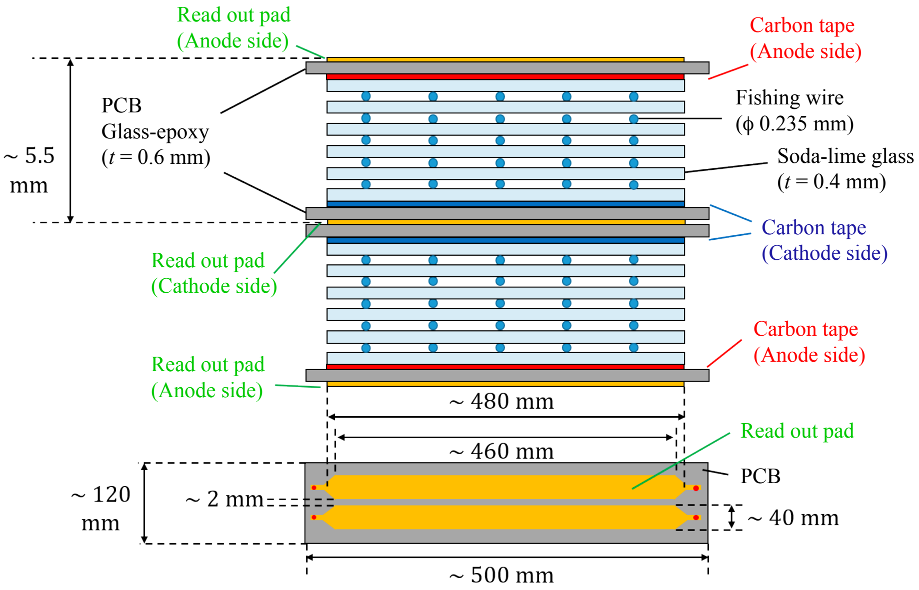

Fig.1. Structure of MRPC seen from side is shown in top. The bottom figure is the top view with correct aspect ratio.

We used 0.4 mm thickness soda-lime glasses for resistive plates. The gas spacing was kept by No. 2 fishing wire (0.235 mm diameter). The read-out pad and the electrode were on the glass-epoxy plate (0.6 mm thickness) and made as a printed circuit board. The electrode was covered by an adhesive carbon tape to increase the resister of the electrode and to decrease charge spread. The summary of material is listed in Table 1.

MRPC was fixed in a box and chamber gas was flowed in the box. We used mixed gas of R-134a (90%) and SF_6 (10%).

The high voltage was applied from outsize via SHV connector. The signal was read through a connector on the side plate of the box. We set an amplifier circuit on outside of the box. Figure 2 shows the circuit diagram of the amplifier.

We only used the anode signal from MRPC. In the first stage, there were resisters in both channels of the anode ant the cathode for the impedance matching. We set differentiator before the non-inverting amplifier in order to get a sharp rising signal. The operation amplifier we chose was AD8000 provided by Analog Devices. The values of resister and capacitor are listed in Table 2. The signal line and circuit board are shown in Fig. 3.

Table 2. Parameter of resister and capacitor.

Parts	values
R	34 Ω
R2	100 Ω
R3	20 Ω
R4	2k Ω
R5	51 Ω
C1	100 pF
C2	0.1 μF
C3, C5	1000 pF
C4, C6	0.1 μF
V_{CC}	5 V
V_{EE}	-5 V

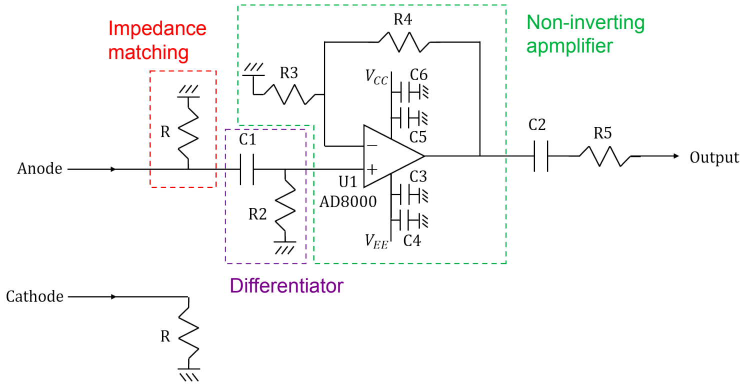

Fig.2. Circuit diagram of the amplifier for the MRPC.

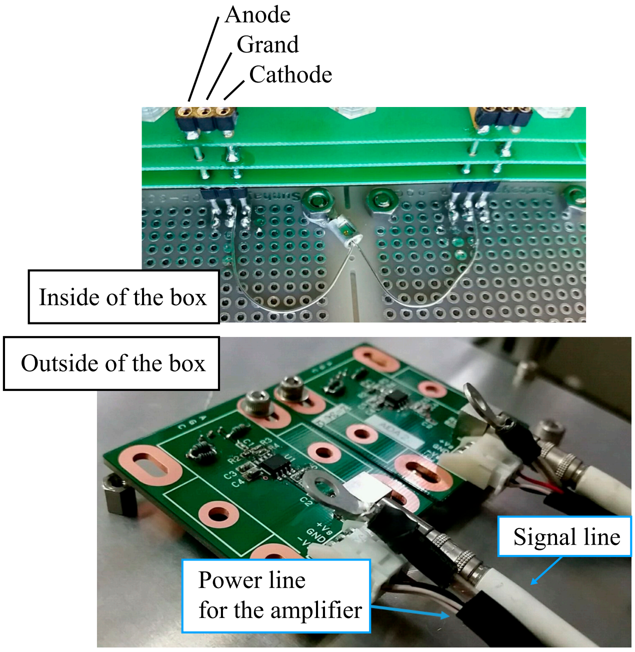

Fig.3. Photo of amplifier.

Note that we also carried the impedance matching test with changing the register value. It will be reported as another manuscript (ELPH experiment: #2890) because of the different proposal to PAC.

§3. The set-up of the experiment

We used the positron beam line in the GeV-γ experimental room. Figure 4 shows the set-up of the experiments. We put the two finger counters, a veto counter, MRPC box, two reference counters, and one finger counter from upstream side.

Three finger counters (single side readout by PMT) was used to guarantee the beam position. The veto counter has a hole (shape: 1 cm × 1 cm square) was located at downstream of two finger counters to avoid counting of beam halo by scattering. We used two thick plastic scintillation counters (double side readout by PMT) as the reference counter of Time-Of-Flight (TOF).

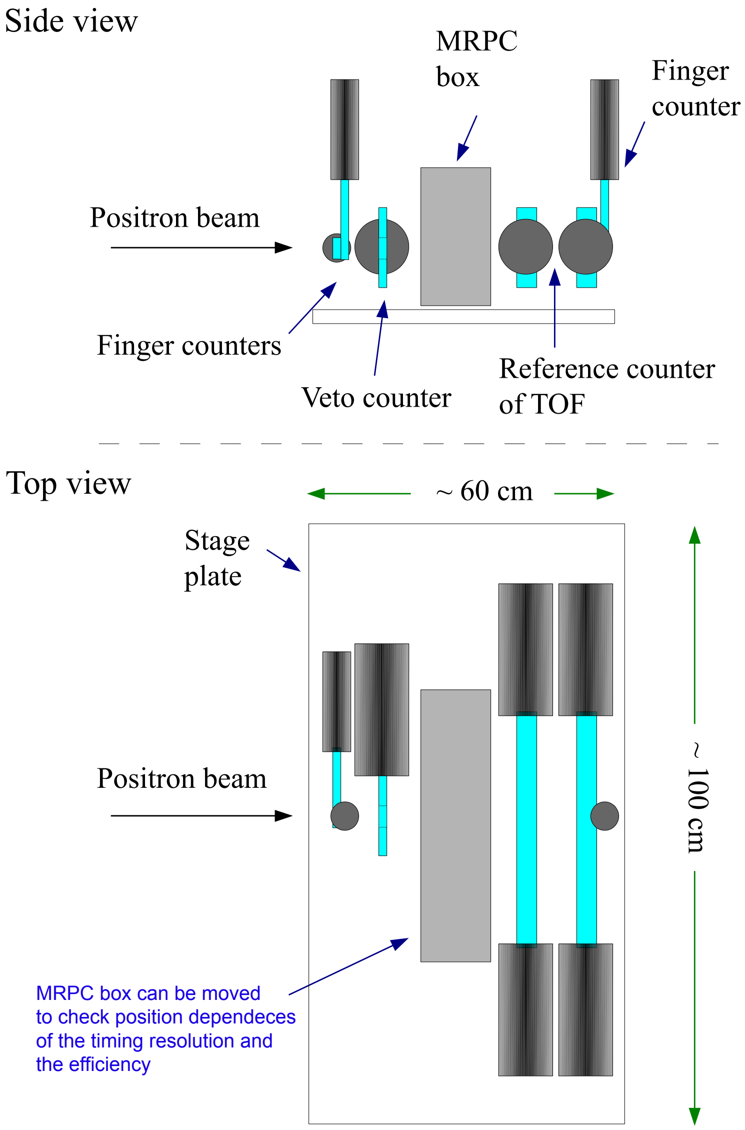

Fig.4. Detector alignment of the experiment are shown. The top figure is the side view and the positron beam travel from left-hand side to right-hand side. The bottom figure is the top view.

We tested beam rate dependence of TOF resolution. The positron beam was generated by electron-positron conversion of gamma beam with a metal target. We used three metals that are prepared in GeV-γ experimental room. The beam rate is defined by the coincidence signal rate among three finger counters and veto counter. If the veto counter had a hit in the same timing with three coincidence of three finger counter, the event was excluded.

The following list is the summary of target materials and beam rates.

- Gold (radiation length 0.006 X_0): 160 Hz/cm^2
- Tungsten (radiation length 0.06 X_0): 320 Hz/cm^2
- Brass (radiation length 0.6 X_0): 570 Hz/cm^2

§4. Results

The intrinsic timing resolution of MRPC was computed via three combination of TOF resolution of combination of two of three counters (TOF1, TOF2, and MRPC). Figure 5 shows the timing resolution of MRPC. The resolution became better (smaller value) with increasing the high voltage. With increasing the beam rate, the resolution is getting worse.

The typical timing resolution of MRPC is about 100 ps. The results were worse than that value. The additional test to investigate the reason was done by using cosmic-ray. The detail discussion will be found the other manuscript (ELPH Experiment: #2890) of the annual report.

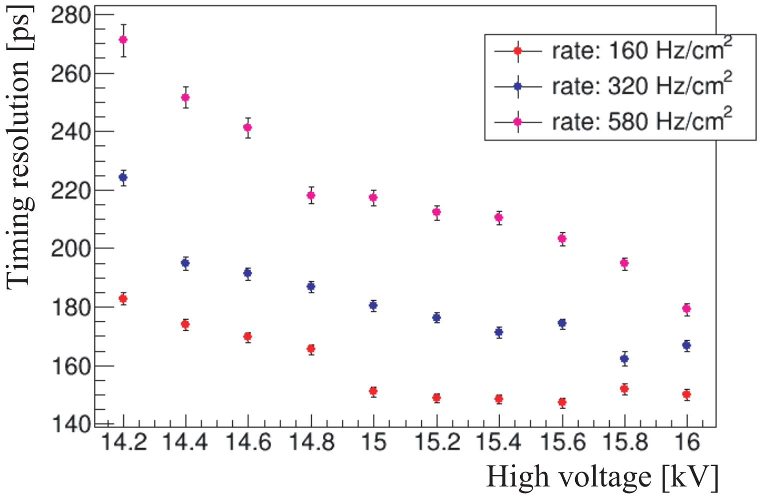

Fig.5. The intrinsic timing resolution of MRPC as a function of induced high voltage for three different beam rates.

§5. Summary

The experiment of performance test of Multi-gap Resistive Plate Chamber was carried out as one of the experimental courses in Graduate Program on Physics for the Universe curriculum in Tohoku University. The student had the experience of the process in elementary particle and nuclear physics.

Acknowledgment

We thank the accelerator staff of ELPH to provide the stable operation of accelerator. The experiment was supported by GP-PU program.

References

[1] http://ijg.pgd.tohoku.ac.jp/english/message/index.html
[2] http://lambda.phys.tohoku.ac.jp/gppu/exp/

(ELPH Experiment : #2890)

The performance test of the amplifier for Multi-gap Resistive Plate Chamber

Masashi Kaneta[1] for the NKS2 collaboration

[1]*Department of Physics, Graduate School of Science, Tohoku University, Sendai, 980-8578*

We are planning the Λn interaction measurement via the final state interaction (FSI) in $\gamma + d \rightarrow K^+ + \Lambda + (n)$ reaction. We proposed the measurement of K^+ cross-section in that reaction to obtain the FSI effect. The separation of Kaon from pion and proton is the essential for the experiment. The Multi-gap resistive Plate Chamber is adopted for the new TOF counter of Kaon identification. We tested different setting of amplifier circuit board to evaluate the timing resolution and the efficiency.

§1. Introduction

We have been developing The Multi-gap Resistive Plate Chamber (MRPC) as a high-resolution Time-Of-Flight detector for the NKS2 experiment. The requirement of the timing resolution is less than 120 ps to separate $\pi/K/p$ with combination of IH as the start counter of TOF. The signal of MRPC is smaller than PMT and then we need to use an amplifier. We had tested the amplifier circuit in the same beam time of ELPH Experiment: #2880. The description of the structure of MRPC, the amplifier circuit, and the setup of the test experiment are shown in the annual report of the #2880.

The LEPS group reported that they needed to impedance matching circuit between MRPC and amplifier to avoid a reflection. The effect of reflection caused a reduction in timing resolution. We adopted the matching circuit in our amplifier circuit board.

Note that the detail discussion of the test is shown in Master's thesis of Mr. Takeuchi [1].

§2. Amplifier circuit

Figure 1 shows the circuit diagram of the amplifier. We selected circuit parameters with a circuit simulator LTSpice. Before the beam time, we selected the two candidate of register value (34 and 43 Ω) with MRPC signal by cosmic-rays.

To distinguish between MRPC performance and circuit performance, the circuit's rate tolerance was tested. We didn't see pile-up and changing the shape of output signals in 5 MHz (200 ns interval) of 50 ns width input signals. We expected 10 kHz maximum hit rates in MRPC and then the rate tolerance of MRPC would not be limited by the circuit.

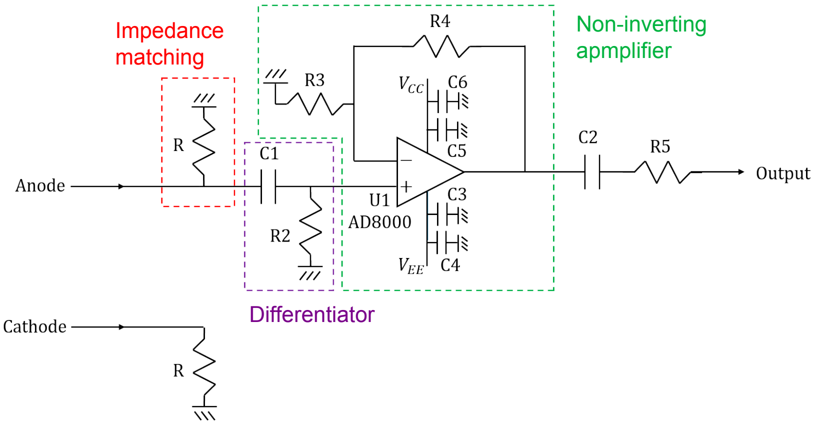

Fig.1. Circuit diagram of the amplifier for the MRPC.

§3. Results

3.1 Beam rate and matching register dependence

The intrinsic timing resolution of MRPC was computed via three combination of TOF resolution of combination of two of three counters (TOF1, TOF2, and MRPC). Figure 2 shows the timing resolution of MRPC. The resolution became better (smaller value) with increasing the high voltage. With increasing the beam rate, the resolution is getting worse.

The typical timing resolution of MRPC is about 100 ps. The results were worse than that value. The additional test to investigate the reason was done by using cosmic-ray.

The detection efficiency of MRPC is defined by the fraction of MRPC hits to trigger hits. The high voltage dependence of the efficiency is shown in Fig. 3.

The timing resolution and the detection efficiency seems to be the best with 16 kV high voltage with 43 Ω matching register. The best value of efficiency is about 98 to 99% that are the same with typical values of MRPC.

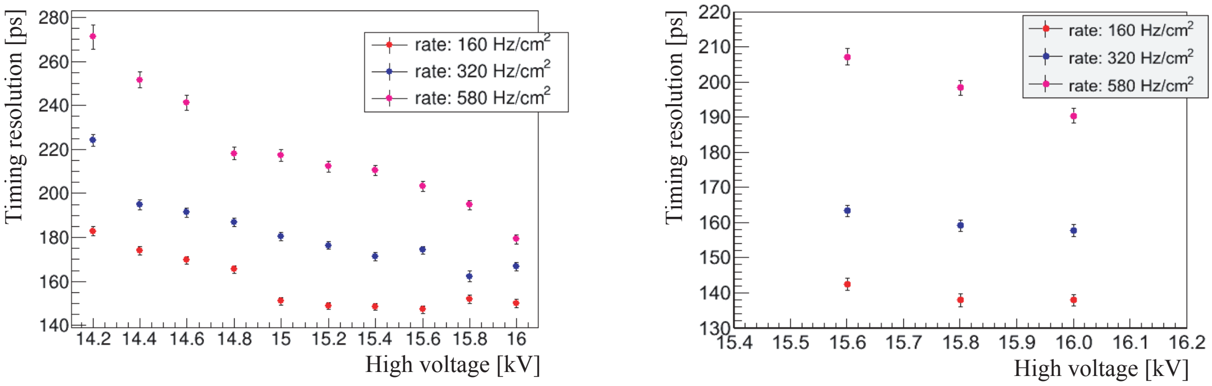

Fig.2. The intrinsic timing resolution of MRPC as a function of induced high voltage for three different beam rates. We used 34 Ω and 43 Ω register for the impedance matching and show left- and right-hand side, respectively.

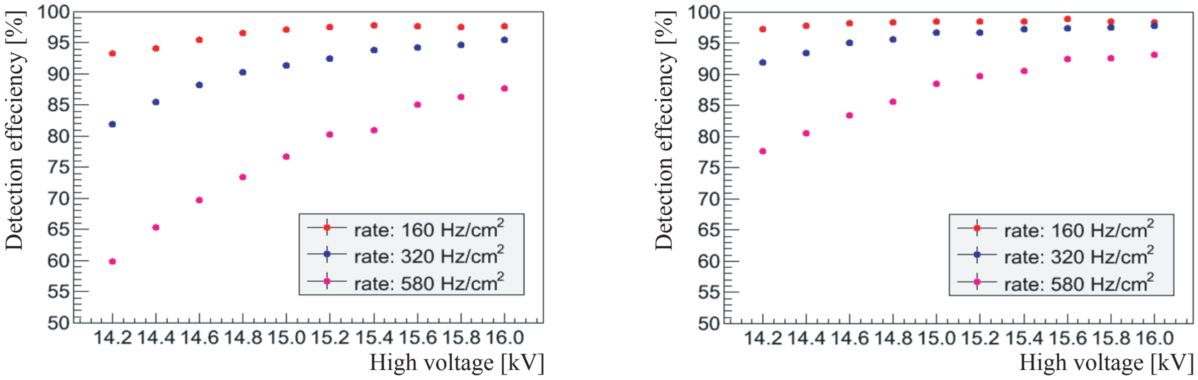

Fig.3. The detection efficiency of MRPC as a function hit position. We used 34 Ω and 43 Ω register for the impedance matching and show left- and right-hand side, respectively.

3.2 Hit position dependence

Figures 4 and 5 show the hit position dependence of the intrinsic timing resolution and the detection efficiency, respectively. The high voltage was fixed as 16 kV and the beam rate is 320 Hz/cm^2 (converter: Tungsten). The left and right was defined as view seen from upstream side.

The results showed that there was position dependence in the timing resolution and the efficiency. If the reason was the reflection of signal, we expected the same dependence in the timing resolution and the efficiency. We guessed that it was due to insufficient gas replacement time and a noise because of the weak connection between MRPC and the amplifier circuit.

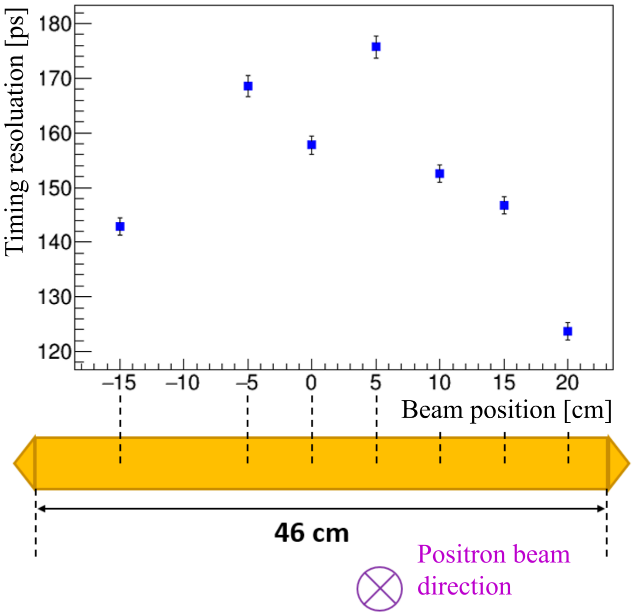

Fig.4. The intrinsic timing resolution of MRPC as a function of induced high voltage for three different beam rate. We used 43 Ω register for the impedance matching.

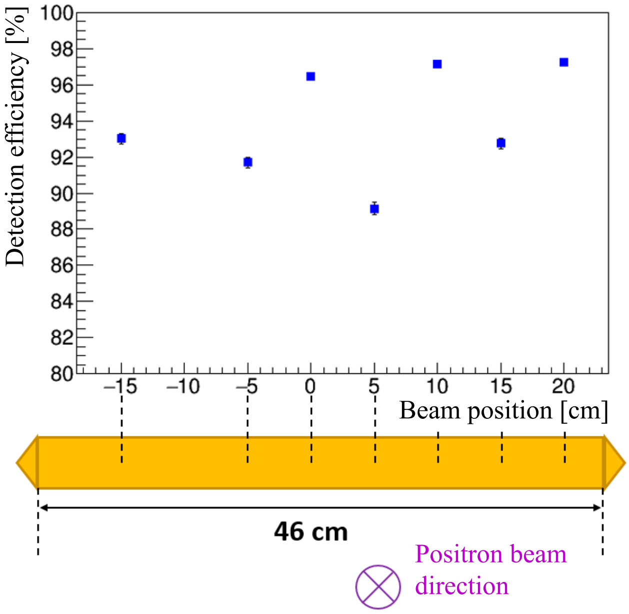

Fig.5. The detection efficiency of MRPC as a function of hit position. We used 43 Ω register for the impedance matching.

§4. Cosmic-ray test

The performance test with positron beam did not show the sufficient result we expected. We introduced longer gas replacement time and additional grand lines.

Before the beam time, we used 3 days for the gas replacement with 30 cc/min flow. We took 10 days for the replacement with 30 cc/min flow before the cosmic-day test.

The reference counters we used in the test is the same plastic scintillation counters with the beam test. Table 1 shows the summary of the intrinsic timing resolution comparing the beam test. The result met our request ($\sigma_{\text{timing}} < 120$ ps).

Table 1. The intrinsic timing resolution of cosmic-ray test.

Induced high voltage [kV]	Intrinsic timing resolution of MRPC [ps]	
	Cosmic-ray test	Beam test
16.0	118.8 ± 2.3	150.1 ± 1.9
15.6	128.1 ± 2.7	147.2 ± 1.7

§5. Summary

We tested two different impedance matching resister on the amplifier circuit board of MRPC in the GeV-γ experimental room at ELPH. The detection efficiency of MRPC tested was about 98 to 99% and it was the same value with typical value of general MRPCs. The timing resolution was not reached 100 ps we expected and there were hit position dependence in the timing resolution and the efficiency. We conclude the worse timing resolution and position dependence were due to less time of gas replacement. After 10 days of gas replacement time, the timing resolution was about 120 ps in the test with cosmic-ray. The resolution was sufficient the request of $\pi/K/p$ separation in the future experiment.

Acknowledgment

We thanks the accelerator staff of ELPH to provide the stable operation of accelerator.

References

[1] 竹内大貴 2018 修士論文「Λn 終状態相互作用研究に向けたMulti-gaps Resistive Plate Chamber の開発」)

(ELPH Experiment : #2899)

Development for the resistive plate chamber (RPC)

Yuto ISHIZUKI*, Jumpei TAKAHASHI*, Daisuke TAKI*, Kento TERADA*,
and Hiroaki Ohnishi*

§1. Introduction

The resistive plate chamber (RPC) is one of the key technologies for Time of Flight (ToF) measurement these days. Figure 1 shows a typical structure of the RPC, which consists of thin glasses with thin gaps made with 0.26 mm diameter fishing line. The most outside of the glass will be covered by a high resistive electrode to apply high voltage on the detector. A produced signal will be read out by the pickup electrode, which is placed outside of the high resistive electrode with 0.4mm thick G10 plate in between. According to the previous experiences, a thin gap will improve timing resolution, however, the efficiency of the detector will be reduced. To overcome the reduction of efficiency, multi gap configuration, which is shown in Figure 1, has been proposed and used as high efficiency and high time resolution detector technology nowadays.

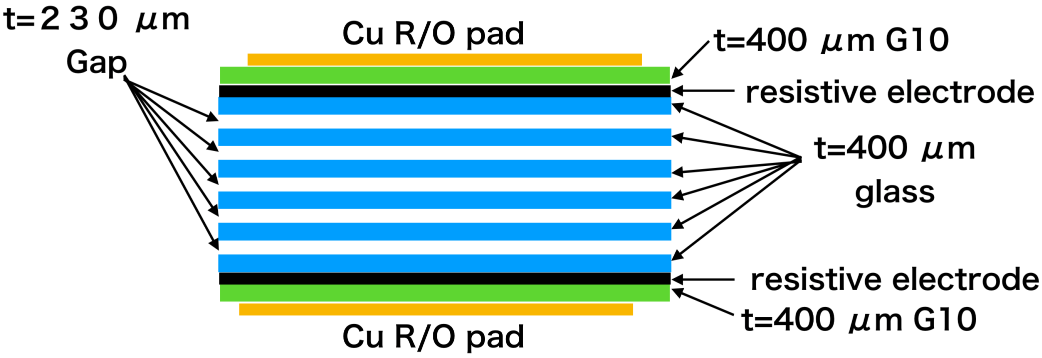

Fig.1. Schematic view of the typical RPC

.

Advantages to use RPC for ToF detector is as follows. First of all, the detector is not using photomultipliers(PMT); thus, the RPC has strong capability against the magnetic field. Second, the RPC will show quite good time resolution, which is an order of 50 ps, and high efficiency, which is more than 99% at the same time. At last, the main component of the RPC is thin glasses. Thus, the construction cost of RPC can be reduced, by keeping high performance, concerning ordinary ToF detector, which consists of scintillator and PMTs. Because of the reasons listed above, RPC is chosen as the primary choice of the ToF detector for high energy and nuclear physics, especially if they need a large area detector.

---

*Present address: Research Center for Electron Photon Science, Tohoku University, Sendai, 982-0826

For instance, large area RPC, such as 2 m long detector has already constructed for the LEPS2 experiment at SPring-8 [1]. Shortly, construction of new large area ToF detector is planing for J-PARC experiment [2]. For the LEPS2/RPC construction, adhesive carbon tapes [3] has been used as the high resistive electrode, because it is easy to use. Moreover, it was commercially available. However, the production of the carbon adhesive tape which has been used was discontinued to date. Therefore, we need to find an alternative solution for the high resistive electrode for future RPC production. As a result of investigating the previous researches, we find high resistive paint is widely used as a resistive electrode for RPC worldwide. In this report, we show the first trial to produce RPC by using high resistive paint as a high resistive electrode.

§2. Resistive paint

The resistive electrode is one of the important element to construct the RPC. The resistivity is very important. It controls cross-talks on signals in the readout electrode. The requirement of the resistivity for the detector electrode is needed to have an order of $10^3 - 10^6\Omega$/sq. We found two candidates on the market. One is COLCOAT PS-2002 by COLCOATCO. Ltd. [4] and the other is SEPLEGYDA AS-MO4D produced by Shin-Etu polymer Co.Ltd. [5]. Table 2 shows basic properties for those paints. That paint seems suitable for the RPC, because the resistivity can be controllable by the thinness of the paint and the paint is water-soluble, I.e., it is not necessary to prepare the organic solvent facility.

Name	Main conductive materials	solvent	surface resistivity [$\Omega/sq.$]
COLCOAT PS-2002	Antimony-doped tin oxide	water / alcohol	$10^6 \sim 10^7$
SEPLEGYDA AS-MO4D	Polythiophene	water / alcohol	10^6

Table 1. Properties of the paint we are used for this test.

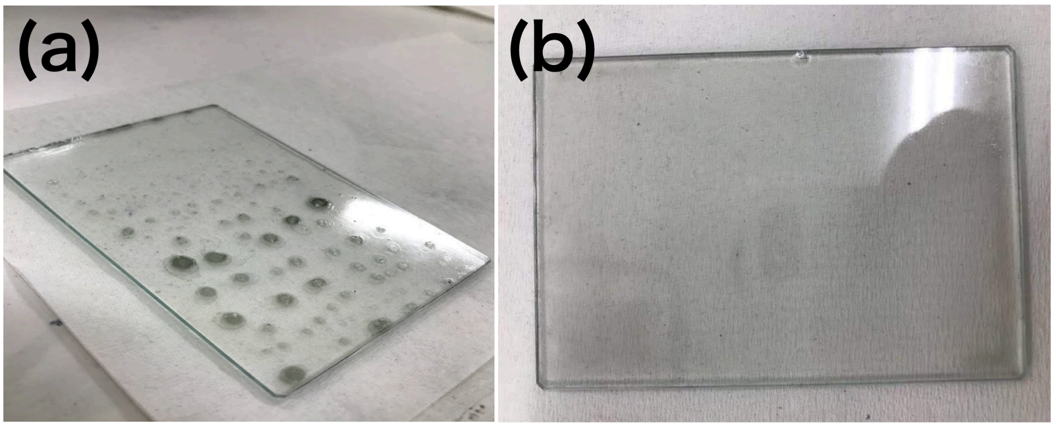

Fig.2. Pictures of painted glasses, without (a) and with (b) surface treatment.

§3. Painting on glasses

First of all, we tried to paint on the glass surface that we chose earlier. The results are shown in the Fig 2.-(a) It was found that the paint cannot be applied uniformly due to the volatility of the glass.

During the discussion with the producer of the paint, they suggested to wash the glass surface by acid, to roughen the surface of the glass. The result is shown in Fig 2-(b). Finally, we succeeded to paint glass surface with the selected paint. Figure 3 shows the relation between paint thickness and volume resistivity. The target thickness of the paint was 35μm. However, the actual thickness measured was scattered about 10-40μm. The result indicates difficulty to control the thickness of the paint. On the other hand, surface resistivity for all paint samples are shown similar value, which is $\sim 10^5\Omega/sq.$

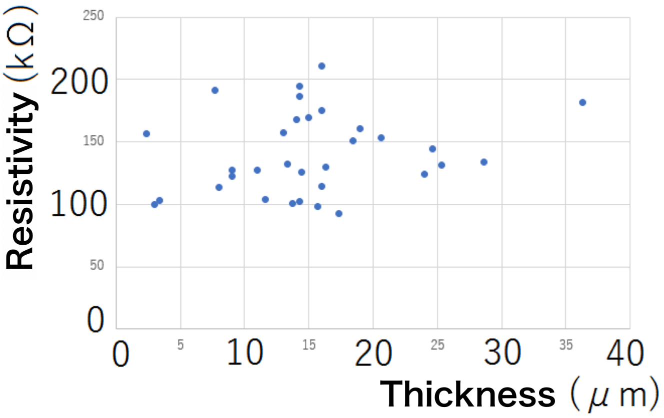

Fig.3. Correlation between surface resistivity and paint thickness. Clear correlation has not seen.

§4. Detector construction

By using the glasses with resistive paint on it, a single gap type of the RPC has been constructed. The size of glass is 55 mm × 80 mm and 1.8 mm thick. The gap of the RPC is set to 0.5 mm, which is kept by 0.5 mm Acrylic plate as a spacer. Signal pick up electrode made with Copper adhesive tape is placed outside of paint electrode with 1.6 mm thick G10 plate in between. For the reference, we also produce an RPC with Adhesive carbon tape, which is used for LEPS2-RPC. Figure 4 shows constructed RPCs. For the test experiment, the standard gas mixture for RPC, i.e., $R134a : C4H10 : SF6 = 90 : 5 : 5$ was used. The initial test has been performed with cosmic rays. The obtained raw signal is shown in Fig 5 The result indicates that the pained electrode seems to work correctly as a resistive electrode. Those constructed detectors are tested with positron beam at ELPH.

§5. Test experiment with positron beam at GeV-γ experimental hall

The test experiment is performed with a positron beam at the GeV-γ experimental hall. Bremsstrahlung γ-ray radiated in BST ring is delivered to the GeV-γ experimental hall. The γ-ray was converted to the electron-positron pairs in the thin lead target which is located in front of the Tag-X magnet. Converted positrons are selected by Tag-X magnetic field and delivered to test experiment area. The momentum of the positrons is selected to be 600 MeV for the test experiment. The typical intensity of the positron is about 300 Hz/cm^2. The experimental setup is shown in Fig.6.

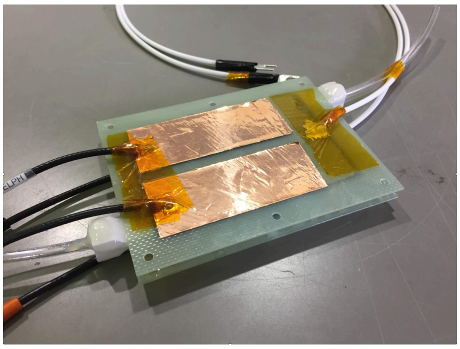

Fig.4. Constructed test detector.

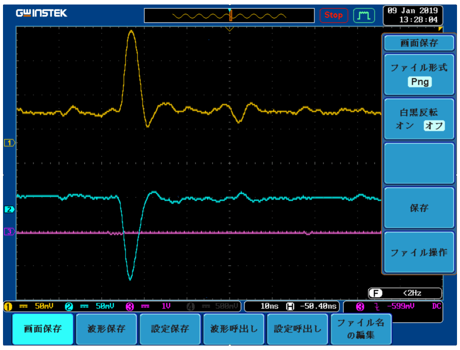

Fig.5. Cosmic ray signal seen by RPC with pained electrode.

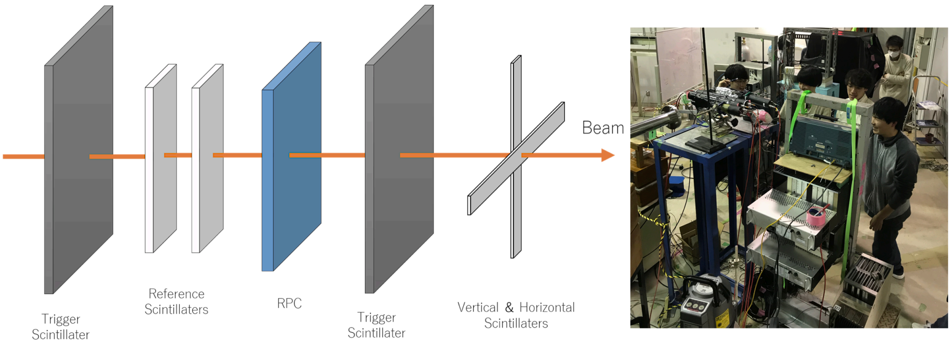

Fig.6. Schematic view of the experimental test setup and a picture during experiment

§6. Results and Discussion

Figure 7 shows detector efficiency as a function of applied voltage. Red(Blue) points show the efficiency of the RPC constructed with paint (ordinary Carbon tape) as resistive electrodes. Both RPC show the efficiency plato $\sim$ 60% efficiency, which indicates that painted electrode is working as same as ordinary Carbon electrode.

To understand the result obtained above, we performed detector simulation by using the detector model describing in the Refrence [6]. The simulation result tells us that the detector efficiency for this configuration must be closed to $\sim$ 98% or more. We employee parameter scan for the detector simulation to match the simulated results to the result obtained by the test experiment. The possible parameters which may make worth detector efficiency will be gap distance and applied voltage. In the simulation, even if we reduced Gap distance down to 0.3 mm, the efficiency is as much as $\sim$ 80%, which is still inconsistent with the test experiment. It should be noted, we use relatively thick glass for this test, i.e., 1.8 mm. Also, we construct a small detector. Thus, It is tough to believe the reason for the low efficiency is coming from gap distance. The applied voltage between the gap is one of another possible source. However, for this test, we do not have a way to measure the electric field between the gap directly. Thus, we have no way to deny this possibility at this moment. Another possibility is, for this test detector, we are using relatively large area space to keep gap distance. If there is surface current flow through the detector, the effective electric field might be reduced. This can be tested with changing spacer to other

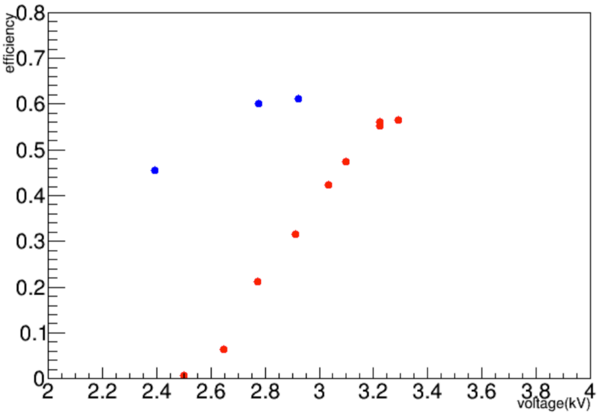

Fig.7. Detector efficiency as a function of applied voltage.

materials. Further investigation should be needed to find the reason.

§7. Summary

The RPC now becomes one of the standard detectors for ToF measurement. Unfortunately, the widely used resistive electrode is not available anymore. Therefore study to found an alternative solution is mandatory. We are trying to produce RPC with high resistivity paint as the electrode. The results indicate promising results. However, many difficulties are found, such as how to control the thickness of paint, uniformity, so forth.

The test experiment has been performed at ELPH by using a positron beam. The result shows similar performance, both ordinary carbon tape, and paint electrode. However, overall detector efficiency seems too low for both detectors compared to the detector simulation results. The reason is now under investigation.

Acknowledgment

We are grateful to the all staff members of ELPH for their extensive efforts on the successful operation of the facility. This work is partly supported by the MEXT Grants-in-Aid for Scientific Research on Innovative Areas “Clustering as a window on the hierarchical structure of quantum systems” Group-A02 (18H05402).

References

[1] K. Watanabe *et al.* Nucl. Instrum. Meth. **A 925**(2019)188
[2] J-PARC E50 proposal, see http://j-parc.jp/reseacher/Hadron/en/Proposal_e.html
[3] https://www.esd-emi.com
[4] https://www.colcoat.co.jp/images/chemical/pdf/kinousei_07.pdf
[5] https://www.shinpoly.co.jp/product/material/seplegyda/seplegyda.html
[6] Werner Riegler *et al.* Nucl. Instrum. Meth. **A 500** (2003)144.

(ELPH Experiment : #2900)

Performance evaluation of a scintillating fiber detector for the high-momentum secondary beamline at J-PARC

T. Aramaki[1], T. Akaishi[2], H. Asano[3], C.-Y. Chang[4], W.-C. Chang[4], R. Honda[1],
Y. Igarashi[5], T. Ishikawa[6], S. Kajikawa[1], Y. Ma[3], K. Nagai[4], H. Noumi[7,5],
H. Sako[8], K. Shirotori[7], T.N. Takahashi[7],
and for the J-PARC E50 collaboration

[1]*Department of Physics, Tohoku University, Sendai 980-8578, Japan*
[2]*Department of Physics, Osaka University, Toyonaka 560-0043, Japan*
[3]*Meson Science Laboratory, RIKEN, Wako, 351-0198, Japan*
[4]*Institute of Physics, Academia Sinica, Taipei 11529, Taiwan*
[5]*Institute of Particle and Nuclear Studies(IPNS), High Energy Accelerator Research Organization (KEK), Tsukuba 305-0801, Japan*
[6]*Research Center for Electron Photon Science(ELPH), Tohoku University, Sendai 982-0826, Japan*
[7]*Research Center for Nuclear Physics (RCNP), Osaka University, Ibaraki, Osaka 567-0047, Japan*
[8]*Advanced Science Research Center (ASRC), Japan Atomic Energy Agency (JAEA), Tokai, Ibaraki 319-1195, Japan*

We are currently developing a scintillating-fiber tracker for the high-momentum secondary beam at the Japan Proton Accelerator Research Complex (J-PARC). The intensity of the beam is expected to be 60 M/spill with a spill duration of 2 s. The fiber tracker is required to measure the position of each charged particle in the high-intensity beam. A prototype of the tracker consists of scintillating fibers with a diameter of 1 mm. Each fiber is connected to a multi-pixel photon counter (MPPC), Hamamatsu S13360-1350PE. We have studied the performance of the prototype using electrons and positrons converted from the high-intensity bremsstrahlung-photon beam at the Research Center for Electron Photon Science (ELPH), Tohoku University. Signals from the MPPCs are directly input to an EASIROC module, and the digitized data are acquired with a developed streaming data acquisition (DAQ) system. The time resolution obtained is better than 1.0 ns at a counting rate of 1 MHz for each fiber. The detection efficiency decreases as the intensity increases. This is caused by a gain drop owing to the over current and by a counting loss owing to a pile-up in the EASIROC chip. The dead time of the EASIROC chip is found to be 48 ns, giving 5% counting loss at 1 MHz for each fiber.

§1. Introduction

We plan to perform a high-statistic Λp scattering experiment. The purpose of this experiment is to investigate the ΛN interaction precisely, especially for the partials waves more that the $\boldsymbol{P}$ wave. Nowadays, the many-body force among Λ and nucleons is considered as a key to solve the hyperon puzzle of the neutron star [1]- [2]. However, present Λp scattering data is not enough precise to discuss the many-body ΛN force from hypernuclear data. Thus, we plan to perform the Λp scattering experiment in the Λ beam momentum range from 0.4 to 2 GeV/c.

The experiment will be performed at the planned high-momentum beamline in the hadron facility in J-PARC. We use a forward spectrometer and a streaming data acquisition (DAQ) system for charmed baryon spectroscopy at the J-PARC E50 physics program [3]. The Λp scattering can share the E50 experimental setup with the main program. The advantage of sharing the E50 experimental setup is that the Λp scattering data can be acquired in parallel with other experiments owing to the streaming DAQ system. The high-intensity secondary beam with 60 M/spill (spill duration of 2 s) is provided using a dispersion matching technique on the high momentum beamline. Since the momentum of the beam particle is different for different horizontal position, we need a tracker device for the beam which can be operated in the high-intensity environment. We are currently developing a scintillating fiber tracker as a tracker device. In this report, we show the performance of the prototype fiber tracker in response to electrons and positron converted from the high-intensity bremsstrahlung-photon beam at ELPH.

§2. Scintillation fiber tracker

The prototype fiber tracker consists of scintillating fibers with a diameter of 1 mm, and the maximum singles rate is expected to be 1 MHz for each fiber. The position resolution of 200 μm and the detection efficiency of 97 % per layer are required for the beam momentum resolution and the beam discrimination efficiency. In addition, the time resolution of 1.0 ns is necessary in order to suppress accidental coincidence.

2.1 Prototype scintillating fiber tracker

The prototype fiber tracker consists of four position detector, each of which is comprised of three layers of fiber hodoscopes oriented to the x, u, and v direction. The prototype fiber tracker has 12 layers in total. In an x-oriented layer, fibers are placed along the y-axis giving the x position from a hit fiber. In a $u(v)$-oriented, fibers are placed along the direction tilted by 30° (-30°) against the y-axis. Fig.1 shows a photo of the prototype fiber tracker, definition of the axes, placement of fibers in the three layers, and its cross-sectional view. In each layer, fibers are arranged in a staggered relation, and two adjacent fibers overlap a 0.5 mm width. The number fibers is 12, 10, and 10 for x, u, and v layers, respectively, giving the number of the readout channels is 128 in total. Each fiber is connected to a MPPC([4]) to readout the scintillation light, and the signal from MPPC is transferred to the NIM EASIROC module.

2.2 NIM EASIROC module

The EASIROC chip [5] has all essential functions to operate MPPC and readout signals from it. The number of readout channels is 32 in a chip. The EASIROC chip has a pre-amplifier, a shaper, and discriminator. The chip also has a digital analog converter (InputDAC) function for adjusting the bias voltage to operate MPPC, wihch is controlled by a field-programmable gate array (FPGA). The NIM EASIROC module is contains two EASIROC chips and a FPGA chip, and the number of readout channels

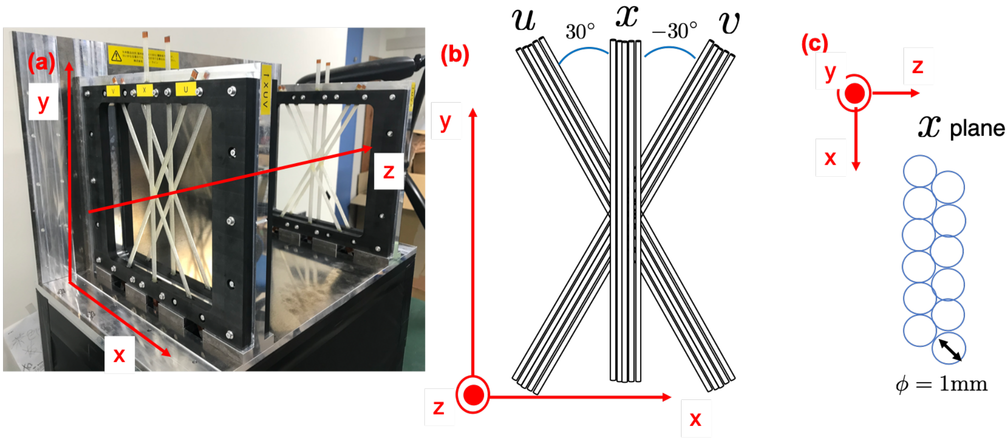

Fig.1. Prototype scintillating fiber tracker. The figure (a), (b) and (c) show a photo of the prototype fiber tracker, placement of fibers in the three layers, and its cross-sectional view.

is 64 in total. The timing signal form an EASIROC chip is transferred to a prototype streaming TDC and sent to personal computer.

§3. The prototype streaming TDC system

In this section, we describe the front-end electronics in the prototype system.

3.1 Hadron universal logic module

The data-streaming-type TDC (streaming TDC) is implemented into an FPGA chip on the hadron universal logic (HUL) module, which is a multi-purpose module developed for hadron experiments at J-PARC. The block diagram of HUL is shown in Fig. 2. The HUL module is the VME 6U size module, and is a kind of the digital module having an FPGA chip, Xilinx Kintex-7, XC7K160T-1FBG676 [6] and does not involve any analog parts such as an amplifier or ADC. The front input ports are connected to the FPGA chip through the differential signal buffers. The back J0 connector is the trigger transceiver port based on the KEK-VME standard [7]. The J1 connector is used only for the power supply. Instead, a giga-bit Ethernet PHY is mounted and the data communication is realized by silicon TCP (SiTCP) implemented in FPGA [8]. The band width of this module is limited to 1 Gbps. An important feature is the mezzanine slots allowing us to expand HUL functions. The master clock transceiver port is given by using the mezzanine card.

3.2 Master clock distributor

The master clock is used to synchronize the streaming TDC among the HUL modules. The master clock distributor (MCD) is a HUL mezzanine card providing the master clock transceiver function in order to connect the master HUL module sending the master clock and the slave HUL modules. This MCD card can treat the signals, which is compatible with the Belle-2 trigger [9]. The signals are transported via a twisted pair cable. Two signals from the master to the slave are defined as CLK and TRG. On the other hand, other two from the slave to the master are defined as ACK and RSV. The MCD card

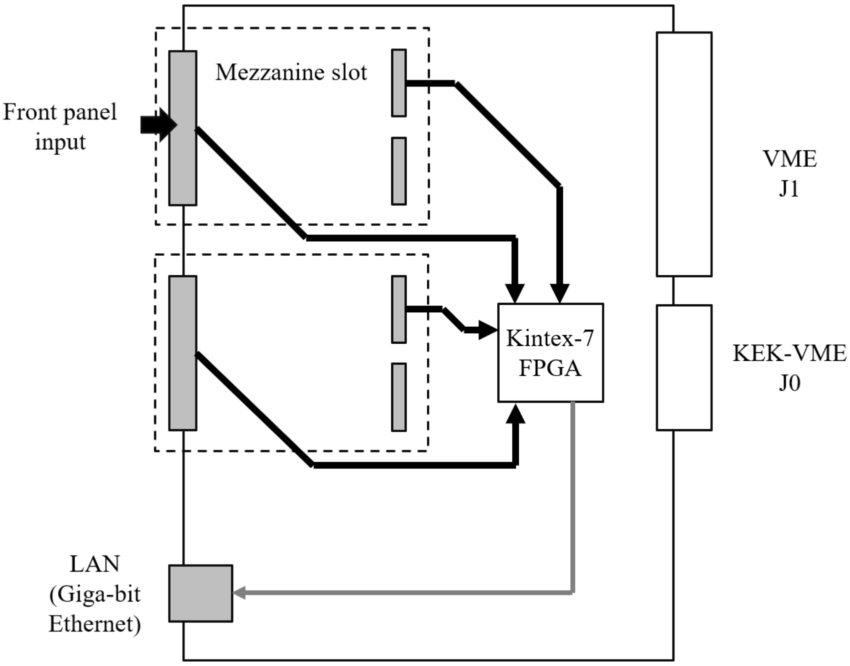

Fig.2. Block diagram of HUL. The HUL module has two input ports on the front panel and two mezzanine card slots. These four are connected to FPGA directly. A LAN port is mounted on the front panel. Giga-bit Ethernet communication can be used with SiTCP implemented in FPGA.

has five ports. One is connected to the upstream module and the other four are connected to the downstream modules. Thus, cascading connections are allowed among MCDs. The CLK pins on these ports are connected to the jitters cleaner, LMK03318.

In this experiment, six HULs were synchronized using cascaded MCD by the 50 MHz master clock. However, the TRG lines were used to distribute the clock instead of the CLK line for simplicity.

3.3 Prototype streaming TDC

The data streaming type TDC implemented into the FPGA chip plays a key role to realize a streaming DAQ system. The block diagram of the prototype streaming TDC is shown in Fig. 3. This firmware consists of two blocks. One is the online data processing (ODP) block, which digitizes the timing of input signals and proceeds some simple correction in parallel. The timings of the leading and the trailing edges of an input pulse are independently digitized with a least significant bit of 0.97 ns realized by the 260 MHz multi-phase clock signals. The digitized data fragments are sent to a paring unit. The unit provides a pair of the leading and the trailing edges from a set of data fragments, and calculates time-over-threshold (TOT) in real time. A data word is defined for the timing to include the leading-edge timing and TOT value. A time-walk of the leading edge timing coming from a different pulse height is corrected online in the next block, the time-walk corrector unit. The correlation plot between the leading edge timing and TOT for β rays from the ^{90}Sr source obtained for the prototype fiber tracker is shown in Fig. 4 (a). Signals from the β rays are observed around a TDC value of 480 and some background events are also found around 450. To save the memory for the look-up tables, this correlation is divided five

TOT regions and then constant correction values are applied in each region instead of using a smooth function as shown Fig. 4 (b). The TOT ranges are determined so that the standard deviation of the raw timings for the regions ranging from 1 to 4 are the same. The performance of this time walk corrector is discussed in Sec. 6. Finally, the data word having a small TOT value is filtered out in the end of the ODP block to reject noise signals.

The other built block is the vital block. Here, we introduce an important technique on the data streaming, that is the heartbeat method. The streaming TDC is required to measure the timing for charged particles randomly arriving on the target with a precision of 0.97 ns during a spill with a few seconds. The dynamic range becomes in the order of 10^{10} and thus a long-bit-length counter is usually necessary. Therefore, the special data, heartbeat, periodically generated by the 16-bit local counter presented as the heartbeat frame counter in Fig. 3 is introduced. By counting the number of heartbeats, one can know the time from the beginning of beam extraction. The heartbeat data is inserted in the heartbeat unit after merging the data path from parallel to serial in the merging unit. Finally, the data are transmitted by SiTCP to the server computer.

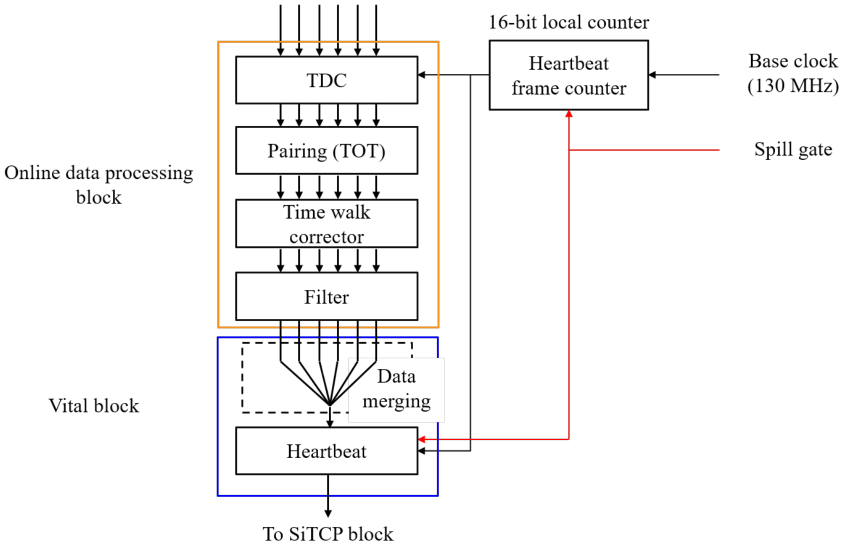

Fig.3. Block diagram of the streaming TDC implemented in the FPGA chip. The timings are measured for the leading and the trailing edges of an input pulse by the TDC unit. The two timings are coupled and TOT is calculated in the pairing unit. A time-walk of the leading-edge timing by the time walk corrector unit. The data word having a small TOT value is discarded by the TOT filter unit. The data path is merged from parallel to serial in the data merging unit. The heartbeat data, which is generated by the heartbeat frame counter, is inserted in the heartbeat unit.

§4. Test using high-rate beam at ELPH

A test was performed at Research Center for Electron Photon Science (ELPH), Tohoku University in December 2018 to evaluate the detector performance at high rates and commission the prototype streaming DAQ system.

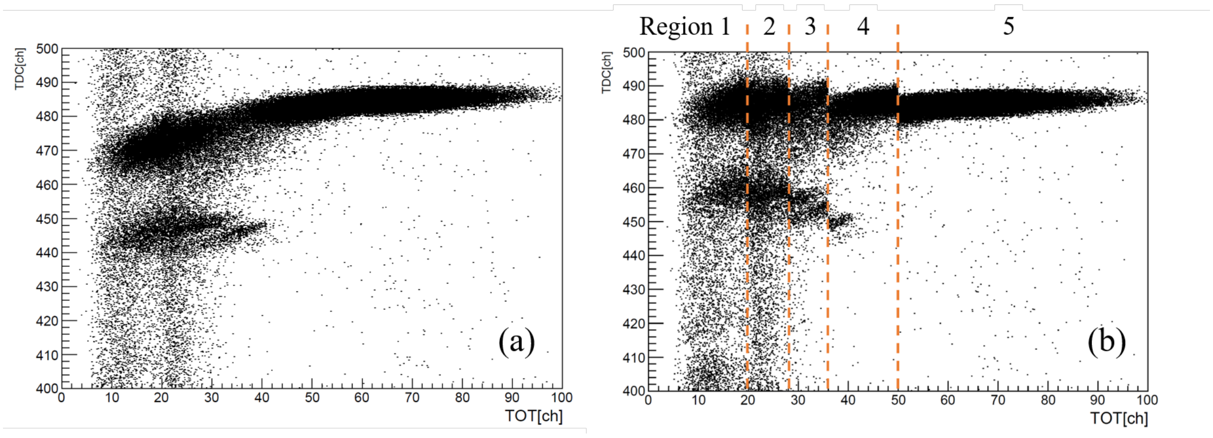

Fig.4. (a) Correlation plot between the leading-edge timing and TOT obtained using β rays from a ^{90}Sr checking source. It should be noted that the direction of the vertical axis is reversed respect to that of in Fig 7. (b) Similar plot after the time walk is corrected in the time-walk corrector unit. The vertical lines in (b) represent the TOT regions.

4.1 Setup

The experimental setup is placed near the BST ring in the second experimental hall at ELPH. The detectors were set up as shown in Fig.5. A high-intensity bremsstrahlung photon beam [10] from the booster storage (BST) ring [11] was converted into electron-positron pairs at the exit window on the flange of the vacuum duct and additional 1-mm-think aluminum-place converter. The timings are recorded from the prototype fiber tracker, the time zero counter, the drift chamber, and timing-reference counters. An analog signal for each detector is converted into the timing signal using the discriminator, the NIM EASIROC module, and amp-shaper-discriminator (ASD). After that, all signals are digitized to time information by the prototype streaming TDC and transferred to the computer.

4.2 Experimental condition of the prototype fiber tracker

The experimental conditions for the prototype fiber tracker are four types of the beam rate (1.3 kHz/fiber, 50 kHz/fiber 500 kHz/fiber, and 1400 kHz/fiber) and three types of gain (40, 30, and 25) Here, for example, the condition described by a gain of 30 denotes that a photo-electron (p.e.) corresponds to an ADC value of 30. The set threshold value corresponded to 3.5 p.e.in the EASIROC chip.

§5. Analysis

5.1 Analytical method

We employed two types of analysis methods, namely the trigger-less analysis and the trigger analysis. In the case of the trigger-less analysis, we analyze all the data of uncorrelated hits among detectors by the streaming TDC. On the other hand, we find coincidence of the reference counters first, and build an event with respect to it in the trigger-based analysis. The trigger analysis method are shown in Fig.6. This figure shows the time and hits information represented by stars of the prototype fiber tracker and reference counter. When the time information of reference counter 1, 2, 3, and 4 coincides with a time

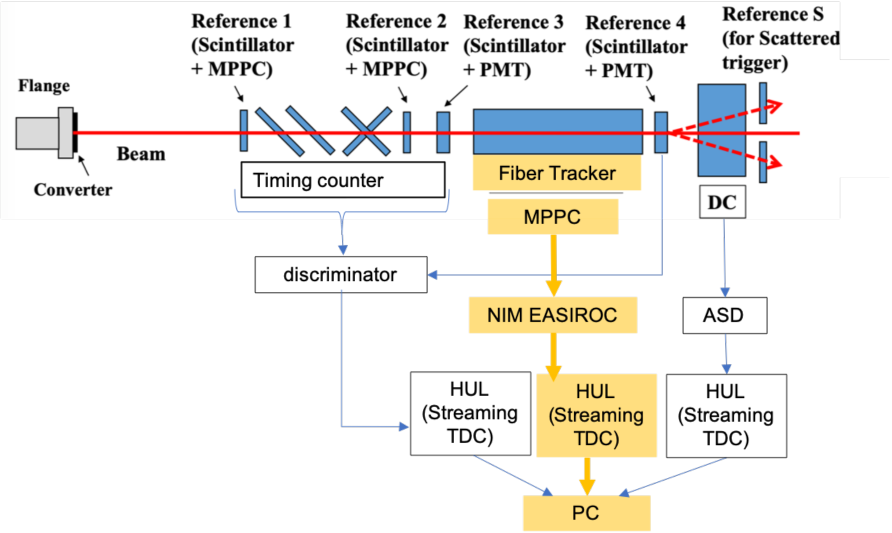

Fig.5. Experimental setup. The red line shows the electron-positron beam form the flange. Those detectors were installed in the order of the reference counter 1, the time zero counter, the reference counter 2, the reference counter 3, the fiber tracker, the reference counter 4 and the drift chamber (DC) form upstream of the beam. Arrows shows a signal flow. An analog signal form each detectors was discriminated by the discriminator, the NIM EASIROC module, and ASD. After that, those signals were digitized to time information by the prototype streaming TDC and transferred to the personal computer.

gate of about 45 ns, we recognize that an event was occurred. The prototype fiber tracker hits falling in the timing range of ±40 ns respect to the reference counter 1 were collected and packed into the event data set. In addition, the time-of-flight of the prototype fiber tracker was defined as the time dereference from the reference counter 1.

5.2 Timing resolution

We used the trigger analysis. In order to correct time walk, we determined the correction function using the data set with the low rate (1.3 kHz/fiber). The figure 7 (a) shows the correlation between TOF and TOT before correction. This plot was fitted by a cubic function as shown in Fig.7 (a) by the red line. The fitting function was phenomenologically chosen in order to reproduce the coronation plot well. The figure 7 (b) shows the correlation between TOF and TOT after correction. The fitting parameters obtained from this data set were applied to the analysis for other data sets.

The rate dependence of the timing resolution was studied. It was obtained as the standard deviation of the corrected TOF peak by fitting a gaussian function. The timing resolution for a certain layer was obtained as shown in Fig.8 as a function of the rate per fiber. The horizontal and the vertical axis represent the timing resolution in sigma and the rate per fiber. Although the timing resolution of the prototype fiber tracker deteriorates as the beam rate increases, the timing resolution of better than 1.0 ns is achieved at 1 MHz/fiber. The obtained timing resolution satisfies our requirement.

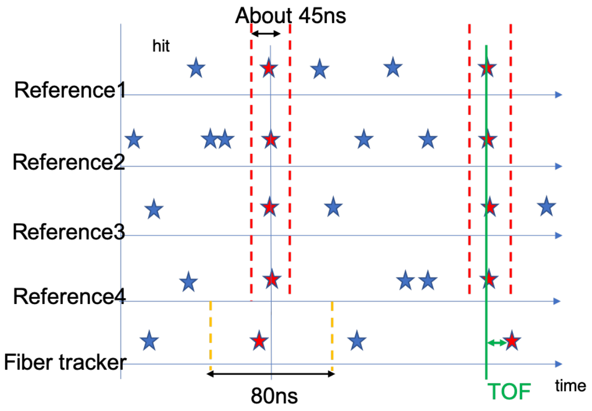

Fig.6. Trigger analysis. This figure shows the time and hit information of the prototype fiber tracker and reference counter. The red line shows a time gate of about 45 ns. The yellow line shows the timing range of ± 40 ns from the reference counter 1. The green line shows the time difference from the reference counter1.

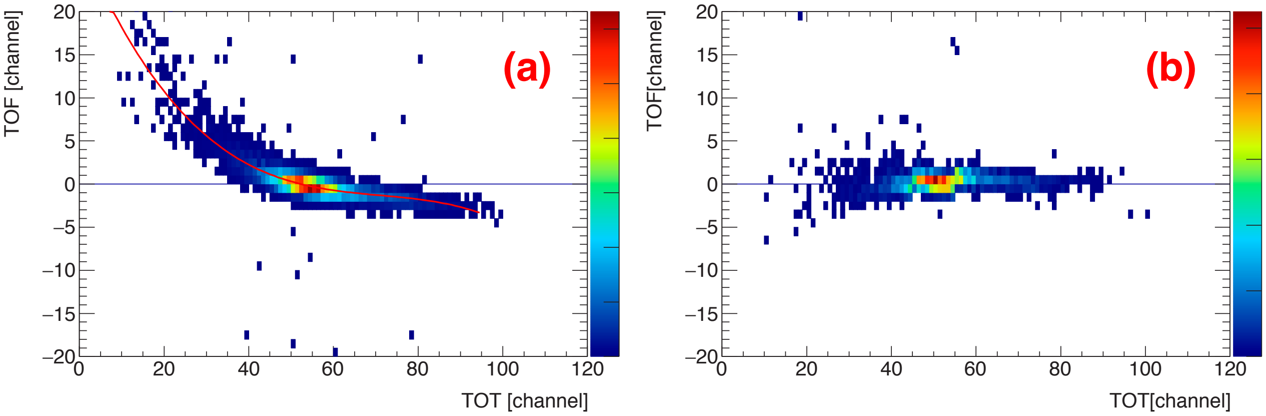

Fig.7. Time walk correction. The figure (a) shows the correlation between TOF and TOT before correction. The red line shows the fitting function. The figure (b) shows the correlation between TOF and TOT affter correction.

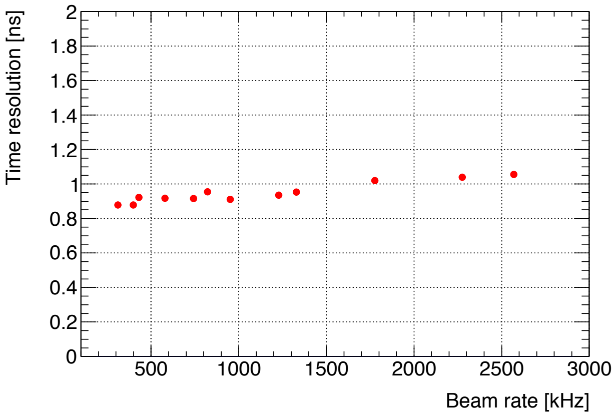

Fig.8. Rate dependence of the timing resolution. The horizontal and vertical axis show the timing resolution in sigma and the rate/fiber.

5.3 Detection efficiency

The detection efficiency at a high rate is evaluated as well as the time resolution by using the trigger analysis. The detection efficiency of each layer was defined by using the equation (1).

$$efficiency = \frac{N_{target\ layer}}{N_{other\ 11\ layers}} \tag{1}$$

Where $N_{other\ 11\ layers}$ is the number of events when all the layers except for the target layer were fired, and $N_{target\ layer}$ was the number of events when the target layer was fired. We recognize that the layer was fired when at least one hit remained after gating the TOF distribution with the 2.8 ns time window corresponding to the 3σ of the timing resolution. The obtained detection efficiency of a certain layer was shown in Fig.9. The markers with different colors represent the results from different gain conditions. The vertical axis show the beam rate per fiber. One can find that the detection efficiency was

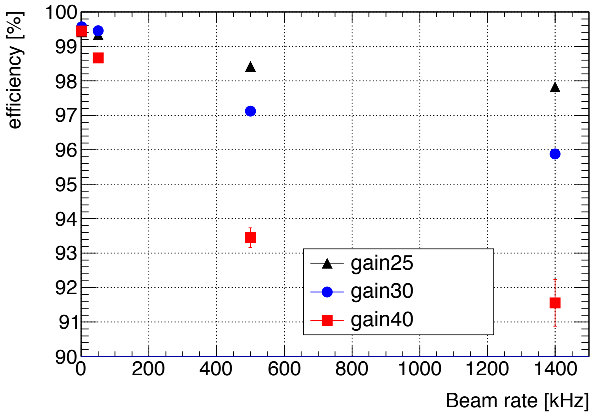

Fig.9. Detection efficiency of the certain layer. The horizontal and vertical axis show the detection efficiency and rate/fiber, respectively. Black, blue and red points show the different gain conditions.

decreased when the beam rate was increased.

We concluded that one reason for the decrease of the detection efficiency is the gain drop due to the over current in the EASIROC chip. The figure 10 shows the TOT distribution of one fiber when the beam rate was increased. The histogram with different colors represent the results from different beam rate. Actually, the TOT peak of the distribution was shifted to the left hand side when the beam rate was increases. In additiion, we concluded that another reason for the decrease of the detection efficiency is the increased counting loss due to the signal pile-up in the EASIROC chip.

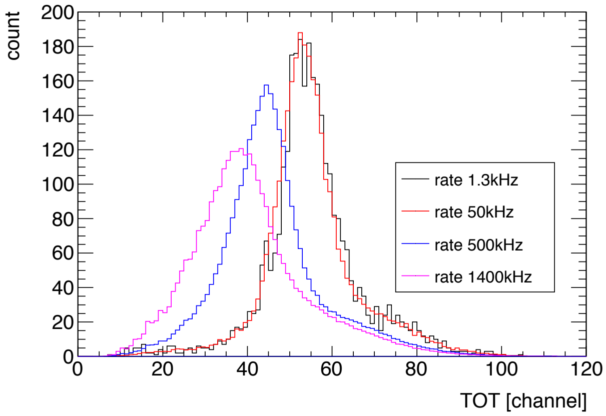

Fig.10. TOT distribution. The different colors show the distribution of different beam rate.

We studied the dead time of the EASIROC chip and the counting loss using the trigger-less analysis. The time interval (ΔT) is defined as the timing difference of leading edges of two signals. The obtained ΔT distribution was shown in Fig.11.

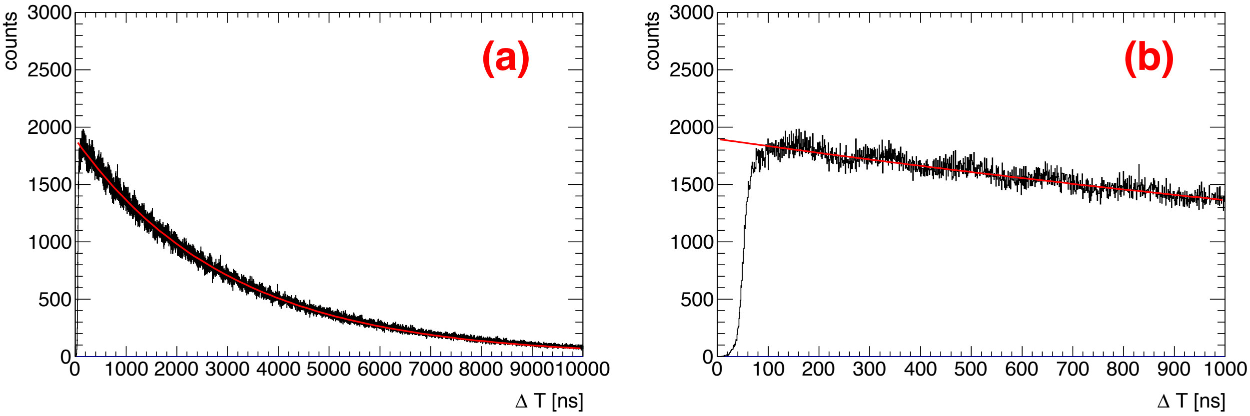

Fig.11. Distribution of ΔT. The figure (a) shows the distribution of ΔT in the range from 0 to 10000 ns. The figure (b) shows the distribution of ΔT in the range from 0 to 1000 ns. The red line shows the fitting function.

The Fig.11 (a) and (b) ware the results from different range of the horizontal axis. In the range from 0 to 100 ns in Fig.11 (b), this plot was fitted by a exponential function by the red line. The exponential function representing the paralyzable model was chosen as the fitting function. In the range from 0 to 100 ns in Fig.11 (b), one can find that the counts decreases due to the counting loss. From this result, the survival ratio is obtained, and is defined as follow.

$$\boldsymbol{Survival\ ratio} = 1 - \frac{S_{count\ loss}}{S_{ideal\ case}} \tag{2}$$

where, $S_{count\ loss}$ is the area of the counting loss. $S_{ideal\ case}$ is the area of the not counting loss which was obtained by the fitting function. In order to evaluate the beam rate dependence of the survival ratio, the beam rate was calculated as follow.

$$\boldsymbol{Beam\ rate} = \frac{\boldsymbol{Observed\ rate}}{\boldsymbol{Survival\ ratio}} \tag{3}$$

where, the observed rate is the counting rate actually observed.

The survival ratio for a certain layer was obtained as shown in Fig.12 as a function of the beam rate per fiber. The horizontal and the vertical axis represent the survival ratio and the beam rate per fiber. One can find that the survival ratio decreases as the beam rate increases. In addition, one can find that the counting loss is 5 % at the beam rate of 1 MHz/fiber. Furthermore, the correlation between the observed rate and beam rate was shown Fig.13. The horizontal and the vertical axis represent the observed rate and the beam rate. This plot was fitted by the the equation (4) which is the paralyzable model function. As the fitting result, it was found that the dead time of EASIROC is about 48ns.

$$\boldsymbol{R_o} = \boldsymbol{R_b} \cdot \exp(-\boldsymbol{R_b} \cdot \boldsymbol{\tau}) \tag{4}$$

where, $\boldsymbol{R_o}$ is the observed rate, $\boldsymbol{R_b}$ is the beam rate , and $\boldsymbol{\tau}$ is the dead time.

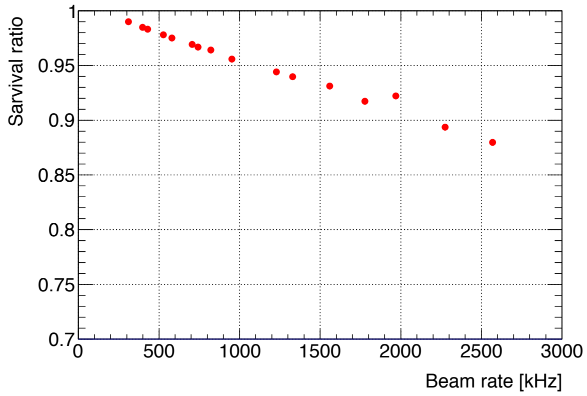

Fig.12. Survival ratio. The horizontal and vertical axis show the survival rate and the beam rate.

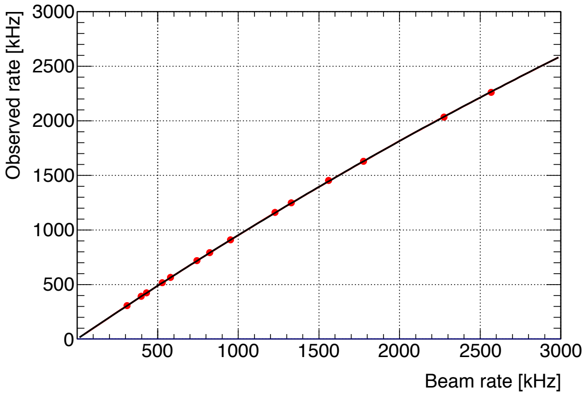

Fig.13. Correlation between the obtained observed rate and beam rate was shown. The horizontal and vertical axis show the observed rate and the beam rate. The paralyzable model function is shown by the black line.

§6. Performance of the ODP block

In this section, we describe the performances of the time walk corrector unit and the TOT filter unit in the online data processing block of the streaming TDC. The motivation to introduce the time walk corrector is to reduce CPU load. When the process searches an event using timing coincidence among detectors in the server computer, the coincidence gate width should be as narrow as possible. For this purpose, the long tail structure due time walk seen in Fig. 4 (a) is undesirable. As the time walk correction can be performed in parallel for each channel, the correction was applied in FPGA instead of CPU to reduce unnecessary CPU load. On the other hand, aim of the TOT filter is to reduce the data size by rejecting dark noise of MPPC. In this analysis, the data set for the beam rate of 1.3 kHz/fiber was used.

6.1 Time walk corrector

As we described in Sec. 3.3, the TDC values were corrected by constant values. Thus, it is difficult to obtain the same timing resolution mentioned in Sec. 5. Here, we focus on the tail structure of the TDC distribution. The TOF distributions of the prototype fiber tracker with and without the time walk corrector are shown in Fig. 14 (a) and (b), respectively. In order to evaluate the length of the tail structure, we defined the timing width from the peak position of the distribution to the horizontal position when the height becomes one thousandth. As shown in Fig. 14, the timing width when time walk was not corrected was about 9.0 ns, however, it becomes shorter to about 6.0 ns. As the result, the time walk corrector shows that it can make the timing distribution narrower, however, the small tail still exists. The number of TOT regions and those intervals of dividing should be studied more.

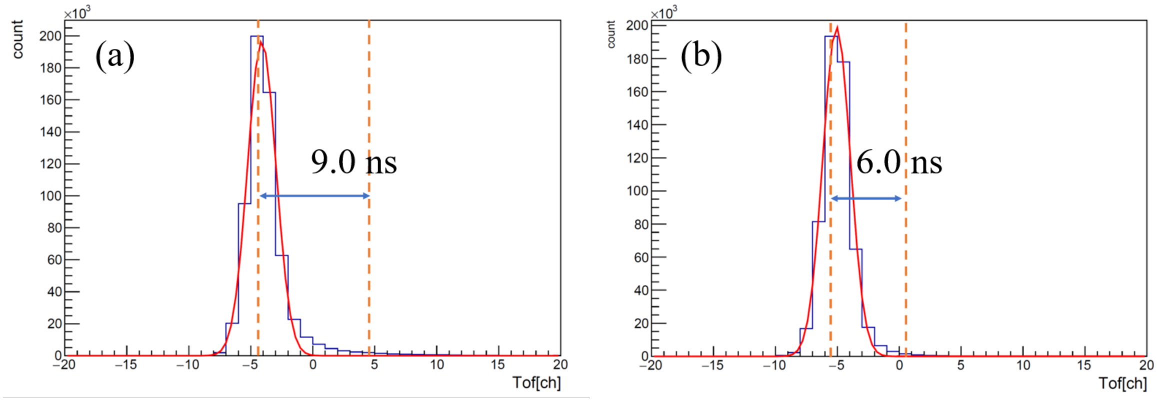

Fig.14. (a) The TOF distribution without the time walk corrector. (b) The same distribution with the time walk corrector. The vertical lines show the x position when the height of these distribution become one thousandth.

6.2 TOT filter

We report the detection efficiency and the data size when discarding data with TOT less than 30 by the TOT filter. As it is known that the dark noise contribution appear mainly below 30 ns in the TOT disribution by the previous study [12], we set the filter threshold to 30. The obtained detection efficiency is 99.82±0.6%, which is the same efficiency shown in the most left side in Fig. 9. Thus, loss due to the TOT filter was quite small. On the other hand, we found that the fraction of the data rate discarded by the TOT filter was 0.15 Mbps. It is clear that the contribution from dark noise to the data size was also quite small. As we set the discriminator threshold in EASIROC to 3.5 p.e., the obtained data reduction was reasonable because the pulse heights of dark noise were mainly single photo electron. The effectiveness of the TOT filter seems to be small, however, we used MPPC that were not damaged by radiation in this experiment. In the future, the effectiveness of the filter for the radiation damaged MPPC should be investigated.

§7. Conclusion

We are planning the high-statistic Λp scattering experiment to better understand the ΛN interaction. The layerd Λp scattering experiment will be conducted in the high-momentum beamline at J-PARC. We developed the prototype fiber tracker in the high-momentum beamline. The prototype fiber tracker consists of scintillating fibers with a diameter of 1 mm. Each fiber is connected to MPPC. The signal from MPPC is read by the NIM EASIROC module. The timing signal from the NIM EASIROC module is transferred to the prototype streaming TDC. In order to evaluate the performance at high rates, the prototype fiber tracker was tested by the ELPH facility. By using the trigger analysis, we found that the prototype fiber tracker showed the timing resolution of better than 1.0 ns at 1 MHz/fiber. The obtained timing resolution satisfies our requirement. However, the detection efficiency was decreased when the beam rate was increased. We concluded that this reason the detection efficiency deteriorated is the gain drop due to the over current and the increased counting loss due to the signal pile-up in the EASIROC chip. By using the trigger-less analysis, it was found that the dead time of EASIROC chip is 48 ns with 5 % counting loss at 1 MHz/fiber. Therefore, in order to prevent the deteriorated detection efficiency at high rate, we need new MPPC readout module with the dead time of 30 ns and the counting loss of 3 % in the future.

§8. Acknowledgements

We would like to acknowledge the outstanding efforts of ELPH. This work was supported by a Grant-in-Aid for Scientific Research(A) (Grants No.16H02188) from the Japan Society for the Promotion of Science.

References

[1] P.B. Demorest *et al.*: Natur **467** (2010) 1081.
[2] J. Antoniadis *et al.*: Science **340** (2013) 1233232.
[3] H. Noumi *et al.*: J-PARC E50 Proposal (2012).
[4] Opto-Semiconductor Handbook, Hamamatsu Photonics K.K.
[5] EASIROC developed by Omega/IN2P3/weeroc, http://omega.in2p3.fr/
[6] Xilinx, https://www.xilinx.com

[7] Y. Igarashi, M. Ikeno, M .Saito, K. Nakayoshi, M. Tanaka, T.N. Takahashi, M. Moritsu, A. Okamura, K. Hosomi, T. Takahashi, K. Itahashi, IEEE Trans. Nucl. Sci. vol. 57, Issue2, (2010), 618-624.

[8] T. Uchida, IEEE Trans. Nucl. Sci. vol. 55, (2008), 1631.

[9] M. Nakano, Timing distribution for the Belle II data aquisition system, JINST, 7 (2012) C01028.

[10] T. Ishikawa *et al.*: Nucl. Instrum. Meth. **A622** (2010) 1.

[11] F. Hinode *et al.*: Proceedings of the 7th International Particle Accelerator Conference, IPAC2016 (2016) 701.

[12] R. Honda, Doctoral thesis, http://lambda.phys.tohoku.ac.jp/d̃b/human_resource/thesis/2005_B_3_D_1.pdf

(ELPH Experiment : #2900)

Development of a beam-timing detector for the charmed-baryon spectroscopy experiment at J-PARC

T. Akaishi[1], T. Aramaki[2], H. Asano[3], C.-Y. Chang[4], W.-C. Chang[4], R. Honda[2],
Y. Igarashi[5], T. Ishikawa[6], S. Kajikawa[2], Y. Ma[3], K. Nagai[4], H. Noumi[7,5],
A. Sakaguchi[1], H. Sako[8], K. Shirotori[7], T.N. Takahashi[7],
and for the J-PARC E50 collaboration

[1]*Department of Physics, Osaka University, Toyonaka 560-0043, Japan*
[2]*Department of Physics, Tohoku University, Sendai 980-8578, Japan*
[3]*Meson Science Laboratory, RIKEN, Wako, 351-0198, Japan*
[4]*Institute of Physics, Academia Sinica, Taipei 11529, Taiwan*
[5]*Institute of Particle and Nuclear Studies (IPNS), High Energy Accelerator Research Organization (KEK), Tsukuba, 305-0801, Japan*
[6]*Research Center for Electron Photon Science (ELPH), Tohoku University, Sendai, 982-0826, Japan*
[7]*Research Center for Nuclear Physics (RCNP), Osaka University, Ibaraki, 567-0047, Japan*
[8]*Advanced Science Research Center (ASRC), Japan Atomic Energy Agency (JAEA), Ibaraki, 319-1195, Japan*

We have developed a beam-timing detector, which gives the time reference for all detectors, for the charmed-baryon spectroscopy experiment at J-PARC. It uses a high-intensity secondary beam of 6.0×10^7/spill (30 MHz for the 2-s extraction) for sufficient yield of charmed baryons. The beam-timing detector has to be operated under a high-counting rate environment. The developed detector is comprised of an X-shaped acrylic Cherenkov radiator and a photo sensor MPPC. To use in a high-counting rate environment, we have employed a narrow width (3-mm) for fine segmentation, and an amplifier for shaping signal into a narrow width (10 ns). We have tested a prototype of the beam-timing detector using positrons and electrons converted from the high-intensity bremsstrahlung-photon beam at ELPH. The typical time resolution is (54.0 ± 0.8) ps (σ) at an intensity of 2–3 MHz, which corresponds to the expected intensity at J-PARC. The developed X-shaped Cherenkov counter can be used for the experiment at J-PARC. We have found the deterioration of the time resolution of the detector at high intensities, and investigated the effects of signal overlapping to the time resolution by analyzing the waveform data.

§1. Introduction

We plan to perform charmed-baryon spectroscopy (J-PARC E50 experiment [1]) at the high-momentum beamline of the hadron experimental facility at J-PARC. In the experiment, we produce excited states of charmed baryons via the $p(\pi^-, D^{*-})Y_c^{*+}$ reaction using π^- beam of 20 GeV/c. We measure the production rates and decay branching ratios of the excited states in a wide mass region by a missing-mass method. Diquark correlation can be revealed from the properties of the excited state of observed charmed baryons. We need a detector system for measuring the arrival timing of a charged particle in the beam on the experimental target. We use a high-intensity secondary beam as high as 6.0×10^7/spill (30 MHz for the 2-s extraction) for sufficient yield of charmed baryons. The beam-timing detector has to be operated under a high-counting rate environment. The time resolution of 60–80 ps (σ) is required to identify a forward scattered particle from the target by Time-of-Flight with TOF counter in the spectrometer. The beam-timing detector is placed where the leakage flux of the magnetic field is not sufficiently small at the entrance of magnet.

§2. Prototype of the beam-timing detector

We have developed a detector comprised an acrylic (PMMA: poly-methyl methacrylate so called the acrylic resin) Cerenkov radiator with a cross section of 3×3 mm^2 and a length of 150-mm and a multi-pixel photon counter (MPPC) (S13360-3050PE). The refractive index of PMMA is 1.49, going a Cherenkov angle of 48 degrees for charged particles with $\beta = 1$. We used the directivity of the Cherenkov light. And, we employed the mean time of the timing of the both side. We devised a X-shaped radiator. It should be noted that this is cut out from an acrylic plate. We can cancel different travelling times of Cherenkov photons to a photo sensor by reading from two directions and expect to improve the time resolution by increasing the light output. This is a novel detector we developed. An I-shaped Cherenkov counter is also tested for comparison, which consists of a single acrylic bar. These Cherenkov counters are placed along 45 degrees close to the emission angle of the Cherenkov light. For a comparison, plastic

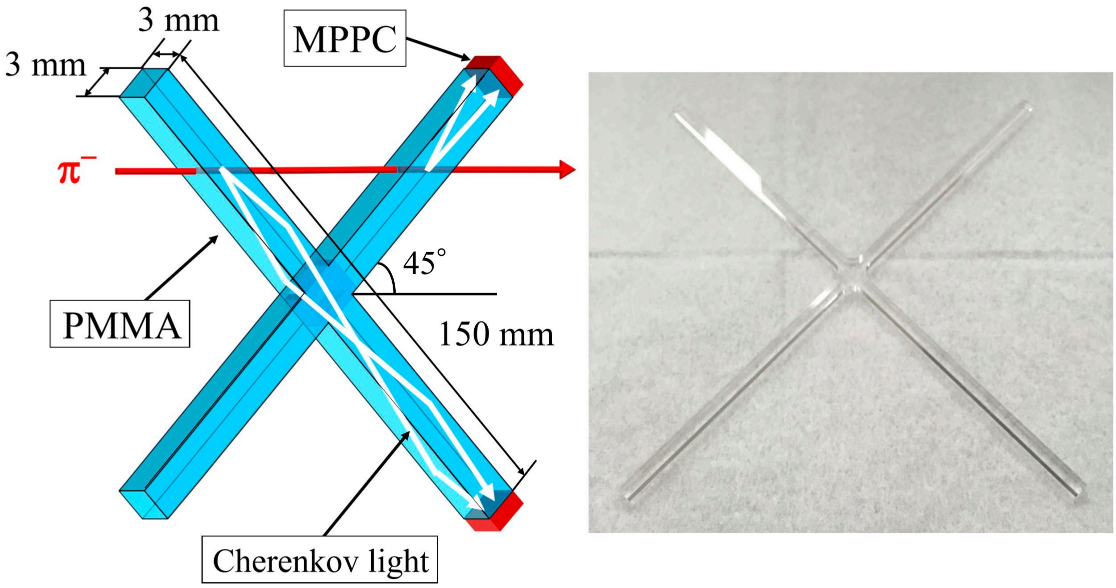

Fig.1. Schematic view (left) and photo (right) of the X-shaped Cherenkov counter. The two acrylic bars are connected each other at the center, and each of them are placed along 45 degrees close to the emission angle of the Cherenkov light from the high-energy pions.

scintillation counter having a cross section of 3×3 mm^2 and a length of 150-mm is also used with MPPC. These three kinds of the prototype detectors are tested by using a high-intensity positron and electron (mixed) beam.

§3. Test experiment

The performance study of the prototype beam-timing detectors were carried out at the second photon beamline in the second experimental hall at ELPH [2]. We used electrons and positrons as a beam converted from the extracted bremsstrahlung-photon beam. The converter was the 1-mm thickness aluminum exit window in the flange of the vacuum duct, and an additional 1-mm thickness aluminum plate. Detectors were installed at the downstream of the beam extraction points to the GeV-γ building. Figure 2 shows the experimental setup. The prototype beam-timing detectors are placed between the two timing reference detectors Ref 1(upstream) and Ref 2 (downstream). To increase the beam intensity, the beam extraction cycle was shortened from 10 s at normal operation to 4 s, and the higher intensity was obtained than 2 MHz for a 3-mm segment. We gradually increased the counting rate by adjusting the beam current of the accelerator and evaluated the performance of the prototype at beam rate up to 5 MHz. Since the intensity was not constant during the extraction period, the counting rate of a detector was measured with the HUL scaler, which could provide the number of signal counts for a 200-ms interval corresponding to the event of interest. Figure 3 shows the rate distribution for the top of the X-shaped Cherenkov counter. We got the three different intensity conditions. Since the measured rates were not constant in each condition, the events are divided into two rate groups. We evaluated performance of detectors at six counting rate regions as shown in Fig.3. We measured the timing of a signal from a prototype detector with two TDC modules, a DRS4 modules [3] and a HUL modules [4]

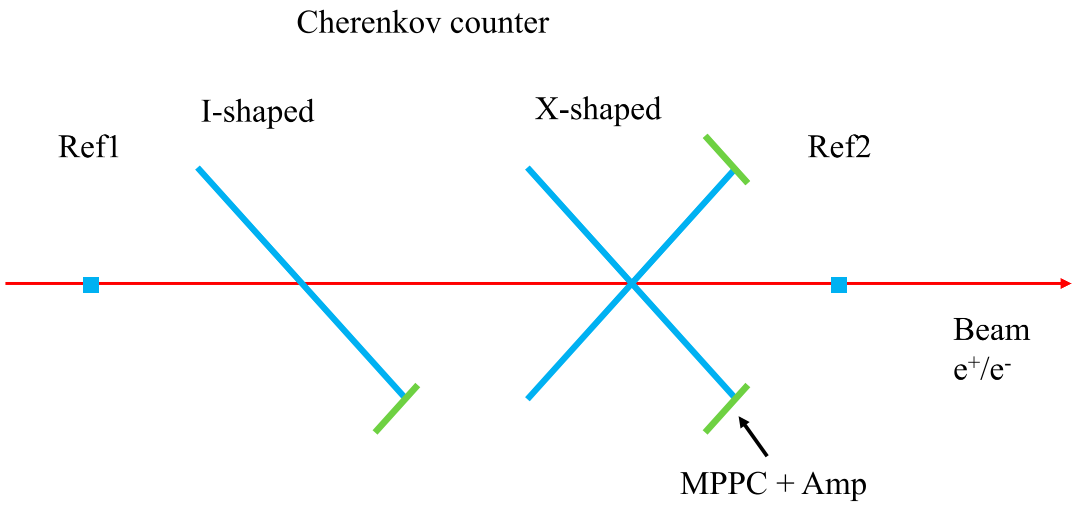

Fig.2. Schematic view of the experimental setup. The prototype beam-timing detectors are placed between the two timing reference detectors Ref 1(upstream) and Ref 2 (downstream). Each of Ref 1 and Ref 2 consists of a plastic scintillator of the size of 3 mm(W) × 3 mm(T) × 150 mm(L) with MPPC.

implemented an FPGA-based high-resolution TDC. The DRS4 module can also get waveform of a input signal. The obtained waveform was only used to determine the pulse height for the time-walk correction, and to analyze the pileup effects in the high-rate conditions. For Cherenkov counters, we used a PMT AMP module for amplifying signals by 10 because pulse heights were low.

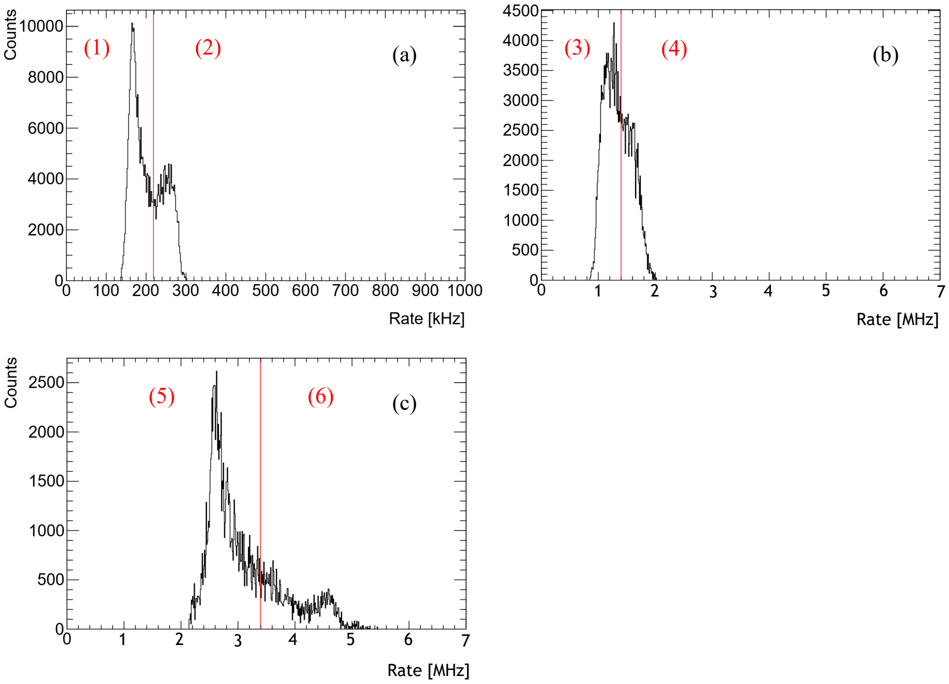

Fig.3. Counting rate distributions for the three different intensity conditions. The average rate is 0.2, 1.5, and 3.0 MHz for a 3-mm segment for (a), (b), and (c), respectively. Since the measured rates scatter in each condition, the events are divided into two rate groups. The vertical lines show the boundary to separate the two groups. Finally, we get six rate groups: (1)0.14–0.22 MHz, (2)0.22–0.30 MHz, (3)0.90–1.40 MHz, (4)1.40–2.00 MHz, (5)2.20–3.40 MHz and (6)3.40–5.00 MHz, respectively.

§4. Analysis

Figure 4 shows the pulse height distributions of the scintillation counter and the Cherenkov counters. To obtain the time resolution for the minimum ionizing particles (MIPs), the events were selected with the pulse height of the MIPs as shown in the red region in Fig.4. Three independent time difference distributions were obtained from three timing signals, t_1 coming from Ref 2, t_2, t_3 from prototype detectors. The pulse height dependence of timing was corrected by using the correlation between the time difference of two counters and the pulse height information. For the correction of the scintillation and Cherenkov counters,

$$f(V) = a + \frac{b}{\sqrt{V}} + c\ln(V) \tag{1}$$

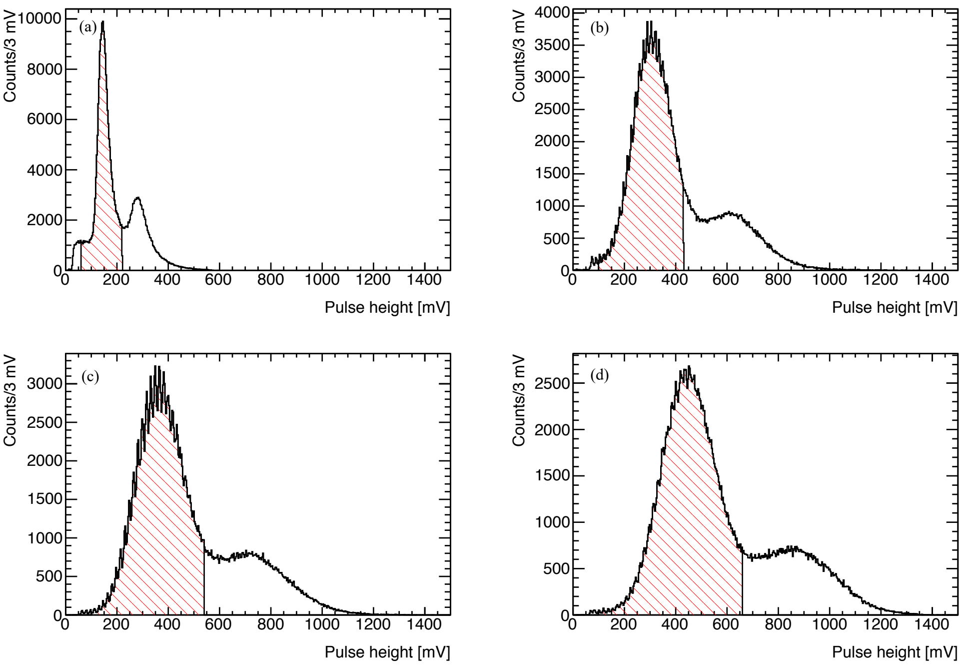

Fig.4. Pulse-height distributions for the prototype detectors: the scintillation counter (a), the I-shaped Cherenkov detector (b), the top (c) and bottom (d) sides of the X-shaped Cherenkov detector. It should be noted that signals are amplified by 10 for the Cherenkov counters.

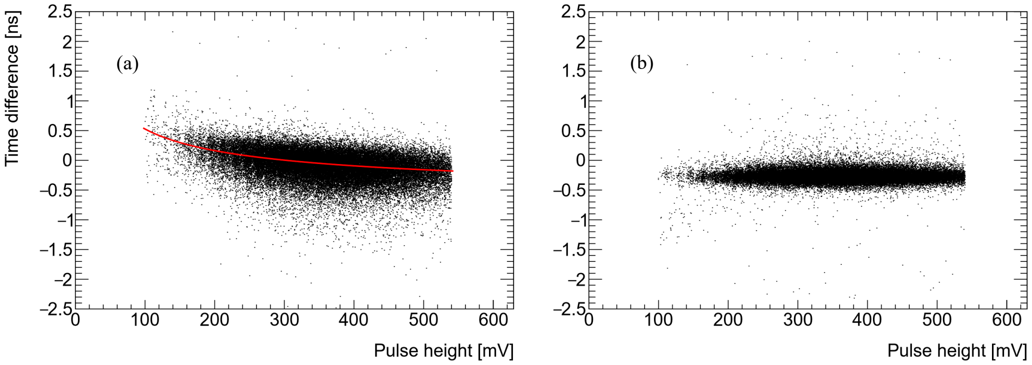

Fig.5. Correlation between the measured time difference and pulse height for the top side of the X-shaped Cherenkov counter (a). After applying the pulse-height time-walk correction (b), the constant timing is obtained independently of the pulse height.

were used, respectively, where "V" means pulse height. We used the maximum value of the timing signal peak from the waveform obtained by DRS4 module as a pulse height. The formula (1) was applied for the scintillation counter, and Eq. (1) with $c = 0$ was used for the Cherenkov counter. Figure 5 shows the correlation between the pulse height and the time difference before (a) and after (b) applying the time-walk correction in the HUL module. The time difference $t_i - t_j$ should have the resolution of $\sqrt{\sigma_i^2 + \sigma_j^2}$, where σ_i and σ_j are resolutions of measured timings t_i and t_j, respectively. Therefore, the widths of three timing difference distributions, $t_2 - t_3$, $t_3 - t_1$, and $t_1 - t_2$, gave the timing resolutions σ_1, σ_2 and σ_3. The timing t_2 of the prototype detector was given by the I-shaped Cherenkov counter.

The timing t_3 of the prototype detector was given by the X-shaped Cherenkov counter. To give timings of the plastic scintillator and the X-shaped Cherenkov counters, we employed the mean time of signals from the both edge of a counter. Since we only measured the timing for a single edge for the I-shaped Cherenkov counter, we were not able to employ the mean time. From three combinations of the time differences, the intrinsic time resolutions of each counter were obtained.

§5. Results

Figure 6 shows the time resolution as a function of the counting rate. The time resolution becomes worse for all the detectors as the counting rate increases. The time resolution of Cherenkov counters measured by both DRS4 and HUL modules are better than 80 ps (σ) at the counting rate of 2–3 MHz. The time resolutions of the X-shaped Cherenkov counter at the expected counting rate of 2–3 MHz were (66.4 ± 0.9) ps (σ) and (54.0 ± 0.8) ps (σ) by the DRS4 and HUL modules, respectively.

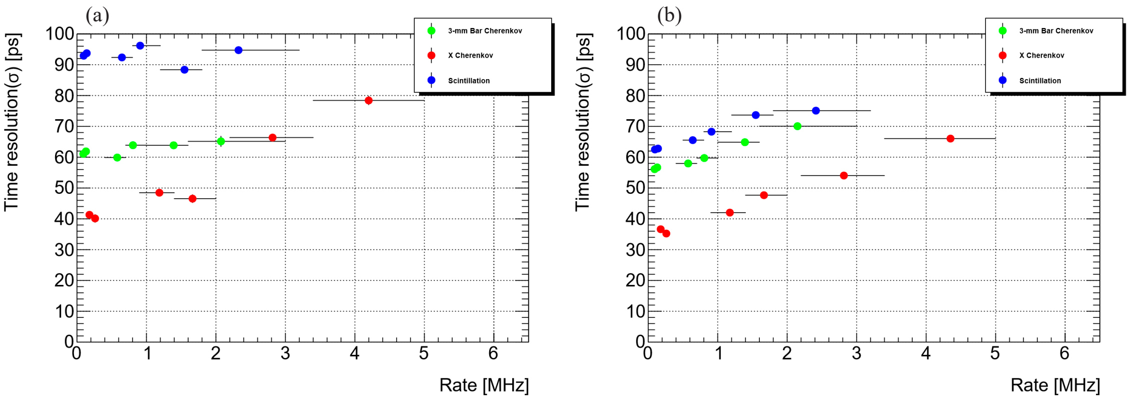

Fig.6. Time resolution as a function of the counting rate for the prototype detectors by the DRS4 module (a) and the HUL module (b), respectively. The horizontal bars represent the range of the counting rate.

We considered the cause of the deterioration of the time resolution under the high-counting rate environment. We acquired the waveform information by the DRS4 module. Figure 7 shows an example of an event that has a signal just before the trigger timing. The signal has small pulses following the main pulse. The effect of the pileup on ringing was investigated by removing the events on the ringing region before the trigger timing signal. Several time windows of the removing region were selected as 50 ns, 100 ns, 150 ns and 200 ns. Figure 8 shows that the time resolution becomes better when the time window becomes wider. As a result, we obtained the time resolution of (59.9 ± 1.8) ps and (39.6 ± 1.9) ps by the DRS4 and the HUL modules, respectively. It was found that the ringing affects the time resolution by deteriorating timings from the baseline changes. Optimization of the shaping circuit is crucial to obtain a better time resolution.

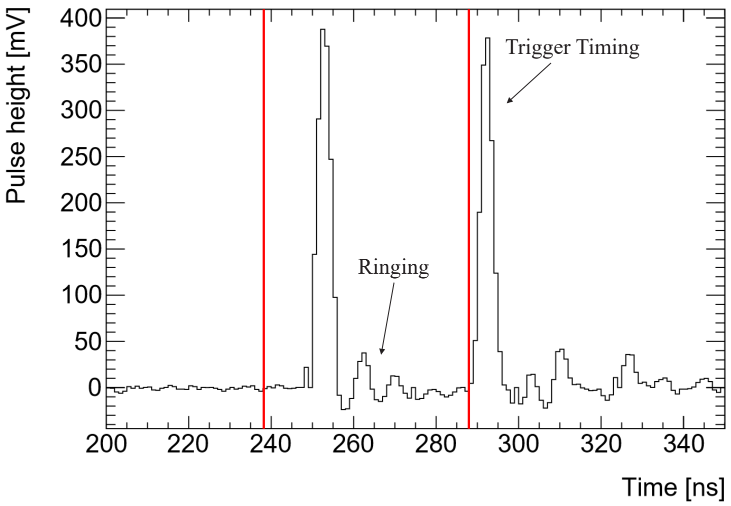

Fig.7. Example of an event that has a preceding signal before the trigger timing. The selection of such an event is made by examining the presence of a preceding signal in the range of the red line.

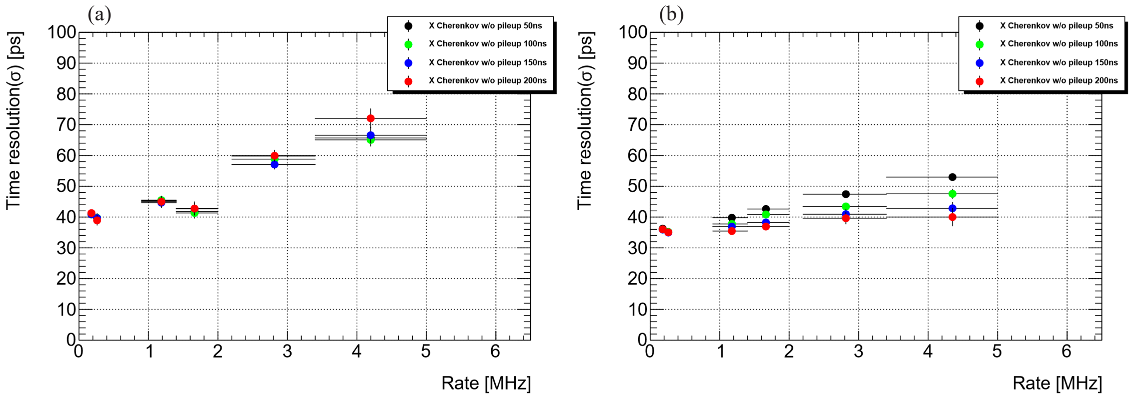

Fig.8. Rate dependence of time resolution after removing the pileup events by the DRS4 module (a) and the HUL module (b), respectively. The horizontal bars show the range of the counting rate by selecting event-by-event scaler counts.

§6. Conclusion

We tested prototype beam-timing counters by using a high-counting beams. The time resolutions of the X-shaped Cherenkov counter at the expected counting rate of 2–3 MHz were (66.4 ± 0.9) ps (σ) and (54.0 ± 0.8) ps (σ) by the DRS4 and HUL modules, respectively. Therefore, we conclude that the X-shaped Cherenkov counter which has the best time resolution provides the best as the beam-timing detector. In the development of the beam-timing detector for the J-PARC E50 experiment, the development of the detector component which fulfills the required performance was achieved by using the X-shaped Cherenkov radiator and MPPC.

For the next step, we need to design the actual detector. For designing the actual detector, we have to perform following things, (1) determination of an arrangement method of the X-shaped acrylic components, (2) time-walk correction without ADC, and (3) shaping circuit improvement for eliminating the ringing effects. (1)When the X-shaped Cherenkov counter becomes the component of beam-timing detector, it should be arranged as close together as possible in order to cover the beam region. (2)In the present study, we performed the time-walk correction using both timing and pulse height of a signal. Since a streaming DAQ system without dead time is used, a normal ADC with a dead time of several μs cannot be used in the charmed-baryon spectroscopy experiment. In addition, if a flash ADC is used, the amount of data becomes enormous and data transfer becomes difficult. For these reason, we have to use a fast signal digitalization without ADC so that we consider to use the Time-over-Threshold method in which the signal width from both leading and trailing timings measured by TDC is used instead of ADC. Since the shaping circuit is designed to shape signals to be narrow by using a simple differentiation circuit, the width of the signal saturated and lost linearity with pulse height information when the pulse height becomes high. It is not sufficient to correct the pulse height from the signals width. We should improve the shaping circuit having the correlation between signal with and pulse height. (3)In order to eliminate the effect of a ringing pileup in high-counting rate environments, we have to reduce the ringing of the shaping circuit. The ringing suppressed by finely adjusting circuit elements such as the time constant, multiplication factor, and the damping resistance of the shaping circuit. We will solve these problems and plan to produce a beam-timing detector in the future.

Acknowledgments

Thanks to three test experiments in #2858, #2870 and #2900, we have succeeded in developing the beam-timing detector. We would like to acknowledge the outstanding efforts of the staff at ELPH. This work was supported in part by a Grant-in-Aid for Scientific Research(A) (Grants No.16H02188) from the Japan Society for the Promotion of Science.

References

[1] H. Noumi *et al.*: J-PARC E50 Proposal (2012).

[2] T. Ishikawa *et al.*: Nucl. Instrum. Meth. A 622 (2010) 1.

[3] T.N. Tomonori *et al.*: RCNP Annual Report 2016 ”Development of a FPGA-based high resolution TDC using Xilinx Spartan-6”

[4] R. Honda *et al.*: http://openit.kek.jp/project/HUL

(ELPH Experiment : #2905)

Test of Detectors and Trigger System for J-PARC E16 Experiment using Positron Beam

M. Naruki[1], S. Ashikaga[1], R. Fujii[1], M. Ichikawa[1], K.N. Suzuki[1], K. Aoki[2],
K. Ozawa[2,3], T.N. Murakami[3], T.N. Takahashi[4], and S. Yokkaichi[4]

[1]*Department of Physics, Kyoto University, Kyoto, 606-8502*
[2]*IPNS, High Energy Accelerator Research Organization (KEK), 1-1 Oho, Tsukuba, Ibaraki 305-0801*
[3]*Department of Physics, University of Tokyo, 7-3-1 Hongo, Bunkyo-ku, Tokyo 113*
[4]*Nishina Center for Accelerator-Based Science, RIKEN, 2-1 Hirosawa, Wako, Saitama 351-0198*
[5]*Research Center for Nuclear Physics (RCNP), Osaka University, 10-1, Mihogaoka Ibaraki, Suita-shi, Osaka 567-0047*

Performances of detectors together with integrated trigger system for the J-PARC E16 experiment have been evaluated using the positron beam at ELPH. A read-out system of the Hadron Blind Detector (HBD) was newly developed for the experiment. The HBD signal for trigger decision is read-out directly from the GEM, Gas Electron Multiplier of HBD. To optimize the trigger tile segmentation of HBD, we have studied trigger efficiencies with the developed system for a variety of input charge. Also the integrated trigger system and the effect of shower leakage of lead-glass calorimeter were studied.

§1. Introduction

The J-PARC E16 experiment aims at studying hadron mass in nuclear matter [1]. The mass of vector meson is a key probe which is able to be directly related to the QCD condensate through the QCD sum rule [2]. Di-lepton is an excellent probe to measure spectral information of vector meson, since it is almost free from the final state interaction. We plan to measure di-electron spectra produced in 30 GeV p + A reactions at J-PARC high-momentum beamline. It is highly important for the measurement to develop PID detectors having capabilities of coping with high interaction rate of 10 MHz. Also the trigger performance is quite important to suppress huge hadronic background mainly originates from pions. In the test experiment at ELPH performed in Autumn 2018, we studied the trigger system of Hadron Blind Detector (HBD), the integrated trigger system and an effect of shower development in several segments of lead-glass calorimeter.

§2. Experimental Setup

Figure 1 shows an experimental setup. As tracking devices, three sizes of GEM tracker will be used in the coming experiment at J-PARC. The largest GEM tracker, named as GTR3, has an active area of 30×30 cm^2 and used to generate a trigger signal. A plate of GTR3 was located at a most upstream side, as in the J-PARC experiment.

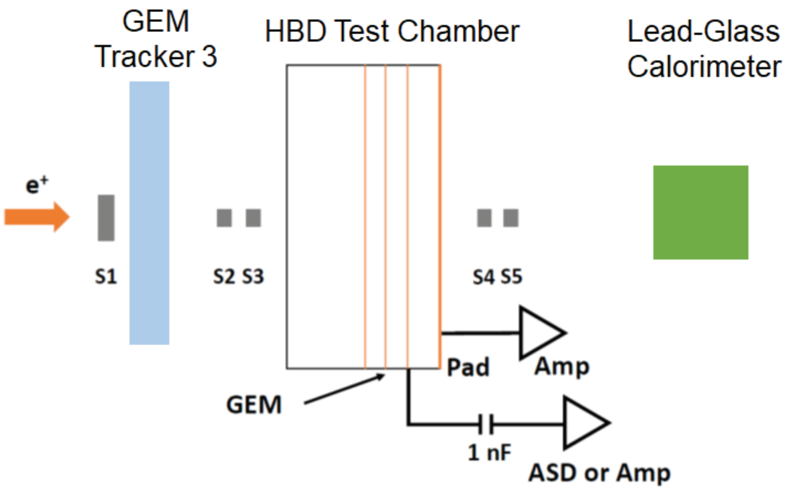

Fig.1. Experimental Setup

In the middle of the setup, the test chamber for the HBD read-out system is located. The HBD is an electron identification detector originally developed by PHENIX collaboration. It is a Cherenkov type detector with three layers of GEM for gas amplification. Whereas the detector signal is read out on a pad plane, the signal for trigger is independently read out from the third GEM to join in the trigger decision making. The new ASD read-out board has been developed for the E16 experiment to make a hit signal for trigger decision. Since an efficiency of making the signal depends on the detector capacitance, the performance has been tested using positrons for several possible capacitances.

In the most downstream side, blocks of lead-glass calorimeter (LG) was placed. It is used for electron identification in a combination of the HBD. The basic performance of LG was studied in the past test experiments performed at ELPH. The development of electric-magnetic shower in two segments of calorimeter was studied this time.

§3. Results

Figure 2 shows the performance of new read-out system of HBD with the detector capacitance of 1.8 nF. The signal level was 134 mV compared with the noise level of 20 mV in one-standard deviation. The required performance of the ASD board is obtained as the efficiency of 99.9% for the input charge of 20 fC. We also evaluated the efficiency with the capacitance of 5.4 nF. In that case, the read-out system can not fulfill the required performance due to the relatively low S/N of 3. The noise level stayed always at 20 mV, however the signal was reduced to 80 mV due to the small capacitance. It is concluded that the trigger tile segmentation of HBD is able to be optimized if the read-out of a GEM foil is divided into 27 tiles, which corresponds to the one-tile capacitance of 2 nF.

Two blocks of lead-glass calorimeter are exposed to the 0.4 GeV/c positron beam to examine the shower development in adjacent segments of calorimeter. Especially the performance has been evaluated on condition that the beam hits the boundary of two blocks. They are arranged as they are in the J-PARC experiment as shown in the top right corner of Fig. 3. The clear anti-correlation has been observed to

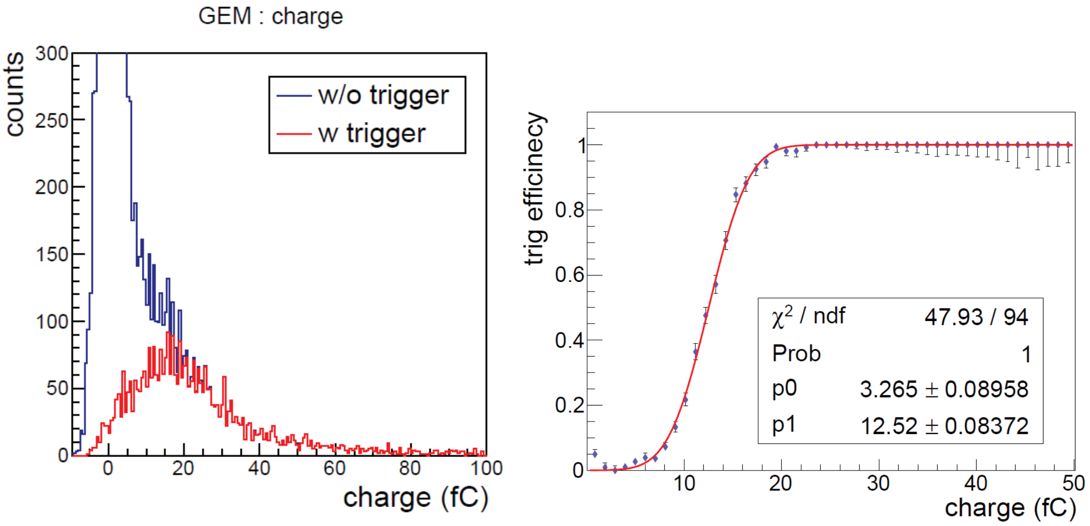

Fig.2. (left) Charge distribution read out from third GEM of HBD. The blue histogram is the calibrated analog output of ASD read-out board, red histogram shows the charge distribution when the digital output of ASD fires. (right) Input charge dependence of trigger efficiency. Both plots are taken from [3].

demonstrate that all energy deposit of a single electron/positron can be measured with clustering of lead-glass segments.

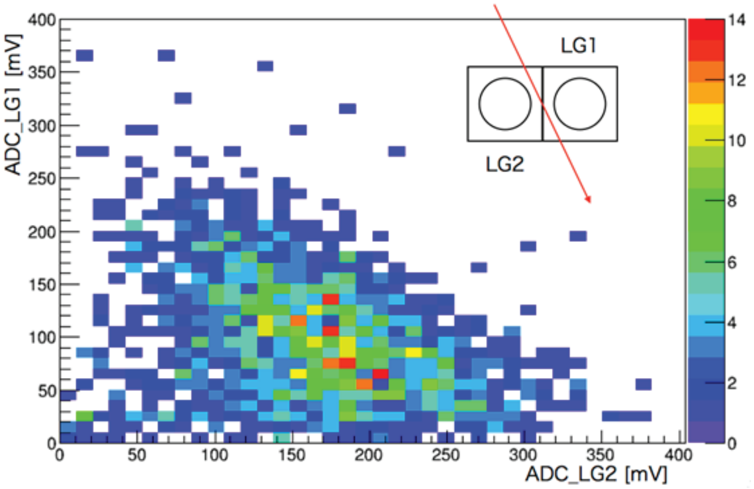

Fig.3. Correlation between two segments of lead-glass calorimeter

The integrated test of the trigger system for the J-PARC E16 experiment was carried out. In the experiment, three types of detectors, GEM tracking detectors (GTR), HBD and LG are used for generating triggers. The trigger system consist of four types modules. Trigger merging modules (TRG-MRG) receive discriminated output signals from detectors and detect the leading edges. The timing information of the edges are transmitted to the trigger decision module (Belle2 UT3) with Aurora protocol. The trigger signal generated with UT3 is distributed to frontend modules using B2TT protocol, through the trigger distribution modules (Belle2 FTSW and RPV260). The performance of the trigger system with all types detectors was evaluated with the positron beam for the first time. In the test experiment, we used three detectors of GEM for GTR, GEM for HBD, and LG as a module of detectors. The DRS4 module was used as a frontend module for LG. As the trigger system, four modules, TRG-MRG, Belle2 UT3, Belle2 FTSW and RPV260 were used. The trigger decision making was performed with the coincidence of three detectors and distributed to the DRS4 ADC/TDC. The timing histogram between a hit information of LG and the trigger signal received with RPV260 is indicated in Fig. 4. The enough performance of the time walk of the trigger system is obtained to be 8 ns in the positron beam experiment.

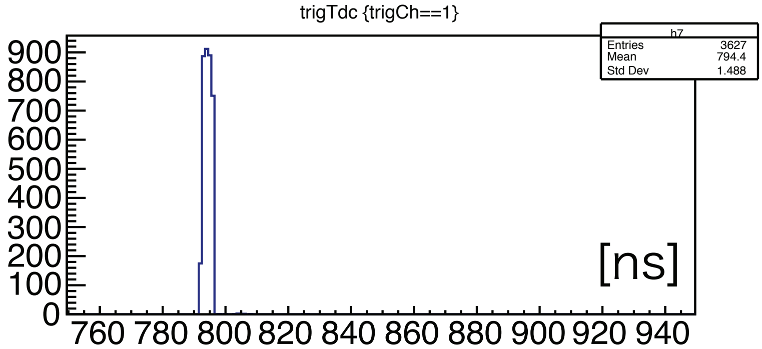

Fig.4. Trigger decision time

Acknowledgment

The authors would like to thank the J-PARC E16 collaboration for their direct and/or indirect assistance. We also would like to express our gratitude to staff members of ELPH for their support. We thank to the KEK electronics system group for their help in developing of the ASD for HBD. This project was supported by the RIKEN SPDR program, Grant-in-Aid for JSPS Fellows 18J20494, and MEXT/JSPS KAKENHI Grant numbers 19654036, 19340075, 21105004, 20360670, 15H05449, 15K17669 and 18H05235.

References

[1] S. Yokkaichi *et al.* : proposal, http://j-parc.jp/researcher/Hadron/en/pac_1707/pdf/E16_2017-10.pdf

[2] P. Gubler and W. Weise: Phys. Lett. **B751** (2015) 396-401.

[3] K.N. Suzuki, Master Thesis, Kyoto Univ. 2019

(ELPH Experiment : #2911)

Performance Evaluation of a Fine-Grained Scintillator Tracker for the T2K Near Detector Upgrade Project

Konosuke Iwamoto[1], Ryo Fujita[1], Kohei Matsushita[1], Masashi Yokoyama[1],
Tsunayuki Matsubara[2], Soichito Kuribayashi[3], Tatsuya Kikawa[3],
Takuji Arihara[4], and Yuito Awataguchi[4]

[1]*Department of Physics, University of Tokyo, Tokyo, 113-0033*
[2]*Institute of Particle and Nuclear Studies, High Energy Accelerator Research Organization (KEK), Tsukuba, 305-0801*
[3]*Department of Physics, Kyoto University, Kyoto, 606-8502*
[4]*Department of Physics, Tokyo Metropolitan University, Tokyo, 192-0397*

The T2K Near Detector ND280 Upgrade project is proposed to reduce the systematic uncertainties of neutrino oscillation measurement from neutrino cross section that can be constrained by the near detector measurement. One of the new detectors introduced in this project is called Super-Fine-Grained Detector (SuperFGD), which consists of $1 \times 1 \times 1\mathrm{cm}^3$ plastic scintillator cubes stacked to form a volume of $192 \times 56 \times 184\ \mathrm{cm}^3$ in width, height, and length, respectively. The scintillator cube production method has recently switched from extrusion method to injection molding method for mass production, and the detector assembly utilizing the ultrasonic welding technique is under consideration. Beam test is performed at ELPH positron beamline to evaluate the cube position dependence of the measurement, cube-cube crosstalk rate, and the effect on the detector performance due to the ultrasonic welding on the cube.

§1. Introduction

T2K [1] is planning to extend its physics run until 2027 to achieve the statistics of 20×10^{21} protons on target with upgraded J-PARC beam intensity. While this statistics allows the T2K neutrino oscillation analysis to reach $> 3\sigma$ sensitivity to charge parity violation in lepton sector, improvement in the total systematic uncertainties from $\sim 6\%$ to the level of 4% enables to achieve the $> 3\sigma$ sensitivity with less statistics therefore earlier than the expected run period. In order to accomplish such goal, ND280 Upgrade proposes to implement new upstream trackers to improve the wide angle acceptance and low momentum threshold [2].

One of the novel technologies introduced in ND280 Upgrade is SuperFGD [3]. It consists of $1 \times 1 \times 1 \times\ \mathrm{cm}^3$ plastic scintillator cubes produced at UNIPLAST Co. (Vladimir, Russia) with reflector surface obtained by chemical etching [4]. The full-size SuperFGD detector is comprised of $192 \times 56 \times 184$ scintillator cubes, as shown in Figure 1, with the active mass of ~ 2 tons. The 1 mm ϕ Wavelength Shifting (WLS) fibers are inserted along 1.5 mm ϕ holes in each side of the cubes to readout the scintillation light from three views by Multi-Pixel Photo-Counters (MPPCs). The first prototype cubes are produced by extrusion method, and SuperFGD mass production method with injection molding process is established by INR RAS, Russia.

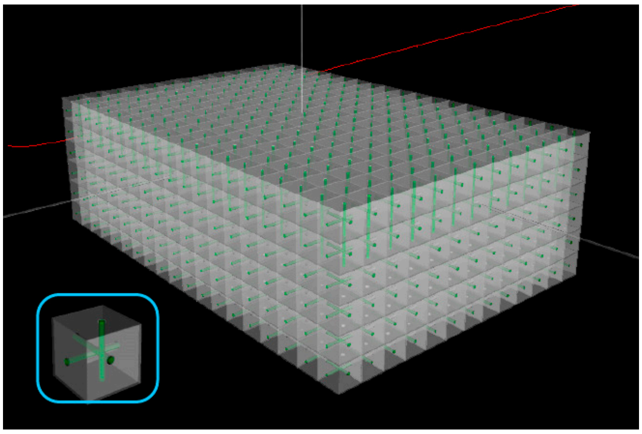

Fig.1. Schematic concept of the SuperFGD structure. The full-size detector consists of 192, 56, and 184 cubes in width, height, and length, respectively. The single cube size is designed to be $1 \times 1 \times 1$ cm^3. The green cylinders indicate the wavelength shifting fibers.

One of the major concerns of the full-size SuperFGD assembly is a method to control gaps between the cubes to pass through the WLS fibers. During the manufacturing process, we expect fluctuations in cube size and hole positions, and considering the fiber insertion through the longest sides with 192 cubes, we expect the maximum hole position tolerance of ± 250 μm per cube. In order to obtain the alignments between the cubes, two assembly procedures are under research and development. One of the methods is named ”fishing-line” method, which utilizes 1.3 mm ϕ flexible, plastic fishing-lines to align the cube hole positions in three dimensions. After the 3D assembly of the cubes with fishing-lines, each thread will be replaced by the WLS fibers to form the full-size detector. An another approach of the full-size assembly is called the ultrasonic welding method. Instead of controlling the gaps by aligning the hole positions, this method aligns cube positions to allow fiber insertion without cube displacements by attaching the cubes on the polystyrene sheets by ultrasonic welding machine. The welding positions and gaps between the cubes on the polystyrene sheets are carefully controlled by the equipments.

There are several validations need to be performed to progress with the cube assembly development. First, the comparison of the performance between different cube production methods, extrusion and injection molding, needs to be done to ensure that the change in the cube manufacturing method is acceptable for the mass production. Also, the effect on the light yield measurement due to the ultrasonic welding assembly needs to be evaluated. Since the ultrasonic welding method melts the surface of the cubes to attach to the polystyrene sheets, possible loss of the light yield due to the leakage from the welded surface is concerned.

§2. Performance Evaluation with a Positron Beam

The beam test is performed at the research center for ELectron PHoton science (ELPH), Tohoku University, to evaluate the performance of the SuperFGD cubes. Namely, the test focused on the measurement of the position dependence in single scintillator cube, validation of the ultrasonic welding method with the optical crosstalk and light yield, and response comparison between the extruded and injected cubes. The 500 MeV/c positron beam is used throughout the measurement performed at the GeV-γ irradiation room. The schematic of the beam test setup is shown in Figure 2.

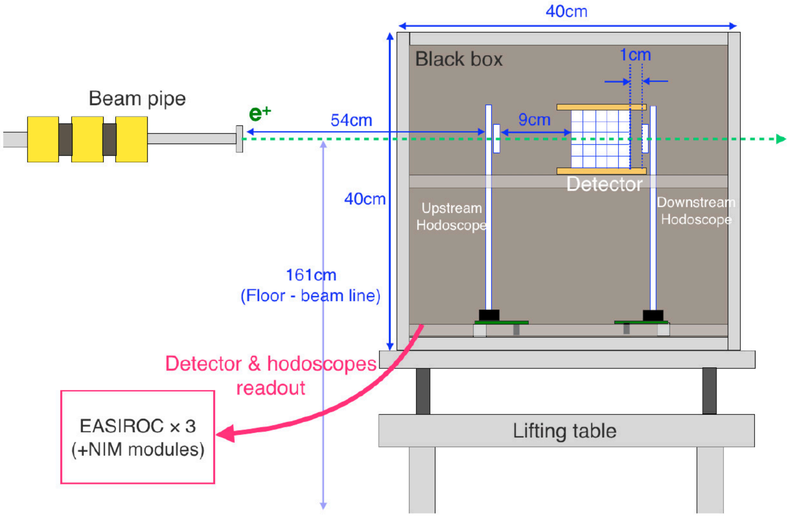

Fig.2. Setup of the ELPH beam test for SuperFGD measurement.

The setup utilizes upstream and downstream hodoscopes to track the incident positron direction and its hit position within the detector located in between them. Each hodoscope consists of pairs of sixteen, aligned 1.5×1.5 mm^2 cross-section polystyrene scintillating fibers stacked perpendicular to each other. The total overlapped hodoscope area is 26×26 mm^2 with 64 channels, and the position of the track is determined by the area which two perpendicular scintillating fibers overlap to form a ”cell.” Event selection is performed by choosing events with hits in the given upstream and corresponding downstream cells with greater than 2.5 photo-electron (p.e.) counts in both scintillating fibers, which is defined as ”good” events. Among the good events, if the cubes are present in the corresponding cells, Landau fit is performed on the light yield distributions obtained by each channel of the hodoscopes to use the most probable values as the observed light yield in that channel. The diagram of the event selection with two hodoscopes is shown in Figure 3.

There are three major detector setups used to perform the desired measurements on the cube performance, as shown in Figures 4-7. The single-cube setup focuses on the measurement of the position dependence of the scintillator response and the performance comparison between the extruded and injected cubes. The light yield measurement with polystyrene sheets welded to the extruded cubes are performed to evaluate the effect on the light yield. Two different thicknesses of 100 μm and 200 μm sheets are used in this study, and separate measurements are performed in cases where the sheet is

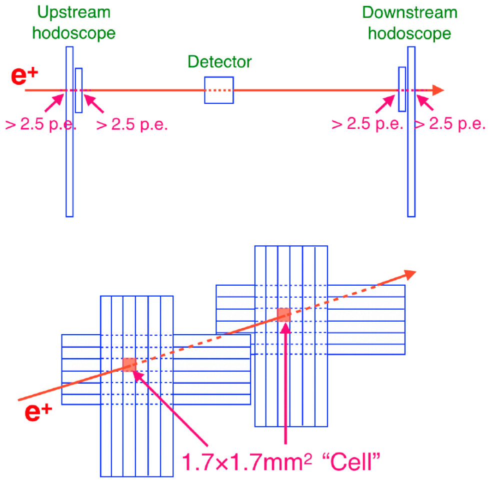

Fig.3. The hodoscope configuration. Events are defined as "good" events when there are hits in the given upstream and corresponding downstream cells with greater than 2.5 p.e. in both scintillating fibers.

parallel or perpendicular to the beam direction. In each measurement the cube is placed in the center of the beamline. The two-cube setup uses the extruded cubes to measure the optical crosstalk rate. One of the cubes is located in the center of the beamline to measure the optical crosstalk to the other cube; the cubes with welded sheets are tested in this setup as well. The nine-cube setup has a 3×3 arrangement of the cubes with the center cube located in the beamline. The optical crosstalk rate to the adjacent cubes are measured and compared between extruded and injected cubes. In each setup, the measurements are performed to obtain at least 300 good events for each cell to obtain sufficient statistics with less than 5% uncertainty. The detailed explanation of the setup is available in [5].

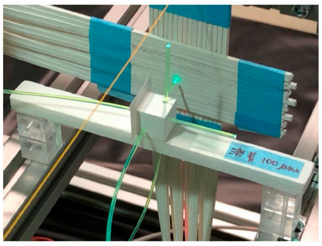

Fig.4. The single-cube setup with the welded sheet parallel to the beamline.

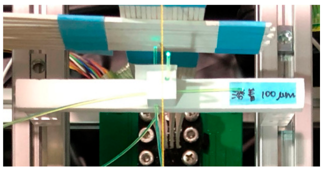

Fig.5. The single-cube setup with the welded sheet perpendicular to the beamline.

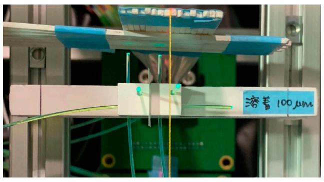

Fig.6. The two-cube setup with welded sheets.

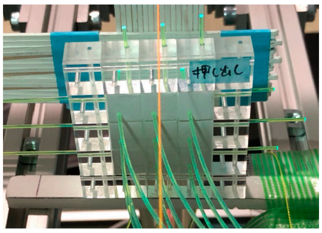

Fig.7. The nine-cube setup.

Figure 8 shows the position dependence of the observed light yield in the single cube obtained from X, Y, and Z readout fibers, which the channels pass through the side, top to bottom, and along the beamline, respectively. The observed light yield in the X, Y, and Z readouts is 28.7 p.e., 25.4 p.e., and 29.6 p.e., respectively. The measured light yield difference is not observed between the extruded and injected cubes. Based on the event selection via cell readouts, we observe that there is a tendency that less light yield is observed at cells which are far from the corresponding fiber readouts. It is suggested that the non-uniformity of the light yield is due to the dependence of the acceptance of the scintillation light and the fiber position. The cross-check with the SuperFGD optical simulation is ongoing to understand this phenomenon.

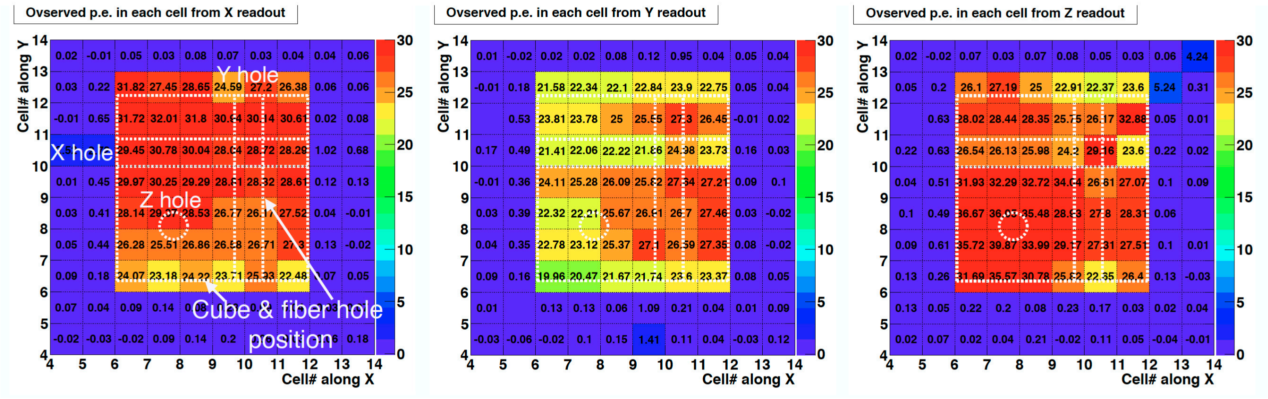

Fig.8. Average light yield of SuperFGD cube obtained in each cell. The left, middle, and right distributions show the cube light yield measurements obtained from X, Y, and Z fiber readouts, respectively. The white, dotted lines show the fiber hole and cub positions.

The light yield measurement with welded polystyrene sheets is summarized in Table 1. The total light yield measured from X, Y, and Z fiber readouts is shown with different welding configurations. As shown in the table, the configuration with welded sheet obtained 5-10% greater light yield measurement than the cube without the welding. This result suggests that the effect of increased reflection with the welded sheet is more significant than the welding iself causing the possible light leakage from the reflector region. The degradation of the cube performance is not observed in this measurement.

Configurations	Total light yield (X+Y+Z) [p.e.]
No welding	81.8
With 100 μm sheet (horizontal)	86.7
With 200 μm sheet (horizontal)	86.9
With 100 μm sheet (vertical)	89.5
With 200 μm sheet (vertical)	86.2

Table 1. Observed total light yield from X, Y, and Z readout fibers with different configuration for the welded sheet, one-cube samples.

The crosstalk probability is measured using the two-cube setup with and without the ultrasonic welding. The events are selected when there are hits in one of the cubes which is in the beamline; the light yield ratio between the adjacent cube and the cube in the beamline is measured. The average values of the light yield ratios are obtained separately for Y and Z readouts, and the crosstalk rates are summarized in Table 2. The crosstalk rates are compared with the measurement obtained without the welded sheets, and the decrease in the crosstalk probability by approximately 30% is observed for the sample with welded sheets.

Configurations	Y readout fiber crosstalk rate [%]	Z readout fiber crosstalk rate[%]
No welding	2.9	3.0
With 100 μm sheet	2.2	2.1
With 200 μm sheet	2.5	2.0

Table 2. Crosstalk rate obtained from two-cube measurement with three different configurations of welded sheets.

The crosstalk probability comparison between the injected and welded cubes are performed with the nine-cube setup. Similar to the two-cube measurement, the light yield ratios between one of the adjacent cubes and the center cube are calculated for X, Y, and Z readout fibers. The cross talk probability measurements for nine-cube setup with extruded and injected cubes are summarized in Table 3 and 4, respectively. The average crosstalk rate for the Z readout fibers are 4.3% are and 3.6% for the extruded and injected cubes, respectively. As the result, approximately 20% crosstalk rate reduction is observed from the extruded to injected cubes. The position dependence of the light yield in nine-cube setup in each readout direction is under investigation.

3.1	1.9	4.4	2.1
(X Center)	4.5	(Z Center)	4.0
4.4	3.3	4.3	3.4
Crosstalk rate [%]	3.8	(Y Center)	3.4

Table 3. Crosstalk rate obtained from nie-cube measurement with extruded cubes.

2.6	1.4	3.6	1.6
(X Center)	3.5	(Z Center)	3.5
4.3	3.7	3.8	1.3
Crosstalk rate [%]	2.9	(Y Center)	2.8

Table 4. Crosstalk rate obtained from nie-cube measurement with injected cubes.

§3. Summary

T2K is preparing for the extended physics runs to achieve $> 3\sigma$ sensitivity to CP violation. ND280 Upgrade plans to implement new upstream trackers to obtain wide angle acceptance and low momentum measurement by near detectors to reduce systematic uncertainties in the oscillation analysis, and SuperFGD is one of the major components of the improvement. In order to ensure the feasibility of the new cube manufactering process and assembly method, positron beam test is performed at ELPH GeV-γ irradiation area. The measurements suggest no degradation of the cube quality by the injection molding production method in terms of light yield or crosstalk probability, and the measurements with the welded sheets show that the light yield reduction or increase in the crosstalk probability are not observed with the assembly method. Further analyses of the beam test measurement to implement the cube response in the detector simulation is in progress.

Acknowledgment

The authors express many thanks to the ELPH accelerator staff for the opportunity to perform the positron beam test, especially Manabu Miyabe for the great support and coordination. The authors are deeply grateful to Yury Kudenko from INR for the donation of the scintillator cubes and Davide Sgalaberna from CERN for the preparation of the WLS fiber optical interfaces which enabled this measurement and analyses. This work was published as the master's thesis of Ryo Fujita from the University of Tokyo. This work was supported by Grant-in-Aid for Specially Promoted Research (16H06288).

References

[1] K. Abe, *et. al.*, *The T2K Experiment*, Nucl. Instrum. Meth. A 659 106.

[2] A. Blondel, *et. al.*, *The T2K-ND280 upgrade proposal*, CERN-SPSC-2018-001. SPSC-P-357.

[3] A. Blondel, *et. al.*, *A fully-active fine-grained detector with three readout views*, 2018_JINST_13_P02006.

[4] Y. Kudenko *et. al.*, *Extruded plastic counters with WLS fiber readout*, Nucl. Instrum. Meth., A 469 (2001) 340. https://doi.org/10.1016/S0168-9002(01)00780-X.

[5] R. Fujita, *Research and development of a new fine-grained scintillator tracker for the upgrade of T2K near detector*, Department of Physics, University of Tokyo Masters Thesis.

(ELPH Experiment : #2913)

Evaluation of number of photon from small aerogel Cherenkov counter

Kazuki Okuyama[1] and Masashi Kaneta[1] for the NKS2 collaboration

[1]*Department of Physics, Tohoku University, Sendai, 980-8578*

We are developing an aerogel counter as an electron/positron veto counter in the NKS2 experiment. The e^-/e^+ are produced by the photon conversion and it is necessary to reject them in trigger level for the higher beam rate experiment in NKS2. We chose the aerogel of index 1.01 and tested whether we can detect enough Cherenkov photons as the veto counter.

§1. Introduction

We are planing the Λn interaction measurement via final-state-interaction in $\gamma + d$ reaction. We would like to higher beam rate than current NKS2 experiment. The electron/positron veto counter is necessary to carry the experiment out with keeping the high DAQ efficiency.

We adopted silica aerogel (index $n = 1.01$) to separate electron/positron and pion and veto the e^-/e^+ in trigger level. The veto counter was expected to locate between two drift chambers in the magnetic field. The size of aerogel was estimated as $30^{\mathrm{D}} \times 60^{\mathrm{W}} \times 40^{\mathrm{H}}$ [mm^3].

We would like to use SiPM (MPPC) as the photon sensor in the magnetic filed to measure the cherenkov photon. Before using the MPPC, we measured number of Cherenkov photon from the aerogel using 2-inch Photo-Multiplier Tube (PMT).

§2. Pre-test using cosmic-ray

We started the test using comsic-ray to check whether we can see the Cherenkov photons. Figure 1 shows the setup. We used the aerogel provided from Japan Fine Ceramic Center (JFCC).

Trigger of the data taking was made with the coincidence of three counters. To identify the muon which has enough speed ($\beta > 1/1.01$) to make the Cherenkov photon in the aerogel, we stacked Pb blocks as 50-cm height. Aerogel was covered with a Teflon sheet as a reflective material and black paper as a light shielding material.

We used CAEN V792 QDC module and V775 TDC module for pulse charge and timing measurement, respectively. The DAQ program we used was UNIDAQ system [1].

The pedestal calibration for QDC module was done by random clock trigger. The one photo-electron peak was found the data with self trigger of PMT that was connected to the aerogel. The peak position for the one photo-electron was used to compute the number of photo-electron distribution later.

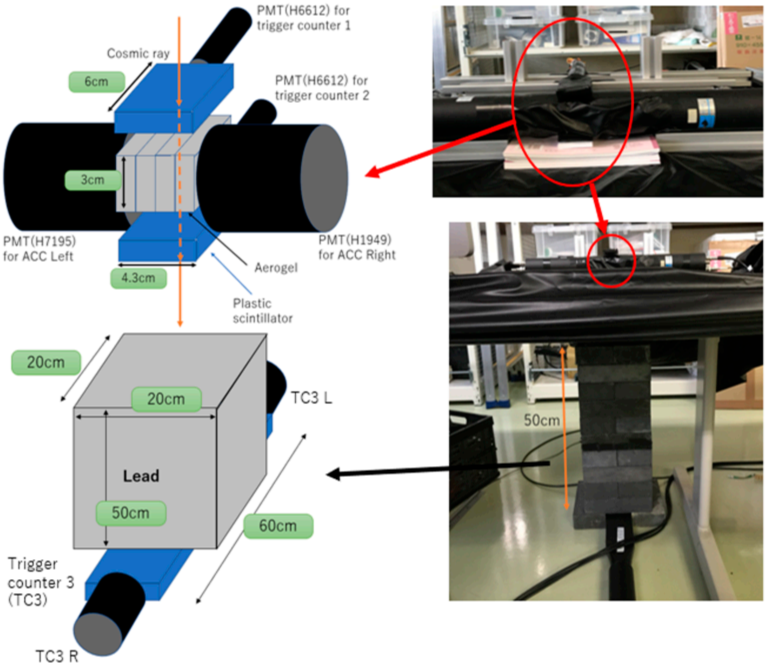

Fig.1. Setup of cosmic-ray test.

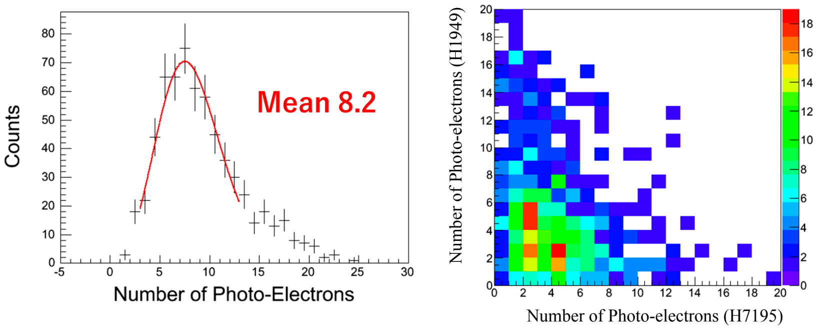

Fig.2. Distribution of the number photo-electrons with summing photo-electrons measured both side of PMTs is shown in the left-hand side. The right hand-side figure shows the correlation of number of photo-electrons left- and right-hand side PMT.

The length of plastic scintillator part of the third trigger counter (located after Pb blocks) was about 60 cm. We select hits on center part from time difference of both side of PMTs. In order to guarantee that it has passed through the middle, he center region was selected from the time-difference distribution of the left and right PMTs.

Figure 2 shows the number of photon distributions from the cosmic-ray test. we took about 1 week for the data taking.

The left-hand side plot is the sum of both side of number of photo-electron peak. The curve in the plot is the result of fitting of Poisson distribution with convolution of a resolution. The fitting result of number of photo-electron was 8.2 and it was consistent with the estimation value 8.3 that was considered geometrical acceptance and the quantum efficiency of PMTs.

We can see the anti-correlation of number of photo-electrons in the two PMT signals (right-hand plot in Fig. 2. In the plot, we can also see the relationship that when more light reaches one PMT, the other decreases. This setup uses different PMTs for the left and right PMTs, but the plot also shows that Cherenkov light can be observed correctly.

§3. Beam test at the 2nd experimental hall

The results used in cosmic ray measurements were data collected for about a week. With beam test, statistics can be accumulated in less time. The purpose here was to verify that the JFCC aerogel used for cosmic ray measurements could obtain equivalent results using the beam. It was also to measure and compare aerogels with the same refractive index of 1.01 made at Chiba University and JFCC.

The test was done at the downstream of NKS2 spectrometer in the 2nd experimental hall at ELPH. Figure 3 shows the alignment of trigger counters and aerogel counters. The trigger counters were the same with cosmic-ray test. The first trigger counter was an active target to make the electron/positron conversion from photon beam.

The data taking was done as a part of the other experiment (ELPH Experiment: #2878). The trigger for data taking was made by that setup and our trigger counter hit information was used in offline analysis.

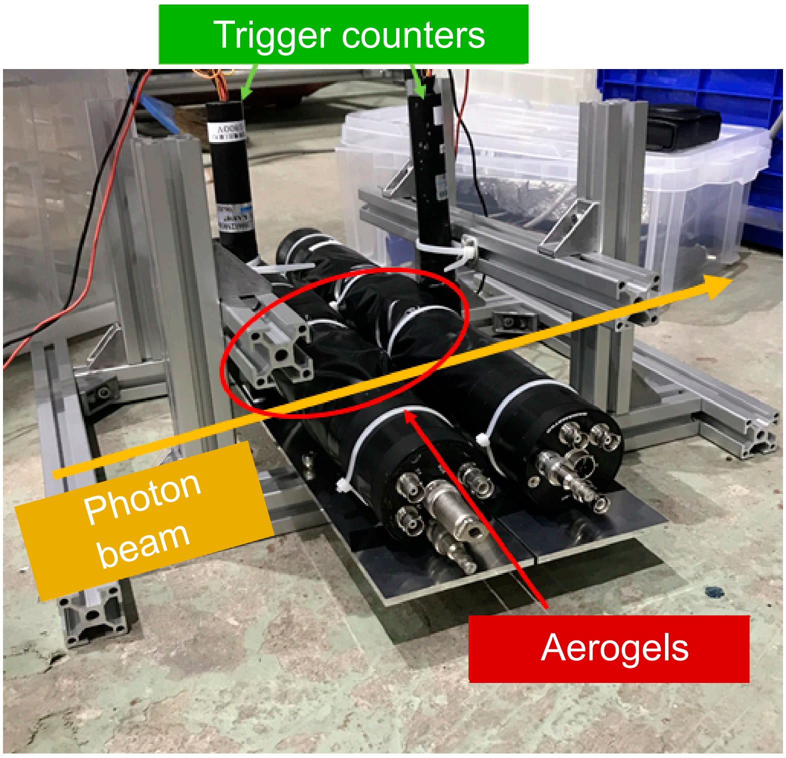

Fig.3. Alignment of counters for the beam test. From upstream of photon beam, we set the trigger counter 1, two aerogel counters, and trigger counter 2.

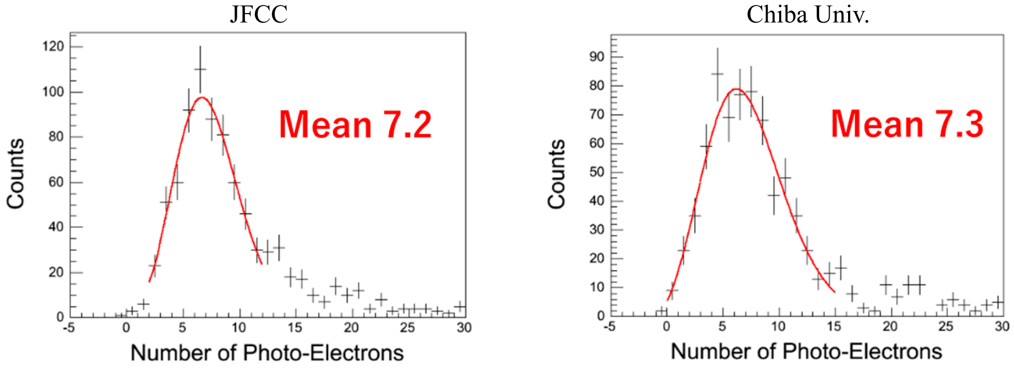

Fig.4. Distribution of the number photo-electrons (NPE) with summing photo-electrons measured both side of PMTs. The left- and right-hand side plot are the distibution of NPE from aerogel provided from JFCC and Chiba University, respectively.

The data we recorded had included not only one charged particle events. We chose candidates of the one charged particle event by selecting in a region on scatter plot of pulse height from both trigger counters. The number of photo-electron distributions are shown in Fig. 4. The pedestal and one photo-electron peak calibrations were done by the same method with cosmic-ray test.

The curve in the plots are the results of fitting by Poisson distribution convoluted the resolution. We saw the similar NPE value from the both aerogels.

Note that the detail description of analysis is shown in Ref. [2].

§4. Summary

We tested the $n = 1.01$ aerogel whether we could measure enough Cherenkov photons for the electron/positron veto counter. The cosmic-ray and the beam test showed about 7 to 8 photo-electrons by using 2-inch PMTs. We are planning to use SiPM (MPPC), which is a semiconductor photo-detector, and MPPC has a higher photo-detection efficiency (PDE) than PMT. Considering the efficiecy, it is expected that about 20 photons will be detected. We conclude that the aerogel of index 1.01 can be used as the electron veto counter.

Acknowledgment

We thanks the accelerator staff of ELPH to provide the stable operation of accelerator.

References

[1] http://www-online.kek.jp/ online/Unidaq/default.htm

[2] Kazuki Okuyama, 2019, Bachelor thesis “Development of a compact airgel Cherenkov counter with MPPC” (written in Japanese).

New Drift Chamber for an electron spectrometer at SCRIT electron scattering facility

K. Tsukada[1], S. Takayama[1], and H. Wauke[1]

[1]*Research Center for Electron Photon Science, Tohoku University, Sendai, 982-0826*

A new drift chamber was installed on the electron spectrometer at the SCRIT electron scattering facility in November 2018, which enables us to reconstruct trajectories of scattered electrons precisely, and study both horizontal and vertical angular dependence of performances of the spectrometer. The spacial resolutions and plane efficienies were studied by electron scattering data with the carbon target. Vertical position resolution of typically 150 μm, and efficiency of almost 98 % were achieved. Further analysis is still ongoing.

§1. Introduction

The SCRIT (Self-Confining Radioactive Isotope Target) [1] electron scattering facility have been constructed at RIKEN to realize electron scattering off unstable nuclei as reported in previous reports [2–4]. Commissioning studies of spectrometers (WiSES : Window-frame Spectrometer for Electron Scattering, LMon : Luminosity Monitor) and target ion generation and transportation systems (ERIS : electron-beam driven RI separator for SCRIT [7], FRAC : fringing-RF-field-activated ion beam compressor [8]) with several stable targets were already performed [5, 6]. In order to realize the experiment with unstable nuclear target, improvements of target preparation systems to achieve much higher luminosity have been conducted. The performance of WiSES will be also updated by introducing a new drift chamber and measuring the three-dimentional magnetic field map because it was found that the momentum resolutions of WiSES were worse than design values at the commissioning experiments. In this report, the design and some result of the performance study of the new drift chamber is reported.

§2. WiSES and new drift chamber

The WiSES consists of a dipole magnet, two drift chambers, trigger scintillation counters and a helium filled bag install between two drift chambers. Drift chambers are set in front of the magnet (FDC) and at the rear of the magnet (RDC) to reconstruct trajectories of scattered electons. Although RDC has vertical and tilted wire to reconstruct electron's trajectories three-dimentionally, original FDC had only vertical wires and is sensitive to only horizontal information of trajectories. Details are reported elsewhere [3]. Figure 1 shows momentum resolutions which are defined as width of the elastic peaks for some electron beam energies. The experimental results are obviously not explained by a simulation which is a Monte Carlo simulation with Geant4 toolkit and includes all materials and realistic detector performances of WiSES. To achieve a good signal to noise ratio, and evaluate an acceptance of the spectrometer accurately, a reason of the discrepancies should be identified. A new drift chamber (FDC2) which has both vertical and horizontal wires to reconstruct the three-dimentional information of electron's trajectory was made and installed in order to study the reason and improve the spectrometer performances.

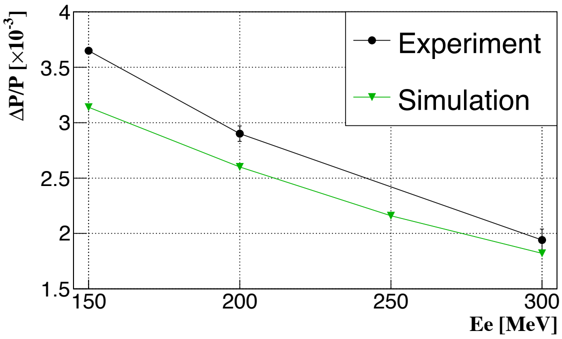

Fig.1. Reconstructed momentum resolutions evaluated from elastic electron scattering data with a carbon target. The width of the peaks were fitted by a gaussain distribution.

Figure 2 is a picture of the FDC2 installed on WiSES. Geometrical parameters of FDC2 are listed in Table 1.

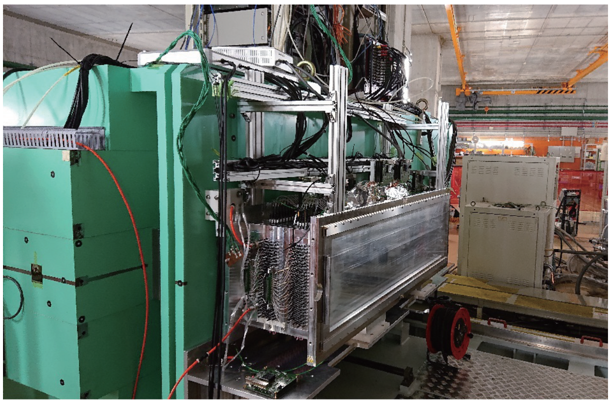

Fig.2. FDC2 installed on WiSES. The spectrometer are moved away from the target for a maintenance.

§3. Performance study

Figure 3 shows normalized counting rate taken by changing the high voltage supplied on field wires and the threshold on the RAINER card. The electron source is a ^{90}Sr put on the side of FDC2. It is found that the plateau region appear around 2200 to 2300 V.

In December 2018, the electron scattering experiment with carbon targets were performed to study the spectrometer performances. Figure 4 shows a drift time spectrum for hits belonging to a reconstructed track. Because the gas is a mixture of helium (80%) and isobutane (20%), the drift velocity

Table 1. Geometrical and operation parameters of new drift chamber (FDC2)

	FDC2
Layer configuration	X-X’ Y-Y’ X-X’ Y-Y’
Cell type	Hexagonal
Cell size (side length)	10 mm
Sense wire	Au-W, 30 μmϕ
Field/Shield wire	Au-Al, 80 μmϕ
Number of channels	64 ch/layer for each X and X’
	13 ch/layer for each Y and Y’
Detector size	1370(w)$\times$430(h)$\times$352(l) mm
Effective area	1117(w)$\times$234(h) mm
Window	aluminized mylar, 25 μm
Operation gas	He+C_2H_6 (80:20)
High voltage	2320 V (X), 2230 V (Y)
Readout	32CH RAINER

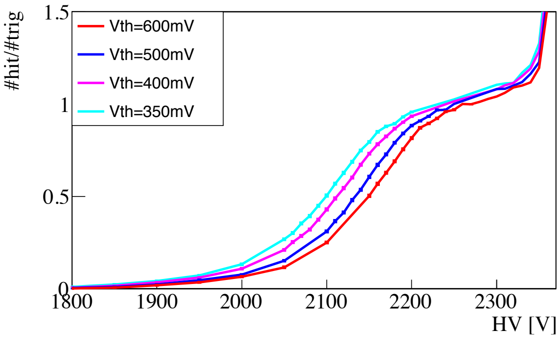

Fig.3. High volutage dependences of counting rate taken by changing the threshold.

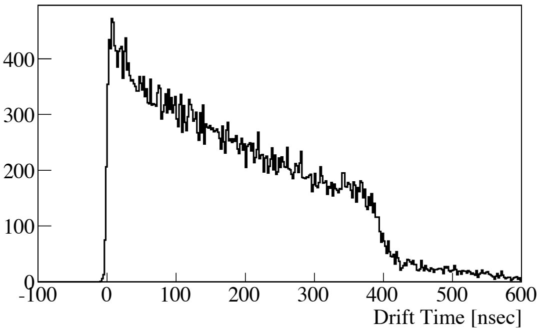

Fig.4. Drift time distribution for hits from which a track is reconstructed.

of electrons in a cell is 20-25 μm/ns. The width of about 400 ns corresponds to the cell size of 10 mm. Figure 5 and 6 show evaluated efficiency of each wire for X layers and Y layers. In whole, efficiency is better than 95%.

Figure 7 shows evaluated resolution of each wire for Y layers. The resolution σ is calculated by a following formula,

$$\sigma = \sqrt{\sigma_1 \sigma_2},$$

where σ_1 and σ_2 are sigmas of residual distribution including and excluding a wire focused, respectively. The resolution of 150 μm are achieved. Furthermore, the drift length dependences of the resolution shown in Fig. 8. It is found that the resolutions reach 100 μm at the middle of the cell, whereas they become about 200 μm near the sense wire and outer circumference of the cell. The analysis for X layers are ongoing.

§4. Conclusion and future prospects

The SCRIT electron scattering facility has been constructed to realize electron scattering off unstable nuclei. In 2016, several commissioning experiments with stable nuclear targets have been preformed.

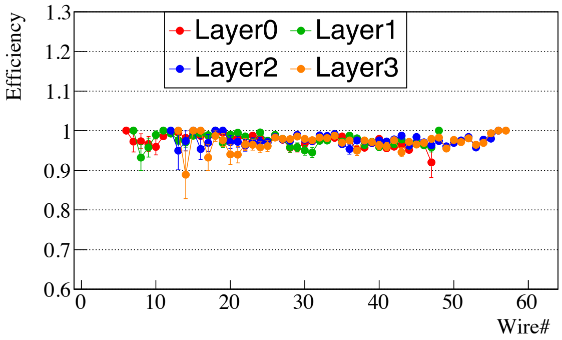

Fig.5. Efficiency of each wire of X layers.

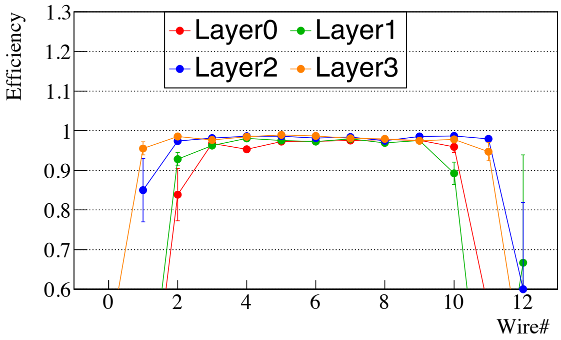

Fig.6. Efficiency of each wire of Y layers.

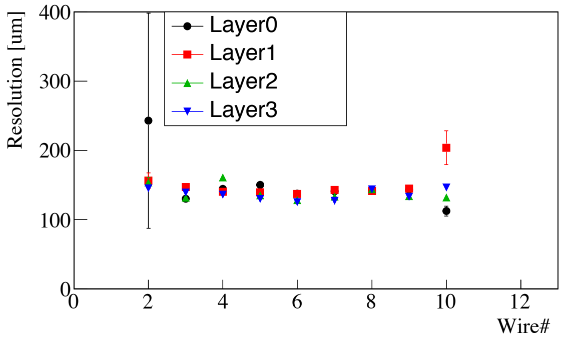

Fig.7. High volutage dependences of counting rate by changing the threshold are plotted.

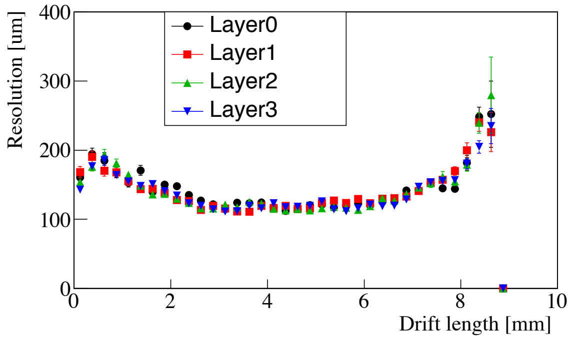

Fig.8. High volutage dependences of counting rate by changing the threshold are plotted.

In order to realize the experiment with unstable nuclear target, improvements of target preparation systems to achieve much higher luminosity have been conducted. The WiSES will be also updated by introducing FDC2 and measuring the three-dimentional magnetic field map. The performance study of FDC2 is still ongoing.

After these improvements, elastic electron scattering experiment for unstable nucleus will be performed soon.

References

[1] M. Wakasugi *et al.*: Nucl. Instr. Meth. B**317**, 668 (2013).

[2] K. Tsukada *et al.*: ELPH Annual Report 2014 Vol. 5, Tohoku University, 125 (2014).

[3] K. Tsukada *et al.*: ELPH Annual Report 2015 Vol. 6, Tohoku University, 99 (2015).

[4] T. Suda and H. Simon: Prog. Part. Nucl. Phys., 96, 1 (2017).

[5] K. Tsukada *et al.*: Phys. Rev. Lett. **118**, 262501 (2017).

[6] K. Tsukada *et al.*: Hyperfine Interact. 240, 102 (2019).

[7] T. Ohnishi *et al.*: Nucl.Instrum.Meth. B317, 357-360 (2013).

[8] M. Wakasugi *et al.*: Rev. Sci. Instrum 89, 095107 (2018).

Status of the LEPS2-solenoid experiment in 2018

Atsushi Tokiyasu[1] for LEPS2 collaboration

[1]*Research Center for Electron Photon Science, Tohoku University, Sendai, 982-0826*

The LES2-solenoid experiment is designed for multi-purpose apparatus to study the hadron photo-production mechanism at SPring-8. One of the detectors of the LEPS2 experiment is Aerogel Cherenkov Counter. The design work for the detector has been completed and performance test is carried out by positron beam at SPring-8. Construction for the main detector components were almost completed, thus the detector commissioning for system integration are performed with available detectors in 2018. γ beam was induced to CH2 target which was installed inside detector systems, and detector performance was evaluated by the charged or non-charged particles from the reaction events. A Significant amount of data have been accumulated for detector performance evaluation and developing analysis codes. Comissioning run will be continued through next FY, and physics experiment is planned after 2020.

§1. The LEPS2-solenoid experiment and detector systems

The LES2-solenoid experiment is designed for multi-purpose apparatus to study the hadron photo-production mechanism at SPring-8. A high intensity γ beam by Backward Compton Scattering is used to search for exotic hadron systems. One of the physics theme is a search for $\boldsymbol{K^-pp}$ bound state. $\boldsymbol{K^-pp}$ bound state was exotic nuclei which contains $\boldsymbol{K^-}$ meson as component.

Two distinguished signals expected from the K-pp bound state have been reported via pi- and K-induced experiment at J-PARC [1] [2].. However, the results, especially for binding energy obtained from those experiments, are not consistent. Moreover, there is no theoretical explanation to describe consistency between those results are available to date. Therefore, a new experiment to identified the $\boldsymbol{K^-pp}$ with a different probe is mandatory. Photo-production reaction is complementary to hadron reaction, and the LEPS2-solenoid experiment will provide essential information to investigate the internal structure of the $\boldsymbol{K^-pp}$ bound state.

Photo-production reaction is complementary to hadron reaction, and the LEPS2-solenoid experiment will provide essential information to investigate the internal structure of $\boldsymbol{K^-pp}$ bound state.

The overview of the LEPS2 solenoid detector system is shown in Fig. 1 The LEPS2 solenoid detector systems is composed of Start Counter(SC), Time Projection Chamber(TPC), Drift Chambers(DCs), Aerogel Cherenkov Counter (AC1, AC2), Resistive Plate Chamber (RPC), and Barrel-γ (Bγ). These detectors are installed inside solenoid magnet with the strength of 1 T, and used to detect both of charged particles

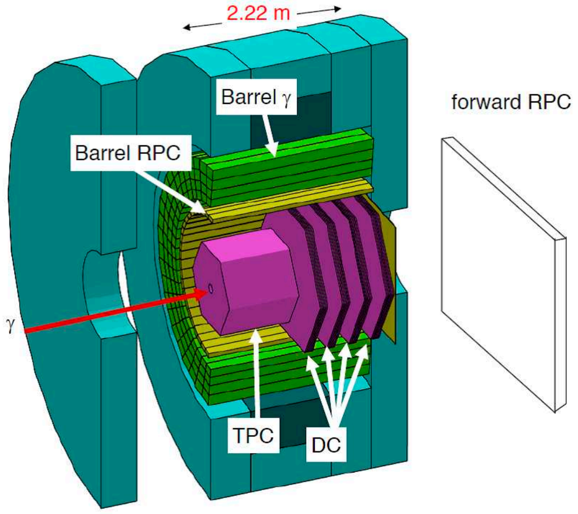

Fig.1. LEPS2 solenoid detector system

and γ from the hadron reactions. Among these detectors, ELPH is taking charge of developing AC2 and Bγ. In the following section, the status of the development these counters will be reported.

§2. AerogleCerenkov Counter

Aerogel Cherenkov Counter (AC) will be used to identify $K^{+/-}$ particles from the target. There are two types of AC. One is AC1 installed between TPC and DC1, and the another is AC2 installed between DC1 and DC2. The difference of two ACs are index of Aerogels. Aerogel with index of 1.05 will be used for AC1, and Aerogel with index of 1.03 are used for AC2. In this Fiscal year the geometrical design of AC2 was determined, and a proto-type detector was produced (Fig. 2). The performance check was performed by using electron beam at SPring-8 and proton beam at CYRIC in Tohoku University. We found the detection efficiency for π is enough, but large background exists coming from reflector materials. Another study for the selection of the material is on-going. The detail for AC2 development is summarized in [3]

§3. Barrel-gammma

The Barrel-γ is a sampling calorimeter system composed of multi-layers of Lead and Scintillator plates. Two PMTs were attached at the both edges to read out the light signals. In 2018, data acquisition system was newly constructed, and by using beam at SPring-8. γ beam was induced to CH2 target which was installed inside the solenoid magnet, and γ from the target was used to evaluated the energy resolution. Non-charged particles are selected by other counters like SC, and pulse charge and time information were collected. Figure 3 shows the correlation between light output ratio time difference of two PMTs, which means the hit positions. We can see clear locus on this plot. Now analysis is on-going to reconstruct π^0 peak.

Fig.2.　A picture of proto-type AC

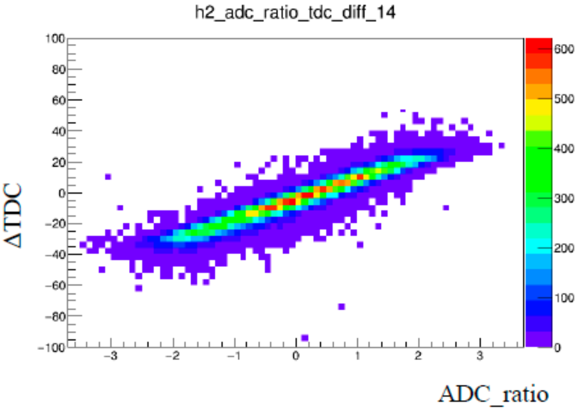

Fig.3.　correlation plot of Bγ signal

§4. Other detectors

In adittion to AC and Bγ, performances of TPC and DCs are also evaluated in comissioning run. Track reconstruction codes for TPC and DCs were developed, and we succeced to reconstruct the tracks from the target. We developed to adjust the relativistic location of DCs too. The evaluation of he position resolution and momentum resolution of TPC and DCs is on-going.

§5. Summary

The LEPS2-solenoid experiment is multi-purpose experiment to study the hadron photoproduction mechanism at SPring-8. Aerogel Cherenkov Counter and Barrel-γ Counter were developed by ELPH. The performance of these detectors were evaluated by electron beam or γ. The beam commissioning of the LEPS2 experiment will be continued in 2019, and after preparing all detectors, physics run will be started.

References

[1] Y. Ichikawa *et al.* :Prog. Theor. Exp. Phys (2015) 021D01

[2] S. Ajimura *et al.*:Phys. Lett. B 789 (2019) 620-625

[3] C. Yoshida : Master Thesis (2018)

Recent results of SPring-8 LEPS2/ BGOegg experiment

N. Muramatsu[1], T. Hashimoto[2], Y. Matsumura[2], M. Miyabe[1], T. Nam[2],
H. Shimizu[1], N. Tomida[2], J.K. Ahn[13], W.C. Chang[4], J.Y. Chen[5], S. Daté[3],
T. Gogami[6], H. Hamano[2], Q.H. He[15], K. Hicks[7], T. Hiraiwa[2], Y. Honda[1],
T. Hotta[2], Y. Inoue[1], T. Ishikawa[1], I. Jaegle[8], J.M. Jo[13], Y. Kasamatsu[2],
H. Katsuragawa[2], S. Kido[1], Y. Kon[2], S. Masumoto[9], K. Miki[12], K. Mizutani[2],
T. Nakamura[12], T. Nakano[2], M. Niiyama[14], Y. Nozawa[18], Y. Ohashi[3],
H. Ohkuma[2], H. Ohnishi[1], T. Ohta[18], M. Oka[2], M. Okabe[1], K. Ozawa[11],
C. Rangacharyulu[16], Y. Sada[1], M. Sasagawa[1], T. Shibukawa[9], R. Shirai[1],
K. Shiraishi[1], E.A. Strokovsky[17,2], Y. Sugaya[2], M. Sumihama[12,2], S. Suzuki[3],
S. Tanaka[2], A. Tokiyasu[1], Y. Tsuchikawa[1], T. Ueda[1], H. Yamazaki[19],
R. Yamazaki[1], Y. Yanai[2], T. Yorita[2], C. Yoshida[1], and M. Yosoi[2]

[1] *Research Center for Electron Photon Science, Tohoku University, Sendai, Miyagi 982-0826, Japan*
[2] *Research Center for Nuclear Physics, Osaka University, Ibaraki, Osaka 567-0047, Japan*
[3] *Japan Synchrotron Radiation Research Institute (SPring-8), Sayo, Hyogo 679-5198, Japan*
[4] *Institute of Physics, Academia Sinica, Taipei 11529, Taiwan*
[5] *National Synchrotron Radiation Research Center, Hsinchu 30076, Taiwan*
[6] *Department of Physics, Kyoto University, Kyoto 606-8502, Japan*
[7] *Department of Physics and Astronomy, Ohio University, Athens, OH 45701, USA*
[8] *Department of Physics and Astronomy, University of Florida, Gainesville, FL 32611, USA*
[9] *Department of Physics, University of Tokyo, Tokyo 113-0033, Japan*
[10] *RIKEN Nishina Center, Wako, Saitama 351-0198, Japan*
[11] *Institute of Particle and Nuclear Studies, High Energy Accelerator Research Organization (KEK), Tsukuba, Ibaraki 305-0801, Japan*
[12] *Department of Education, Gifu University, Gifu 501-1193, Japan*
[13] *Department of Physics, Korea University, Seoul 02841, Republic of Korea*
[14] *Department of Physics, Kyoto Sangyo University, Kyoto 603-8555, Japan*
[15] *Department of Nuclear Science & Engineering, College of Material Science and Technology, Nanjing University of Aeronautics and Astronautics, Nanjing 210016, China*
[16] *Department of Physics and Engineering Physics, University of Saskatchewan, Saskatoon, SK S7N 5E2, Canada*
[17] *Laboratory of High Energy Physics, Joint Institute for Nuclear Research, Dubna, Moscow Region, 142281, Russia*
[18] *Department of Radiology, The University of Tokyo Hospital, Tokyo 113-8655, Japan*
[19] *Radiation Science Center, High Energy Accelerator Research Organization (KEK), Tokai, Ibaraki 319-1195, Japan*

§1. Introduction

At SPring-8 LEPS2 beamline, a tagged photon beam is available in the energy range of 1.3–2.4 GeV by laser Compton scattering [1]. A beam intensity reaches 1–5 × 10^6 cps. This beamline has been constructed at the long straight section of the electron storage ring, where a beam divergence is locally suppressed to 12 μrad for the horizontal direction, so that the photon beam can be extracted to the LEPS2 experimental building about 130 m apart from the Compton scattering point. The LEPS2 experimental building has a large space, which enables to run two experimental setups: namely, the BGOegg

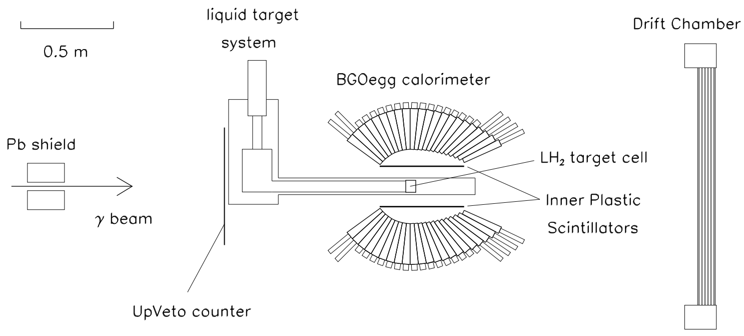

Fig.1. Setup of the BGOegg experiment. Only the apparatus closely related to the signal selection of single meson photoproduction is shown in a side view. A wall of resistive plate chambers (RPC) is also located 12.5 m of the target in the forward acceptance.

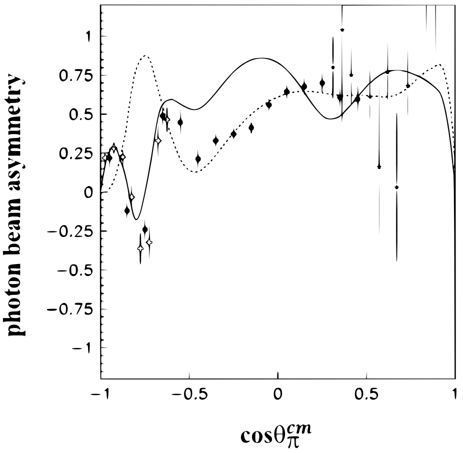

Fig.2. Photon beam asymmetries for π^0 photoproduction, measured by BGOegg (closed circles), LEPS (open crosses), and Daresbury (closed stars) at $2200 < E_\gamma < 2300$ MeV. Solid and dashed curves represent partial wave analysis calculations by SAID and Bonn-Gatchina groups, respectively.

experiment with a high precision electromagnetic calorimeter and the charged particle spectrometer experiment using a large solenoid magnet. Both experiments have assembled large solid angle detector systems, and they are separately running while adjusting experimental periods.

The BGOegg experiment has been carried out in the first phase of LEPS2 beamline operation. In 2014–2016, experimental data have been alternatively collected by using a 54 mm-thick liquid hydrogen target or a 20 mm-thick carbon target. Figure 1 shows the BGOegg experimental setup. The polar angles from 24° to 144° around the target are covered by an electromagnetic calorimeter, which consists of $1,320$ BGO crystals in an egg shape and is therefore called “BGOegg”. The charge identification of BGOegg calorimeter hits is done by using inner plastic scintillators (IPS), arranged in a cylindrical shape. The energy resolution of the BGOegg calorimeter is 1.3% for 1 GeV γ rays, providing the highest performance in the world [2]. For the forward acceptance hole of the BGOegg calorimeter, a planar drift chamber (DC) and resistive plate chambers (RPC) are placed to detect charged particles.

§2. Single meson photoproduction off the proton

We have analyzed the liquid hydrogen target data in order to search for baryon resonances in the s-channel of single meson photoproduction reactions, such as $\gamma p \to \pi^0 p$, ηp, and ωp. The masses and widths of baryon resonances are not well described by constituent quark models, except for ground and low excited states. Experimental investigation of baryon mass spectra is recognized to be important for understanding hadron structures. Because excited baryon states have wide widths and overlap with each other, it is effective to study various photoproduction reactions systematically and to accumulate measured observables with the use of photon beam polarization. For example, π^0 photoproduction is contributed from both nucleon and Δ resonances, while photoproduction of the η or ω meson arises only from nucleon resonances thanks to an isospin filter. If polarization observables are measured together with differential cross sections for these reactions, highly excited states with weaker amplitudes can be extracted through an interference effect. However, the results of photon beam asymmetries, obtained by using linear polarization, are insufficient in the photon beam energy range of 2 GeV or more for all the above reaction modes. The LEPS2 beamline has an advantage for generating a linearly polarized photon beam via laser Compton scattering, and the BGOegg experiment has obtained such new experimental results.

In the analyses, the π^0 and η mesons are identified by detecting a $\gamma\gamma$ decay, and the ω meson is reconstructed from a $\pi^0\gamma$ decay. The energy and flying direction of those final state γ's are measured at the BGOegg calorimeter. A recoil proton is detected by the BGOegg calorimeter or the forward drift chamber to measure its emission angle. Simultaneously, the energy of an incident photon beam is determined event by event on the basis of a momentum analysis for a recoil electron at laser Compton scattering. Then, a kinematic fit is performed by requiring four-momentum conservation. Here the invariant mass of $\gamma\gamma$ is also constrained to the nominal value of π^0 or η, which are available by Particle Data Group (PDG) [3]. A χ^2 probability cut after the kinematic fit eliminates background event, resulting in the clean signal samples of π^0, η, and ω photoproduction of about 650K, 56K, and 37K events, respectively.

The detailed results of differential cross sections and photon beam asymmetries for π^0 photoproduction are described in another paper [4]. The statistical accuracies of them are comparable to the existing experimental results. The obtained differential cross sections generally agree with the results of CLAS, GRAAL, and LEPS experiments [5–7]. On the other hand, a difference from the CB-ELSA and CBELSA/TAPS results is seen for backward π^0 production angles in the low energy region of $E_\gamma < 1.9$ GeV [8, 9]. As for the photon beam asymmetries, we have achieved a wide angle coverage at $E_\gamma > 1.9$ GeV, for the first time. A steep drop of the photon beam asymmetry has been observed at extremely backward π^0 angles in this high energy region, as shown in Fig. 2. None of the existing partial wave analysis models reproduce the measured photon beam asymmetries at high energies [10, 11]. In the analyses for η and ω photoproduction, the measurements of differential cross sections and photon beam asymmetries are also in progress, showing differences from the existing partial wave analysis models in the high energy region where the multipole amplitudes are not well fixed. In particular, the differential cross sections of η photoproduction at the most backward angles suggests a wide bump structure around $\sqrt{s} \sim 2.2$ GeV.

§3. η' meson mass in nuclei

The η' meson gains a large mass due to the $U_A(1)$ anomaly, and it has been discussed that its mass may be reduced inside a nucleus by the partial restoration of chiral symmetry breaking under a high-density environment. While theories such as the linear sigma model [12] and the NJL model [13] predict a large mass reduction of 80-150 MeV/c^2, the $\eta' N$ scattering length measurement at COSY-11 [14] and the measurements of transparency ratio and sub-threshold cross sections at CBELSA/TAPS

[15, 16] indirectly suggest smaller amounts of reduction, which do not exceed about 50 MeV/c^2. In the BGOegg experiment, we are aiming for more direct observation of an η' mass change by using the carbon target data. For this purpose, we have adopted two analysis methods, searching for (1) nuclear medium modification signals in the $\gamma\gamma$ invariant mass distribution from η' decays, and (2) nuclear bound states of the η' meson in the missing mass distribution with a high energy proton detection at extremely forward angles.

3.1 Medium modification of the η' mass

In order to explore the change of η' meson mass in carbon nuclei, we detect $\eta' \to \gamma\gamma$ decays, whose branch fraction is 2.22% in vacuum, at the BGOegg calorimeter, and measure the invariant mass distribution of two γ rays. There is a benefit that the calorimeter can detect those γ rays without much influence of interaction in the target substance. As the produced η' meson has a smaller momentum, the rate of decay in the carbon nucleus increases, possibly enhancing mass reduction signals below the peak structure due to η' decays outside the nucleus in the $\gamma\gamma$ invariant mass distribution.

In searching for the medium modification of the η' mass, it is important to understand the $\gamma\gamma$ invariant mass spectrum shape of decays outside the nucleus. This shape is influenced by energy and angular resolutions for γ detection, and is evaluated by a realistic Monte Carlo (MC) simulation that reproduces the detector setup and response in the BGOegg experiment. The validity of the mass resolutions obtained by MC simulations is proved by confirming it matches with the real data resolutions in any momentum range for the processes $\eta \to \gamma\gamma$ and $\omega \to \pi^0\gamma \to \gamma\gamma\gamma$. The mass resolution estimated using a MC simulation is also consistent with that for the liquid hydrogen target data.

In addition to the η' meson decays outside the nucleus, photoproduction of multiple π^0's, $\pi^0\eta$, etc. are large background soures against the search for medium modification. These processes include many γ rays in the final state, but are contaminated into the signal sample by missing some of them in the forward acceptance hole of the BGOegg calorimeter. The reaction $\gamma p' \to \pi^0\pi^0 p$ contributes as a main background caused by a physical process. In the region of a large invariant mass, there also remain backgrounds from unphysical processes, in which particles originating from cosmic rays and upstream interactions are detected by the BGOegg calorimeter. The invariant mass spectra and amounts of these processes are estimated by MC simulations and individual background-tagged samples in the real data. It has been confirmed that the mass spectra can be fitted reasonably with a smooth function represented by $\exp(p_0 + p_1 x + p_2 x^2)$ for any process. This function can be also applied to the invariant mass distribution added with the ratio of each evaluated background amout. The χ^2 for this overall fit does not change even if variation is given to the background ratio.

The obtained background spectra have been simultaneously fitted to the $\gamma\gamma$ invariant mass distribution in the real data, as shown in Fig 3. This figure is plotted for events where the momenta of η' mesons are over 1 GeV/c. In the small invariant mass region, a background component due to the reaction $\omega \to \pi^0\gamma \to \gamma\gamma\gamma$ with a missing γ ray is also considered. The reduced χ^2 of the background fit for the high momentum region is 61.8/59, indicating no signals of medium modification. For more

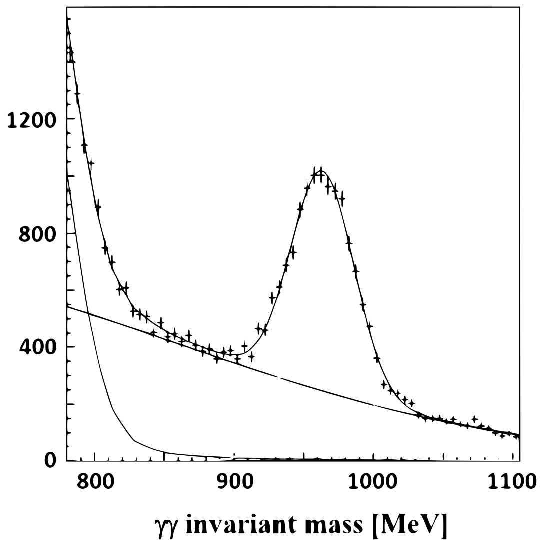

Fig.3. A background fit to the $\gamma\gamma$ invariant mass distribution in the carbon target data. η' momenta are required to be greater than 1 GeV/c.

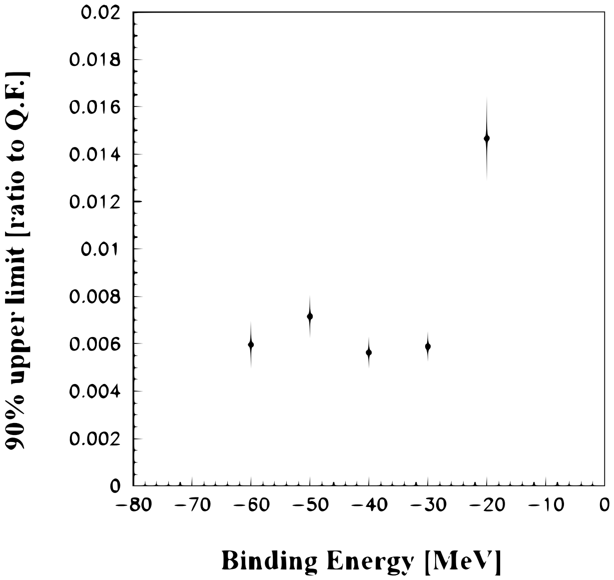

Fig.4. Sensitivity of η' mass modification for the near future BGOegg experiment using a copper target.

quantitative evaluation of statistical significance, the invariant mass distributions of medium modification signals are derived from simulations with various assumptions of mass reduction and width. Then, χ^2 fits are performed in two cases, when only the background functions are fitted and when the signal function is additionally included. The signal significance is calculated based on the difference of χ^2's. Before scanning the signal significance, the condition to select η''s with lower momenta has been decided to be a region below 1 GeV/c so that a statistical figure of merit for the ratio of decays inside the nucleus should be maximized over background fluctuation. The final siginificance evaluation will be soon carried out for the low momentum region.

3.2 η'-mesic nuclei

As another way to probe the decrease of η' mass inside the nucleus, we are also searching for nuclear bound states of the η' meson. In this method, high-energy protons emitted to extremely forward angles are detected by RPC for tagging photoproduction of low-momentum η' mesons in carbon nuclei. Proton momenta are measured from time-of-flight with high precision, and missing masses for the $C(\gamma, p)$ reaction are calculated to seek the bound state signals below the threshold of quasi-free η' production. Furthermore, we increase a S/N ratio by using the BGOegg calorimeter, which detects signals that the bound η' mesons are absorbed by protons in the nucleus and cause conversions to back-to-back η-p. Becase the nuclear absorption rate of the η' meson is unknown, it is ideal to advance the two complementary analyses with the $\gamma\gamma$ invariant mass and the $C(\gamma, p)$ missing mass.

The search for the nuclear bound states of the η' meson has been performed earlier in the $C(p, d)$ reaction experiment at GSI, resulting in no sign of such signals in the missing mass distribution [17]. In contrast, the BGOegg experiment is characterized by trying to detect the absorption and conversion signals at the same time. The BGOegg experiment can also detect quasi-free photoproduction of η'

mesons, enabling the normalization of theoretical predictions for the differential cross sections of bound signals. Importance of the latter point is understandable from the existing pionic atom experiments, where the bound level spectrum has been well reproduced by theoretical calculations but it has been difficult to match their differential cross sections. We have measured the experimental yield of η' escapes from the carbon nucleus by detecting a forward proton at the RPC and an $\eta' \to \gamma\gamma$ decay at the BGOegg calorimeter. Our measurement indicates this yield is about 1/4 of the theoretical calculation [18].

In the analysis detecting the conversion signals to η-p, the processes like η photoproduction with a scattering of the reaction product from other nucleons remain as final backgrounds. These backgrounds have kinematic features such as η mesons or protons are likely to be produced in the forward direction. Event selection conditions with a sufficient S/N ratio for signal detection are being determined, and the existence of bound signals will be inspected in the missing mass distribution for the extremely forward proton. We also compare the measured spectrum with the theoretical calculation of missing mass distribution based on the NJL model [18].

3.3 Near future plan

The forward detectors for charged particles in the BGOegg experimental setup have been replaced by an additional electromagnetic calorimeter, called a “Forward Gamma” detector. It consists of 252 $PbWO_4$ (PWO) crystals, each of which has a size of $22 \times 22 \times 180$ mm^3. The charge of a Forward Gamma hit is identified by a two-dimensional hodoscope array (Forward Plastic Scintillators) [19], placed in front of this calorimeter. By covering most of solid angles with calorimeters, an ambiguity in judging reaction processes, caused by missing particles, are efficiently reduced. In terms of the medium modification search for the η' meson, a main background coming from the reaction $\gamma p' \to \pi^0\pi^0 p$ decreases less than one order of magnitudes. This feature provides great advantage in suppressing fluctuation of a background spectrum, which fakes medium modification signals.

In the BGOegg experiment, the target is being changed to copper, which has a larger nuclear radius, for further data collection using the new detector setup described above. In 2017, we have collected test data with a copper target, whose thickness corresponds to 0.1 radiation length in the same way as the previous program with a carbon target. Because the uncertainty of a reaction point is reduced by the change of target thickness from 20 mm to 1.5 mm, the resolution of $\gamma\gamma$ invariant mass for η' is improved from 20 MeV/c^2 to 13 MeV/c^2. Moreover, in 2018, we have increased the thickness of a copper target by a factor of 5, and finished short-term data taking with partial operation of the Forward Gamma detector and the Forward Plastic Scintillators. After the preparation of a data acquisition system for the new setup is completed, the BGOegg experiment will be resumed while adjusting time sharing of the LEPS2 beamline with the solenoid experiment. Figure 4 shows the signal sensitivity of medium modification that can be achieved by planned data collection as a function of the binding energy. It is assumed that a copper target with 0.5 radiation length will be irradiated by a photon beam of 2×10^6 cps for 4 months and that a background level will be reduced by an order of magnitude with the new experimental setup. The vertical axis represents 90% upper limits for a background fluctuation of $\sigma \sim 13$ MeV/c^2 to be recognized as medium modification signals in the form of a percentage to the quasi-free η' photoproduction. If the momentum range of produced η' mesons is limited up to several hundreds MeV/c, the rate of $\gamma\gamma$ decays inside the nucleus is expected to be a few percent, so that the planned data collection must provide enough signal sensitivity.

§4. Summary

The BGOegg experiment is conducted as research programs to understand hadron natures by using a 1.3–2.4 GeV photon beam at the SPring-8 LEPS2 beamline. Data collected using a liquid hydrogen target is analyzed to search for baryon resonances. In particular, photon beam asymmetries have been measured with the advantage of high linear polarization in a high energy region where experimental results are scarce. The collected data will be further utilized to study highly excited baryons through the photoproduction of η' or multiple mesons. In addition, we analyze the carbon target data to investigate medium modification of the η' mass in the $\gamma\gamma$ invariant mass and to search for nuclear bound states in the $C(\gamma, p)$ missing mass. In the near future, we will use a copper target whose thickness is increased to 0.5 radiation length, and will employ an experimental setup to cover the forward acceptance hole of the BGOegg calorimeter with another electromagnetic calorimeter made of PWO crystals. The contribution of backgrounds due to multiple π^0 photoproduction must be largely suppressed, and medium modification signals can be detected with sufficient statistical accuracy in half-year data collection. The new experimental setup with increased calorimeter acceptance allows the detection of all final state particles with charge identification, and enables data collection even for a deuterium target.

References

[1] N. Muramatsu, et al., Nucl. Instr. Meth. A **737** (2014) 184; N. Muramatsu, ELPH Report 2044-13 (2013) or arXiv:1307.6411.

[2] T. Ishikawa, et al., Nucl. Instr. Meth. A **837** (2016) 109.

[3] M. Tanabashi, et al. (Particle Data Group), Phys. Rev. D **98** (2018) 030001.

[4] N. Muramatsu, et al., Phys. Rev. C **100** (2019) 055202.

[5] M. Dugger, et al., Phys. Rev. C **76** (2007) 025211.

[6] O. Bartalini, et al., Eur. Phys. J. A **26** (2005) 399.

[7] M. Sumihama, et al., Phys. Lett. B **657** (2007) 32.

[8] O. Bartholomy, et al., Phys. Rev. Lett. **94** (2005) 012003.

[9] V. Crede, et al., Phys. Rev. C **84** (2011) 055203.

[10] http://gwdac.phys.gwu.edu/

[11] https://pwa.hiskp.uni-bonn.de/

[12] S. Sakai and D. Jido, Phys. Rev. C **88** (2013) 064906.

[13] H. Nagahiro, M. Takizawa, and S. Hirenzaki, Phys. Rev. C **74** (2006) 045203.

[14] P. Moskal, et al., Phys. Lett. B **482** (2000) 356; E. Czerwinski et al., Phys. Rev .Lett. **113** (2014) 062004.

[15] M. Nanova, et al., Phys. Lett. B **710** (2012) 600.

[16] M. Nanova, et al., Phys. Lett. B **727** (2013) 417.

[17] Y.K. Tanaka, et al., Phys. Rev. Lett. **117** (2016) 202501.

[18] H. Nagahiro, JPS Conf. Proc. **13** (2017) 0100010.

[19] T. Ueda, Master Thesis, Tohoku University (2019).

Production of a high energy γ beam via inverse Compton scattering of soft x-rays from a short undulator

Norihito Muramatsu[1], Masahiro Okabe[1], Shinsuke Suzuki[2], Schin Daté[2],
Hajime Shimizu[1], Haruo Ohkuma[3], Kazuhiro Kanda[4], Shuji Miyamoto[4],
Tetsuo Harada[4], Takeo Watanabe[4], Manabu Miyabe[1], and Atsushi Tokiyasu[1]

[1]*Research Center for Electron Photon Science, Tohoku University, Sendai, Miyagi 982-0826, Japan*
[2]*Japan Synchrotron Radiation Research Institute (SPring-8), Sayo, Hyogo 679-5198, Japan*
[3]*Research Center for Nuclear Physics, Osaka University, Ibaraki, Osaka 567-0047, Japan*
[4]*Laboratory of Advanced Science and Technology for Industry, University of Hyogo, Kamigori, Hyogo 678-1205, Japan*

§1. Introduction

Usually, a high-power laser beam is injected into the electron storage ring for the production of a high-energy γ beam via inverse Compton scattering. In our project, soft x-rays of about 92 eV are being injected instead, in order to achieve much higher energies for the γ beam. Figure 1 shows the energy spectrum of such a beam at SPring-8-II, where the electron beam energy will be lowered to 6 GeV. This γ beam must be useful for new generation experiments of hadron physics by enabling the production of heavier particles [1].

We plan to carry out a series of demonstration experiments to develop techniques for the inverse Compton scattering of soft x-rays at NewSUBARU, whose electron energy is 1 or 1.5 GeV. In case of the 1 GeV operation, the maximum energy of a γ beam is extended to 585 MeV at Compton edge, compared with 51 MeV by the injection of 355 nm ultraviolet laser. For the demonstration experiments, we use a short undulator (total length: 2.28 m, period length: 7.6 cm) at BL07 [2] as an x-ray source, and then reflect the radiated x-rays backwardly into the original straight section. A Mo/Si multi-layer mirror will be installed at BL07A for this reflection.

§2. Preparation of beamline chambers and associated detectors

In FY2018, the experimental setup was designed for NewSUBARU BL07A in detail. Accordingly, two vacuum chambers were newly installed at this beamline. One large chamber with a size of $W1120 \times D820 \times H610$ mm^3 has been set up 16.7 m downstream of the undulator center. A multi-layer mirror will be placed on high precision stages inside this chamber with cooling water circulation. The other chamber, shown in Fig. 2(a), has been installed 2.6 m upstream of the large mirror chamber, in order to monitor radiated and reflected x-rays. A wire scanning detector was mounted for the measurement of their profiles and relative intensities based on an increase of micro current due to a photoelectric effect at $\phi0.2$ mm tungsten wires. The tugsten wires were directed vertically and horizontally with a moving stage attached to an air cylinder.

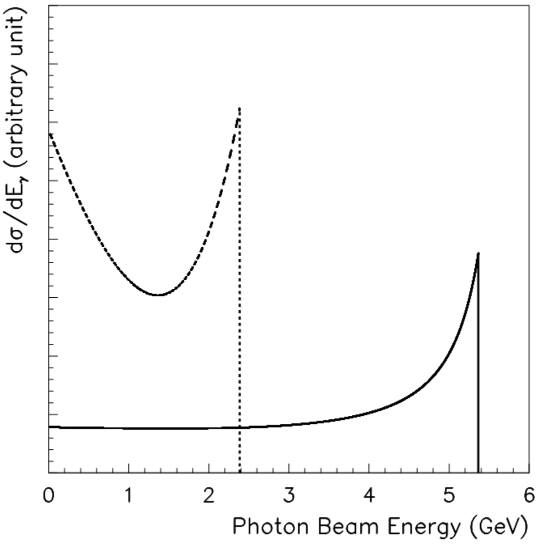

Fig.1. An energy spectrum of a γ beam via inverse Compton scattering of 92 eV x-rays from 6 GeV electrons at SPring-8-II (solid line). The other spectrum (dashed line) indicates the inverse Compton scattering of 355 nm laser light from 8 GeV electrons at SPring-8.

For the energy measurement of a γ beam produced by inverse Compton scattering, a high resolution electromagnetic calorimeter ($\Delta E/E = 1.7\%$ at 1 GeV) was made by assembling nine PbWO4 (PWO) crystals, the individual size of which is $20 \times 20 \times 200$ mm^3. It was set up just downstream of the switching mirror for BL07A and BL07B inside the storage ring tunnel, as shown in Fig. 2(b). A γ-beam profile monitor was also prepared by crossing 1 mm^2 scintillating fibers in the area of 50×50 mm^2. The readout of scintillating fibers were done in each two channels (namely, 2 mm digitization) by using multi-pixel photon counters (MPPC). For making a trigger signal at data taking, a veto counter, a thin lead converter, and a trigger counter were additionally placed upstream of the profile monitor and the PWO calorimeter.

§3. Development of a cylindrical x-ray mirror

A base plate for the Mo/Si multi-layer mirror was developed with a low thermal expansion glass ceramic (Zerodur). Because the switching mirror of BL07 possesses a spherical surface, the x-rays at the reflection mirror chamber are parallel in the horizontal direction but divergent for the vertical component. This feature was confirmed by the ray trace simulation SHADOW [3], as shown in Fig 3. In order to focus the reflected x-rays at the straight section of BL07, we need a cylindrical multi-layer mirror with a curvature radius of 16.7 m, which corresponds to the distance between the mirror and the Compton scattering point. A good focusing behavior was also confirmed by SHADOW.

Based on this study, we developed a cylindrical x-ray mirror base with a unique method by using a 5 mm-thick and 80×80 mm^2 Zerodur plate. Details of the cylindrical mirror production are described in Ref. [4]. The Zerodur plate has been finally cut in 50×50 mm^2, which is large enough comapred with the x-ray beam size of about 20×20 mm^2. The produced curvature radius was confirmed by measuring

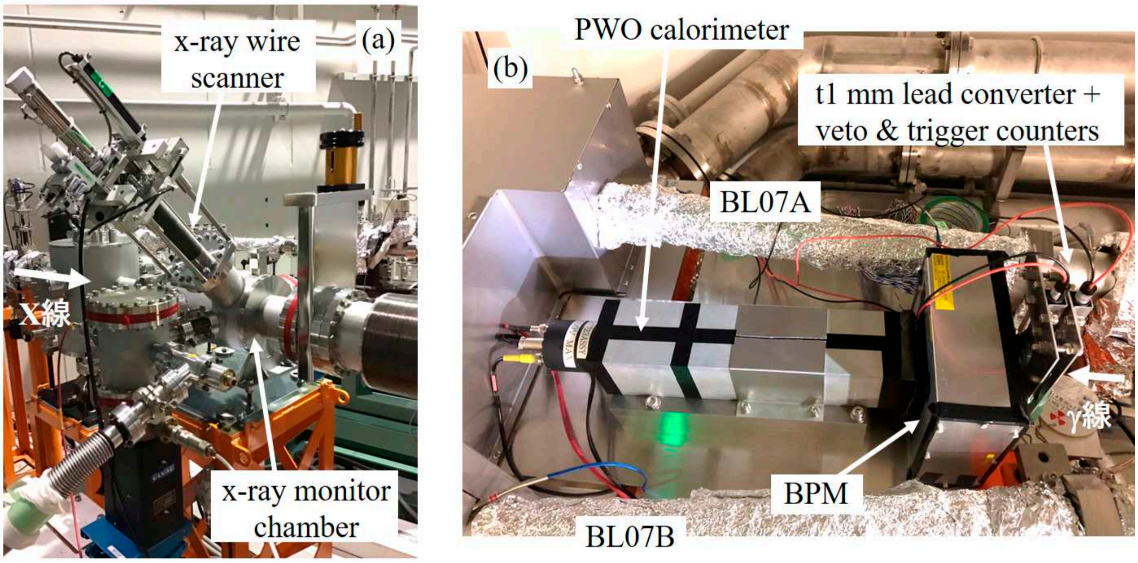

Fig.2. Pictures of (a) x-ray monitor chamber and (b) γ-beam detectors, installed at NewSUBARU BL07A.

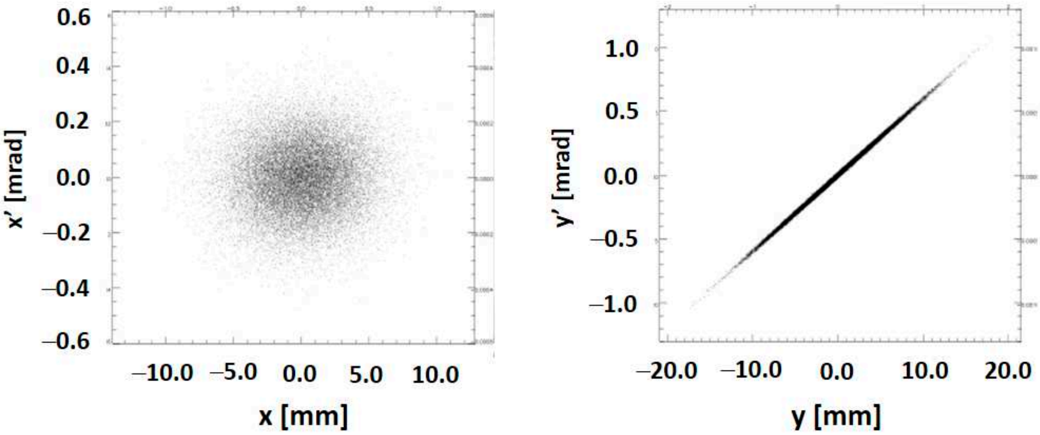

Fig.3. SHADOW simulation results of the x-ray positions and slopes at the reflection mirror chamber in the horizontal (x / x') and vertical (y / y') directions.

the maximum depth at the mirror surface center with a micro-gauge (18.7 μm for the 50 mm width) and alternatively counting the number of Newton fringes with a flat plate under a Na lamp (128 interference fringes for the 50 mm width). The mirror base is now in the process of multi-layer coating by Mo/Si. The reflectivity will reach 60% for the backward reflection of 92 eV x-rays [5].

§4. A test experimet with a bremsstrahlung γ beam

The performance of x-ray and γ-beam detectors has been tested by using x-rays from the BL07 short undulator and a γ beam from gas bremsstrahlung inside the storage ring. Fig. 4(a) shows the vertical profile of undulator x-rays at the wire scanning detector. A wire position during the air cylinder operation was determined based on the voltage measurement by a potentiometer. This test measurement was performed with a narrow slit, so the observed x-ray beam size was about 1 mm in σ. A variation of

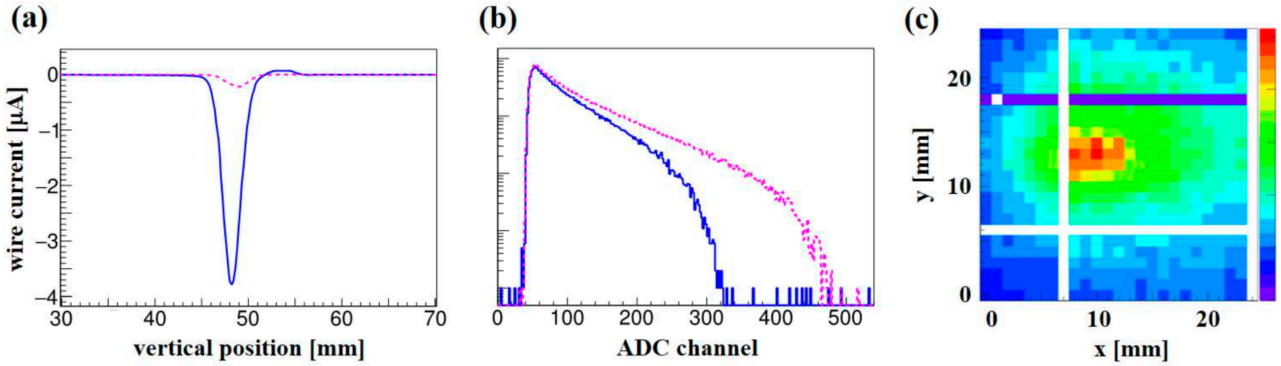

Fig.4. (a) Vertical profiles of undulator x-rays at the wire scanning detector. The solid and dashed lines were obtained when the undulator gap was set to 48 mm and fully opened, respectively. (b) Energy spectra of a bremsstrahlung γ beam at the PWO calorimeter. The solid and dashed lines correspond to the storage-ring operation energies of 1 and 1.5 GeV, respectively. (c) A Two-dimensional profile of a bremsstrahlung γ beam at the γ-beam profile monitor.

the x-ray beam intensity is clearly seen depending on the undulator gap setting.

Fig. 4(b) shows the energy spectra of γ beams from gas bremsstrahlung. Both spectra with New-SUBARU operation at 1 and 1.5 GeV were measured by using the PWO calorimeter. The linearity of energy measurement can be confirmed by comparing the upper edges of two spectra. Fig. 4(c) shows a result of γ-beam profile measurement by using the γ-beam profile monitor, made of scintillating fibers. The γ beam is narrow enough with a gaussian sigma of about 6 mm.

§5. Prospect of the demonstration experiments

After the completion of the Mo/Si multi-layer coating, we will test the production of a γ beam via inverse Compton scattering of undulator x-rays. We will confirm technical issues on the heat load of an x-ray mirror, the cooling capacity of a mirror holder, the reflectivity of x-rays, the focussing performance of a cylindrical x-ray mirror, and so on. Then we will measure the energy spectrum and intensity of an x-ray induced γ beam for comparison with theoretical estimations. Based on these developments, we will move on a next step towards the production of a high energy and intensity γ beam, usable realistically for next-generation hadron experiments. The developed techniques can be applied as one of beamlines at electron storage ring facilities like SPring-8-II, KEK PF-AR, and SLiT-J.

This project is in progress under the support by JSPS KAKENHI for Challenging Research (Pioneering) Grant No.18H05325 [6].

References

[1] E. Klempt and A. Zaitsev: Phys. Rep. **454** (2007) 1.

[2] K. Kanda, Y. Haruyama, M. Fujisawa and S. Matsui: Nucl. Instrum. Methods Phys. Res. A **467-468** (2001) 500.

[3] Using the old version ‘xop2.3’ available from http://www.esrf.eu/Instrumentation/software/data-analysis/xop2.4

[4] M. Okabe, N. Muramatsu, and I. Ishikawa, ELPH Annu. Rep. **2018** (2019) 102.

[5] T. Feigl, S. Yulin, N. Benoit, and N. Kaiser, Microelectron. Eng. **83** (2006) 703.

[6] http://www.rcnp.osaka-u.ac.jp/ mura/kaitaku/

Development of Multilayer Mirror for Producing a Next-generation Photon Beam

Masahiro Okabe[1], Norihito Muramatsu[1], and Isamu Ishikawa[2]

[1]*Research Center for Electron Photon Science, Tohoku University, Sendai, Miyagi 982-0826*
[2]*IK Technology Co., Minoh, Osaka 562-0045*

Photon beams produced by inverse Compton scattering are commonly used in several facilities. For example LEPS and LEPS2 experiments at Spring-8, where laser photons are used as incident photons. The energy of produced gamma-rays becomes higher if soft X-rays are used instead of laser. In this experiment, we developed a unique mirror to reflect soft X-rays from an undulator to a storage ring. Because it was designed to have an extremely small and cylindrical curvature, we established a new method for bending glass plates and utilizing a property of shape restoration to make them curved. Mechanical polishing is widely used to producing a spherical surface, but it is not suited for a cylindrical one. When the new method to produce a high energy gamma-ray beam becomes available, we will be able to study heavier hadrons than those in the current research programs with laser injection.

§1. Introduction

The maximum energy of gamma rays produced by inverse Compton scattering is expressed by

$$E_\gamma = \frac{4\omega_0 E_e^2}{m^2c^4 + 4\omega_0 E_e}, \tag{1}$$

where ω_0 and E_e represent the energy of incident photons and electrons, respectively, and m represents electron mass. When the energy of storage ring electrons is 8 GeV and that of incident photons is 3.5 eV, which corresponds to the laser wavelength of 355 nm used at LEPS2, the maximum energy of gamma rays is 2.4 GeV. If incident photon is soft X-ray photons with the energy of about 100 eV, it becomes 7.4 GeV.

To verify energy raise by inverse Compton scattering, we are researching at New SUBARU synchrotron radiation facility, which has 1.0 GeV storage ring (the maximum energy is 1.5 GeV). There is an undulator on the ring and it can produce about 100 eV X-ray beam. We are trying to reflect undulator photons backwardly into the storage ring. The experimental setup is shown in Fig.1. The beam line has a feature that a photon beam has a divergence in the vertical direction, which arises from its specific structure. To solve this problem, we need a mirror which has a cylindrical surface, whose radius of curvature is 16.7 m. A commonly used method is rotating glass plate and mechanical polishing for a high-precision spherical surface. However it's not suited to a cylindrical surface. We developed a new method to make glass plates that met performance mentioned above.

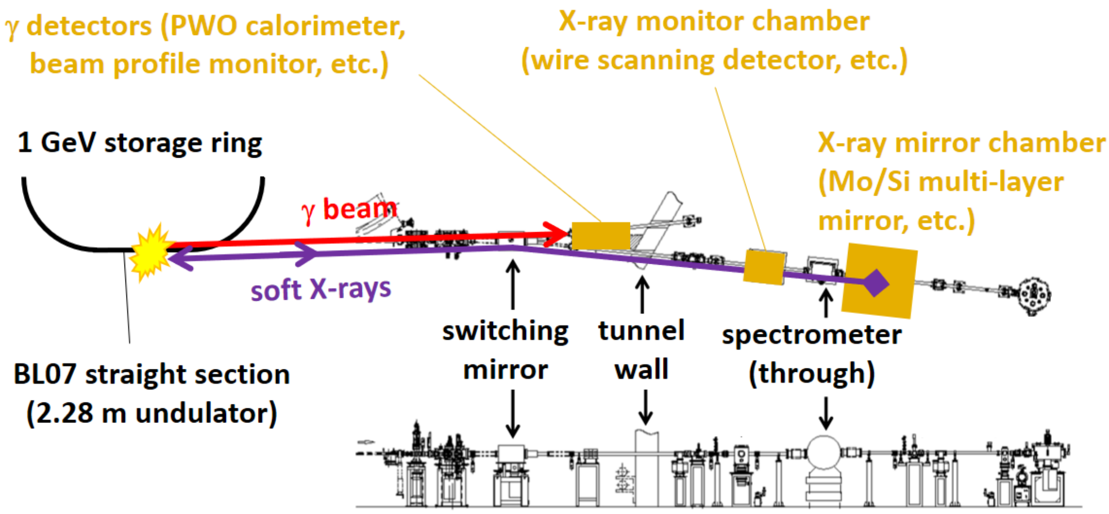

Fig.1. Setup at New SUBARU beam line

§2. Method of mirror base production

The process to make glass plates curved is illustrated in Fig. 2. The glass we have adopted is Zerodur, which possesses a low thermal-expansion property. First of all, we pressed the edges of them to make convex curves and fixed with epoxy resin adhesive. Then we polished the convex surfaces until they became flat with the surface roughness of a few nm. The adhesive can be melted when it's heated above about $200°C$. After solving the bending stress of the glass plates, the flatly polished planes have concave curves.

To accomplish this process, we made a jig tool shown in Fig. 3. The left panel describes a conceptual design, and the picture of the constructed jig is shown in the right panel. We put two stainless wires of a 0.2 mm diameter with an interval of 30 mm. We pressed the glass edges with a lab-jack to make convex surfaces. Because it was necessary to apply equal pressures on both edges, we assembled a jig as shown in the upper side of the left panel of Fig. 3 (right). A scale was used to measure the applied pressure.

To check the curvature radius during and after the production process, we performed a Newton Fringe (NF) test. It represents an interference pattern of a convex surface relative to a flat reference plane. The actual picture of NF is shown in figure4. We compared the observed interference pattern with the ideal calculation result, and adjusted the applied pressure.

Following the production process mentioned above, the glass plates were pressed with a stress of 50 kg. Then we prepared two sets of bended glass plates which were fixed with adhesive. Even after releasing them from the jig, the curvatures of convex surfaces were kept. Thereafter they were polished flatly and relaxed from adhesive fixing at IK Technology Co. Currently they are in a process of forming a Mo/Si multilayer on their reflection surface at NTT Advanced Technology Corporation. The multilayer is suitable for reflecting soft X-rays. The mirrors will be tested in terms of their reflectivity and focusing performance.

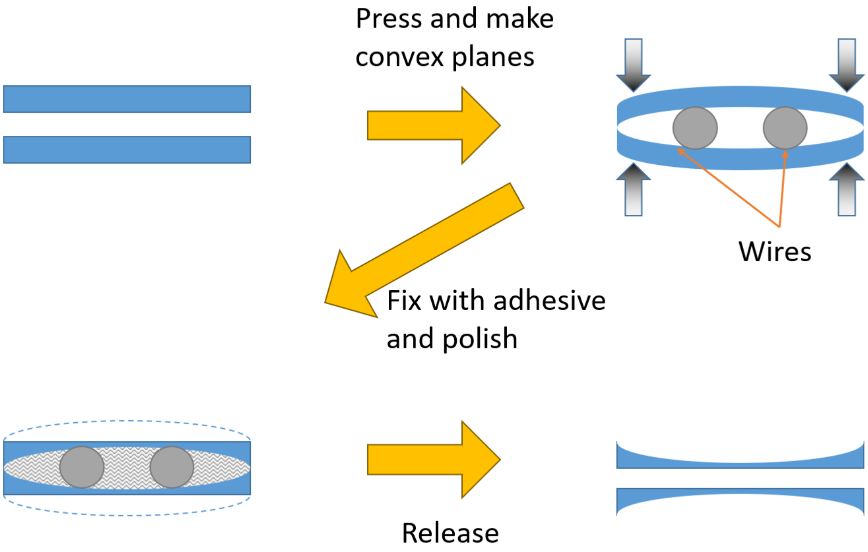

Fig.2.　Process to make concave curve

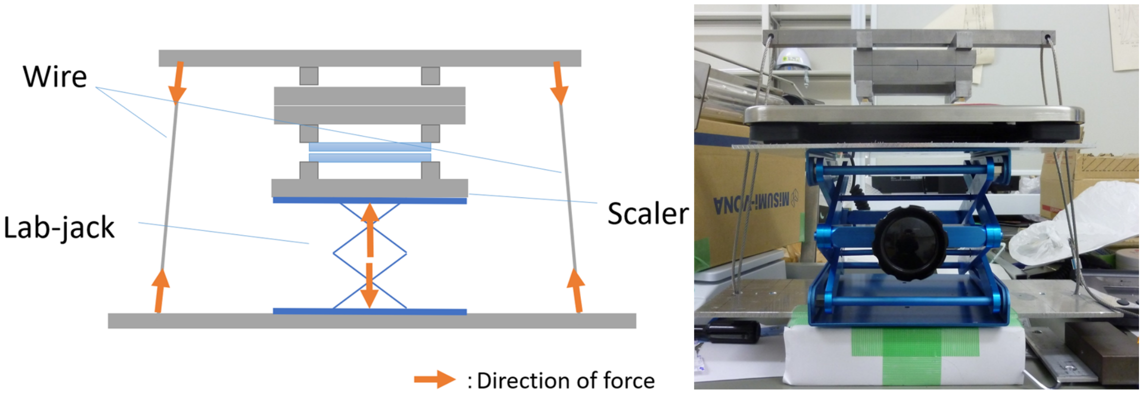

Fig.3.　Abstract (left) / concrete (right) picture of equipment

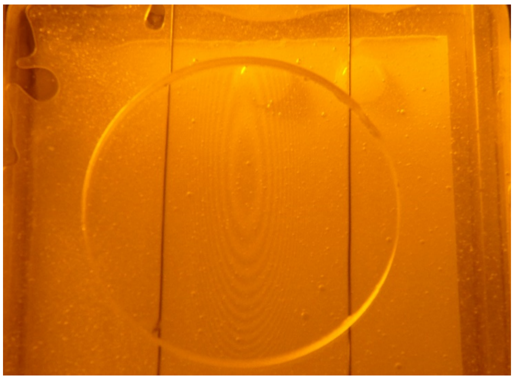

Fig.4.　Typical example of Newton fringe

(ELPH Experiment: #2887)

Phantom production for a multiple-isotope β-ray imaging system

T Fukuchi,[1] H. Haba,[2] and H. Kikunaga[3]

[1] RIKEN Center for Biosystems Dynamics Research, Kobe 650-0047, Japan
[2] RIKEN Nishina Center for Accelerator-Based Science, Wako, Saitama 351-0198, Japan
[3] Research Center for Electron Photon Science (ELPH), Tohoku University, Sendai 982-0826, Japan

We have been developing a new type of β-ray imaging system, which is useful for multiple tracers by detecting coincidence γ-rays with β-rays. To evaluate the performances of our developing systems, we produced an imaging phantom of β-γ emitter ^{22}Na. From a dual-isotope imaging using the produced phantom and a standard source, we can clearly separate each nuclide by absence or presence of the γ-ray coincidences.

§ 1. Introduction

Beta-ray imaging systems are widely used for various objects to obtain a 2-dimensional distribution of β-ray emitting radioisotopes. A conventional β-ray imaging system is unsuitable for multiple-tracer imaging, because the continuous energy distribution of β-rays makes it difficult to distinguish among different tracers by energy information. Accordingly, we have been developing a new type of β-ray imaging system, which is useful for multiple tracers by detecting coincidence γ-rays with β-rays.

Figure 1 shows a photograph of the developing β-ray imaging system. Our β-ray imaging system is composed of position-sensitive β-ray and γ-ray detectors. The β-ray detector is a 35×35×1-mm^3 Ce-Doped (La, Gd)$_2$Si$_2$O$_7$ (La-GPS) scintillation detector [1], which has a 300-µm pitch of pixels by grooving processing [2, 3]. The γ-ray detector is a 43×43×16-mm^3 bismuth germanium oxide (BGO) scintillation detector. In this system, the β-γ coincidence measurement can be performed in parallel with β-ray single measurement.

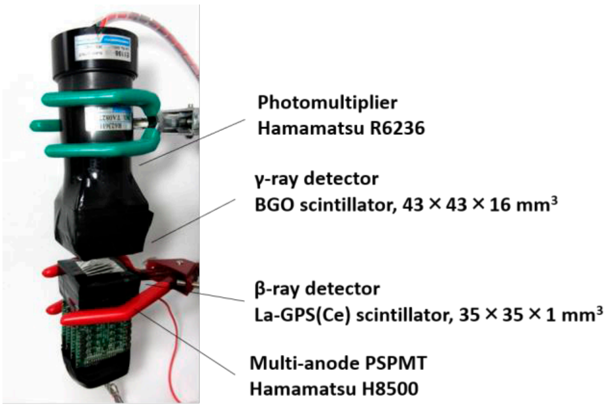

Fig. 1. Our developing β-ray imaging system with an additional γ-ray detector.

§ 2. Phantom production

In order to evaluate the performances of our system, it is necessary to perform the phantom imaging experiment, which visualize the already-known radio-tracer distributions. Therefore, we carried out production of a β-γ emitter ^{22}Na phantom. Sodium-22 is a positron-γ emitter with a half-life of 2.6 years and emits a prompt γ-ray with energy of 1275 keV.

We prepared a thin disk-shape target made of natural Mg (^{24}Mg isotope ratio: 79%) for production of imaging phantom. This has 8 mm in diameters and 0.5-mm thicknesses. The 3 hours high-energy photon irradiation was performed by the ELPH accelerator with electron energy of 50 MeV. Sodium-22 was produced by ^{24}Mg(γ, *pn*)^{22}Na reaction, and produced radioactivity of ^{22}Na is 2.85 kBq.

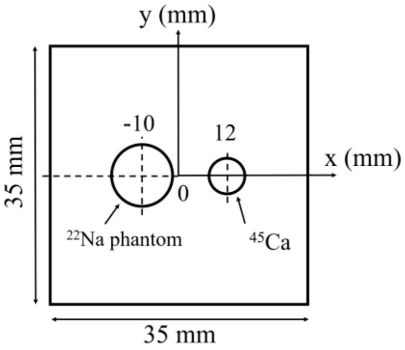

Fig. 2. Source positions for dual-isotope imaging of ^{22}Na and ^{45}Ca. Sources were allocated just on the surface of β-ray detector.

§ 3. Imaging experiment

To investigate the performance of multiple-isotope imaging, a measurement using produced ^{22}Na phantom and a standard source ^{45}Ca were carried out. The ^{45}Ca standard source has 5-mm diameter and an activity of 1.41 kBq. Sources placement for this measurement is shown in Fig. 2. The measurement was performed for 1 hour.

The reconstructed images from the single or coincidence data are shown in Fig. 3. We can clearly observe the ^{22}Na and ^{45}Ca phantoms in the image of the single data in Fig. 3 (a). While in the image from the coincidence data (Fig. 3(b)), we successfully extracted the isolated image of the ^{22}Na phantom.

In order to perform the multiple-tracer imaging for more practical objects, we are planning to produce phantom of different nuclides and more complicated structure in the future.

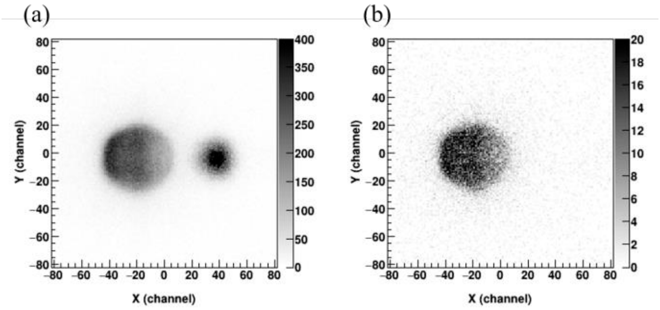

Fig. 3. Dual-isotope images ^{22}Na and ^{45}Ca) of β-ray single (a) and β-γ coincidence (b)

Acknowledgements

The authors thank to the facility staffs of ELPH in Tohoku University for supplying the high-quality electron beam. The authors thank Prof. Yamamoto for the development of the imaging devices. This work was supported by JSPS KAKENHI Grant Number JP15H04770.

References

[1] A. Yoshikawa *et al.*: Crys Grow and Des. 15 (2015) 1642.
[2] T. Oshima *et al.*: Nucl Inst and Meth A803 (2015) 8.
[3] S. Yamamoto *et al.*: Jour of Inst 13 (2018) P05028.

(ELPH Experiment : #2896)

Application of Single Comparator Method to Instrumental Photon Activation Analysis

M. S. Reza[1], R. Taniguchi[1], J. Kaneko[1], and Y. Oura[1]

[1]*Department of Chemistry, Tokyo Metropolitan University, Hachioji, 192-0397*

Single comparator method was applied to instrumental photon activation analysis. Various kinds of samples, mainly geochemical reference samples, were analyzed by IPAA using single comparator method and accuracy of detemined elemental concentrations was examined. For many elements, the determined values were consistent with literature values regardless of samples. Although systematic small deviations (-40 % - +50%) from literature values were observed for some elements, the accuracy of the determination by our single comparator method is generally concluded to be good.

§1. Introduction

An activation analysis is a multielemental nondestructive analytical methods and has high sensitivity. Popular activation analytical method is instrumental neutron activation analysis (INAA) using (n, γ) reaction induced by reactor neutrons. Instrumental photon activation analysis (IPAA) is one of activation analytical methods and uses mainly (γ, n) reaction induced by bremsstrahlung from an electron accelerator. Since IPAA uses different nuclear reactions with INAA, IPAA can determine some elements which INAA cannot determine and is a complementary method to INAA. However, radioactivities of radionuclides produced by (γ, n) reactions induced by bremsstrahlung are difficult to be estimated because suitable lists of their reaction yields for IPAA users are not available. So we have determined photonuclear reaction yields to estimate induced radioactivity for IPAA and relative reaction yields to ^{58}Ni(γ, n)^{57}Ni reaction were obtained for about 40 elements. Using our relative reaction yields, elemental concentartions are able to be determined by single comparator method, which is a method that elemental analysis is possible by comparison with one reference element for any elements. Single comparator method is not so popular in IPAA and relative method, which requires reference elements for all elements to be determined, is usually used to determine. So single comparator method was applied to IPAA for various samples and an accuracy of the determination by single comparator method was examined. This mehod is expected to be easy to use for users who are not familiar with activation analysis.

§2. Experimental

Four geochemical reference samples (JB-1a, JSO-2, JZn-1, JCu-1) issued by Geological Survey of Japan (GSJ), two alloys (german silver, stainless steel) and three metals (cobalt, copper, zinc) were subjected to analysis. About 50 - 70 mg of each powdered sample was taken into a container (10 mmϕ)

made of high purity Al foil and it was pressed to make tablet. Several tablets were prepared for each kind of sample. All samples were put into a quartz tube together with Ni foils(10 mmϕ), which were placed at every three or four samples.

Two sets of samples placed in quartz tubes were irradiated for ca. 30 minutes and for ca. 6 hours, respectively, by bremsstrahlung of maximum end point energy (E_0) of 20 , 25, and 30 MeV from the electron linac of the Research Center for Electron Photon Science (ELPH), Tohoku University. After irradiation, produced radionuclides with shorter half-lives in irradiated samples were measured for γ-rays using HPGe detector at the ELPH as soon as possible. But for long irradiated samples, measurements were executed at the laboratory of radioisotopes, Tokyo Metropolitan University to detect radionuclides with longer half-life.

Elemental concentrations were determined by both relative method and single comparator method. In relative method, concentrations were calculated by comparison between radioactivity in the sample and one in JB-1a or metal samples. For single comparator method, Ni is the comparator and concentrations (C) were calculated with eq.(1) ;

$$C = \frac{A_x}{A_{Ni}/w_{Ni}} \times \frac{M_x}{M_{Ni}} \div \frac{r_x}{r_{Ni}} \div \frac{Y_x}{Y_{Ni}} \div \frac{1-e^{-\lambda_x t}}{1-e^{-\lambda_{Ni} t}} \div W \times 100 \quad (1)$$

where, C is elemental concentration in %, A is induced radioactivity, w is mass of element, M is atomic weight, r is isotopic abundance, Y is reaction yield, λ is decay constant, t is irradiation time, and W is mass of sample. Subfixs, x and Ni, show the parameter for a sample and Ni monitor, respectively. Yield ratio, Y_x/Y_{Ni}, determined for about 40 elements by our group [1] was used. Specific activity of ^{57}Ni, A_{Ni}/w_{Ni}, in Ni monitors placed at every a few samples in the quartz tube decreased exponentially against integrated sample mass [2]. Specific activity of ^{57}Ni for each sample was calculated by least square method.

§3. Results and Discussion

In this report, the results for irradiation by E_0 = 20 MeV were reported.

Four samples and two samples were irradiated for JB-1a and the other samples, respectively. Determined concentrations were consistent within their uncertainties among four samples or between two samples. Therefore, correction with Ni monitors for flux variation among irradiated samples in the quartz tube was concluded to be success. And reproducibility of determination by our single comparator method is good.

Determined elemental concentrations in geochemical reference samples and alloys by the single comparator method were compared with literature values [3, 4] and concentrations determined by the relative method, respectively. For example, the ratios of determined concentration value to lirerature value for some elements are shown in Figs.1 - 6. Determination values of Fe, Na, Ni, Rb, Y and Zr were consistent with literature values within ± 10% for all samples. Calcium concentrations were determined by using both ^{48}Ca (γ, n)^{47}Ca and ^{44}Ca(γ, p)^{43}K reactions. Determined concentrations by ^{44}Ca(γ, p)^{43}K reaction were consistent with literature values within ± 10% for all samples. On the other hand, concentrations determined by ^{48}Ca (γ, n)^{47}Ca reaction were systematically about 1.5 times higher than literature values for all samples (Fig.1). For Ce, Co, Cu, Mn, Sb, Sr and Zn, the ratios were generally more than 1.1 and the ratios were generally less than 0.9 for titanium. Especially, the ratios for Cr and Nb were systematically higher than 1.1, about 1.3 in average. And Ti concentrations for four JB-1a samples are not consistent. Although systematic deviations of concentrations were obtained by the single comparator method for some elements, their concentrations detemined by the relative method were consistent with literature values. This consistensy means that induced radioactivity in samples were produced in proportion to the elemental mass and the correction for the flux variation by our method using Ni monitors were right. Thus yield ratio values, Y_x/Y_{Ni}, used in calculation with eq.1 for some elements were possibly guessed not to be reasonable and to cause such systematic deviations in the determination by the single comparator method. So, yield ratios for concerned elements will be reexamined.

Although the determination value by our single comparator method has a small systematic deviation for some elements at this time, it is concluded that the application of the single comparator method to IPAA is fundamentally success and our determined yield ratios are reasonable because determined concentration values by the single comparator method were consistent with literature values or values by the relative method by -40% to +50% for all elements and for all samples.

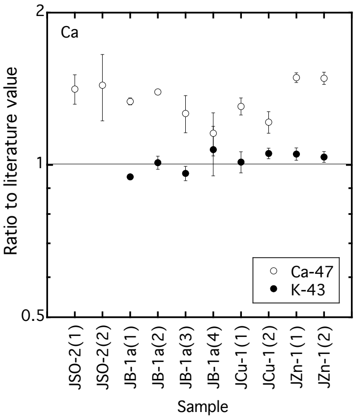

Fig.1. Comparison of the determined concentration values with the literature values for Ca. Calcium concentrations were determined by using ^{47}Ca and ^{43}K produced by (γ, n) and (γ, p) reactions, respectively.

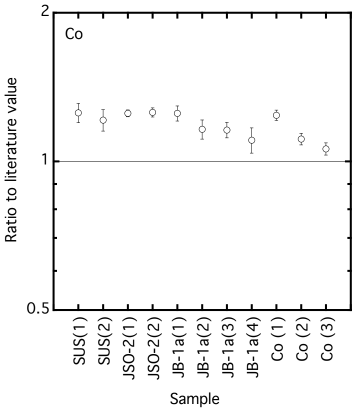

Fig.2. Comparison of the determined concentration values with the literature values for Co.

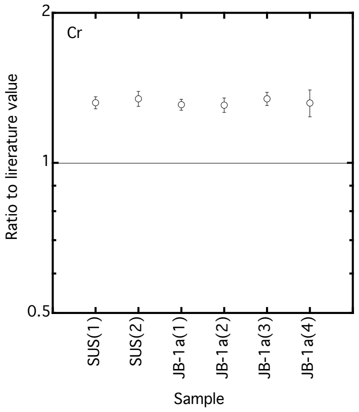

Fig.3. Comparison of the determined concentration values with the literature values for Cr.

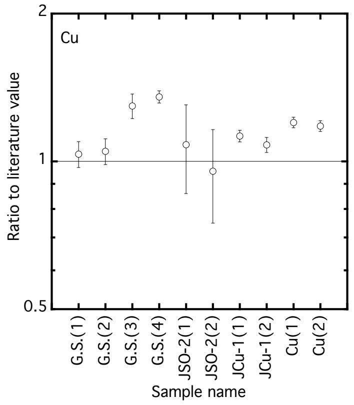

Fig.4. Comparison of the determined concentration values with the literature values for Cu. G.S. means german silver alloy.

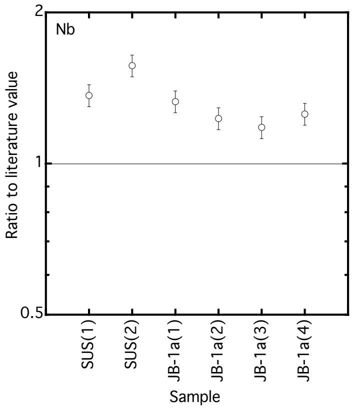

Fig.5. Comparison of the determined concentration values with the literature values for Nb.

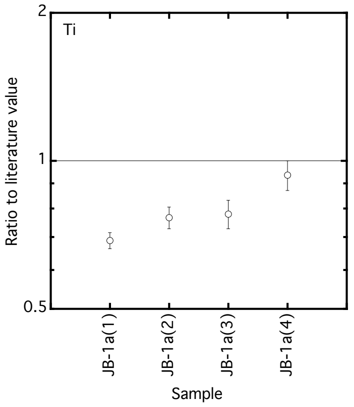

Fig.6. Comparison of the determined concentration values with the literature values for Ti.

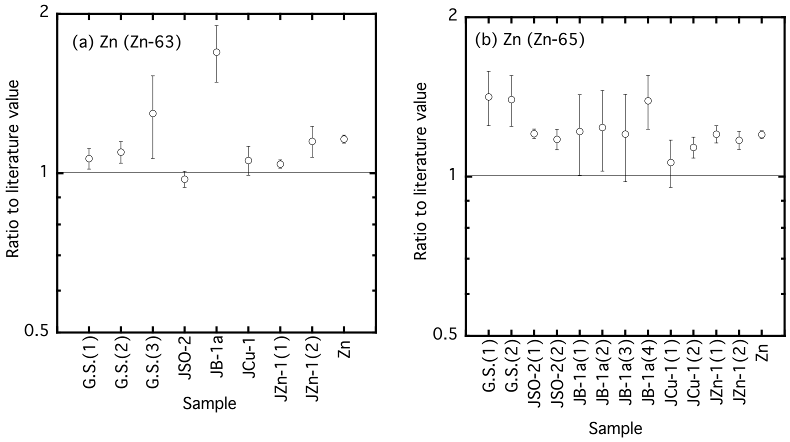

Fig.7. Comparison of the determined concentration values with the literature values for Zn. (a) ^{63}Zn and (b)^{65}Zn. G.S. means german silver alloy.

Acknowledgment

The authors are indebted to Drs. H. Kikunaga and K. Tsukada, and the operation crew members of ELPH for their invaluable cooperation and providing excellent beams.

References

[1] Y. Oura *et al.*: ELPH Annual report (2017) .

[2] M. Ebihara *et al.*: J. Radioanal. Nucl. Chem. **244** (2000) 491.

[3] N. Imai *et al.*: Geostandards Newsletter **19** (1995) 135.

[4] S. Okai *et al.*: Bunseki Kagaku **51** (2002) 973.

(ELPH Experiment : #2898, #2906)

Identification of Elemental Composition and Preparation of Radio-tracer for Recovery of Rare Metals in Household Garbage Incineration Slag by Photon Activation Method 2.

K. Akiyama[1,**], K. Takano[1], H. Sugiyama[1], Ahmed S. A. Ali[1], K. Irfan[1],
S. Kubuki[1], and H. Kikunaga[2]

[1] *Department of Chemistry, Tokyo Metropolitan University, Hachioji, Tokyo 192-0397*
[2] *Research Center for Electron Photon Science, Tohoku University, Sendai, 982-0826*

The composition of the household garbage incineration slag for each month among a year is determined by photon activation method. The homogeneity in the elemental composition among identical samples is found to be within 40% in relative standard deviation. The contents of the elements for each slag sample among a year is found to be slmost constant. Surprisingly, the contents of **Cu** is found to be almost same as that of **Cu** in a chalcopyrite which is the one of the major resource of copper ore.

§1. Introduction

Amount of burnable garbage emitted from households is estimated to be about 650 million tons annually in OECD member countries, and also in japan it is estimated to be about 50 million tons per year [1]. Although these garbage are usually incinerated and then buried as incineration ashes, there are same problems, such as securing the site for the burial disposal, because the emissions of these incineration ashes are enormous. In Tokyo, it is attempted for the improvement of the site problems to reduce of volume by melting and vitrifying of incineration ash and also to reuse these vitrified ash as the roadbed materials, the concrete aggregate, and the agent for the soil improvement. [2]

Kubuki and co-workers reported the chemical composition of vitrified ash of incinerated household garbage (incinerated slag) by induced coupled plasma optical emission spectroscopy (ICP-OES) measurements of their nitric acid solution and also the similarity of their composition with aluminosilicate including iron [3]. It is known that the vitrified solids of aluminosilicate indicate the decomposing ability of organic materials under the light irradiation [4]. If the incinerated slag of similar chemical composition with aluminosilicate indicates the decomposing ability of organic materials, it is possible to use the incinerated slag for the environmental purification, such as water purification, it could be expected as the new effective way to use of incinerated slag. However, incinerated slag contains many impurities, unlike aluminosilicate glass synthesized from the reagents. Since the impurities in incinerated slag include valuable metal elements such as cobalt and manganese, if it is possible to recover these elements by chemical separation, it will lead to effective use of waste so called ”Urban mine” and also to a solution

---

[*] Correspondence Address: Department of Chemistry, Tokyo Metropolitan University, Hachioji, Tokyo 192-0397

to the universal theme in the contemporary society.

In this study, we aim to recover valuable metal elements from incinerated slag and to develop the recovery method by chemical separation. In this paper, we report the validity of chemical composition in incinerated slag per collecting month in 2018 quantified by photon activation method.

§2. Experimental

Approximately 100 **mg** of incinerated slag collected in January to December, 2018, were powdered with a handy agate mill. These powdered slag were wrapped in high purity aluminum foil, and then sealed under reduced pressure in a quartz tube for the irradiation with bremsstrahlung. we used JB-1a, whose elemental composition is quantitatively well assigned in National Institute of Advanced Industrial Science and Technology (AIST) Geological Survey of Japan, and some elemental standard dropped and dried on a metal foil as the comparative standard for the photon activation analysis. Irradiation with Bremsstrahlung was carried out at Tohoku University, Research Center for Electron Photon Science (ELPH) under the conditions of maximum electron beam energy of 20 **MeV**, 0.1 **mA**. After that, γ ray emitted from samples were measured with a high purity **Ge** semiconductor detector (SEIKO EG&G).

§3. Results and Discussion

3.1 Homogeneity in the elemental composition among identical samples

In the previous report, we could not have determined some elements because these elements were basically absent in the JB-1a used as the comparative standard [5]. To improve this situation, it is important to find more optimal standard for this analysis. It can be said to be an effective improvement to employ a slag sample that has already been quantified for a candidate of a comparative standard material. However, such a slag sample cannot be used for the standard if the homogeneity of the sample is not guaranteed. For such reason, we individually prepared and irradiated the slag1709 sample for each beam time. Table 1 shows the average contents of each element and their relative standard deviation of slag1709 sample.

Table 1. Average composition and their relative standard deviation (RSD) of slag1709

Element	Contents g/g	RSD	JB-1a g/g	Element	Contents g/g	RSD	JB-1a g/g
Ca	1.980.E-01	16.4%	6.65.E-02	**Ni**	5.3E-05	40.0%	1.39E-04
Fe	6.94.E-02	16.2%	6.33.E-02	**Co**	3.89E-05	8.0%	3.86E-05
Na	2.26.E-02	9.9%	2.03.E-02	**Ce**	3.01E-05	17.1%	6.59E-05
Mg	1.82.E-02	11.9%	4.72.E-02	**Nb**	2.33E-05	11.6%	2.69E-05
Ti	1.37.E-02	11.3%	7.7.E-03	**Y**	1.62E-05	12.2%	2.4E-05
Cu*	2.8.E-03	23.2%	5.67.E-05	**Rb**	9.65E-06	9.3%	3.92E-05
Mn	2.38.E-03	10.7%	1.15.E-03	**Mo**	1.57E-05	34.1%	1.57E-06
Ba	1.39.E-03	20.5%	5.04.E-04	**Sc**	5.6E-06	13.8%	2.79E-05
Cr	1.3.E-03	7.2%	3.92.E-04	**Sb**	3.1E-06	26.1%	2.5E-07
Zn	1.1.E-03	37.8%	8.21.E-05	**Cs**	5.3E-07	29.6%	1.31E-06
Sr	5.66.E-03	11.2%	4.42.E-04	**Au***	1.858E-07		7.1E-10
Zr	1.63.E-04	10.8%	1.44.E-04				

The determined value of astarisk marked elements was basically quantified not from JB-1a but from the comparation of solution standard because the contents of these elements in JB-1a were not enough for the quantitation by photon activation alanysis. The contents of **Au** is found to be not homogeneous because γ-ray peak of ^{196}**Au**, which is used for the determinatin of **Au**, is sometimes absent in the obtained γ-ray spectra of this slag samples. Except for these element, there are some elements whose contents is difficult to determine, such as **Mo**, and **Sb**, becouse of their contents in JB-1a being extremely lower than those in Slag samples. For the use of this slag sample for the comparative standard, it is found that it is required to quantitate the amount of these elements precisely.

3.2 Variation in composition of slag during a year

Figure 1 shows the contents of each element determined by photon activation analysis (PAA) dureling a year. The contents of some elements, such as **Ce**, **Mo**, and **Au**, are found to be dispersed but those of other elements are basically almost constant. From the view point of resource recovery, it is desirable that the amount of the elements is stablely constant in slag. Surprisingly, contents of **Cu** is found to be almost same as that of **Cu** in a chalcopyrite which is the one of the major resource of copper ore. In addition, it is found that The contents of **Mo** and **Au** are exceeded the abundance in the earth's crust of these elements. Considering about the availability of resources, Household garbage incineration slag may be a useful resource as an urban mine in the future.

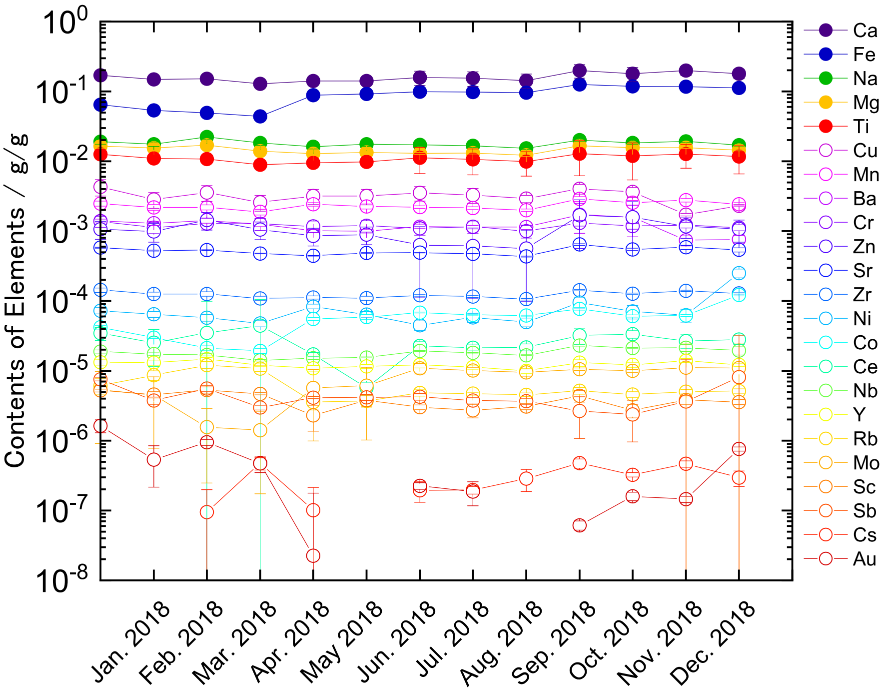

Fig.1. Contents of each element determined by PAA for each month.

Acknowledgment

We deeply thank to the facility staffs of research center for electron photon science at Tohoku University for supplying the high-quality electron beam. And also we thank to Doctor Kyo Tsukada for helping us in the sample irradiation. This work was supported by Tokyo Metropolitan Government Advanced Research Grant Number (H29-1).

References

[1] OECD, “ Municipal Waste ” , in *OECD Factbook 2015-2016: Economic, Environmental and Social Statistics*, OECD Publishing. DOI: 10.1787/factbook-2015-en (2016).

[2] Waste Report ed. Clean Authority of Tokyo, (2018) vol. 23, p. 7.

[3] S. Ishikawa, B. Kobzi, K. Sunakawa, S. Nemeth, A. Lengyel, E. Kuzmann, Z. Homonnay, T. Nishida, S. Kubuki, Pure Appl. Chem., **89**, 535 (2017).

[4] Y. Iida, K. Akiyama, B. Kobzi, K. Sinkó, Z. Homonnay, E. Kuzmann, M. Ristić, S. Krehula, T. Nishida, S. Kubuki, J. Alloys Compd., **645**, 1 (2015).

[5] K. Akiyama, K. Ito, S. Kubuki, H. Kikunaga, ELPH Annual Report (2017) 117.

(ELPH Experiment : #2904)

Development of simultaneous production method for carrier-free RI multitracer of potassium, rubidium and cesium

H. Ikeda[1,2*], H. Kikunaga[2], and H. Watabe[1]

[1]*Cyclotron and Radioisotope Center, Tohoku University, Sendai, 980-8578*
[2]*Research Center for Electron Photon Science, Tohoku University, Sendai, 982-0826*

We developed a method for producing carrier-free RI tracers of potassium, rubidium, and cesium using photonuclear reactions with an electron linear accelerator in the Research Center for Electron Photon Science (ELPH), Tohoku University. And these RIs have been supplied to researchers in Japan. In this study, our purpose was the development of simultaneous production method for the carrier-free RI multitracer mixed potassium, rubidium and cesium.

The radioisotopes of potassium, rubidium and cesium were produced by irradiating bremsstrahlung, which was generated by an electron linear accelerator of ELPH, to calcium oxide, strontium oxide and barium oxide. After mixing the three irradiated targets, the radioisotopes of the alkali metals were separated from the target materials by an oxalate precipitation method, and were purified by cation exchange column chromatography. The yield of radioisotopes in the precipitation method and column chromatography was determined by gamma spectrometry using a high purity germanium detector.

We demonstrated that carrier-free RI multitracer of potassium, rubidium and cesium can be purified by chemical separation simultaneously. The yield of chemical separation was about 85-90% for each alkali metal tracer. The loss of them was mostly due to the precipitation method.

§1. Introduction

The behavior of alkali metal elements, sodium (Na), potassium (K), rubidium (Rb) and cesium (Cs) in plants have been interested. Especially, K is an essential plant element, and demand for ^{42}K ($T_{1/2}$ = 12.4 h) and ^{43}K ($T_{1/2}$ = 22.3 h) is increasing as its radioisotope (RI) tracer. However, RIs of K cannot be purchased because they are short-lived nuclides with half-lives of less than 1 day, except for ^{40}K ($T_{1/2} = 1.28 \times 10^9$ y). We developed that production method of ^{42,43}K tracers by bremsstrahlung irradiation of ^{nat}CaO target using electron linear accelerator of Research Center for Electron Photon Science (ELPH), Tohoku University. A method of chemical separation of carrier-free K tracers from the target was reported (Fig. 1) [1]. On the other hand, Na, Rb and Cs are available for purchase however are very expensive. We have also developed of production for carrier-free RI tracer of Rb and Cs by the similar method from K tracer. If they can be produced and separated at the same time as K, experiments

---

[*] Cyclotron and Radioisotope Center, Tohoku University, Sendai, 980-8578

with three elements can be performed simultaneously. This is expected to make the studies of element dynamics in plants more efficient.

In this study, we researched the production possibility of a mixed sample of K, Rb, and Cs as a multitracer of alkali metal elements. Since each element has similar properties, it is reasonable to perform chemical operations at the same time. It needs to investigate the radioactivity of Rb and Cs tracers produced by the similar method to production of ^{42,43}K tracers. Rb and Cs tracers were produced by bremsstrahlung irradiation with ^{nat}SrO and ^{nat}BaO, respectively. The conditions of chemical separation were researched by the method improved (Fig. 1) [1]. The RIs measured were ^{42}K ($T_{1/2}$ = 12.4 h), ^{43}K ($T_{1/2}$ = 22.3 h), ^{83}Rb ($T_{1/2}$ = 86.2 d), ^{84}Rb ($T_{1/2}$ = 32.8 d), ^{86}Rb ($T_{1/2}$ = 18.6 d), ^{132}Cs ($T_{1/2}$ = 6.48 d) and ^{136}Cs ($T_{1/2}$ = 13.2 d).

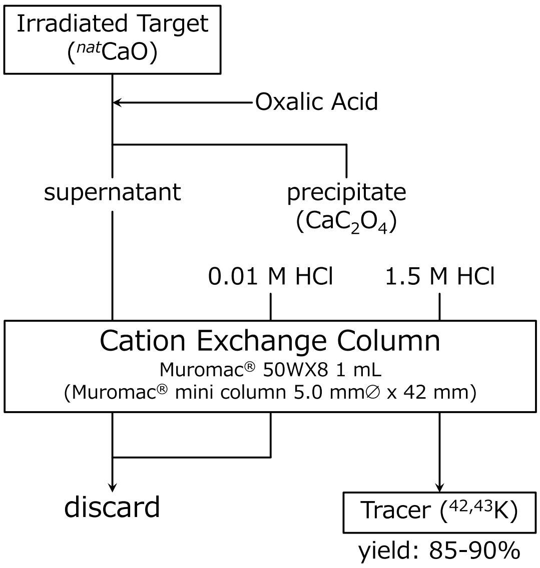

Fig.1. Chemical procedure for the preparation of carrier-free ^{42,43}K tracer. ^{nat}CaO was added water and oxalic acid, and Ca^{2+} is precipitated as calcium oxalate (CaC_2O_4). The supernatant is charged into the cation exchange column (1 mL). The column is flushed by 10 mL of 0.01 M HCl to remove impurities. It is flushed 10 mL of 1.5 M HCl, and K tracer is eluted.

§2. Experiment

Powdered ^{nat}CaO, ^{nat}SrO or ^{nat}BaO were pressed into pellets. The pellets and nickel (Ni) foils were sealed in a T-shaped quartz tube replaced with helium gas. The component of sealed pellets was oxide of a single element. This tube was irradiated in the #1 Experiment Room of ELPH. The target tube behind the three of 1 mm thickness tantalum plates was irradiated by electron beam while cooling with water. The energy of electron beam was 50 MeV, beam current was 20 μA, and irradiation time was 30 minutes.

The radioactivity of alkali metals, ^{42}K, ^{43}K, ^{83}Rb, ^{84}Rb, ^{86}Rb, ^{132}Cs and ^{136}Cs, in the targets and solutions were measured by a high purity germanium detector. ^{47}Ca ($T_{1/2}$ = 4.54 d), ^{83}Sr ($T_{1/2}$ = 32.4 h) and ^{135m}Ba ($T_{1/2}$ = 28.7 h) produced simultaneously with alkali metal RIs were also measured. In addition,

^{57}Ni ($T_{1/2}$ = 35.6 h) produced by irradiation of Ni foils were measured for correction of radioactivity of alkali metals [1, 2].

The pellets of ^{nat}CaO, ^{nat}SrO and ^{nat}BaO were placed into the same tube, and water was added. The aqueous solution of oxalic acid ($H_2C_2O_4$) was added to precipitate as oxalate salts (CaC_2O_4, SrC_2O_4 and BaC_2O_4). The supernatant was charged onto a cation exchange column. The eluent was concentrated hydrochloric acid (conc. HCl), and the elution curve was drawn. Muromac® 50WX8 100-200 mesh was used as a cation exchange resin. 2 mL of the resin was filled into the Muromac® Mini-column (size M). This column was flushed with 20 mL of H_2O, 20 mL of conc. HCl 20 mL and 20 mL of 0.01 M HCl in a sequential order for conditioning.

§3. Results

Table 1 shows the productions of ^{42,43}K, ^{83,84,86}Rb, and ^{132,136}Cs corrected by the radioactivity of ^{57}Ni in the Ni foils. From this data, about 620 mg of ^{nat}CaO is required to produce 10 MBq of ^{43}K if the electron beam conditions are 50 MeV and 120 μA. Similarly, we found that about 400 mg of ^{nat}SrO was required to produce 1 MBq of ^{86}Rb, and about 740 mg of ^{nat}BaO was needed to produce 1 MBq of ^{136}Cs. Table 2 shows the radioactivity of alkali metal RIs co-precipitated in oxalate. Every RI showed a loss of about 10-15%. When purifying the alkali metal tracer by our proposed method, it should be noted that the yields of the alkali metal RIs in supernatant are 85-90%. The elution curve is shown in Fig. 2. Almost all alkali metals were eluted in about 2 column volumes. No radioactivity of alkaline earth metal RI (^{47}Ca, ^{83}Sr and ^{135m}Ba) was observed in the eluent. Thus, a method for chemical separation of three alkali metal RIs (^{42,43}K, ^{83,84,86}Rb and ^{132,136}Cs) has been established.

Table 1. Prodution yields of alkali metal RIs.

RI	Yield (Bq/mg/μA/h)
^{42}K	21.0 ± 2.3
^{43}K	45.1 ± 4.2
^{83}Rb	0.582 ± 0.109
^{84}Rb	0.498 ± 0.034
^{86}Rb	6.93 ± 0.91
^{132}Cs	0.362 ± 0.112
^{136}Cs	3.77 ± 0.93

Table 2. Co-precipitated ratios of alkali metals RIs.

RI	co-precipitated (%)
^{42}K	11.9 ± 1.0
^{43}K	14.6 ± 1.6
^{83}Rb	12.3 ± 8.0
^{84}Rb	14.3 ± 5.2
^{86}Rb	15.6 ± 3.2
^{132}Cs	12.8 ± 5.5
^{136}Cs	9.0 ± 2.6

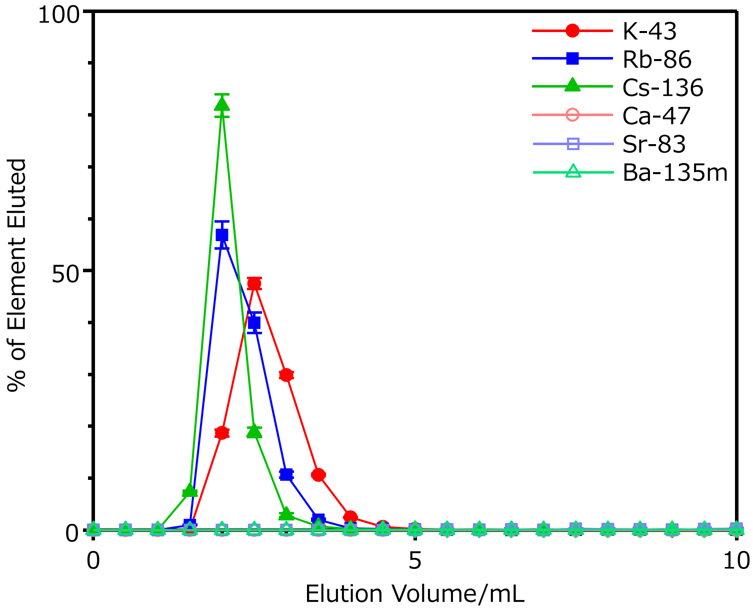

Fig.2. Elution curves of cation exchange chromatography for alkali metals (^{43}K, ^{86}Rb and ^{136}Cs) and target elements (^{47}Ca, ^{83}Sr and ^{135m}Ba). Conc. HCl was used for eluent. 100% is the total radioactivity in the charged solution.

References

[1] H. Kikunaga *et al.*: ELPH Annual Report (2015) 105.

[2] H. Kikunaga *et al.*: ELPH Annual Report (2014) 144.

(ELPH Experiment : #2914)

Investigation of optimal thicknesses of W converters in electron linac production of ^{99}Mo

Jaewoong Jang[1], Hidetoshi Kikunaga[2], Shun Sekimoto[3], Makoto Inagaki[3],
Tomohiko Kawakami[4], Tsutomu Ohtsuki[3], Shigeru Kashiwagi[2],
Ken Takahashi[2], Kyo Tsukada[2], and Mitsuru Uesaka[1,5]

[1]*Department of Bioengineering, University of Tokyo, Bunkyo, Tokyo 113-8656, Japan*
[2]*Research Center for Electron Photon Science (ELPH), Tohoku University, Sendai, Miyagi 982-0826, Japan*
[3]*Institute for Integrated Radiation and Nuclear Science, Kyoto University (KURNS), Sennan, Osaka 590-0494, Japan*
[4]*Kaken Inc., Mito, Ibaraki 310-0903, Japan*
[5]*Nuclear Professional School, University of Tokyo, Naka, Ibaraki 319-1188, Japan*

Increasing the specific yield of ^{99}Mo is one of the most important tasks in realizing accelerator production of ^{99}Mo. In this study, we attempt to increase the specific yield of ^{99}Mo through adjusting the thicknesses of tungsten converters. A series of Monte Carlo simulations was performed, and the results were validated by irradiation experiments.

§1. Introduction

Technetium-99m ($^{99\text{m}}$Tc), the most widely used radionuclide in nuclear medicine, is obtained through generation from the decay of molybdenum-99 (^{99}Mo). For decades, ^{99}Mo has been produced via the fission of enriched uranium-235 (^{235}U) in research reactors. As most of the ^{99}Mo production reactors will need to shut down in about 10 years (Fig. 1 [1]), alternative methods of ^{99}Mo/$^{99\text{m}}$Tc production need to be developed. A promising alternative is to produce ^{99}Mo via the ^{100}Mo(γ,n)^{99}Mo reaction, where the high-energy photons (γ) are generated using an electron linear accelerator (linac).

One of the key issues in electron linac production of ^{99}Mo is to increase the yield and specific yield of ^{99}Mo. Several approaches are available, among which adjusting the thickness of tungsten (W) converters is relatively simple and practical. In order to investigate such optimal W thicknesses, we performed Monte Carlo (MC) simulations and experimentally validated the calculation results.

§2. Calculation

2.1 Theory

The production yield of ^{99}Mo can be expressed as [2]

$$Y_{\text{Mo-99}}(t_{\text{irr}}) = [1-\exp(-\lambda_{\text{Mo-99}} t_{\text{irr}})]\, \mathcal{V}_{\text{Mo-tar}}\, \rho_{\text{Mo-100}}\, I_{\text{e}^-} \int_{E_{\gamma,\text{th}}}^{\infty} \Phi_{\text{Mo-tar}}(E_\gamma)\, \sigma(E_\gamma)\, \mathrm{d}E_\gamma, \tag{1}$$

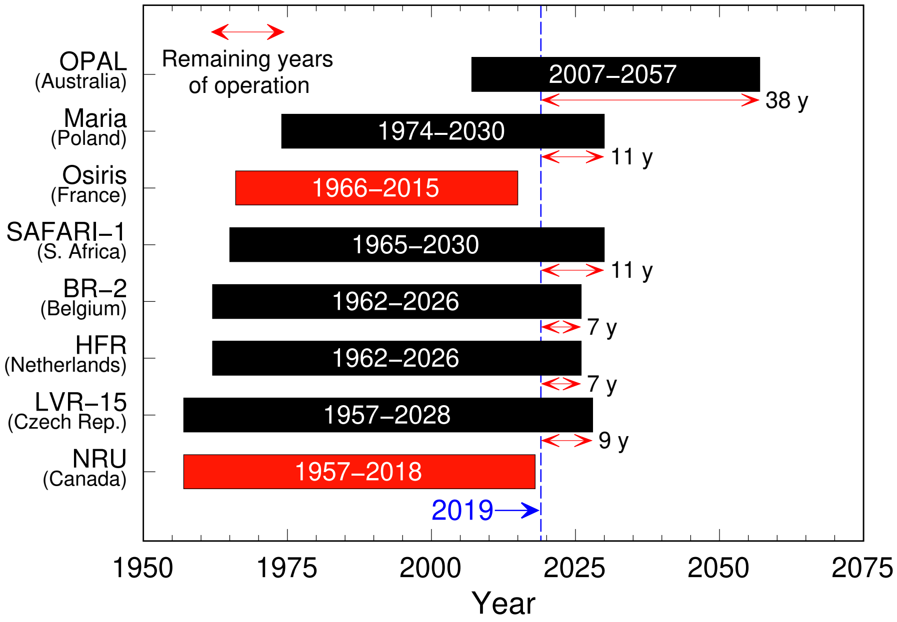

Fig.1. Operation years of ^{99}Mo production reactors

where $\lambda_{\text{Mo-99}}$ is the decay constant of ^{99}Mo, t_{irr} the irradiation time, $\mathcal{V}_{\text{Mo-tar}}$ the volume of a Mo target, $\rho_{\text{Mo-100}}$ the mass density of ^{100}Mo, I_{e^-} the electron beam current, $E_\gamma = E_\gamma(E_{\text{e}^-})$ the photon beam energy, $\Phi_{\text{Mo-tar}}(E_\gamma)$ the photon fluence in the Mo target, and $\sigma(E_\gamma)$ the excitation function for the ^{100}Mo(γ,n)^{99}Mo reaction. Eq. (1) shows that by increasing $\Phi_{\text{Mo-tar}}(E_\gamma)$, the ^{99}Mo yield can be increased without having to change beam parameters and irradiation conditions. In this study, we attempt to increase $\Phi_{\text{Mo-tar}}(E_\gamma)$ by adjusting the W converter thicknesses.

2.2 Parametric simulations

2.2.1 Initial simulation runs

To simulate various W thicknesses with different beam energies, MC simulations were performed using `PHITS` v3.02 [3] and `EGS5`, with `phitar` [4] used as the frontend program. `phitar` is a `PHITS` wrapper program that we developed to perform multivariate simulations [5]. The simulation conditions were as follows.

- Electron beam size: 4.5 mm in full width at half maximum (FWHM), Gaussian
- Electron beam energy: 20–50 MeV, monoenergetic
- W thickness: 1.0–7.0 mm
- MoO_3 target: 5 mm in thickness and 10 mm in diameter
- Distance between W and MoO_3: 13 mm

Some of the photon tracks calculated for $E_{\text{e}^-} = 50$ MeV are shown in Fig. 2 and Fig. 3 [5]. Based on the simulation results, we conducted irradiation experiments using the high-intensity electron linac at the Research Center for Electron Photon Science (ELPH), Tohoku University.

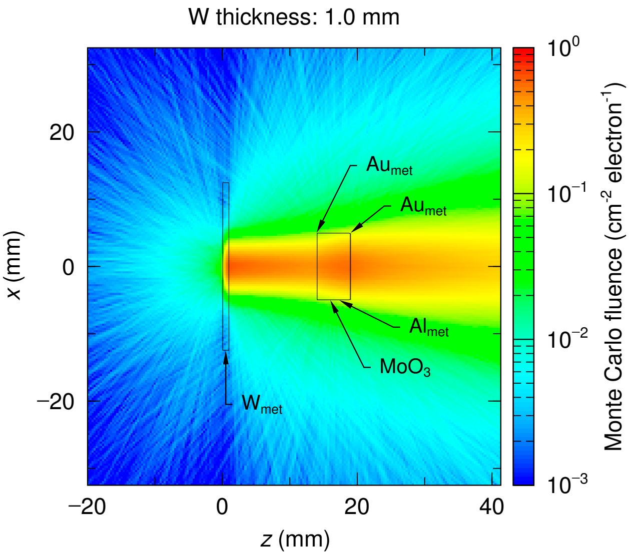

Fig.2. Photon tracks calculated for a 1-mm W converter

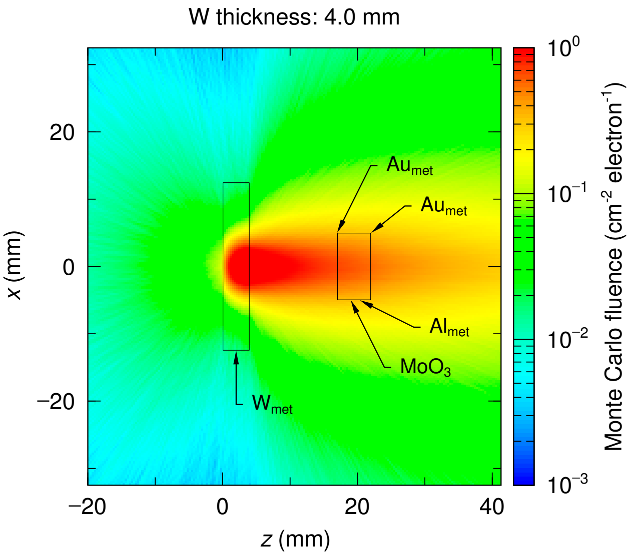

Fig.3. Photon tracks calculated for a 4-mm W converter

2.2.2 Simulation reruns

The dimensions of targetry materials and beam sizes used in experiments differed from the conditions explained above. Therefore, we performed again MC simulations, now with respect to the actual experimental conditions.

§3. Experimental

3.1 Outline

For respective electron beam energies out of 20, 35, and 50 MeV, three W converters having different thicknesses were investigated. A set of a MoO_3 target and Au foils was placed at the downstream side of a W converter for each irradiation run (Fig. 4(C)). In this targetry configuration, the W thickness at which the greatest ^{99}Mo and ^{196}Au activities are induced can be considered the optimal W thickness for the beam energy in question.

3.2 Materials

W plates having nominal thicknesses of 0.5–2 mm and Au foils of 50 μm in thickness were purchased (Nilaco Corp., Japan). W thicknesses were adjusted by combining the W plates of different thicknesses.

On the other hand, we directly prepared MoO_3 targets by sintering nonenriched MoO_3 powder (Kojundo Chemical Laboratory Co., Ltd., Japan) using a pulsed electric current sintering (PECS) machine (SPS1050, Izumi Technology, Japan).

Finally, the MoO_3 targets and pairs of Au foils were wrapped with 12-μm thick aluminum foils. These target materials were then placed on an order-made target holder. The target holder was designed such that the W thickness can be adjusted (Fig. 4(C)).

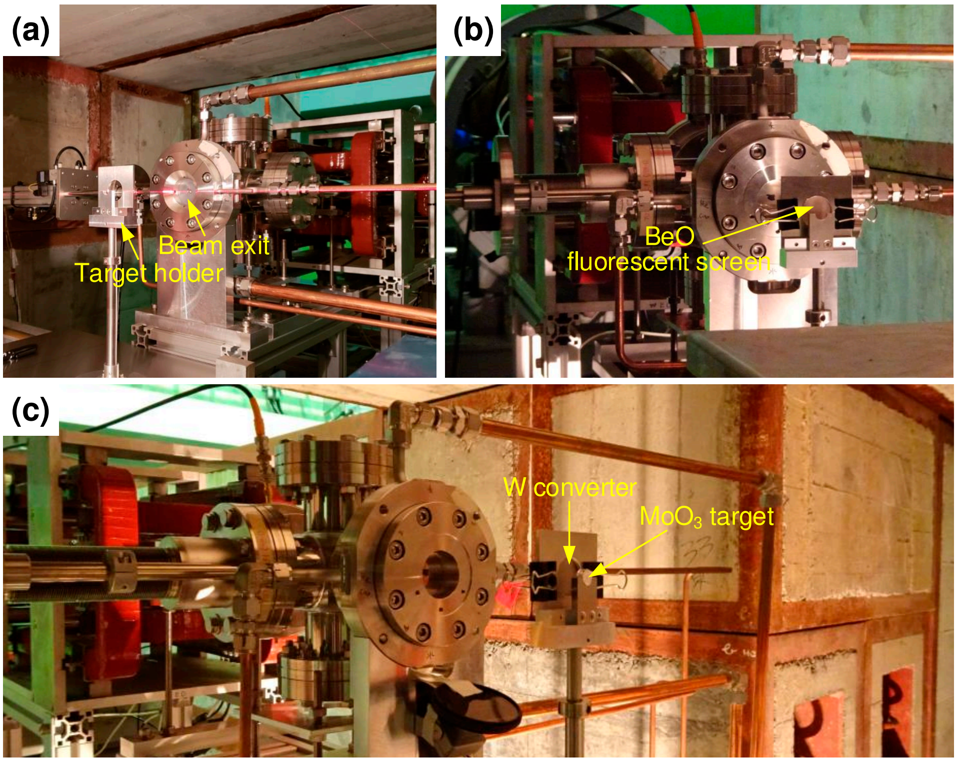

Fig.4. (a) Adjusting the position of target holder using laser. (b) Adjusting the irradiation center using a BeO fluorescent screen. (c) Targetry set up for irradiation

3.3 Irradiation and gamma-ray spectrometry

The W converters were irradiated with electron beams of 20, 35, and 50 MeV. The detailed irradiation conditions are summarized in Table 1 [5].

After the irradiation, the ^{99}Mo and ^{196}Au activities were measured using germanium detectors. The MoO_3 targets were dissolved in 6-*M* NaOH(aq) prior to the gamma-ray spectrometry. On the other hand, no preprocessing was performed on the Au foils. The units of the measured activities were adjusted to kBq g^{-1} μA^{-1}, so that the different target masses and different beam currents (Table 1) do not affect the activity comparison.

Table 1. Irradiation (Irr.) conditions. The symbols σ_h and σ_v denote the horizontal and vertical Gaussian beam sizes, respectively

Beam energy (MeV)	Irr. No.	Beam size (mm) σ_h	σ_v	Average beam current (μA)	Irradiation time (min)
20	1	10.8	3.2	15.8±1.7	10
	2			15.7±1.4	
	3			17.1±0.4	
35	4	4.4	4.8	17.7±0.3	5
	5			18.1±1.2	
	6			18.7±0.4	
50	7	4.8	2.5	19.4±0.6	5
	8			20.3±0.5	
	9			20.7±0.5	

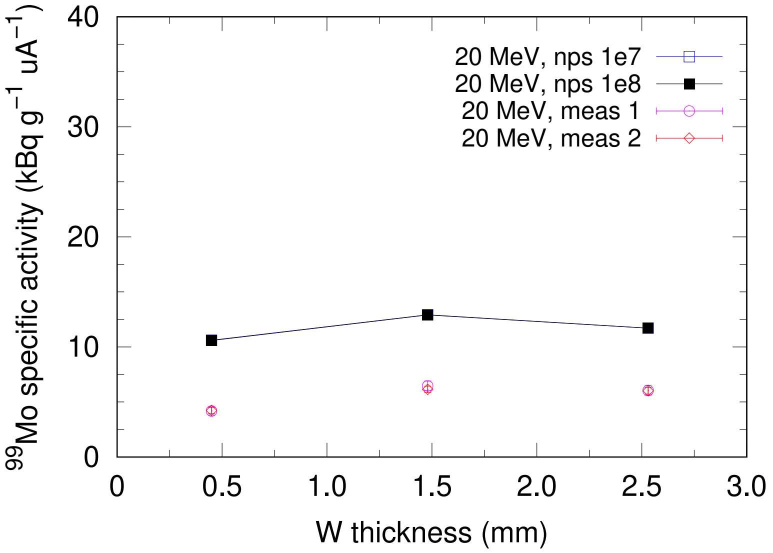

Fig.5. Calculation and experimental results of ^{99}Mo specific activities as functions of W thickness. The electron beam energy was 20 MeV

§4. Results and discussion

The specific activities of ^{99}Mo for $E_{e^-} = 20$ MeV and $E_{e^-} = 35$ MeV are plotted in Figs. 5 and 6, respectively. For these beam energies, the optimal W thicknesses were in agreement between the calculation and experimental results:

- The greatest ^{99}Mo specific activity for $E_{e^-} = 20$ MeV was calculated to be 12.91 kBq g^{-1} µA^{-1}at the W thickness of 1.48 mm
- The greatest ^{99}Mo specific activity for $E_{e^-} = 20$ MeV was measured to be 6.14 kBq g^{-1} µA^{-1}at the W thickness of 1.48 mm
- The greatest ^{99}Mo specific activity for $E_{e^-} = 35$ MeV was calculated to be 26.80 kBq g^{-1} µA^{-1}at the W thickness of 2.58 mm
- The greatest ^{99}Mo specific activity for $E_{e^-} = 35$ MeV was measured to be 32.29 kBq g^{-1} µA^{-1}at the W thickness of 2.58 mm

On the other hand, the specific activities of ^{99}Mo for $E_{e^-} = 50$ MeV (Fig. 7) differed between the calculation and experimental results:

- The greatest ^{99}Mo specific activity for $E_{e^-} = 50$ MeV was calculated to be 50.50 kBq g^{-1} µA^{-1}at the W thickness of 3.16 mm
- The greatest ^{99}Mo specific activity for $E_{e^-} = 50$ MeV was measured to be 52.25 kBq g^{-1} µA^{-1}at the W thickness of 2.13 mm

The differences are attributed to the following factors.

- *Beam energy spread.* In the MC simulation runs, monoenergetic electron beams were transported. In the irradiation experiments, however, the electron beams exhibited energy spread. Electron beams having unintended energies could result in photons of different energies, which could in turn affect the yield of the ^{100}Mo(γ,n)^{99}Mo reaction.
- *Beam current fluctuation.* The average beam currents shown in Table 1 are actually the means

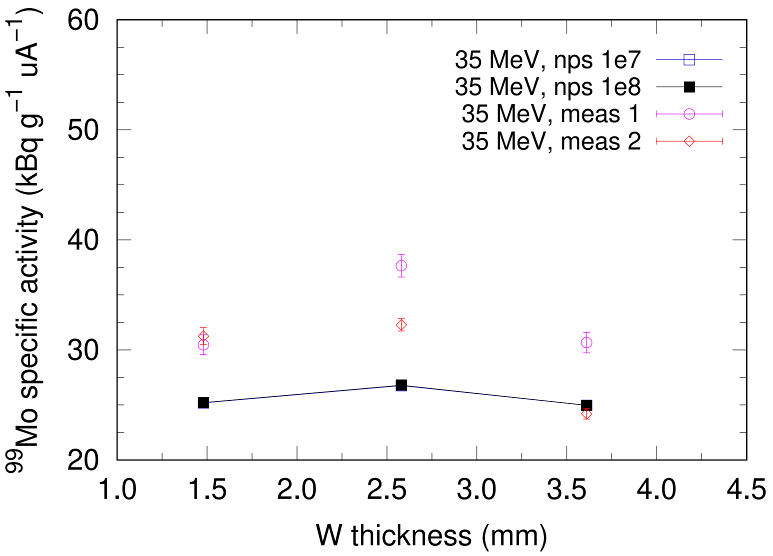

Fig.6. Calculation and experimental results of ^{99}Mo specific activities as functions of W thickness. The electron beam energy was 35 MeV

Table 2. The calculated and experimental ^{196}Au specific activities of upstream Au foils

Beam energy (MeV)	W thickness (mm)	^{196}Au specific activity (kBq g^{-1} μA^{-1}) Calculation	Experimental
20	0.45	61.29	33.84
	1.48	104.34	74.08
	2.53	97.85	65.77
35	1.48	180.65	193.51
	2.58	210.60	248.18
	3.61	202.07	234.23
50	2.13	365.18	275.15
	3.16	395.38	366.92
	4.21	381.27	245.56

of average beam currents measured over irradiation times. As can be seen from the standard deviations in Table 1, some of the irradiation runs were accompanied by beam current fluctuations, which could affect the absolute values of experimental ^{99}Mo specific activities.

The ^{196}Au specific activities of the upstream Au foils are summarized in Table 2, and those of the downstream Au foils in Table 3. The W thicknsssess leading to the greatest ^{196}Au specific activities were the same between calculation and experimental results in the upstream Au foils, but not in the downstream Au foils. Considering the overall agreement in the upstream Au foils and the overall discrepancy in the downstream Au foils, it is thought that the beam interactions within the MoO_3 targets could affect the ^{197}Au(γ,n)^{196}Au reactions in the downstream Au foils.

§5. Summary

To improve the ^{99}Mo production yield, we investigated optimal W thicknesses for electron beam energies of 20, 35, and 50 MeV. The calculated results were compared with experimental results, and

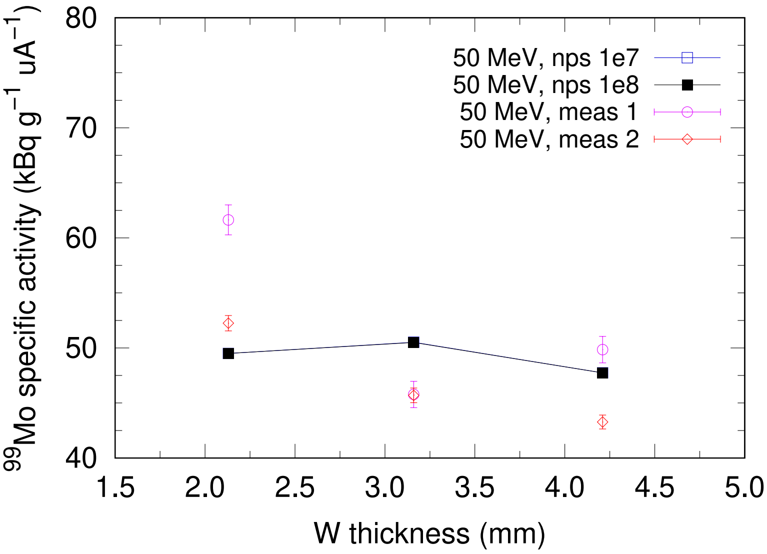

Fig.7. Calculation and experimental results of ^{99}Mo specific activities as functions of W thickness. The electron beam energy was 50 MeV

Table 3. The calculated and experimental ^{196}Au specific activities of downstream Au foils

Beam energy (MeV)	W thickness (mm)	^{196}Au specific activity (kBq g^{-1} µA^{-1}) Calculation	Experimental
20	0.45	85.21	46.47
	1.48	84.93	54.00
	2.53	75.31	51.39
35	1.48	178.01	194.06
	2.58	175.05	204.45
	3.61	159.64	190.07
50	2.13	340.84	129.33
	3.16	333.38	300.21
	4.21	308.48	324.15

the overall results of MoO_3 targets and upstream Au foils agreed between calculations and experiments.

The agreeing W thicknesses of the MoO_3 results for 20 MeV and 35 MeV, together with the acceptably small differences in the overall calculation and experimental results, suggest that the parametric calculations of the optimal W thicknesses can be valid.

However, it should be noted that the above results hold only for the intertarget distance of our target holder, or 13 mm, and for the beam sizes used in the experiments (Table 1): for a different set of an intertarget distance and a beam size, the contributions of photon tracks are modified, and so is the balanced W thickness. Our program `phitar` can be used in such cases, which can calculate targetry- and beam-specific optimal thicknesses of converter materials.

Acknowledgments

We are grateful to K. Tatenuma and Y. Natori (Kaken) for helping the preparation of MoO_3 targets, and to Y. Inoue (UTokyo) for experimental assistance. We would also like to express our gratitude to the

ELPH staffs for the operation of the high-intensity electron linac.

References

[1] Jaewoong Jang and Mitsuru Uesaka. Influence of enriched ^{100}Mo on Mo reaction yields. *Journal of Physics Communications*, 3(5):055015, 2019.

[2] Jaewoong Jang, Masashi Yamamoto, and Mitsuru Uesaka. Design of an X-band electron linear accelerator dedicated to decentralized ^{99}Mo/$^{99\mathrm{m}}$Tc supply: From beam energy selection to yield estimation. *Physical Review Accelerators and Beams*, 20(10):104701, 2017.

[3] Tatsuhiko Sato, Yosuke Iwamoto, Shintaro Hashimoto, Tatsuhiko Ogawa, Takuya Furuta, Shin-ichiro Abe, Takeshi Kai, Pi-En Tsai, Norihiro Matsuda, Hiroshi Iwase, Nobuhiro Shigyo, Lembit Sihver, and Koji Niita. Features of particle and heavy ion transport code system (PHITS) version 3.02. *Journal of Nuclear Science and Technology*, 55(6):684–690, 2018.

[4] Jaewoong Jang. `phitar` - A PHITS wrapper for targetry design (v1.03), 2019. Zenodo.

[5] Jaewoong Jang. *Parametric analyses in electron linac production of* $^{99}Mo/^{99m}Tc$. PhD thesis, University of Tokyo, Tokyo, Japan, 2019.

III. Status Report

Status of Accelerator Facilities in FY2018

F. Hinode, K. Kanomata, S. Kashiwagi, S. Miura, T. Muto, I. Nagasawa,
K. Nanbu, Y. Shibasaki, K. Takahashi, H. Hama

Accelerator group in ELPH, Tohoku University, Sendai, 982-0826

The total operating time of the electron accelerator complex; high intensity 60 MeV linac, 90 MeV injector linac and 1.3 GeV BST (booster-storage ring) exceeded 2000 hours in FY 2018, including the operation of the test accelerator t-ACTS. While the machines had stably operated during the user's time, some upgrade works for the accelerator complex were also conducted, such as a replacement of rf power source for BST, improvements of beam line and irradiation system for the high intensity linac, etc. In this article, status and some improvements of accelerator complex are reported.

§1. High intensity linac

The electron beam from the high intensity linac was supplied with the energy range of 10-60 MeV depending on a requirement of individual machine user. The typical beam current was 120 μA for 50 MeV operation. The operating beam time of the high intensity linac in FY 2018 exceeded 340 hours.

On the summer shutdown in 2018, upgrade work of the beam transport line was carried out. Construction of new beam line for an experiment of electron scattering with extremely low energy transfer (ULQ2) was also started partially. Originally beam tuning in the high-intensity linac had been extremely difficult due to the lack of properly installed beam monitors and focusing magnets. To improve this, 8 quadrupole magnets and orbit correction magnet were newly added or replaced to the appropriate locations, as well as two profile monitors. Figure 1 shows a schematic layout of the entire beam line after the upgrade work. Figure 2 also shows pictures of the beam transport line before and after the installation of new magnets. Although the beam transmission seems to have been improved by this upgrade work, further study is underway.

In this summer shutdown, upgrade of irradiation system was also conducted [1]. Before the upgrade, the converter for gamma rays had been installed in the irradiation pool together with the sample target, but it was changed to separated structure. This modification was intended to increase the yield of gamma rays by bringing the irradiated sample closer to the electron beam extraction window. Furthermore, it was also expected to reduce the exposure during the exchange work of sample target. By this improvement in addition to the upgrade of beam transport line, the yield of produced RI was enhanced by 6.5 times comparing with the previous irradiation with 20 MeV. Figure 3 shows the 3D model and picture of new irradiation system.

Although the linac was operating almost stably in this year, there were some troubles. So far, linac operation has been frequently suspended due to the trouble, so-called "vacuum explosion", in which the

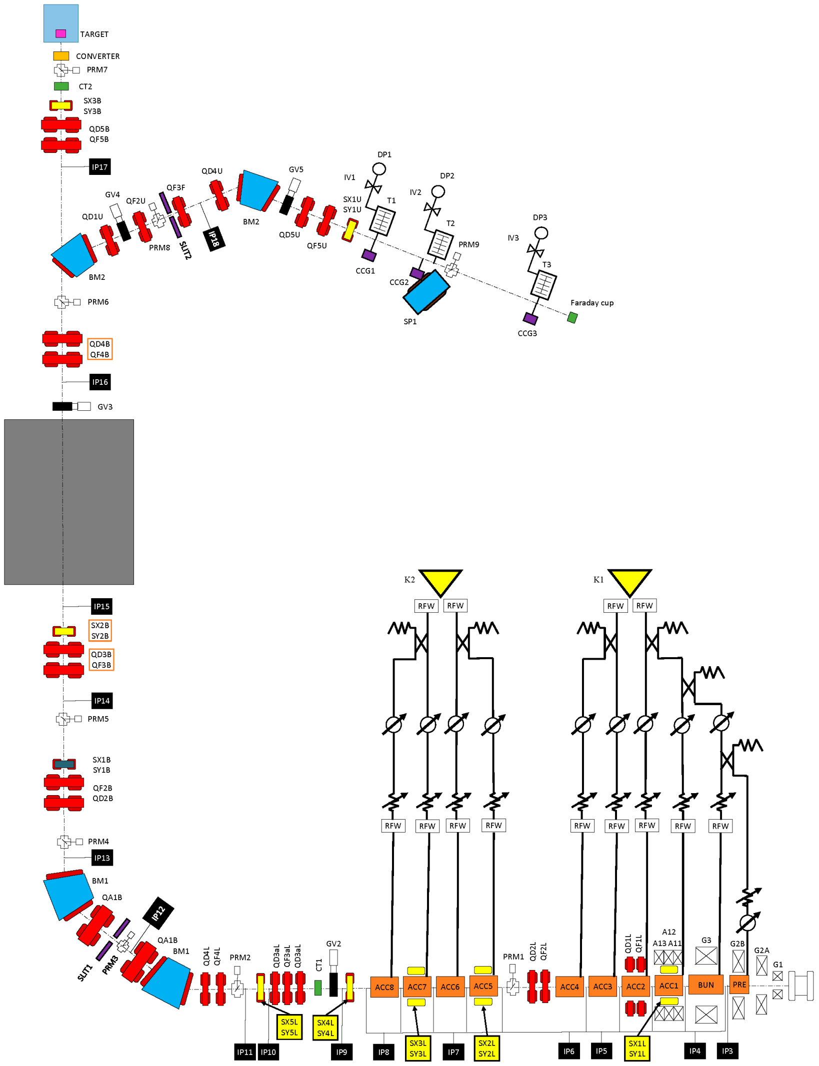

Fig.1. Schematic layout of the entire beam line after the upgrade work. QF4L, QD4L are newly added to the end of linac. Two doublets QD2B, QF2B and QF4B, QD4B are replaced with new magnets, while a doublet QF3B, QD3B and steering magnet Sxy2B are newly added in the beam transport line.

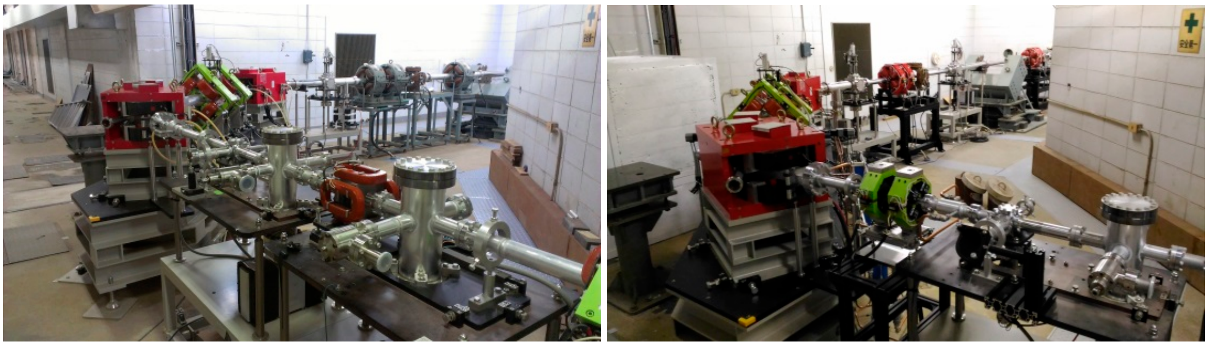

Fig.2. Before (left) and after (right) the installations of new magnets in the beam transport line.

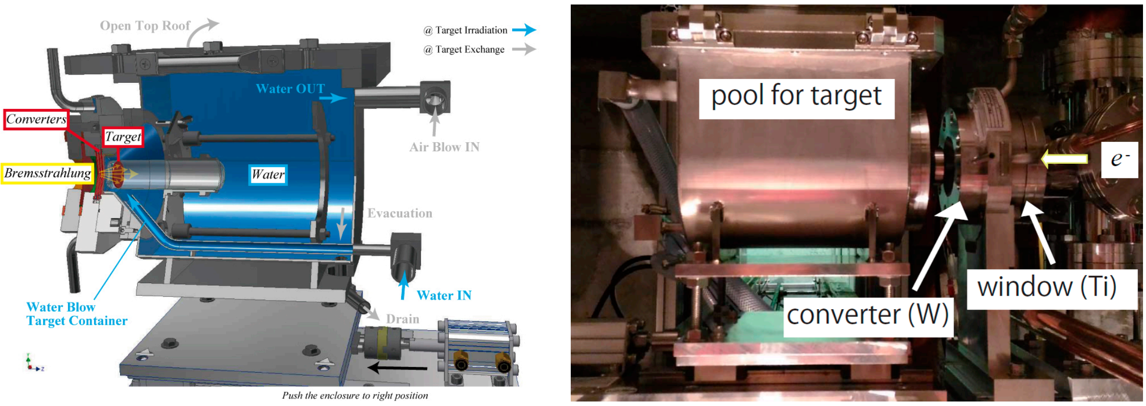

Fig.3. 3D model (left) and picture (right) of the new irradiation system.

vacuum pressure of beam line suddenly increases and finally results in the trip of ion pumps. As the frequency of explosions increased, vacuum leak hunting was carried out again for the entire beam line. As a result, there were two small leaks; one was found at a small crack on the beam window, and the other one was located at the flange part in front of the ULQ2 dipole magnet. After this leak hunting, the frequency of explosions has decreased significantly for a while. However, recently it has begun to occur again, although it is less frequent. Since the ion pump itself is presumed to be degraded, some ion pumps with high base pressure will be replaced during the next summer shutdown.

The old electron gun has been also problematic, because the cathode is no longer supported by supplier. Currently installed cathode has been operated more than 10 years and still working with a nominal emission current of 300 mA. At present, new spare cathode is no longer in stock, so we are preparing a new replaceable electron gun based on EIMAC Y646B. The installation of the new electron gun will be implemented during the long shutdown period next summer after testing the electron gun on the test bench.

§2. Injector linac

The injector linac stably supplies an electron beam to the BST ring with energy of 90 MeV. However, there is a problem with recent thermionic rf guns, that discharges has been starting to occur in the gun cathode cells about a year after the installation of the new cathode. Currently, this problem is coped by replacing the cathode once a year. It is known that the reason for the discharge is due to the unusual deposition of carbon-like material between the cathode and the cavity wall, but the cause for the deposition is currently under investigation.

§3. BST ring

1.3 GeV BST ring has well operated to generate high energy gamma rays via bremsstrahlung from internal target wire inserted to the electron beam orbit. Generated gamma rays are not only utilized to the experiment for quark/hadron physics, but also supplied to the test beam line for testing of detectors used in high energy experiments.

For the klystron high-voltage power supply in BST, the effects of aging over 20 years after production had been concerned. In fact, in 2017, there was a trouble that an IGBT in one of the ten high voltage units was damaged during operation. This IGBT was no longer supported and it was impossible to get a replacement, so it had been forced to work with 8 units. In addition, the impact of recent increases in the unit price of electricity and also in the cost of heavy oil for air conditioning equipment is serious, getting to make it difficult to secure a budget for operating the facility accelerator. In particular, the use of klystron (E3774, Toshiba Corp.) transferred from KEK-PF was inefficient. Because 10 kW was enough for the current user even though it was possible to output large power of 100 kW level. This year, therefore, we decided to replace the klystron with a low-power solid-state amplifier. The maximum output power was set to 15 kW in anticipation of a future increase in circulating beam current. Table 2 shows the specifications of the rf amplifier (CA500BW1-7272R, RandK Co. Ltd.).

Table 1. RF power amplifier, CA500BW1-7272R

	Specification @500 MHz	Measured
Frequency Range	500±0.5MHz	-
Output Power	15 kW @P2dB/CW	15.5 kW
Gain	+72 dB (min.)	+73.17 dB
Gain Flatness	0.5dB (max.)	±0.01dB
Harmonics	-30dBc (max.)	-41.83dBc
Spurious	-70dBc (max.)	<-80.00dBc
Return Loss	-14dB (max.) input	-24.21dB
	-10dB (max.) output	-19.84dB
Power Dissipation	38kVA (max.)	31.5kVA

To keep costs down, the frequency band was set to 500 ± 0.5 MHz. It is configured to output the rated power by combining the module of the amplifier unit using LDMOS. The output of the driver amplifier is divided into 6 ports, each of which is input to the 4-channel amplifier unit and amplified to about 700 W per channel. After that, the outputs of 6 amplifier units (24 channels in total) are combined with the radial combiner to output a total power of 15kW in maximum. The RF power finally output from the WX-77D coaxial tube is converted into a WR-1500 waveguide and then supplied to the accelerating cavity through the existing microwave circuit. Each channel in the amplifier unit has a circulator to protect against reflected power. In addition, if only the final stage amplifier fails, operation can continue within the scope of redundancy. Figure 4 shows the new RF power souce installed in March, 2019. All elements are housed in a 2 m high rack and the entire system is very compact. By replacing to this new RF source , the electric power required for operation was reduced by 180 kW as expected. This is equivalent to about 15% of the electricity power contracted this year.

Fig.4. New RF power souce installed to BST.

References

[1] K. Takahashi *et al.*, Proc. of the 15th Annual Meeting of Particle Accelerator Society of Japan, p.688, (2018)

User Support Office Report in FY2018

M. Miyabe[1] and the user support office[1]

[1]*Research Center for Electron Photon Science, Tohoku University, Sendai, 982-0826, Japan*

The User Support Office coordinate across the users and our facility for management of the beam-time. In 2018 financial year, we had provided the electron, photon and positron beam without apparent problems except for Photon beamline I. In May 2018, because the failure of the accelerator has occurred, we couldn't provide any user beam-time because of the repairing work about one month.

§1. Introduction

ELPH has three accelerators for Joint Usage/Research. Our facility could provide several beams with following three beam lines,

- 70 MeV electron linear accelerator (linac) at the first irradiation lab (For Radiochemistry)
- Tagged photon beam from 1.3 GeV electron synchrotron called BST ring with 90 MeV injector at the second irradiation lab (For Hadron Physics, **Photon beamline I**)
- Tagged photon beam at the GeV-γ irradiation room (For Hadron Physics, **Photon beamline II**)

In addition, positron/electron beam line for testing detectors is located at the GeV-γ irradiation room. The 70 MeV electron linear accelerator was utilized for the Radiochemistry experiments by photo-nuclear reactions. It could produce radio active source with its high intensity. Both tagged photon beam line was used for Hadron physics experiments. NKS2 and FOREST/BLC experiment have bean held in recent years.

§2. Beamtime operated

The total radiation time was 300 hours for the RI linac operation and 1627 hours for the BST operation, and it was 1927 hours in total. Table 1 summarizes the radiation times, and user beam times in fiscal.

Many experiments for testing detectors were made by positron beam line. Positron beam was produced by bremsstrahlung photon beams from the synchrotron. Total 26 shifts experiments are performed using this positron beam in this financial year.

A Next generation FOREST experiments (FOREST/BLC) was started by GeV-γ group in ELPH. New bending magnet was installed on the downstream of FOREST detectors and it covers the most forward angle. These new experimental setup enable the zero degree proton detection for the $\gamma d \to p\eta n$ reaction at $E_\gamma \sim 0.9$ GeV. This reaction gives the zero relative momentum between the η and n. This situation will enable to determine the ηn scattering length. In this financial year, physical data was taken with hydrogen and deuteron target. Total 76 shifts of FOREST/BLC experiment were carried out and are equivalent to 1/3 of its goal.

In Photon beam line I, New detectors research and developments for NKS2 experiment has been carried out in this financial year.

one experiment was carried out for the undergraduate students. this experiment (#2899: H. Ohnishi, ELPH, Tohoku University) is for the education of the undergraduate students in ELPH.

Table 1. Radiation times, and user beamtimes in financial year 2018. They are given by the sum of the times that the beam is coming to the beamline, and that the beam is provided to the users.

Month	RI Linuac radiation (h)	BST Ring radiation (h)
April	23	142
May	37	90
Jun	35	531
July	29	2
August	0	0
September	0	0
October	32	457
November	44	202
December	27	94
January	31	89
February	41	0
March	0	26
Sum	300	1627

§3. ELPH workshops and ELPH seminars

In this fiscal year, ELPH supported four ELPH workshops. The first one is hadron physics (C023: H. Nagahiro, Nara Women's University), the second one is SNP school 2018 (C022: S. N. Nakamura, Tohoku University), the third one is nuclear physics (C021: T. Suda, ELPH Tohoku University).

17 ELPH seminars were held in this fiscal year. Seminars title and talker are listed below.

- Michael Kohl, 米国・ハンプトン大, ”Anomalies in proton observables - old physics or new physics?”
- 吉田 純也, 原研先端研, ”ダブルハイパー核検出実験 J-PARC E07 と原子核乾板技術の現在”
- 谷田 聖, 原研先端研, ”スピン偏極で見るバリオン構造”
- 中川 格, 理化学研究所, ”RHIC における高エネルギー横偏極陽子＋陽子衝突の超前方 π^0 生成左右非対称性と陽子のスピンパズル問題”
- Alessandro Scordo, イタリア、INFN-Frascati 研究所, ”SIDDHARTA-2 experiment at DAFNE: ready for the first measurement of kaonic deuterium（on behalf of SIDDHARTA & SIDDHARTA-2 collaborations）”
- 早野 仁司, 高エネルギー加速器研究機構, ”超伝導加速空洞の最先端：表面の技術”
- 佐藤 大輔, 産業総合研究所, ”IrCe カソード及びセラミックス加速管”
- 吉岡正和, KEK 名誉教授、東北大学客員教授、岩手大学客員教授, ”国際リニアコライダー計画（ILC）の最近の状況と 100km リングヒッグスファクトリー（CEPC ＠中国）計画”

- 岸田 昌浩, 九州大学大学院工学研究院, ”水素と金属によって生じる異常発熱現象の従来科学的検証”
- 尾立 晋祥, 東京理科大学名誉教授, ”An attempt for the low-temperature nuclear synthesis”
- Chayut Thanapirom, ”Terahertz Technology Laboratory, NECTEC, Thailand Research Status of TTL – SSDRU – NECTEC”
- ”配管等継ぎ手の取扱い安全講習会（学内限定）”
- 門叶 冬樹, 山形大学理学部, ”炭素１４を用いた AMS 研究（兼 定期放射線教育の特別講演）”
- 阪井 寛志, 高エネルギー加速器研究機構, ”窒素処理を用いた超伝導加速空洞の高加速勾配、高 Q 値に向けた研究開発”
- 山口 貴之, 埼玉大学理工学研究科, ”重イオン蓄積リングを用いた RI ビーム物理実験の現状と将来”

Radiation Safety Report 2018

Radiation Safety Office

放射線安全管理室より、2018 年度（平成 30 年 4 月～平成 31 年 3 月）の報告を以下の通り行う。

§1.　許認可申請

H30 年　4 月　1 日　　氏名等の変更　（総長交代のため）

H30 年　5月21日　　放射線取扱主任者　選任　（南部健一、時安敦史）

§2.　個人管理

2.1　放射線業務従事者登録

185 人（　東北大　71 人　学外　97 人　研究者以外　17 人）

2.2　個人被ばく管理

1 年間の個人被ばく線量　　5 mSv　以下　185 人

2.3　教育訓練

定期講習

平成 30 年 7 月 9 日　登録前教育 15 人　再教育 81 人

特別講演の内容：

山形大学理学部　門叶冬樹　氏　「炭素 14 を用いた AMS 研究」

不定期の講習

再教育　16 回　42 人

登録前教育（新規教育）　22 回　46 人

§3. 自主点検

年 2 回実施　　平成 30 年 9 月 26 日、平成 31 年 3 月 25 日

§4. 放射性同位元素製造記録

2018 年度に本加速器施設で製造され，共同研究に使用された放射性同位元素は次の通りである。

核種	数量（kBq）
Na−22	801
Na−24	500
K−42	8,200
K−43	40,481
Ti−44	9
Sc−46	12,000
Ca−47	80
Sc−47	9,000
V−48	600
Fe−53	300
Ni−56	1,000
Co−57	2,283
Ni−57	9,050
Se−75	600
Rb−84	4.8
Sr−85	660
Rb−86	680
Zr−88	2,500
Nb−95	400
Mo−99	44,000
mAg−106	1
Ba−131	20
Cs−132	1,008
mBa−135	4,800
Cs−136	11,280
Pm−143	200
Ta−180	10,000
Tl−202	9,000
Hg−203	1,400
全 29 核種	計 170,857.8 kBq

IV. List of Publication

List of Publication (論文リスト) (2018)

Papers Published in Refereed Journals

Bunch Length Measurement Employing Cherenkov Radiation from a Thin Silica Aerogel

K. Nanbu, Yuki Saito, Hirotoshi Saito, Shigeru Kashiwagi, Fujio Hinode, Toshiya Muto and H. Hama

Particles, 1(1), 305-314 (2018).

Observation of coherent undulator radiation in THz region

Shigeru Kashiwagi, Taro Abe, Hirotoshi Saito, Fujio Hinode, Ken Kanomata, Sadao Imura, Toshiya Muto, Ikuro Nagasawa, Ken-ichi Nanbu, Shingo Ninomiya, Nobuyuki Nishimori, Yuki Saito, Ken Takahashi and H. Hama

Infrared Physics & Technology 93, 335-339, (2018).

Measurement of Proton Charge Radius by Low-Energy Electron Scattering

T. Suda, T. Aoyagi, Y. Honda, Y. Maeda, S. Miura, T. Muto, K. Namba, K. Nanbu, K. Takahashi, T. Tamae and K. Tsukada

Journal of Particle Accelerator Society of Japan, 15 (2018) 52-59.

Extraction behavior of rutherfordium as a cationic fluoride complex with a TTA chelate extractant from HF/HNO_3 acidic solutions

A. Yokoyama, Y. Kitayama, Y. Fukuda, H. Kikunaga, M. Murakami Y. Komori, S. Yano, H. Haba, K. Tsukada, A. Toyoshima

Radiochimica Acta 107 (2019) 27-32

Use of different surface covering materials to enhance removal of radiocaesium in plants and upper soil from orchards in Fukushima prefecture

M. Sato, H. Akai, Y. Saito, T. Takase, H. Kikunaga, N. Sekiya, T. Ohtsuki, K. Yamaguchi

Journal of Environmental Radioactivity 196 (2019) 204-211

短寿命 RI 供給プラットフォーム実現のための放射線障害防止法上の手続きについて

鈴木智和，渡部浩司，菊永英寿，羽場宏光，福田光宏

日本放射線安全管理学会誌 17 (2018) 121-124

Distribution of LAT1-targeting PET tracer was independent of the tumor blood flow in rat xenograft models of C6 glioma and MIA PaCa-2

Masanao Aoki, Tadashi Watabe Shushi Nagamori, Sadahiro Naka, Hayato Ikeda, Pornparn Kongpracha, Genki Horitsugi, Yasukazu Kanai, Eku Shimosegawa, Yoshikatsu Kanai, Jun Hatazawa

Annals of Nuclear Medicine, in press.

Ultracompact Compton camera for innovative gamma-ray imaging

J. Kataoka, A. Kishimoto, T. Taya, S. Mochizuki, L. Tagawa, A. Koide, K. Sueoka, H. Morita, T. Maruhashi, K. Fujieda, T. Kurihara, M. Arimoto, H. Okochi, N. Katsumi, S. Kinno, K. Matsunaga, H. Ikeda, E. Shimosegawa, J. Hatazawa, S. Ohsuka, T. Toshito, M. Kimura, Y. Nagao, M. Yamaguchi, K. Kurita, N. Kawachi

Nuclear Instruments and Methods in Physics Research Section A: Accelerators, Spectrometers, Detectors and Associated Equipment 912, 1–5 (2018).

Application of astatine-210: evaluation of astatine distribution and effect of pre-injected iodide in whole body of normal rats

Hayato Ikeda, Yoshihiko Hayashi, Naruto Takahashi, Tadashi Watabe, Yasukazu Kanai, Atsushi Shinohara, Hiroki Kato, Hiroshi Watabe, Eku Shimosegawa, Jun Hatazawa

Applied Radiation and Isotopes 139, 251–255 (2018).

Observation of a Be double-Lambda hypernucleus in the J-PARC E07 experiment

H. Ekawa et al.

Prog. Theor. Exp. Phys. 2019 (2019) 021D02(1-11)

N-myristoylation and S-acylation are common modifications of Ca^{2+} regulated Arabidopsis kinases and are required for activation of the SLAC1 anion channel

Saito, S., Hamamoto, S., Moriya, K., Matsuura, A., Sato, Y., Muto, J., Noguchi, H., Yamauchi, S., Tozawa, Y., Ueda, M., Hashimoto, K., Köster, P. Qiuyan. D., Held, K., Kudla, J., Utsumi, T. and Uozumi, N.

New Phytol. 218, 1504-1521 (2018)

In vitro and in vivo characterization of modulation of the vacuolar cation channel TRPY1 from Saccharomyces cerevisiae

Hamamoto, S., Mori, Y., Yabe, I. and Uozumi, N.

FEBS J. 285, 1146–1161 (2018)

Reduction of spermidine content resulting from inactivation of two arginine decarboxylases increases biofilm formation in Synechocystis sp. PCC 6803

Kera, K., Nagyama, T., Nanatani, K., Saeki-Yamoto, C., Tominaga, A., Souma, S., Miura, N., Takeda, K., Kayamori, S., Ando, E., Higashi, K., Igarashi, K. and Uozumi, N.

J. Bacteriol. 200 (9), E00664-17 (2018)

Ion channels regulate nyctinastic leaf opening in Samanea saman.

Oikawa, T., Ishimaru, Y., Munemasa, S., Takeuchi, Y., Washiyama, K. Hamamoto, S., Yoshikawa, N., Mutara, Y., Uozumi, N. and Ueda, M.

Current Biology 28, 2230–2238 (2018)

Measurement of mechanical properties of single Synechocystis sp. strain PCC6803 cells in different osmotic concentrations using robot integrated microfluidic chip

Chang,D., Sakuma, S., Kera, K., Uozumi, N. and Arai F.
Lab Chip 18, 1241-1249 (2018)

Identification and characterization of compounds that affect stomatal movements

Toh, S., Inoue, S., Toda Y., Yuki, T., Suzuki, K., Hamamoto, S., Fukatsu, K., Aoki, S., Uchida, M., Asai, E., Uozumi, N., Ayato S. and Kinoshita, T.
Plant Cell Physiol. 59, 1568-1580 (2018)

Coupled-channels analyses for ^{9,11}Li+^{208}Pb fusion reactions with multi-neutron transfer couplings

K.-S. Choi, M.-K. Cheoun, W.Y. So, K. Hagino, and K.S. Kim,
Phys. Lett. B780 (2018) 455-460.

Origin of a maximum of astrophysical S factor in heavy-ion fusion reactions at deep subbarrier energies

K. Hagino, A.B. Balantekin, N.W. Lwin, and Ei Shwe Zin Thein,
Phys. Rev. C97 (2018) 034623.

Role of hexadecapole deformation of the projectiles in heavy-ion subbarrier fusion reactions of the ^{28}Si nucleus

G. Kaur, K. Hagino, and N. Rowley,
Phys. Rev. C97 (2018) 064606.

Disappearance of nuclear deformation in hypernuclei: a perspective from a beyond-mean-field study

H. Mei, K. Hagino, J.M. Yao, and T. Motoba,
Phys. Rev. C97 (2018) 064318.

Hot fusion reactions with deformed nuclei for synthesis of superheavy nuclei: an extension of the fusion-by-diffusion model

K. Hagino,
Phys. Rev. C98 (2018) 014607.

Branching ratios for deexcitation processes of daughter nuclei following invisible dinucleon decays in ^{16}O

K. Hagino and M. Nirkko,
J. of Phys. G45 (2018) 105105.

A compensated multi-gap RPC with 2 m strips for the LEPS2 experiment

K. Watanabe, S. Tanaka, W.C. Chang, H. Chen, M.L. Chu, J.J. Cuenca-Garcia, T. Gogami, D. Gonzalez-Diaz, M. Niiyama, Y. Ohashi, H. Ohnishi, N. Tomida, M. Yosoi
Nuclear Instrument and Method, A925 (2019) 188-192

"K^-pp ", a $\bar{K}$-Meson Nuclear Bound State, Observed in ^{3}He(K^-,Λp)n Reactions

S. Ajimura, H. Asano, G. Beer, C. Berucci, H. Bhang, M. Bragadireanu, P. Buehler, L. Bussog, M. Cargnelli, S. Choi, C. Curceanu, S. Enomoto, H. Fujioka, Y. Fujiwara, T. Fukuda, C. Guaraldo, T. Hashimoto, R.S. Hayano, T. Hiraiwa, M. Iio, M. Iliescu, K. Inoue, Y. Ishiguro,

T. Ishikawa, S. Ishimoto, K. Itahashi, M. Iwasaki, K. Kanno, K. Kato, Y. Kato, S. Kawasaki, P. Kienle, H. Kou, Y. Ma, J. Marton, Y. Matsuda, Y. Mizoi, O. Morra, T. Nagae, H. Noumi, H. Ohnishi, S. Okada, H. Outa, K. Piscicchia, Y. Sada, A. Sakaguchi, F. Sakuma, M. Sato, A. Scordo, M. Sekimoto, H. Shi, K. Shirotori, D. Sirghii, F. Sirghii, K. Suzuki, S. Suzuki, T. Suzuki, K. Tanida, H. Tatsuno, M. Tokuda, D. Tomono, A. Toyoda, K. Tsukada, O. VazquezDocei, E. Widmann, T. Yamaga, T. Yamazaki, Q. Zhang, J. Zmeskal

Physics Letter B789 (2019) 620-625

Non-strange dibaryons studied in the $\gamma d \rightarrow \pi^0 \pi^0 d$ reaction

T. Ishikawa, H. Fujimura, H. Fukasawa, R. Hashimoto, Q. He, Y. Honda, T. Iwata, S. Kaida, H. Kanda, J. Kasagi, A. Kawano, S. Kuwasaki, K. Maeda, S. Masumoto, M. Miyabe, F. Miyahara, K. Mochizuki, N. Muramatsu, A. Nakamura, K. Nawa, S. Ogushi, Y. Okada, K. Okamura, Y. Onodera, K. Ozawa, Y. Sakamoto, M. Sato, H. Shimizu, H. Sugai, K. Suzuki, Y. Tajima, Y. Taniguchi, Y. Tsuchikawa, H. Yamazaki, R. Yamazaki, H.Y. Yoshida.

Phys. Lett. B 789, 413 (2019).

Development of a transmittance monitor for high-intensity photon beams

Y. Matsumura, T. Ishikawa, Y. Honda, S. Kido, M. Miyabe, I. Nagasawa, K. Nanbu, H. Shimizu, K. Takahashi, Y. Tsuchikawa, H. Yamazaki

Nucl. Instrum. and Meth. A 902, 103 (2018).

Profile measurement of circulating electrons in a synchrotron by inserting a carbon wire,

Y. Obara, T. Ishikawa, H. Hama, F. Hinode, H. Kanda, S. Kashiwagi, M. Miyabe, T. Muto, K. Ozawa, H. Shimizu, A.O. Tokiyasu

Nuclear Instruments and Methods in Physics Research Section A 922, 108-113 (2019).

Possible $\eta' d$ bound state and its s-channel formation in the $\gamma d \rightarrow \eta d$ reaction

T. Sekihara, H. Fujioka, T. Ishikawa

Physical Review C 97, 045202 (2018).

First measurement of coherent ϕ-meson photoproduction from ^{4}He near threshold

T. Hiraiwa, M. Yosoi, M. Niiyama, Y. Morino, Y. Nakatsugawa, M. Sumihama, D. S. Ahn, J. K. Ahn, W. C. Chang, J. Y. Chen, S. Daté, H. Fujimura, S. Fukui, K. Hicks, T. Hotta, S. H. Hwang, T. Ishikawa, Y. Kato, H. Kawai, H. Kohri, Y. Kon, P. J. Lin, Y. Maeda, M. Miyabe, K. Mizutani, N. Muramatsu, T. Nakano, Y. Nozawa, Y. Ohashi, T. Ohta, M. Oka, C. Rangacharyulu, S. Y. Ryu, T. Saito, T. Sawada, H. Shimizu, E.A. Strokovsky, Y. Sugaya, K. Suzuki, A. O. Tokiyasu, T. Tomioka, T. Tsunemi, M. Uchida, T. Yorita

Phys. Rev. C97 (2018) 035208.

Differential cross section and photon-beam asymmetry for the $\gamma p \rightarrow \pi^+ n$ reaction at forward π^+ angles at E_γ=1.5–2.95 GeV

H. Kohri, S.Y. Wang, S.H. Shiu, W.C. Chang, Y. Yanai, D.S. Ahn, J.K. Ahn, J.Y. Chen, S. Daté, H. Ejiri, H. Fujimura, M. Fujiwara, S. Fukui, W. Gohn, K. Hicks, A. Hosaka, T. Hotta, S.H. Hwang, K. Imai, T. Ishikawa, K. Joo, Y. Kato, S. H. Kim, Y. Kon, H.S. Lee, Y. Maeda, T. Mibe, M. Miyabe, Y. Morino, N. Muramatsu, T. Nakano, Y. Nakatsugawa, M. Niiyama, H. Noumi, Y. Ohashi, T. Ohta, M. Oka, J.D. Parker, C. Rangacharyulu, S.Y. Ryu, T. Sawada, H. Shimizu, Y. Sugaya, M. Sumihama, T. Tsunemi, M. Uchida, M. Ungaro, and M. Yosoi (LEPS Collaboration)

Physical Review C 97, 015205 (2018).

Differential Cross Section and Photon-Beam Asymmetry for the $\gamma p \rightarrow \pi^- \Delta^{++}(1232)$ Reaction at Forward π^- Angles for E_γ=1.5–2.95 GeV

H. Kohri, S.H. Shiu, W.C. Chang, Y. Yanai, D.S. Ahn, J.K. Ahn, J.Y. Chen, S. Daté, H. Ejiri, H. Fujimura, M. Fujiwara, S. Fukui, W. Gohn, K. Hicks, A. Hosaka, T. Hotta, S.H. Hwang, K. Imai, T. Ishikawa, K. Joo, Y. Kato, Y. Kon, H.S. Lee, Y. Maeda, T. Mibe, M. Miyabe, Y. Morino, N. Muramatsu, T. Nakano, Y. Nakatsugawa, S.i. Nam, M. Niiyama, H. Noumi, Y. Ohashi, T. Ohta, M. Oka, J.D. Parker, C. Rangacharyulu, S.Y. Ryu, T. Sawada, H. Shimizu, E.A. Strokovsky, Y. Sugaya, M. Sumihama, T. Tsunemi, M. Uchida, M. Ungaro, S. Y. Wang, and M. Yosoi (LEPS Collaboration)

Physical Review Letters 120, 202004 (2018).

Photoproduction of Λ and Σ^0 hyperons off protons with linearly polarized photons at E_γ=1.5-3.0 GeV

S. H. Shiu, H. Kohri, W. C. Chang, D. S. Ahn, J. K. Ahn, J. Y. Chen, S. Daté, H. Ejiri, H. Fujimura, M. Fujiwara, S. Fukui, W. Gohn, K. Hicks, T. Hotta, S. H. Hwang, K. Imai, T. Ishikawa, K. Joo, Y. Kato, Y. Kon, H. S. Lee, Y. Maeda, T. Mibe, M. Miyabe, K. Mizutani, Y. Morino, N. Muramatsu, T. Nakano, Y. Nakatsugawa, M. Niiyama, H. Noumi, Y. Ohashi, T. Ohta, M. Oka, J. D. Parker, C. Rangacharyulu, S. Y. Ryu, T. Sawada, H. Shimizu, Y. Sugaya, M. Sumihama, T. Tsunemi, M. Uchida, M. Ungaro, and M. Yosoi (LEPS Collaboration)

Phys. Rev. C 97(2018)015208

Direct measurements of the lifetime of medium-heavy hypernuclei

X. Qiu,L.Tang, C. Chen, A. Margaryan, S.A. Wood, P. Achenbach, A. Ahmidouch, I. Albayrak, D. Androic, A. Asaturyan, R. Asaturyan, O. Ates, R. Badui, P. Baturin, W. Boeglin, J. Bono, E. Brash, P. Carter, X. Chen, A. Chiba, M.E. Christy, M.M. Dalton, S. Danagoulian, R. DeLeo, lD. Doi, M. Elaasar, R. Ent, H. Fenker, Y. Fujii, M. Furic, M. Gabrielyan, L. Gan, F. Garibaldi, D. Gaskell, A. Gasparian, T. Gogami, O. Hashimoto, T. Horn, B. Hu, EdV. Hungerford, M. Jones, H. Kanda, M. Kaneta, D. Kawama, H. Khanal, M. Kohl, A. Liyanage, W. Luo, K. Maeda, P. Markowitz, G. Marikyan, T. Maruta, A. Matsumura, V. Maxwell, A. Mkrtchyan, H. Mkrtchyan, S. Nagao, S.N. Nakamura, A. Narayan, C. Neville, G. Niculescu, M.I. Niculescu, A. Nunez, Nuruzzaman, Y. Okayasu, T. Petkovic, J. Pochodzalla,

J. Reinhold, V.M. Rodriguez, C. Samanta, B. Sawatzky, T. Seva, A. Shichijo, V. Tadevosyan, N. Taniya, K. Tsukada, M. Veilleux, W. Vulcan, F.R. Wesselmann, T. Yamamoto, Z. Ye, K. Yokota, L. Yuan, S. Zhamkochyan, L. Zhu

Nuclear Physics A 973 (2018) 116-148.

Revealing Color Forces with Transverse Polarized Electron Scattering

Armstrong, W. and Kang, H. and Liyanage, A. and Maxwell, J. and Mulholland, J. and Ndukum, L. and Ahmidouch, A. and Albayrak, I. and Asaturyan, A. and Ates, O. and Baghdasaryan, H. and Boeglin, W. and Bosted, P. and Brash, E. and Butuceanu, C. and Bychkov, M. and Carter, P. and Chen, C. and Chen, J.-P. and Choi, S. and Christy, M. E. and Covrig, S. and Crabb, D. and Danagoulian, S. and Daniel, A. and Davidenko, A. M. and Davis, B. and Day, D. and Deconinck, W. and Deur, A. and Dunne, J. and Dutta, D. and El Fassi, L. and Ellis, C. and Ent, R. and Flay, D. and Frlez, E. and Gaskell, D. and Geagla, O. and German, J. and Gilman, R. and Gogami, T. and Gomez, J. and Goncharenko, Y. M. and Hashimoto, O. and Higinbotham, D. and Horn, T. and Huber, G. M. and Jones, M. and Jones, M. K. and Kalantarians, N. and Kang, H-K. and Kawama, D. and Keith, C. and Keppel, C. and Khandaker, M. and Kim, Y. and King, P. M. and Kohl, M. and Kovacs, K. and Kubarovsky, V. and Li, Y. and Liyanage, N. and Luo, W. and Mack, D. and Mamyan, V. and Markowitz, P. and Maruta, T. and Meekins, D. and Melnik, Y. M. and Meziani, Z.-E. and Mkrtchyan, A. and Mkrtchyan, H. and Mochalov, V. V. and Monaghan, P. and Narayan, A. and Nakamura, S. N. and Nuruzzaman, A. and Pentchev, L. and Pocanic, D. and Posik, M. and Puckett, A. and Qiu, X. and Reinhold, J. and Riordan, S. and Roche, J. and Rond¥'on, O. A. and Sawatzky, B. and Shabestari, M. and Slifer, K. and Smith, G. and Soloviev, L. F. and Solvignon, P. and Tadevosyan, V. and Tang, L. and Vasiliev, A. N. and Veilleux, M. and Walton, T. and Wesselmann, F. and Wood, S. and Yao, H. and Ye, Z. and Zhang, J. and Zhu, L. (SANE Collaboration),

Physical Review Letters 122 (2019) 022002-1-7.

Novel optical interferometry of synchrotron radiation for absolute electron beam energy measurements

P. Klag, P. Achenbach, M. Biroth, T. Gogami, P. Herrmann, M. Kaneta, Y. Konishi, W. Lauth, S. Nagao, S.N. Nakamura, J. Pochodzalla, J. Roser, Y. Toyama

Nuclear Instruments and Methods in Physics A, 910 (2018) 147-156

Experimental techniques and performance of Λ-hypernuclear spectroscopy with the (e, e'K^+) reaction

T. Gogami, C. Chen, Y. Fujii, O. Hashimoto, M. Kaneta, D. Kawama, T. Maruta, A. Matsumura, S. Nagao, S.N. Nakamura, Y. Okayasu, J. Reinhold, L. Tang, K. Tsukada, S.A. Wood, L. Yuan

Nuclear Instruments and Methods in Physics A, 900 (2018) 69-83

Neutral Kaon Spectrometer 2

M. Kaneta, B. Beckford, T. Fujii, Y. Fujii, K. Futatsukawa, Y.C. Han, O. Hashimoto, K. Hirose, T. Ishikawa, H. Kanda, C. Kimura, K. Maeda, S.N. Nakamura, K. Suzuki, K. Tsukada, F. Yamamoto, H. Yamazaki

Nuclear Instruments and Methods in Physics A, 886 (2018) 88-103

Search for $K_L \to \pi^0 \nu \bar{\nu}$ and $K_L \to \pi^0 X^0$ Decays at the J-PARC KOTO Experiment

J. K. Ahn, B. Beckford, J. Beechert, K. Bryant, M. Campbell, S. H. Chen, J. Comfort, K. Dona, N. Hara, H. Haraguchi, Y. B. Hsiung, M. Hutcheson, T. Inagaki, I. Kamiji, N. Kawasaki, E. J. Kim, J. L. Kim, Y. J. Kim, J. W. Ko, T. K. Komatsubara, K. Kotera, A. S. Kurilin, J. W. Lee, G. Y. Lim, C. Lin, Q. Lin, Y. Luo, J. Ma, Y. Maeda, T. Mari,T. Masuda, T. Matsumura, D. Mcfarland, N. McNeal, J. Micallef, K. Miyazaki, R. Murayama, D. Naito, K. Nakagiri, H. Nanjo, H. Nishimiya, T. Nomura, M. Ohsugi, H. Okuno, M. Sasaki, N. Sasao, K. Sato, T. Sato, Y. Sato, H. Schamis, S. Seki, N. Shimizu, T. Shimogawa, T. Shinkawa, S. Shinohara, K. Shiomi, S. Su, Y. Sugiyama, S. Suzuki, Y. Tajima, M. Taylor, M. Tecchio, M. Togawa, Y. C. Tung, Y. W. Wah, H. Watanabe, J. K. Woo, T. Yamanaka, and H. Y. Yoshida

Physical Review Letters 122(2) · January 2019

Excess heat evolution from nanocomposite samples under exposure to hydrogen isotope gases

A. Kitamura, A. Takahashi, K. Takahashi, R. Seto, T. Hatano, Y. Iwamura, T. Itoh, J. Kasagi, M. Nakamura, M. Uchimura, H. Takahashi, S. Sumitomo, T. Hioki, T. Motohiro, Y. Furuyama, M. Kishida, H. Matsune

International Journal of Hydrogen Energy 43 (2018) 16187-16200.

Direct measurement of astrophysical factor S(E) and screening potential for $^{9}\mathrm{Be}(p,\alpha)^{6}\mathrm{Li}$ reaction at low energy

Kaihong Fang, Zhang Qian, Chen Bingjun, Zhang Zhengwei, Wang Qiang, Wang Tieshan, Jirohta Kasagi, Hu Jun, Xu Shiwei

Phys. Lett. B785 (2018) 262-267.

Papers Published in International Conference Proceedings

A DESIGN STUDY OF THE ELECTRON-DRIVEN ILC POSITRON SOURCE INCLUDING BEAM LOADING EFFECT

Hisayasu Nagoshi, Masao Kuriki, Tohru Takahashi, Kentaro Negishi, Tsunehiko Omori, Masanori Satoh, Yuji Seimiya, Junji Urakawa, Yoske Sumitomo, Shigeru Kashiwagi,

Proceedings of the 9th Particle accelerator conference (IPAC2018),

Vancouver, BC, Canada, MOPMF077, pp311-314, 2018

AN OPTIMIZATION OF POSITRON INJECTOR OF ILC

M. Kuriki, Y. Seimiya, T. Okugi, M. Satoh, J. Urakawa, S. Kashiwagi, Proceedings of the 9th Particle accelerator conference (IPAC2018), Vancouver, BC, Canada, MOPMF077, pp1334-1336, 2018

Study on Generation of Variable Polarized Coherent THz Radiation Using a Crossed Undulator,

H. Saito, H. Hama, F. Hinode, K. Kanomata, S. Kashiwagi, S. Miura, T. Muto, I. Nagasawa, K. Nanbu, S. Ninomiya, K. Takahashi

Proc. 29th Linear Accelerator Conf. (LINAC'18), Beijing, China, Sep. 2018, pp. 157-159.

The SCRIT Electron Scattering Facility Project at the RIKEN RI Beam Factory

T. Ohnishi, A. Enokizono, M. Hara, M. Hori, S. Ichikawa, M. Wakasugi, M. Watanabe, K. Adachi, T. Fujita, T. Hori, K. Kurita, M. Togasaki, N. Uchida, K. Yamada, T. Suda, T. Tamae, K. Tsukada

Acta Phys. Polon. B49 (2018) 483

Beyond the neutron-drip line: two-neutron decay of unbound nuclei

K. Hagino and H. Sagawa

JPS Conf. Prof. 23 (2018) 012010 (8 pages).

Development of a new photon tagging system for GeV-γ beam line

M. Sasaki, T. Ishikawa, M. Iwasa, M. Miyabe, N. Muramatsu, H. Shimizu, Y. Tajima, A.O. Tokiyasu, H. Yamazaki, H.Y. Yoshida

2017 IEEE Nuclear Science Symposium and Medical Imaging Conference (NSS/MIC 2017) - Conference Proceedings (2018) 8532685.

Invited Talk and Oral Presentations at International Conferences

Latest Status Accelerator Science Activities at Tohoku, Japan (Oral presentation)

Hiroyuki Hama

National Synchrotron Radiation Laboratory, University of Science and Technology, Hefei, China, Dec. 26, 2018.

SLiT-J, a project of high brilliant compact 3 GeV light source in Japan (Invited oral presentation)

Hiroyuki Hama

Huazhong University of Science & Technology, Wuhan. China, Dec. 27, 2018

Latest Status Accelerator Science Activities at Tohoku, Japan (Oral presentation)

Hiroyuki Hama

National Synchrotron Radiation Research Center, Hsinchu, Taiwan, Nov. 8, 2018.

Accelerator-based Tunable Polarized THz Source (Oral presentation)

Hiroyuki Hama

Int. Conf. on Radiation and Emission in Materials (ICREM2018), Chiang Mai, Thailand, Nov. 22, 2018.

ELPH present status (Oral presentation)

Hiroyuki Hama
Scandinova Systems, Uppsala, Sweden, Mar. 12, 2018.

Experiments of Short Bunch Production and Coherent Radiation at t‐ACTS (Oral presentation)
Fujio Hinode
NSRRCELPH Oneday Workshop on SHORT BUNCH PRODUCTION and COHERENT THz RADIATION SOUCES, Hsinchu (Taiwan), Nov. 8‐9, 2018, (Oral)
Tsukuba International Congress Center, Tsukuba, Ibaraki, Japan,2018/Nov/13-17

Elastic electron scattering for proton charge radius determination
SUDA Toshimi
International workshop on the structure of the proton, 2019 年 2 月、山形、日本（招待講演）

Electron scattering for proton charge radius and charge density distribution of short-lived nuclei
SUDA Toshimi
International workshop on Proton and Neutron Densities and Radii in Nuclei and Related Topics, 2018 年 12 月、北京、中国（招待講演）

Proton Charge Radius
SUDA Toshimi
Physics of Muonium and Related Topics, 2018 年 12 月、名古屋、日本（招待講演）

Elastic Electron Scattering for Proton Charge Radius Determination
SUDA Toshimi
Correlation in Partonic and Hadronic Interaction 2018, 2018 年 9 月、エレバン、アルメニア（招待講演）

Elastic electron scattering off proton using 60 MeV electron linac of Tohoku University
SUDA Toshimi
The Proton Radius Puzzle and Beyond, 2018 年 7 月、マインツ、ドイツ（招待講演）

Electron scattering
SUDA Toshimi
20th Northeastern Asian Symposium on Nuclear Physics in the 21th Century, 2018 年 9 月、名古屋、日本（招待講演）

Present status of the SCRIT electron scattering facility
TSUKADA Kyo
5th Joint Meeting of the APS Division of Nuclear Physics and the Physical Society of Japan
Waikoloa, Hawaii, USA, October 23-27, 2018 (一般講演)

Present status of the SCRIT electron scattering facility
TSUKADA Kyo
5th Joint Meeting of the APS Division of Nuclear Physics and the Physical Society of Japan
Waikoloa, Hawaii, USA, October 23-27, 2018 (一般講演)

Electron scattering from ^{208}Pb and ^{132}Xe ions at the SCRIT facility

TSUKADA Kyo

The 7th international conference on Trapped Charged Particles and Fundamental Physics (TCP2018) Traverse, Michigan, USA, September 30-October 5, 2018 (招待講演)

Present status of the electron scattering experiments at the SCRIT facility

TSUKADA Kyo

ECT* conference “Probing exotic structure of short-lived nuclei by electron scattering”, Trento, Italy, July 16-20, 2018 (一般講演)

Elastic electron-proton scattering with low-energy electron beam at ELPH,

HONDA Yuki

5th Joint Meeting of the APS Division of Nuclear Physics and the Physical Society of Japan, Hilton Waikoloa Village Waikoloa, Hawaii, USA, October 23-27, 2018 (招待講演)

Status of ULQ2 experiment

HONDA Yuki

The 17th muon g-2/EDM collaboration meeting, KEK, Tsukuba, November 20-23, 2018 (口頭発表)

Summary of HYP2018

TAMURA Hirokazu

The 13st International Conference on Hypernuclear and Strange Particle Physics (HYP2018), Portsmouth, VA, USA,　June 24-29, 2018（招待講演）

Recent results in Hypernuclear physics

TAMURA Hirokazu

International School of Nuclear Physics 40th Course “The Strong Interaction: From Quarks and Gluons to Nuclei and Stars”, Erice, Italy, September 16-24, 2018　（招待講演）

Gamma-ray spectroscopy of hypernuclei

TAMURA Hirokazu

International Conference on Physics, Mandalay 2018 (ICPM21018) Mandalay, Myanmar, November 25-27, 2018　（招待講演）

Strangeness Nuclear Physics

TAMURA Hirokazu

The 8th International Conference on Quarks and Nuclear Physics Tsukuba, Japan, November 13-17, 2018（招待講演）

Optimum Control of Cellular Homeostasis in Photosynthetic Organism, Cyanobactria and Plant Cells

UOZUMI Nobuyuki

プラズマフォーラム　平成31年1月21-22日　仙台市

Heavy-ion fusion reactions for superheavy elements（Invited oral)

K. Hagino

Workshop on New Frontiers in Nuclear Physics and Nuclear Astrophysics,

Akdeniz University, Antalya, Turkey, May 28- June 1, 2018.

Fusion barrier distribution and superheavy elements（Invited oral)

K. Hagino

XLI Brazilian Meeting on Nuclear Physics, Maresias, Brazil, Sep. 2-6, 2018.

Mechanism of fusion reactions for superheavy nuclei（Invited oral)

K. Hagino

Workshop on Physics and chemistry of the heaviest elements and nuclei, Fifth Joint Meeting of the Nuclear Physics Division of the APS and the JPS, Hawaii, Octber 23, 2018

Future experiments at J-PARC (Invited oral presentation)

Hiroaki Ohnishi

Future opportunities toward studies in low-energy hadron physics with strangeness,

Stefan Meyer Institute for Subatomic Physics, Vienna, AUSTRIA, December 3-5, 2018

Charmed meson in Nuclei at J-PARC (Invited oral presentation)

Hiroaki Ohnishi

Hadron structure and interaction in dense matter,

KEK Tokai campus, Tokai, Japan, November 11-12, 2018

Hadron physics at J-PARC (Invited oral presentation)

Hiroaki Ohnishi

SMI-Seminar, Stefan Meyer Institute for Subatomic Physics, Vienna, AUSTRIA,

December 5, 2018

Light meson photoproduction at SPring-8 LEPS2/BGOegg experiments (Invited oral presentation)

N. Muramatsu for the BGOegg collaboration

PWA10/ATHOS5 2018 (The International Workshop on Partial Wave and Advanced Tools for Hadron Spectroscopy), IHEP, Beijing, July 16–20, 2018.

Photoproduction of light mesons at SPring-8 LEPS2/BGOegg experiments (Oral presentation)

N. Muramatsu, T. Hashimoto, T. Nam for the BGOegg collaboration

Fifth Joint Meeting of the Nuclear Physics Divisions of the APS and the JPS, Hawaii, Oct. 23–27, 2018.

Baryon resonance studies at SPring-8 LEPS2/BGOegg experiments (Invited oral presentation)

N. Muramatsu, T. Hashimoto, T. Nam for the BGOegg collaboration

The 52nd Reimei Workshop “Experimental and Theoretical Hadron Physics: Recent Exciting Developments”, J-PARC, Tokai, Jan. 9–11, 2019.

ω photoproduction on the proton near the threshold, (Invited oral plresentation)

Takatsugu Ishikawa

The 52nd Reimei Workshop "Experimental and Theoretical Hadron Physics: Recent Exciting Developments",
Ibaraki Quantum Beam Research Center (IQBRC), Tokai, Japan
January 09--11, 2019

Non-strange dibaryon resonances observed in coherent double neutral-pion photoproduction on the deuteron (Invited oral presentation, Keynote speech)

Takatsugu Ishikawa
8th International Conference on Quarks and Nuclear Physics,
Tsukuba, Japan, November 13-17, 2018.

Study of non-strange dibaryon resonances via coherent double neutral-meson photoproduction from the deuteron (Oral presentation)

Takatsugu Ishikawa
XXII International Conference on Few-Body Problems in Physics,
Caen, France, July 9-13, 2018

AXION Experiment in Japan (Invited oral presentation)

A. O. Tokiyasu
Revealing the history of the universe with underground particle and nuclear research 2019,
Sendai, Japan, Mar.7 – Mar. 9, 2019

Spectroscopy of elctro-produced hypernuclei at JLab (Invited Oral presentation)

Satoshi Nakamura
13th International Conference on Hypernuclear and Strange Particle Physics (HYP2018),
Portsmouth, USA 24-29 June 2018.

Topics on (e,e'K^+) spectroscopy of Λ hypernuclei at JLab (Plenary, Invited oral presentation)

Satoshi Nakamura
5th Joint Meeting of the APS Division of Nuclear Physics and the Physical Society of Japan
(Hawaii2018), Hawaii Island, USA, 23-27 Oct. 2018

Status of Λn Interaction study via the final state interaction in γ+d→K^++Λ+n production (Oral presentation)

Masashi Kaneta
Fifth Join Meeting of the Nuclear Physics Divisions of the APS and the JPS
Hilton Wailoloa vilage, Hawaii, USA
2018/Oct/23-28

Status of Λn Interaction study via the final state interaction in γd→$K^+\Lambda$n production (Oral presentation)

Masashi Kaneta
8th International COnference on Quark and Nuclear Physics (QNP2018)
Tsukuba International Congress Center, Tsukuba, Ibaraki, Japan

2018/Nov/13-17

Electromagnetic Calorimeter BGOegg for Quark Nuclear Physics (Invited oral)

H. Shimizu

The 33th Workshop on Radiation detectors and their uses, KEK, Jan. 28-30, 2019.

Anomalous Heat Effects Induced by Metal Nanocomposites and Hydrogen Gas (Oral presentation)

Y. Iwamura,

The 21st International Conference for Condensed Matter Nuclear Science, Colorado State University, Fort Collins, CO, USA, June 3 - 8, 2018.

Recent Advances in Heat Generation Experiments using Nano-sized Metal Composite and Hydrogen Gas at Condensed Matter Nuclear Reaction Division of Tohoku University (Invited oral)

Yasuhiro Iwamura,

2019 LANR/CF Colloquium at MIT, Massachusetts Institute of Technology, Cambridge, MA, USA, March 23-24, 2019.

Search for γ-ray radiation in NiCuZr nano-metals and H_2 gas system generating large excess heat（Oral presentation）

Jirohta Kasagi,

The 21st International Conference on Condensed Matter Nuclear Science ICCF21, Fort Collins, Colorado, USA, June 3-8, 2018.

STUDY ON GENERATION OF VARIABLE POLARIZED COHERENT THz RADIATION USING A CROSSED UNDULATOR （Poster presentation）

Hirotoshi Saito

The 29th Linear Accelerator Conference, LINAC 18, (Beijin, China), 16-21 September 2018.

Beam Diagnostics Employing Cherenkov Light from Hollow Silica Aerogel Radiator of Low Refractive Index（Oral presentation）

Shingo Ninomiya

NSRRC-ELPH One-day Workshop on SHORT BUNCH PRODUCTION and COHERENT THz RADIATION SOUCES, (Taiwan), 8-9 November 2018,.

Crossed-undulator for Variable Polarized THz Source （Oral presentation）

Hirotoshi Saito

NSRRC-ELPH One-day Workshop on SHORT BUNCH PRODUCTION and COHERENT THz RADIATION SOUCES, (Taiwan), 8-9 November 2018.

A high-resolution spectrometer for low-energy electron scattering for proton charge radius（Oral presentation）

T. Aoyagi他

5th Joint Meeting of the APS Division of Nuclear Physics and the Physics Society of Japan, ハワイ、米国, 2018年10月.

Development of an Aerogel Cherenkov counter for the LEPS2 experiment at SPring-8 （Oral presentation）

吉田千尋、

Fifth Joint Meeting of the Nuclear Physics Divisions of the APS and the JPS, Hawai, USA, October 25, 2018.

Development of the Aerogel Cherenkov counter for the LEPS2/SPring-8 experiment to search for the K^-pp bound state （Poster presentation）

吉田千尋

International School for Strangeness Nuclear Physics (SNP School 2018),
RCNP, Osaka University, Osaka, August 1-3, 2018.

学位論文（電子光理学研究センター所属）

修士論文 「陽子半径測定用の低エネルギー電子スペクトロメータ」
青柳 泰平，平成 30 年度，東北大学
修士論文 「陽子半径測定用スペクトロメータの焦点面検出器」
南波 和希，平成 30 年度，東北大学
修士論文 「LEPS2 実験のためのシリカエアロゲルチェレンコフ検出器の開発」
吉田 千尋，平成 30 年度，東北大学
修士論文 「光反応による核内 η’中間子に関する研究」
上田 惟行，平成 30 年度，東北大学
修士論文 「チェレンコフ光リングを用いた非破壊型ビームモニターの研究」
二宮 慎吾，平成 30 年度，東北大学

学位論文（他機関所属）

修士論文 「^{3}H(e,e’K$^+$)X 実験における K$^+$中間子識別手法とその評価」
板橋 浩介，平成 30 年度，東北大学
修士論文 「ハイパー核寿命測定実験用の新型粒子飛行時間測定器の開発」
小西 由浩，平成 30 年度，東北大学
修士論文 「Research and development of a new fine-grained scintillator tracker for the upgrade of T2K near detector」
藤田 亮，平成 30 年度，東京大学

V. Members of Committees

Steering Committee

2018

Hiroyuki HAMA*	ELPH
Toshimi SUDA	ELPH
Hiroaki OHNISHI	ELPH
Fujio HINODE	ELPH
Shigeru KASHIWAGI	ELPH
Norihito MURAMATSU	ELPH
Hidetoshi KIKUNAGA	ELPH
Hirokazu TAMURA	Graduate School of Science
Satoshi NAKAMURA	Graduate School of Science
Kouichi HAGINO	Graduate School of Science
Fuminori MISAIZU	Graduate School of Science
Yasushi KINO	Graduate School of Science
Nobuyuki UOZUMI	Graduate School of Engineering
Shigeo MATSUYAMA	Graduate School of Engineering
Masaki FUJITA	Institute for Materials Research
Yuji TAKAKUWA	Institute of Multidisciplinary Research for Advanced Materials
Takeo EJIMA	Institute of Multidisciplinary Research for Advanced Materials
Keiichi EDAMATSU	Research Institute of Electrical Communication
Masatoshi ITOH	Cyclotron and Radioisotope Center
Kenji TSUDA	Frontier Research Institute for Interdisciplinary Sciences

* Chairperson

General Advisory Committee

2018

Hiroyuki HAMA*	ELPH, Tohoku University
Toshimi SUDA	ELPH, Tohoku University
Hiroaki OHNISHI	ELPH, Tohoku University
Hidetoshi KIKUNAGA	ELPH, Tohoku University
Hirokazu TAMURA	Graduate School of Science, Tohoku University
Yasushi KINO	Graduate School of Science, Tohoku University
Masatoshi ITOH	CYRIC, Tohoku University
Kenji TSUDA	Frontier Research Institute for Interdisciplinary Sciences, Tohoku University
Tomohiro UESAKA	RIKEN Nishina Center
Daisuke JIDO	School of Science, Tokyo Institute of Technology
Takashi NAKANO	RCNP, Osaka University
Tomohumi NAGAE	Graduate School of Science, Kyoto University
Ryukou KATO	Accelerator Laboratory, KEK
Hideaki OHGAKI	IAE, Kyoto University
Akihiko YOKOYAMA	College of Science and Engineering, Kanazawa University
Yasuji OURA	Graduate School of Science and Engineering, Tokyo Metropolitan University

* Chairperson

Program Advisory Committee

2018

Toshimi SUDA	ELPH, Tohoku University
Hiroaki OHNISHI	ELPH, Tohoku University
Shigeru KASHIWAGI	ELPH, Tohoku University
Hidetoshi KIKUNAGA	ELPH, Tohoku University
Satoshi NAKAMURA*	Graduate School of Science, Tohoku University
Kazumasa SUGIYAMA	Institute for Materials Research, Tohoku University
Kiyoshi TANIDA	ASRC, Japan Atomic Energy Agency
Megumi NARUKI	Graduate School of Science, Kyoto University
Masaru YOSOI	RCNP, Osaka University
Yoshihiko SHOJI	LASTI, University of Hyogo
Yasuji OURA	Graduate School of Science and Engineering, Tokyo Metropolitan University
Koichi TAKAMIYA	Research Reactor Institute, Kyoto University

* Chairperson

VI. Approved Experiments

平成 30 度前期採択課題一覧

課題番号	課　題　名	申込責任者
2892	T2K 実験高度化のための 細分型プラスチックシンチレータ検出器の性能評価	松原 綱之
2893	SCRIT 実験用ドリフトチェンバーの性能評価	塚田 暁
2894	FOREST 超前方荷電粒子検出で拓く物理	石川 貴嗣
2895	Measurement of ${}^{4}_{\Lambda}\mathrm{H}$ lifetime with photon beam	永尾 翔
2896	単一コンパレータ法を用いた光量子放射化分析	大浦 泰嗣
2897	電子ライナックを用いた長寿命/短寿命有用放射性トレーサー製造法の開発	菊永 英寿
2898	家庭ごみ焼却スラグに含まれる希少金属元素の回収を目指した光量子放射化法による成分同定およびトレーサー作成 2	秋山 和彦

平成30度後期採択課題一覧

課題番号	課　題　名	申込責任者
2899	4年生学生実験：電子ビームによる Multi-Gap Resistive plate Chamberの基礎研究	大西 宏明
2900	Performance evaluation of the next generation DAQ system with high-rate detectors for the J-PARC E50 experiment	Ma Yue
2905	J-PARC E16実験のための電子同定システムとMRPC検出器の性能評価	小沢 恭一郎
2909	Multi-gap Resistive Plate Chamber の時間分解能性能評価 (国際共同大学院「宇宙創成物理学」高度実験)	金田 雅司
2910	吸収層からの光読み出しを利用し高いエネルギー精度を実現するサンプリング型カロリメータの性能検証	竹下 徹
2911	T2K 実験前置検出器アップグレード計画における細分型プラスチックシンチレータ検出器の性能評価	岩本 康之介
2903	無担体203Hgトレーサ製造のための205Tl(γ,pn)203Hg反応の励起関数測定	後藤 真一
2904	電子ライナックを用いたアルカリ金属のキャリアフリーRIトレーサー製造法の開発	池田 隼人
2906	家庭ごみ焼却スラグに含まれる希少金属元素の回収を目指した光量子放射化法による成分同定およびトレーサー作成３	秋山 和彦
2907	光量子放射化法によるプロメチウム（Pm）内包金属フラーレンの合成を目的としたRI製造 IV	秋山 和彦
2908	冷却CCDを用いた非密封RI用イメージング装置の開発	菊永 英寿
2912 (随時)	J-PARC E16実験のためのMRPC検出器の性能評価	小沢 恭一郎
2913 (随時)	小型のエアロジェルチェレンコフ検出器の光量評価	金田 雅司
2914 (随時)	Mo-100(γ,n)Mo-99反応の収率向上のためのWコンバータの最適厚さの検討	上坂　充
2919 (随時)	ミューオン g－2/EDM 実験と陽子半径測定実験に向けた読み出し回路一体型シリコンストリップ検出器の性能評価試験	本多 佑記

ELPH ANNUAL REPORT 2018

December 2019

Research Center for Electron Photon Science, Tohoku University
1-2-1, Mikamine, Taihaku, Sendai 982-0826, Japan

印刷所　株式会社　東北プリント
仙台市青葉区立町24番24号
TEL　022（263）1166㈹